Plasmonic Gold Nanoparticles: Combining Photoacoustic Imaging and Photothermal Therapy for New Cancer Treatments

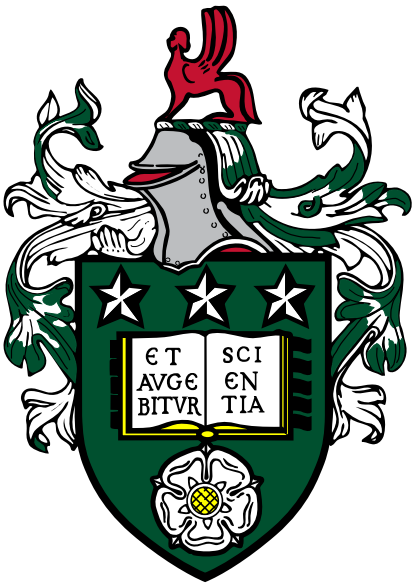

Oscar Brenchley Knights

Ultrasound Group
School of Electronic and Electrical Engineering

University of Leeds

Submitted in accordance with the requirements for the degree of

Doctor of Philosophy

May 2019

The candidate confirms that the work submitted is his own, except where work which has formed part of jointly authored publications has been included. The contribution of the candidate and the other authors to this work has been explicitly indicated below. The candidate confirms that appropriate credit has been given within the thesis where reference has been made to the work of others.

The work in chapter 3 of the thesis has appeared in the following publications:

- O. B. Knights, S. Ye, N. Ingram, D. M. J. Cowell, A. F. Markham, S. Freear, and J. R. McLaughlan, "Optimising gold nanorod size for maximum photoacoustic response while minimising cell toxicity," *Proc. Mtgs. Acoust.*, vol. 30, no. 1, pp. 020 001–, Jun. 2017
- O. Knights and J. McLaughlan, "Gold nanorods for light-based lung cancer theranostics," *International journal of molecular sciences*, vol. 19, no. 11, p. 3318, 2018
- O. B. Knights, D. M. Cowell, T. M. Carpenter, S. Freear, and J. R. McLaughlan, "Plasmonic gold nanoparticles for combined photoacoustic imaging and plasmonic photothermal therapy using a pulsed laser," in *2018 IEEE International Ultrasonics Symposium (IUS)*. IEEE, 2018, pp. 1–4
- O. B. Knights, S. Ye, N. Ingram, S. Freear, and J. R. McLaughlan, "Optimising gold nanorods for photoacoustic imaging in vitro," *Nanoscale Advances*, 2019

The work in chapter 4 of the thesis has appeared in the following publications:

- O. Knights and J. McLaughlan, "Gold nanorods for light-based lung cancer theranostics," *International journal of molecular sciences*, vol. 19, no. 11, p. 3318, 2018
- O. B. Knights, D. M. Cowell, T. M. Carpenter, S. Freear, and J. R. McLaughlan, "Plasmonic gold nanoparticles for combined photoacoustic imaging and plasmonic photothermal therapy using a pulsed laser," in *2018 IEEE International Ultrasonics Symposium (IUS)*. IEEE, 2018, pp. 1–4

The work in chapter 5 of the thesis has appeared in the following publications:

- O. Knights and J. McLaughlan, "Gold nanorods for light-based lung cancer theranostics," *International journal of molecular sciences*, vol. 19, no. 11, p. 3318, 2018
- O. B. Knights, D. M. Cowell, T. M. Carpenter, S. Freear, and J. R. McLaughlan, "Plasmonic gold nanoparticles for combined photoacoustic imaging and plasmonic photothermal therapy using a pulsed laser," in *2018 IEEE International Ultrasonics Symposium (IUS)*. IEEE, 2018, pp. 1–4

Oscar Brenchley Knights was responsible for devising and conducting all experimental work, processing and analysing data, and writing (and presenting) the manuscripts detailed above.

James R. McLaughlan provided supervision and guidance for experimental work, assisted in analysing data, and provided funding for lab equipment and supplies, and feedback on all manuscripts.

In publications with additional authors, their contributions were as follows:

Sunjie Ye assisted with analysing cell-related imagery, and provided feedback and guidance with manuscript writing and responding to reviewers. Nicola Ingram supplied the lung cancer cells and provided feedback and guidance with analysing cell-related data and manuscript writing. Steven Freear provided funding for lab equipment and supplies. Thomas Carpenter designed and built the ultrasound research platform. David Cowell assisted in building the ultrasound research platform. Alexander Markham provided funding for both Sunjie Ye and Nicola Ingram.

In memory of my childhood companion, Benji (2003 - 2018).
If the kindest souls were rewarded with the longest lives, dogs would outlive us all.

Acknowledgements

This thesis and its contents would not exist without the aid and support of a wide network of people around me. I would therefore like to take this opportunity to express my sincerest gratitude.

Firstly, I thank my supervisors Dr. James McLaughlan and Prof. Steven Freear for securing the funding that enabled me to undertake a PhD in the first place, and for providing the excellent laboratory facilities.

In particular, I would like to express my appreciation for Dr. James McLaughlan's valuable insights and constructive suggestions with regards to all aspects of my PhD. I am profoundly grateful for the support and guidance you so willingly gave me.

My thanks go to Dr. David Cowell, Mr Thomas Carpenter, and everyone else who contributed to the state-of-the-art facilities. A special thanks must be given to Dr. Sevan Harput who, with his strong coffee and sociable attitude, brought the entire group closer together.

My grateful thanks extends to Dr. Sunjie Ye, for teaching me many of the lab techniques I used in my experimental work, and to Dr. Nicola Ingram, for providing the cells I needed to complete my work and willingness to give her time so generously.

I am profoundly grateful to my office friends, Abdulrhman Alshaya, Asraf Mohamed, Safeer Hyder, and Chunqi Li, who were admirable companions in our collective ambition to accomplish a PhD.

A very special thanks goes to Chris Adams and Luzhen Nie. I am forever grateful for our enlightening conversations and all-round good times, and without you both, I would never have made it this far. I look forward to the day our paths cross again.

To my mum and dad, Alison and Brenchley Knights. I thank you for all the support and encouragement you have given, and continue to give me, in everything that I do. You got me through some of the toughest times of my PhD and made me who I am today.

Finally, my heartfelt thanks go to my partner Emma Pendlebury, for accommodating my ups and downs with such love and generosity, and supporting me in my pursuit of a PhD, and to my dog Layla, for being a stable pillar of unwavering love. This truly would not have been possible without you both.

Abstract

Cancer is a complex disease with significant variability between cases, and as a result, is one of the leading causes of death worldwide. Lung cancer is a particularly difficult form of cancer to diagnose and treat, due largely to the inaccessibility of lung tumours and the limited available treatment options. There is a need for highly targeted, minimally invasive treatment options that facilitate the complete removal of cancer from a patient while minimising damage to non-malignant tissue.

The development of plasmonic gold nanoparticles has lead to their potential use in a large range of disciplines, and in particular, they have shown great promise for application in biomedicine. Plasmonic gold nanoparticles possess many desirable characteristics, such as controllable size and shape during synthesis, the biocompatible and inert nature of gold, the potential functionalisation and surface modification prospects, and tunable surface plasmon resonances, that make them excellent candidates for biological use. These beneficial properties facilitate their use as contrast agents to further enhance existing light-based biomedical techniques, such as photoacoustic imaging and photothermal therapy, while possessing the ability to form new combined treatments.

In this thesis, gold nanorods - a subset of gold nanoparticles - will be investigated as a means to mediate photoacoustic imaging and photothermal therapy for combined lung cancer theranostics, while demonstrating their ability to improve current clinical practice. Since gold nanorods can be synthesised to be almost any size, and their aspect ratio governs their peak surface plasmon resonance, there may be an optimal sized AuNR for use in biomedical modalities that absorbs light at a particular wavelength. Four different sized gold nanorods (widths of 10, 25, 40, and 50 nm) with similar aspect ratios and therefore similar surface plasmon resonances (815 ± 26 nm) were considered for use in photoacoustic imaging. It was shown that the larger gold nanorods produced the highest photoacoustic amplitude at an equivalent number of nanoparticles, but were the most toxic, while the smallest gold nanorods were optimal at an equivalent total mass. The results indicate the importance for determining the dependence of total mass or number of nanoparticles on cellular targeting and uptake *in vivo*.

Gold nanorods can also be used as photoabsorbers for therapeutic modalities, such as photothermal therapy. Conventionally, continuous wave lasers are used to generate bulk heating in gold nanorods, that are situated in a target region, and the diseased tissue is destroyed via hyperthermia. However, there are potential negative side-effects of heat-induced cell death, such as the risk of damage to healthy tissue due to heat conducting to

the surrounding environment, and the development of heat and drug resistance. Therefore, the use of pulsed lasers for photothermal therapy was investigated and compared with continuous wave lasers. It was shown that, for continuous wave lasers, a larger number of gold nanorods in the absorbing region resulted in increased cell death, whereas with pulsed lasers, the location of the gold nanorods, with respect to the cells, was the most important factor governing laser-induced toxicity. Furthermore, gold nanorods targeted to lung cancer EGFR receptors showed enhanced therapeutic efficacy under pulsed laser illumination.

Finally, the potential for gold nanorods to enhance endobronchial ultrasound - an existing clinical procedure for guiding lung cancer needle biopsies - was considered. This routine practice uses conventional B-mode ultrasound and a wide field of view to facilitate the locating of lymph nodes and guide the staging of lung cancer. This technique could be further improved with the use of gold nanorod-mediated photoacoustic imaging with potentially minimal adaptation, since the underlying technology required to combine these modalities already exists. It was shown that inclusions of gold nanorods can be observed under pulsed laser illumination using imaging and transducer parameters comparable to that of endobronchial ultrasound. The potential for this promising new multimodality was demonstrated, with the aim of guiding future development.

Overall, the work presented in this thesis provided valuable insights into the development of gold nanorods for biomedicine, and has demonstrated the potential for improving new and existing theranostic modalities.

Contents

List of Figures

List of Tables

Abbreviations

AEDP	3-[(2-aminoethyl)dithio] propionic acid
ANOVA	Analysis of variance
ANSI	American national standards institute
AuNR	Gold nanorod
BSI	British standards institute
CEM_{43}	Cumulative equivalent minutes (at 43 °C)
CIRS	Computerized imaging reference systems
CT	Computed tomography
CTAB	Cetyltrimethylammonium bromide
DAPI	4,6-diamidino-2-phenylindole
DAQ	Data acquisition
DAS	Delay and sum
DMAS	Delay multiply and sum
DMEM	Dulbecco's modified eagle's medium
DMSO	Dimethyl sulfoxide
DNA	Deoxyribonucleic acid
DPBS	Dulbecco's phosphate-buffered saline
EBUS	Endobronchial ultrasound
EGFR	Epidermal growth factor receptor
EPR	Enhanced permeability and retention
FBS	Fetal bovine serum
FDMAS	Filter delay multiply and sum
FFT	Fast Fourier transform
FOV	Field of view
fPAM	Functional photoacoustic microscopy
HIFU	High intensity focused ultrasound
IF	Immunofluorescence
LA	Laser ablation
LEMAS	Leeds electron microscopy and spectroscopy

MHDA	Mercaptohexadecanoic acid
MPE	Maximum permissible exposure
MRI	Magnetic resonance imaging
MSOT	Multispectral optoacoustic tomography
MTAB	(16mercaptohexadecyl)trimethylammonium bromide
MTT	Thiazolyl blue tetrazolium bromide
NIR	Near infrared
NR	Nanorods
NSCLC	Non-small cell lung cancer
OPO	Optical parametric oscillator
PAA	poly(acrylic acid)
PAH	poly(allyamine hydrochloride)
PAI	Photoacoustic imaging
PA-PPTT	Photoacoustic plasmonic photothermal therapy
PEG	(Poly)ethylene glycol
PET	Positron emission tomography
pMPC-b-pLA	poly(2-methacryloyloxyethyl phosohorylcholine)-b-poly(lipoic methacrylate)
PPTT	Plasmonic photothermal therapy
PW-PPTT	Pulsed wave plasmonic photothermal therapy
PRF	Pulse repetition frequency
PWI	Plane wave imaging
RF	Radio frequency
ROI	Region of interest
SCLC	Small cell lung cancer
SDK	Software development kit
SPR	Surface plasmon resonance
TBNA	Transbronchial needle aspiration
TEM	Transmission electron microscope
TID	Thermal isoeffective dose
UARP	Ultrasound array research platform

List of Symbols

α	Optical attenuation coefficient
α_a	Acoustic attenuation coefficient
β	Thermal expansion coefficient
Γ	Grüneisen parameter
γ	Speed of sound through the medium
ϵ_{billi}	Optical extinction coefficients (bilirubin)
$\epsilon_{\beta C}$	Optical extinction coefficients (β-carotene)
θ_n	Beam steering angle
λ	Optical wavelength
λ_{SPR}	Longitudinal surface plasmon resonance
μ_a	Optical absorption coefficient
$\mu_{a.\text{deoxy}}$	Optical absorption coefficient (deoxygenated blood)
$\mu_{a.\text{fat}}$	Optical absorption coefficient (fat)
$\mu_{a.\text{melanosome}}$	Optical absorption coefficient (melanosome)
$\mu_{a.\text{oxy}}$	Optical absorption coefficient (oxygenated blood)
$\mu_{a.\text{water}}$	Optical absorption coefficient (water)
μ_s	Optical scattering coefficient
μ_s'	Reduced scattering coefficient
τ_{end}	Final time point of thermal treatment
τ_p	Laser pulse width
τ_T	Time period between laser pulses
τ_{th}	Thermal relaxation time
B	Average blood volume fraction
b_{Mie}	Scattering power
C_4	Constant for calculating maximum permissible exposure
C_{Billi}	Bilirubin concentration
$C_{\beta C}$	β-carotene concentration
CEM_{43}	Cumulative equivalent minutes (at 43 °C)
c_{p}	Specific heat capacity at constant pressure
dt	Time interval held at temperature T
E_{pulse}	Energy of a single laser pulse

F	Laser fluence
Fa	Fat content
f_c	Central frequency
f_{Mie}	Fraction of Mie scattering
f_{Ray}	Fraction of Rayleigh scattering
g	Anisotropy of scattering
I_0	Initial maximum light intensity
IC_{50}	Half maximal inhibitory concentration
$I(z)$	Optical intensity
i	Element number
L	Aperture length
M	Melanosome volume fraction
MPE_{skin}	Maximum permissible exposure for skin
N_{lines}	Number of lines required to build image
n	Number of angles
PRF(Hz)	Pulse repetition frequency
P_0	Maximum initial pressure
$P_{\text{peak}}(W)$	Peak power
p	Statistical significance
R	Aspect ratio
R_{CEM}	Approximated parameter for thermal dose equation
S	Haemoglobin oxygen saturation of vasculature
$T(t)$	Temperature at time t
$t(s)$	Laser exposure duration
$t_{\text{RX}}(x_f, z_f)$	Receive propagation time
$t_{\text{TX}}(x_f, z_f)$	Transmission propagation time
t_{image}	Time to record one image
$t_i(x_f, z_f)$	Total time-of-flight of propagating ultrasound wave
W	Water content
x_f	Lateral position of point in space
x_i	Lateral position of element
z	Distance (or depth)
z_f	Depth of point in space

Chapter 1

Introduction

Michael Faraday is often regarded as one of the first scientists to spark an interest in the study of light interactions with small particles when he gave a lecture in 1857 that was later awarded the Royal Society Bakerian Lecture prize [5]. In it, he explored a variety of experiments regarding how light interacts with a range of different materials, including silver, copper, platinum, tin, iron, mercury, rhodium, and iridium. His main interest, however, was in the phenomena surrounding that of colloidal gold particles: "I do not pretend that they are of great value in their present state, but they are very suggestive, and they may save much trouble to any experimentalists inclined to pursue and extend this line of investigation". He was referring to the extraordinary ability of colloidal gold to reflect, refract and absorb light of different colours based on a "mere variation in the size of its particles". We now know that there are many factors governing the wavelength of light that interacts with these unique particles, but for centuries, gold colloids were used as pigments in stained glass windows, potteries, fabrics, and even in medicine, with the observed optical effects believed to arise from the intrinsic colour of the particles. It was not until Faraday became interested in light-matter interactions, and delivered this ground-breaking Bakerian lecture, that many distinguished scientists, such as John Tyndall [6], Lord Rayleigh [7, 8], Sir C.V. Raman [9], and Gustav Mie [10], saw the potential in these particles, and the study of nanotechnology, nanoscience and plasmonics was born.

Since then, plasmonic nanoparticles have seen a steady growth in interest over the past few decades and have found uses in a vast array of disciplines from renewable energy through to health [11]. Our continued ability to manipulate the many different factors that make up a plasmonic nanoparticle has seen novel applications appear in unprecedented areas. In biomedicine alone, nanoparticles are used to deliver drugs and genes to specific areas of the body [12, 13]; as optical contrast agents in imaging modalities such as magnetic resonance imaging (MRI) [14]; for the detection of specific disease related biomolecules and proteins by acting as biosensors [15]; and as diagnostic and therapeutic agents for the detection and elimination of cancer [16, 17]; among others [18].

1.1 Scope

Scientific advances in the study of nanotechnology and bioengineering have enabled targeted therapies - that are designed to specifically target a patients disease - to increasingly become a reality. However, the complex nature of nanoparticles and their interactions with the human body suggest there is a substantial amount of research that is needed before safe clinical translation is possible. The work in this thesis aims to investigate and progress some of the key research areas required to advance the field of nanoparticle-based biomedicines, by focusing on gold nanoparticles for cancer diagnostics, therapy, and combined multimodal approaches, often termed 'theranostics'. Specifically, a subset of gold nanoparticles, known as gold nanorods, are explored as a means to mediate photoacoustic imaging and plasmonic photothermal therapy for lung cancer theranostics. Questions such as: what is the optimal gold nanorod size that provides the highest photoacoustic efficacy? how toxic are they on their own, and does their size affect this? and can gold nanorods be used in combined theranostic modalities to reduce waiting times and improve patient outcome?, will be investigated with valid conclusions drawn.

1.2 Motivation

Life-changing discoveries in nanotechnology and biomedicine have the potential to revolutionise the medical world on a global scale. Currently, it is estimated that approximately one sixth of all deaths worldwide is due to cancer, with the highest mortality rates originating from patients with lung cancer due to limited diagnostic and treatment options. The results from continued research into nanotechnology have shown considerable promise, with nanoparticles expected to dramatically improve clinical outcomes through innovative and novel approaches, in addition to improving upon already existing techniques [19]. In the case of developing new diagnostic and treatment options, extensive research is required to meet the strict regulations for safe human use, before a new modality can be routinely used in the clinic. This is especially true when developing a scheme based on something as complex as nanoparticles.

Gold nanoparticles have shown to be one of the most promising agents for biomedical uses, especially in modalities such as photoacoustic imaging and photothermal therapy. These two techniques are effective on their own, and with the use of gold nanoparticles as optical-absorbing agents, their efficacy can be greatly improved. Furthermore, since these techniques are both optical-based, there is the potential for them to be combined into a single gold nanoparticle-mediated theranostic modality. Techniques with dual-functionalities, such as this, may provide a means to treat otherwise untreatable diseases, and are the basis of future medical approaches known as precision medicines. Since gold nanoparticles are at the core of these procedures, it is clear that continued research into these particles is necessary to successfully develop new, effective and highly specific treatment options.

1.3 Objectives of this work and thesis layout

The work in this thesis was centred around the concept of translating gold nanoparticles from imaging to therapy, for the diagnosis and treatment of lung cancer, while demonstrating their ability to improve upon current clinical practice. The overall aims were to aid in the creation of dual-modality biomedical approaches by continuing the research and development of gold nanorods as optical absorbers in lung cancer theranostics, and to improve upon existing techniques such as endobronchial ultrasound, a clinical lung cancer staging modality, by combining it with gold nanorod-mediated photoacoustic imaging.

Starting with chapter 2, the necessary background information required to understand the rest of the presented work was provided. Important ideas and phenomena were described by way of a literature review and critical discussion. Gold nanorods were discussed in terms of their relevant properties, such as optical interactions and surface plasmon resonance, cytotoxicity and interaction with cells, and synthesis and functionalisation prospects, framed in context of application in lung cancer treatments. This was followed by introducing and discussing photoacoustic imaging and plasmonic photothermal therapy, and the role of gold nanorods in these modalities. The penultimate section considers an existing clinical technique for diagnosing lung cancer and the potential for improving this technique. Finally, the current use of gold nanorods as theranostic agents in the literature are discussed.

The aims and objectives of chapter 3 were to investigate the size-dependent effects of gold nanorods on aspects related to lung cancer photoacoustic imaging. Specifically, the effects of gold nanorod size was considered in relation to photoacoustic response across a range of incident laser fluences (taking into consideration other important aspects such as nanoparticle concentrations defined in terms of both mass and number of nanoparticles), the toxicity of gold nanorods to a common non-small cell lung cancer cell line, their photostability and melting thresholds under laser illumination, and an indication of lung cancer cellular uptake. These objectives will provide a greater understanding of the importance of gold nanorod since for application in photoacoustic imaging and aid in their future development. Since multiple sized gold nanorods were used throughout this thesis, a consistent naming format was followed based on their width and SPR. For example, 'Au10-811' had a width of 10 nm and SPR of 811 nm. The work in this chapter has been published in the following manuscripts:

- O. B. Knights, S. Ye, N. Ingram, D. M. J. Cowell, A. F. Markham, S. Freear, and J. R. McLaughlan, "Optimising gold nanorod size for maximum photoacoustic response while minimising cell toxicity," *Proc. Mtgs. Acoust.*, vol. 30, no. 1, pp. 020 001–, Jun. 2017
- O. Knights and J. McLaughlan, "Gold nanorods for light-based lung cancer theranostics," *International journal of molecular sciences*, vol. 19, no. 11, p. 3318, 2018
- O. B. Knights, D. M. Cowell, T. M. Carpenter, S. Freear, and J. R. McLaughlan, "Plasmonic gold nanoparticles for combined photoacoustic imaging and plasmonic

photothermal therapy using a pulsed laser," in *2018 IEEE International Ultrasonics Symposium (IUS)*. IEEE, 2018, pp. 1–4

- O. B. Knights, S. Ye, N. Ingram, S. Freear, and J. R. McLaughlan, "Optimising gold nanorods for photoacoustic imaging in vitro," *Nanoscale Advances*, 2019

Chapter 4 continued with the development of gold nanorods, by moving from their diagnostic abilities in photoacoustic imaging, to investigating their use as therapeutic agents in plasmonic photothermal therapy. The optical source used for delivering light to the gold nanorods was considered, with the aim of determining whether pulsed lasers are able to replace continuous wave lasers for plasmonic photothermal therapy. The specific objectives of this chapter were to understand the differences between using continuous wave or pulsed lasers, in combination with gold nanorods, to reduce cell viability in a lung cancer cell line with low laser energies, and to understand how targeting gold nanorods to lung cancer cells can improve therapeutic efficacy under both continuous wave and pulsed laser illumination. Furthermore, the size of the gold nanorods used as optical absorbers was considered in terms of their photothermal conversion efficacy under continuous and pulsed wave laser irradiation, and laser-induced toxicity to a lung cancer cell line. The work in this chapter aims to aid in the development of optical-based therapeutic modalities that rely on gold nanorods, by considering the use of pulsed lasers as the optical source in plasmonic photothermal therapy, leading to future therapeutic techniques with potentially reduced complexities and costs, and improved patient outcome. Some of the work in this chapter has been published in the following manuscripts:

- O. Knights and J. McLaughlan, "Gold nanorods for light-based lung cancer theranostics," *International journal of molecular sciences*, vol. 19, no. 11, p. 3318, 2018

- O. B. Knights, D. M. Cowell, T. M. Carpenter, S. Freear, and J. R. McLaughlan, "Plasmonic gold nanoparticles for combined photoacoustic imaging and plasmonic photothermal therapy using a pulsed laser," in *2018 IEEE International Ultrasonics Symposium (IUS)*. IEEE, 2018, pp. 1–4

In chapter 5, the focus then shifted to the development and enhancement of endobronchial ultrasound by demonstrating the capability of combining the existing technique with gold nanorods and a pulsed laser system for added photoacoustic imaging functionalities. The objectives of this chapter were to explore the necessary transducer requirements for both conventional B-mode imaging and photoacoustic imaging with gold nanorods, and to demonstrate the potential benefits of combining these techniques. This work aims to aid in the future development of endobronchial ultrasound into an improved lung cancer diagnostic tool, with the potential for a dual-modality approach by enabling a therapeutic avenue through plasmonic photothermal therapy. Some of the work in this chapter has been published in the following manuscripts:

- O. Knights and J. McLaughlan, "Gold nanorods for light-based lung cancer theranostics," *International journal of molecular sciences*, vol. 19, no. 11, p. 3318, 2018
- O. B. Knights, D. M. Cowell, T. M. Carpenter, S. Freear, and J. R. McLaughlan, "Plasmonic gold nanoparticles for combined photoacoustic imaging and plasmonic photothermal therapy using a pulsed laser," in *2018 IEEE International Ultrasonics Symposium (IUS)*. IEEE, 2018, pp. 1–4

Finally, chapter 6 provided a summary of the thesis along with major conclusions and the discussion of future work.

Chapter 2

Gold nanorods in medicine

The aim of this chapter is to provide the necessary background and context for understanding this thesis by way of a literature review and discussion.

2.1 Cancer

Cancer is the name given to a large group of diseases that share a variety of similar characteristics, such as the growth of tumours and ability to spread to other parts of the body, known as metastasis [20]. It is one of the leading causes of death worldwide, with a predicted 70 % increase in new cases by 2034 [21]. The most prevalent forms of cancer are lung and breast, however the highest mortality rates occur in patients with lung cancer (1.76 million deaths compared with 862 000 deaths for colorectal cancer, the second most common cause of death by cancer) [21]. This exceedingly high mortality rate can be attributed to the lack of early diagnosis - an important aspect for successful treatment of any cancer type - and the limited available treatment options.

Due to the large variety of cancer types and the complex nature of the condition, the prescribed diagnosis and treatment options must be tailored to the specific case at hand, often with the aid of large multidisciplinary teams. The idea that there may exist a 'silver bullet' for treating all forms of cancer is a steadily diminishing one, as our understanding grows. In 1976, Peter Nowell suggested that cancerous tumours were a collection of diverse cells that were highly individual to the patient and may require a specific, personalised treatment [22]. This sparked an interest into studying the tumours more closely with regards to their cellular makeup, but it was not until scientists sequenced the genetic code of single cells, 35 years later, that we realised just how diverse cancerous tissue was. The considerable variety of cell types within a single tumour can cause major problems when it comes to targeted therapies (particularly with treatments involving drugs that target specific cells) and has been suggested as a leading contributor to the failure of a lot of treatments [23].

One of the biggest problems with many of the current cancer therapies is the unwanted

destruction of healthy, non-cancerous tissues during treatment. For example, chemotherapy is the second most common cancer treatment and it relies on the use of highly toxic chemicals to disrupt cell mitosis and damage rapidly proliferating cells [24]. This passive treatment option helps to suppress the spread of cancer by preventing certain cells from reproducing, however it does not selectively target cancerous cells. This indiscriminate elimination of cells can result in negative sides effects, such as immunosuppression [25], gastrointestinal distress [26], anaemia [27], hair loss [28], and others [29, 30, 31, 32, 33].

Radiotherapy is another common treatment option that destroys cancerous tissue by utilising ionising radiation to damage the structure of dividing cells. This can be to either completely destroy the tumour, known as curative radiotherapy, or to make other treatments more effective, such as chemotherapy or surgery. Similar to chemotherapy, the beam of radiation (usually x-rays) does not selectively destroy cancer cells but instead causes damage to the DNA of any cells in the path of the beam [34]. While this treatment is more localised than chemotherapy (the radiation is directed at the tumour location, rather than the entire body), there is still collateral damage as a result of the radiation passing through healthy tissue to reach the tumour site.

The surgical removal of tumours remains the most common treatment method prescribed in the clinic [35]. The tumour, and a section of surrounding healthy tissue, is removed surgically to ensure the complete resection of the tumour volume. This treatment option is particularly useful in the early stages of cancer since the tumour volume will likely be small and the boundaries easier to locate. Surgical resection can be an effective method for eliminating cancer from the body, although it is not always a possibility (or it can result in major operations) due to factors such as tumour location and size [36]. For example, a tumour located in breast tissue that is larger than 5 cm is likely to result in a mastectomy.

Patients diagnosed with lung cancer can receive one or all of the discussed treatments, depending on the stage of the cancer, however their efficacy still remains low. While these treatment protocols are routinely used in the clinic to treat patients with many different forms of cancer, they all cause unwanted collateral damage to normal, healthy tissues, and the resulting side effects can be serious and long-lasting. There is a clear need for highly targeted, minimally invasive treatment options that facilitate the complete clearance of cancer from a patients body without causing unwanted damage to non-cancerous tissues.

Laser therapy is a clinically used, minimally invasive treatment option that aims to reduce or completely destroy a tumour volume by way of laser ablation [37]. The laser light is delivered via a laser fibre to a cancerous region where the high intensity focused light heats the tissue to temperatures typically in excess of $48 - 50\,^{\circ}\mathrm{C}$, resulting in tissue necrosis [38]. It is predominantly used for the treatment of superficial cancers, however it can also be used to treat lung cancer. This would involve inserting a bronchoscope, with a laser fibre attached, through the mouth and into the lung, where ablation of the tumour tissue would be performed from close proximity [39]. Generally, for lung cancer treatment, this procedure is only used when a patient is having difficulty breathing due to

the tumour blocking airways and restricting airflow [37], or in some cases, it may be used for treating early-stage lung cancers (stage 1). It is also often used in combination with other treatments, such as radiation therapy, chemotherapy, and surgery, to enhance the efficacy of these treatments and improve patient outcome [40]. However, it is rarely used as a sole therapeutic procedure for treating lung cancer. Hyperthermia-based therapies, such as these, are generally low risk treatments with few negative side effects due to their targeted nature. In addition, hyperthermia has been shown to enhance the efficacy of many anticancer drugs by increasing the cancer cell sensitivity to the drugs [41]. These therapies have the potential to be further enhanced through the use of gold nanoparticles as optical-absorbing agents, and may facilitate their use as a primary treatment option.

It is widely established that early diagnosis of cancer is an essential aspect that governs survival rates and patient outcome following treatment [42]. In the case of lung cancer, symptoms do not typically appear in the early stages of the tumour development and this often leads to detection occurring during the later stages when treatments are less effective. If indicative symptoms do arise, then the process for diagnosing lung cancer would first involve a physical examination by a doctor, followed by an imaging technique, such as X-ray, magnetic resonance imaging (MRI), computed tomography (CT) and positron emission tomography (PET) scans [43]. If these methods provided an indication that cancer was present in the lung, then further examination would be carried out to determine whether the tumour was either small cell lung cancer (SCLC) or non-small cell lung cancer (NSCLC), malignant or benign, and the present stage of the cancer. This information would then be used to form a prognosis and guide treatment. Endobronchial ultrasound transbronchial needle aspiration (EBUS-TBNA) is one such method for mediastinal staging of lung cancer (discussed further in section 2.5), and is preferred over other techniques such as mediastinoscopy [44]. It is capable of reaching the interlobar, mediastinal, and hilar lymph nodes, with the exception of lymph node stations 5 (subaortic) and 6 (para-aortic) [45], and combined with its high detection sensitivity, minimal invasiveness, ease of restaging, and in some cases, its lack of a need for general anaesthesia [43]; this procedure is routinely administered to diagnose and stage lung cancer. While this technique is already highly effective, there are potential ways to enhance its efficacy further and extend its capabilities, by combining it with additional imaging techniques (discussed further in section 2.5 and chapter 5).

2.2 Gold nanoparticles and their properties

Nanoparticles have long been seen as a valuable resource for applications in a wide range of disciplines [11, 46, 47, 48, 49, 50]. They can be synthesised to be any shape (e.g. sphere, rod, star, tube, disc) or size, and almost any composition, be that organic (e.g. liposomes, vesicles, micelles, dendrimers), or inorganic (e.g. copper, silver, gold, carbon, quantum dots, iron oxide). For application in biomedicine, the choice between using organic or inorganic nanoparticles relies on the specific needs and desired outcomes of the modality in which it

is to be used.

Organic nanoparticles have typically been shown to be less toxic than inorganic nanoparticles, making them inherently more biocompatible [51]. Furthermore, organic nanoparticles have the benefit of being biodegradable, which reduces many of the concerns surrounding their biodistribution when injected into a patient and their post-treatment clearance from the body [51]. These advantages over inorganic nanoparticles may mean fewer obstacles preventing them from clinical translation. However, there are still many issues in the development of organic nanoparticles that are limiting their efficacy as therapeutic agents [52], such as difficulties achieving uniform sizes, morphologies, and structures with large-scale synthesis [53]. Furthermore, for optical absorption-based biomedical modalities that rely on the efficient conversion of light to heat, organic nanoparticles pose significant challenges, such as a lack of intrinsic near-infrared (NIR) optical absorption, difficulties in controlling their optical properties, concerns with treatment efficacy due to low photostability, and the risk of photobleaching [54, 55, 56, 57, 58]. Nevertheless, organic nanoparticles that overcome these barriers are starting to emerge [59, 60].

Inorganic nanoparticles are capable of solving many of the issues with organic nanoparticles (a reason why interest has been so high), however they exhibit problems of their own. For example, the intrinsic biodegradability that organic nanoparticles possess does not apply to their inorganic counterparts, and there are concerns over long-term toxicity. However, there are many benefits of using inorganic nanoparticles, especially with regards to optical absorption-based approaches [61], since inorganic nanoparticles, such as metallic nanoparticles, show excellent photothermal conversion efficacies, high optical absorption cross-sections, easily tuneable optical properties, and no risk of photobleaching [62, 63]. Of the many inorganic nanoparticles currently in development, gold has shown to be one of the most promising compositions.

Bulk gold is widely-established as being one of the least reactive elements in the periodic table [64]. It is non-reactive with air or water (and so will not oxidise), is extremely resistant to corrosion, and does not react with chemicals inside or outside the body (a reason why jewellery is often made from gold) [65]. It has even been used to treat various illnesses, such as rheumatoid arthritis [66], by medical practitioners for thousands of years [67], suggesting its potential medicinal benefits and low toxicity in biological systems. Gold nanoparticles also share these favourable attributes for biological use, however when bulk gold is reduced to the nanoscale, biological interactions become significantly more complex (see section 2.2.1) [68].

Gold nanoparticles can be synthesised to be a large range of shapes, with nanorods, nanoshells, nanocages, and nanostars being studied extensively due to their strong absorption in the NIR [69]. While these have all shown promise for biomedical uses, this thesis will focus solely on the gold nanorod (AuNR), due to a combination of desirable characteristics, such as, comparatively easy synthesis for large-scale production, the possibility for fine-tuning its optical-absorption by dimensional control (and therefore a large range of

possible sizes), a generally higher cellular uptake and lower toxicity compared with other shapes, and a large absorption cross section for its size - all of which are important aspects for clinical translation.

AuNRs have the potential to improve patient care by improving current clinical practice in both diagnostic and therapeutic areas. As discussed in section 2.1, lung cancer is particularly difficult to diagnose and treat, and treatments such as laser therapy have limited use. AuNRs may broaden the versatility of these treatments by facilitating increased penetration depths and therapeutic access to tumours that would otherwise be inaccessible. The important properties and development aspects of AuNRs that make them interesting for biomedical use and support their continued progression into clinical translation will be discussed in the following sections.

2.2.1 Cytotoxicity and synthesis

The mechanisms with which AuNRs interact with biological systems as they are distributed, metabolised and eliminated, are key aspects in understanding where cytotoxicity arises from and how to prevent it. While it has been shown that AuNRs are not toxic under certain conditions [70, 71], there are many factors that must be considered when determining toxicity, such as the chemicals left behind during the synthesising process. One of the most common methods for fabricating AuNRs is by seed-mediated growth, and the simplest form of this process requires the use of a cationic surfactant known as cetyltrimethylammonium bromide (CTAB) [72, 73]. CTAB is a capping agent that helps to form more accurately shaped AuNRs and prevent them from aggregating [74], though it has been shown to be toxic to biological cells [75], especially if there is free-floating CTAB in the AuNR solution [76]. Careful removal of the free-floating CTAB in the supernatant is needed before the AuNRs can be safely used in a clinical setting [75, 77]. However, on the surface of the AuNR, the CTAB forms a bilayer that is usually left behind after removal of the supernatant from the AuNR solution [78]. This CTAB bilayer is not static and can dynamically desorb from the surface of an AuNR, leading to cellular toxicity. However, the CTAB bilayer is responsible for preventing aggregation, and removing this coating can result in other problems, such as a reduction in tumour uptake and a shift in SPR. This can be mitigated by replacing the CTAB with other, less-toxic coatings (as discussed in section 2.2.3).

Another common capping agent for gold nanoparticles is a citrate layer [79]. While it is possible to synthesise spherical gold nanoparticles by way of a citrate-based chemical process (originally developed by Turkevich et. al. [80] and improved by Frens et. al. [81]), citrate-capped AuNRs can only be synthesised by either displacing or adsorbing onto the existing CTAB layer of a AuNR that has been synthesised using CTAB [82]. Citrate-capped AuNRs that have been synthesised in this way have shown to be less toxic to a variety of cell lines, compared with CTAB-capped AuNRs, due to the reduced toxicity of citrate itself and the complete removal of CTAB during the synthesising process [83, 84, 85]. The loosely-bound citrate layer on the AuNRs can also be easily exchanged with a multitude of

thiolated molecules, such as peptides, proteins, and DNA [86], which is an important aspect for biomedical applications (discussed further in section 2.2.3). Furthermore, there have been reports that citrate-stabilised gold nanoparticles do not induce platelet aggregation or a change in plasma coagulation time in human blood [87], indicating their potential biocompatibility.

In addition to CTAB and citrate mentioned previously, many other surface coatings for AuNRs have been tested in the literature, such as mercaptohexadecanoic acid (MHDA), polyethylene glycol (PEG), poly(acrylic acid) (PAA), poly(allyamine hydrochloride) (PAH), poly(2-methacryloyloxyethyl phosohorylcholine)-b-poly(lipoic methacrylate) (pMPC-b-pLA), (16-mercaptohexadecyl)trimethylammonium bromide (MTAB), 3-[(2-aminoethyl)dithio] propionic acid (AEDP), transferrin, plasmid, rhodamine, and many more [88]. The multitude of possible surface coatings makes the process for testing toxicity difficult since each new chemical must go through the same rigorous testing required to ensure safety.

Further to ensuring the chemicals and coatings on the surface of AuNRs are not toxic, it is also important to understand the other potential routes for AuNRs to induce toxicity [89], including cellular stresses and biological responses that may not necessarily result in the death of cells [90]. Their interactions with biological tissues and cells as they flow through the circulatory system may lead to unwanted cytotoxicity or cell disruption, such as oxidative stress, inflammation, mutagenesis, DNA damage, and protein up/down regulation, among others [91, 92, 93], as they interfere with some of the vital cellular components, such as the cell membrane, mitochondria, or nucleus. For example, citrate-capped gold nanoparticles were shown to alter the expressions of genes related to detoxification, lipid metabolism, cell cycle, defence response, and circadian rhythm, in the spleen and liver of rats [94]. There have been many reports on the properties of AuNRs that can disrupt normal cellular behaviour, such as their dimensions, overall size, coatings, and surface charge, and results vary between both in vivo and in vitro testing, with additional differences occurring between different cell lines [76]. Some of the literature that considers these different routes for in vitro toxicity have been summarised in table 2.1.

Another crucial feature in the development of AuNRs for biomedical uses is the ability to scale-up production. Improving the methods of synthesising AuNRs to produce large volumes of AuNRs, that exhibit highly controllable dimensions and properties, will make clinical uses of AuNRs more feasible due to reduction in costs and increase in reliability [95]. Furthermore, the clinical translation of AuNRs will require the production to meet specific regulatory criteria, known as 'good manufacturing practice' (GMB) [96], that ensures the quality and reproducibility of new medical drugs and devices. Citrate-mediated synthesis has shown to meet the need for large-scale production [97], however there are improvements to be made with regards to monodispersity. There are many methods for synthesising AuNRs, such as chemical reduction, polymer-mediated, biological, and electrochemical methods [98, 99, 100, 101, 102], and the continued development and refinement of these techniques will assist in delivering AuNRs that are ready for clinical use.

Table 2.1: Cytotoxicity of gold nanorods in the literature.

Dimensions	Surface Coating	AuNR Concentration	Cell Line	Exposure	Cell Viability	Author (Year)
$100 \times 200\,\mathrm{nm}$	AEDP, plasmid, rhodamine, transferrin	$750\,\mu\mathrm{g\,mL^{-1}}$	HEK293	4 h	$750\,\mu\mathrm{g\,mL^{-1}} \approx 50\,\%$	Salem (2003) [103]
$11 \times 65\,\mathrm{nm}$	PEG, CTAB	$0.01 - 0.5\,\mathrm{nmol}$	HeLa	24 h	0.05 nmol: CTAB $\approx 20\,\%$, PEG $\approx 90\,\%$	Niidome (2006) [104]
AR = 4.1	CTAB, PAA, PAH	0.4 nmol	HT-29	96 h	CTAB $\approx 30\,\%$, PAA $\approx 90\,\%$, PAH $\approx 80\,\%$	Alkilany (2009) [105]
$8 \times 26\,\mathrm{nm}$ $10 \times 36\,\mathrm{nm}$ $9 \times 32\,\mathrm{nm}$	CTAB, MHDA, PEG	$5 - 100\,\mu\mathrm{g\,mL^{-1}}$	HaCaT	24 h	$50\,\mu\mathrm{g\,mL^{-1}}$: CTAB $\approx 10\,\%$, MHDA $\approx 110\,\%$, PEG $\approx 100\,\%$	Grabinski (2011) [90]
$10 \times 42\,\mathrm{nm}$	CTAB, MTAB	$100\,\mu\mathrm{g\,mL^{-1}}$	MCF7	24 h	CTAB $\approx 5\,\%$, MTAB $\approx 95\,\%$	Vigderman (2011) [106]
$25 \times 52\,\mathrm{nm}$	No coating	$2.5 - 15\,\mu\mathrm{g\,mL^{-1}}$	A549	4 h	$5\,\mu\mathrm{g\,mL^{-1}} \approx 75\,\%$, $15\,\mu\mathrm{g\,mL^{-1}} \approx 10\,\%$	Tang (2015) [107]
$65 \times 534\,\mathrm{nm}$	Residual oxygen species from synthesis	$200\,\mu\mathrm{g\,mL^{-1}}$, $400\,\mu\mathrm{g\,mL^{-1}}$	Human dermal fibroblast	96 h	$200\,\mu\mathrm{g\,mL^{-1}} \approx 80\,\%$, $400\,\mu\mathrm{g\,mL^{-1}} \approx 75\,\%$	Favi (2015) [108]
$10 \times 90\,\mathrm{nm}$	No coating	$0.01 - 5\,\mathrm{mg\,mL^{-1}}$	ARPE-19	72 h	$0.01\,\mathrm{mg\,mL^{-1}} \approx 90\,\%$, $0.1\,\mathrm{mg\,mL^{-1}} \approx 35\,\%$	Karakoçak (2016) [109]
$15 \times 50\,\mathrm{nm}$	CTAB, pMPC-b-pLA	$30\,\mu\mathrm{g\,mL^{-1}}$	MCF-7	72 h	CTAB $\approx 20\,\%$, pMPC-b-pLA $\approx 100\,\%$	Jiang (2017) [110]

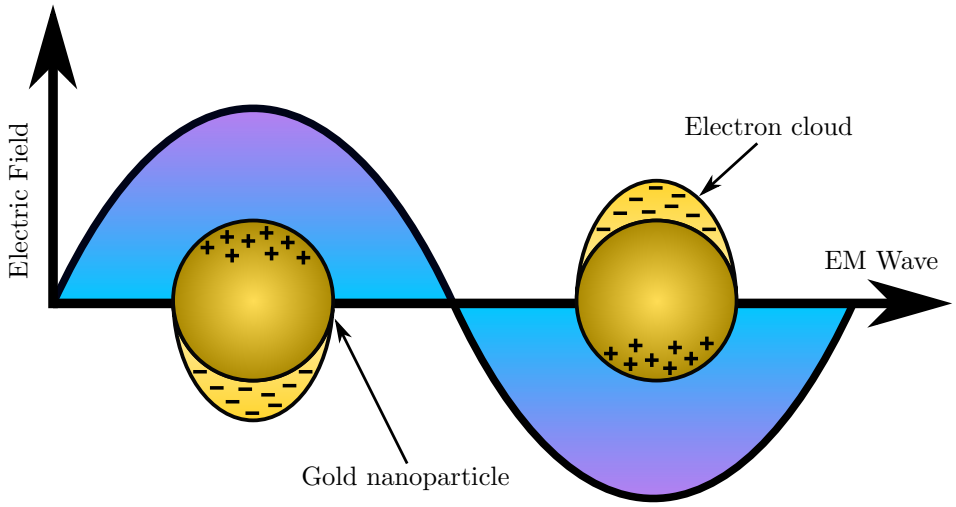

Figure 2.1: The conduction band electrons of a plasmonic nanoparticle begin to coherently oscillate in the presence of an electromagnetic field, when the frequency of incident light is in resonance with the oscillation.

2.2.2 Optical properties

Gold nanoparticles exhibit interesting optical properties when compared with bulk gold. When a plasmonic nanoparticle, such as a AuNR, is under the influence of an electromagnetic (EM) field, the surface conduction electrons are excited, and begin to coherently oscillate with the EM field (see figure 2.1) [111]. The negatively charged 'electron cloud' is displaced by the EM field and the positively charged lattice pulls back on the coherent collection of electrons via a Coulomb restoring force. It occurs only when the wavelength of the incident EM wave corresponds to the resonant frequency of the electron cloud [112]. This phenomena is known as a localised surface plasmon resonance (SPR) [113], and the underlying physical mechanisms can be likened to a dampened spring [114].

As a result of this extraordinary ability to interact with light, and enhance the surrounding EM-field, AuNRs are able to strongly absorb and scatter EM radiation. The incoming light absorbed by the nanoparticle is converted into heat via electron-electron and electron-phonon relaxations [115], and enables the possibility for medical techniques, such as photoacoustic imaging (PAI) and plasmonic photothermal therapy (PPTT), to emerge (discussed further in sections 2.3 and 2.4). This heightened interaction with light is unique to plasmonic nanoparticles and the optical absorption is approximately 5 or 6 orders of magnitude larger than that of other conventional contrast agents used in medicine [116].

The SPR of plasmonic nanoparticles only occurs at a particular wavelength of incident light, and this is influenced by the composition of the nanoparticle, as well geometrical properties such as size and shape [117]. For example, nanoparticles of various compositions and sizes have been used for thousands of years (possibly without knowledge) for visual

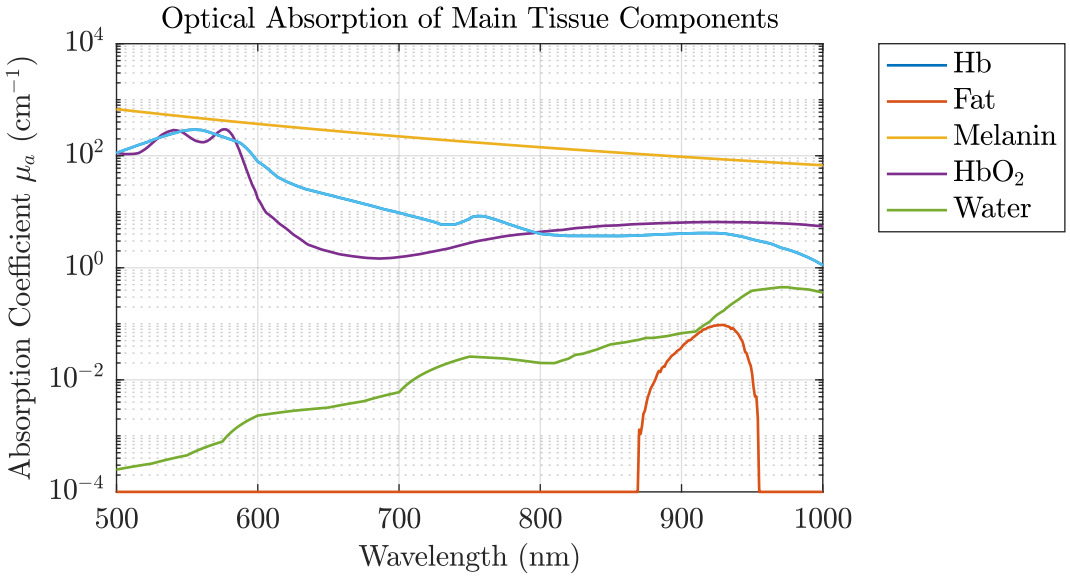

Figure 2.2: Absorption coefficient of the five main tissue components: deoxygenated haemoglobin (blue), fat (orange), melanin (yellow), oxygenated haemoglobin (purple), and water (green), contributing to overall optical absorption as a function of wavelength. Data is based on work by Jacques et. al. (2013).

effects in objects such as stained glass windows or the renowned Lycurgus Cup [118]. In the case of spherical gold nanoparticles (gold nanospheres), the SPR can only be shifted (from approximately 520 - 550 nm) by altering its size [119], since the composition and shape is fixed, and they exhibit only one absorption band. AuNRs, however, possess two SPR bands - a transverse and longitudinal band - due to their specific shape, and the ratio between the width and length, i.e. aspect ratio, of the AuNR is the most significant contributor to the absorption bands. An increase in aspect ratio leads to a blue-shift in the transverse SPR and a red-shift in the longitudinal SPR [120], with the longitudinal SPR, λ_{SPR}, scaling linearly with aspect ratio, R, according to [121],

$$\lambda_{\mathrm{SPR}} = 95R + 420 \tag{2.1}$$

This relationship provides a method of fine-tuning their SPRs to absorb at a desired wavelength, approximately within the range $750 - 1400$ nm, by synthesising the AuNRs with a particular aspect ratio. This is particularly useful for medical applications since biological tissues exhibit a reduced optical attenuation in two distinct near-infrared (NIR) wavelength regions [122, 123]. The first ranges from approximately $650 - 900$ nm and is a region where the optical absorption of water and haemoglobin (the two main absorbers of light) are minimal (figure 2.2) [116, 124], and the second ranges between $1000 - 1350$ nm [125]. Light penetration is much deeper in these regions (commonly referred to as the first and second 'biological windows') and has been shown, in extreme cases, to travel as deep

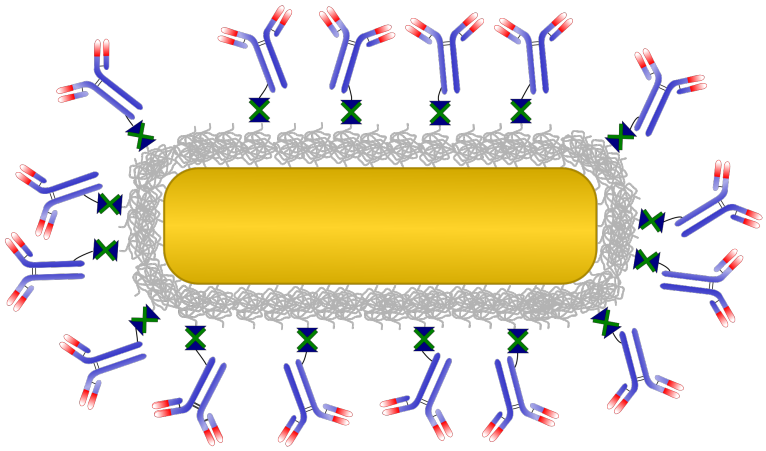

Figure 2.3: A schematic showing a functionalised gold nanorod.

as 10 cm into tissue [126]. The ability to tune the longitudinal SPR peak into the NIR allows for the use of infrared lasers in biomedical applications, and facilitates access to deep regions of tissue. The majority of AuNRs have been developed to absorb light in the first NIR window, with the number of second NIR window-absorbing AuNRs remaining limited. This is largely to due the difficulty in synthesising high aspect ratio AuNRs that absorb above 1000 nm but remain smaller than 100 nm [127]. The second NIR window has added benefits such as the further increase in optical penetration due to the large reduction in absorption of haemoglobin and blood.

2.2.3 Functionalisation and targeting

One of the many potential benefits of using AuNRs for biomedical applications is their ability to be functionalised with a wide range of organic and inorganic molecules [128]. Gold has the ability to form strong gold-thiolate bonds that facilitate surface modification [129]. The surface of a AuNR can be modified to achieve one or many different outcomes that support the AuNRs reaching their desired location. When attempting to deliver a dose of gold nanorods to a tumour site the injected bolus must overcome a series of complex barriers, both physiological and chemical, such as particle diffusion, aggregation, protein adsorption, flow and shear forces, renal clearance, and phagocytic sequestration [130]. For example, when nanoparticles enter the blood stream of a patient they undergo opsonisation, and resident macrophages of the mononuclear phagocyte system (MPS) subsequently begin to uptake the AuNRs, which leads to a build up of AuNRs in the reticuloendothelial system (RES) (i.e. the liver and spleen) [131]. This non-specific, high accumulation of AuNRs in healthy organs is undesirable as it reduces the numbers that reach the target region, limiting treatment efficacy. Furthermore, the complex nature of tumour growth - interrupted vasculature, aggressive cellular growth, dense extracellular matrix, and impaired lymphatics

- can be a significant barrier for AuNRs to overcome since it produces a high intratumoral pressure gradient that can prevent AuNRs from crossing the tumour boundaries [132]. If these barriers are not addressed, then significantly reduced treatment efficacy could be observed as an insufficient number of AuNRs reach the tumour location. Alternatively, a highly concentrated dose of AuNRs would need to be administered to a patient to achieve sufficient uptake in the tumour, which could increase overall treatment costs and potentially elevate the required dose above the safe human limit.

The bloodstream of living organisms are diverse mixtures of many different molecules, such as proteins, nutrients, and electrolytes, and these have been shown to interact with nanoparticles in previously unexpected ways [133]. Proteins and molecules will adsorb onto the surface of AuNRs almost immediately after introduction into blood and form what is known as a 'corona' around the AuNRs. Its composition is governed by the nanoparticle material, size, and surface chemistry, as well as the temperature and length of exposure to the surrounding physiological fluid [134]. The corona has been shown, not only to affect the properties of the AuNRs themselves, but also induce structural rearrangements of the proteins that are bound to it [135, 136], while also facilitating the rapid clearance of AuNRs via the RES [137]. Furthermore, the toxicity, uptake, pharmacokinetics, and immunogenicity of the AuNRs are also affected since the corona is what the cells 'see' when the AuNRs come into contact with them [133]. In this case, the AuNRs can essentially be treated as entirely new particles, since the proteins and molecules that non-specifically bind to the AuNRs surface alter the physical size of the AuNRs in a dynamic manner. This creates an inhomogeneous distribution of sizes that differ from the original population, while also affecting their shape, surface charge, and colloidal stability [138, 139, 140]. A study by Chithrani et. al. (2007) demonstrated that citrate-capped nanoparticles enhanced cellular uptake, when compared with transferrin-coated nanoparticles, since proteins were able to easily adsorb to the citrate layer which facilitated improved cell-surface interactions and cellular recognition [141]. These AuNR-biological interactions also translate into in vitro testing, since the many components that make up cell growth media have been shown to affect the physiochemical properties of AuNRs by altering their colloidal stability, surface charge, surface chemistry, size, and toxicity, in much the same way [142, 143]. However, it is possible to overcome some, if not all, of these biological barriers by 'functionalising' the AuNRs. When attempting to deliver AuNRs to a region of interest (ROI), there are two main approaches:

Passive targeting: The passive approach to targeting cancerous tissues exploits the natural processes that occur when a tumour is present inside the body. To facilitate the rapid growth of a tumour, and its need for large amounts of nutrients and other growth factors, vessels grow abnormally to enable sufficient blood flow to the tumour site [144]. These atypical, leaky vasculatures - that can be up to 2 mm in size [145] - can facilitate the method of delivery for AuNRs. Furthermore, tumours exhibit an impaired lymphatic drainage that can hinder the AuNRs ability to leave the tumour and result in

the gradual collection of AuNRs within the tumour volume. These unique structural features give rise to the well-characterised enhanced permeability and retention (EPR) effect [146, 147, 148]. To successfully take advantage of EPR, the AuNRs must be of a particular size. In order to enter the tumour via blood perfusion, the AuNRs must to be small enough to allow them to extravasate into the tumour tissues, but large enough so that they remain within the tumour site for sufficient time for diagnosis or treatment to be administered. It has been suggested that AuNRs smaller than 100 nm are able to achieve this in mice [149], and human studies are now starting to emerge [150]. However, little is known about the efficacy of this effect in humans due to the limited number studies [151]. Furthermore, relying solely on this approach may result in the inability for AuNRs to reach all of the tumour sites since the abnormal growth of vasculature creates irregularities in the blood supply to the entire tumour volume, and the heterogeneous distribution of cells within the tumour tissue will affect how the AuNRs are taken-up [152].

Active targeting: In addition to relying solely on natural processes, it is possible to 'functionalise' or 'target' the AuNRs with specific tumour targeting ligands, such as peptides, monoclonal antibodies or small molecules [153, 154]. The molecularly targeted AuNRs (figure 2.3) travelling through the bloodstream will bind to specific tumour receptors as they come into contact with them, resulting in the accumulation of AuNRs in and around the tumour site [155]. This in turn can initiate, and in many cases improve endocytosis [154, 156, 157], leading to the internalisation of the AuNRs [158]. One of the most common methods of molecularly targeting AuNRs is the conjugation with anti-epidermal growth factor receptor (EGFR) antibodies [159]. A large number of solid tumours have been shown to overexpress EGFR on the cell cytoplasm membrane [160], including approximately 80 % of non-small cell lung cancer (NSCLC) [161], leading to a large amount of research being conducted around this idea [162].

Other benefits of altering the surface chemistry of AuNRs with various ligands are prolonged circulation times in the bloodstream [154], increased colloidal stability [163], enhanced thermal stability [164], and improved photothermal conversion efficacy [165], among others [166, 167, 168, 169]. Ligands such poly(ethylene glycol) (PEG) have been shown to not only significantly reduce cytotoxicity and prevent aggregation [137], but also 'mask' the AuNRs from the immune system as they circulate through the bloodstream, leading to longer circulation times [104], a less adverse immune response, and an increase in tumour uptake [76]. These added benefits in combination with an increased blood half-life - a measure of how long it takes for the RES organs to deplete the number of circulating nanoparticles by half [155] - can enhance diagnostic and therapeutic efficacy by ensuring the deliverability of AuNRs to a desired target region, while negating the possible side-effects of introducing AuNRs into the circulatory system [170].

Silica-coating is another surface modification that has shown to be beneficial in many ways [171]. Gold nanoparticles can be synthesised with a surrounding layer of silica on the

surface of the gold that has either a dense or porous structure [172]. This silica shell has shown to improve the photostability of the surface-modified gold nanoparticles, and therefore reduce the risks associated with losing its peak optical absorption due to reshaping. The silica shell can also enhance the photothermal conversion efficacy under laser irradiation and heighten effects, such as photoacoustic emission amplitudes and nanoparticle heating [173, 174]. Moreover, silica-coated AuNRs have shown to exhibit enhanced colloidal stability and biocompatibility compared with AuNRs without this coating, as well as excellent potential as drug carriers [175]. While these added benefits are important for biomedical efficacy, large-scale synthesis and surface functionalisation of silica-coated AuNRs still remains one of the biggest challenges, and ultimately limits their potential for future clinical translation [176], although new methods are beginning to appear [177]. Furthermore, the addition of the silica-shell around the core gold nanoparticle increases the overall size of the nanoparticle which potentially leads to other issues around cellular uptake and deliverability to a tumour site, since nanoparticle size is important for delivery.

If the AuNRs can indeed be delivered to a tumour, then the AuNRs must remain there long enough to allow for therapy to be administered [178]. The natural tendency for AuNRs to remain inside a tumour, governed by the EPR effect, in conjunction with functionalising and molecularly-targeting AuNRs to cell surface-receptors, can facilitate the large up-take and retention of AuNRs. Current research into the therapeutic efficiency of targeted AuNRs has shown promise [179], however there is a need to develop more effective methods for analysing targeting efficiency and tumour uptake if successful clinical translation of AuNRs is to occur [130].

2.3 Photoacoustics with gold nanorods

Photoacoustic imaging (PAI) is a non-invasive, non-ionising imaging modality that utilises the photoacoustic (PA) effect to image targeted areas of biological tissues [180]. It combines the high-contrast and spectral specificity of optical-based imaging methods with the high spatial resolution of ultrasound [181]. The photoacoustic phenomenon occurs when short laser pulses (generally nano- or femto-second) are absorbed by a material and the near-instantaneous deposition of energy causes rapid heating ($< 0.1\,\mathrm{K}$ [182]) of the area under laser-illumination. The thermal expansion of the target results in the emission of broadband acoustic waves in the 1-50 MHz range [183]. Any material can exhibit this effect, as long as the laser pulse width, τ_p, is shorter than the required time for the mechanical stress to propagate through the heated region and return to equilibrium, τ_{th}, simply given by $\tau_p < \tau_{th}$ [184]. This is known as the stress confinement condition, and if satisfied, a high thermoelastic pressure increase will be observed [183].

The maximum initial pressure increase, P_0, experienced by the material undergoing

Table 2.2: Tissue components for characterising absorption.

Tissue components	Description
S	HGb oxygen saturation of vasculature
B	Average blood volume fraction
W	Water content
C_{Billi}	Bilirubin concentration
$C_{\beta C}$	β-carotene concentration
Fa	Fat content
M	Melanosome volume fraction

thermal expansion is related to the incident laser fluence, F, given by,

$$P_0 = \frac{\beta\gamma^2}{c_{\text{p}}}\mu_a F, \tag{2.2}$$

where β is the thermal expansion coefficient (or isobaric volume expansion coefficient), γ is the speed of sound through the medium, c_{p} is the specific heat capacity at constant pressure, and μ_a is the absorption coefficient of the absorbing material. This can be simplified by grouping the first term into a dimensionless, thermodynamic parameter known as the Grüneisen Parameter (or coefficient), given by $\beta\gamma^2/c_{\text{p}}$. Equation 2.2 then becomes,

$$P_0 = \Gamma\mu_a F, \tag{2.3}$$

When attempting to generate a photoacoustic signal in a medical setting, the light from a laser pulse incident on the skin, for example, will travel through the various tissues, experiencing absorption and scattering events as it travels, until the light energy diminishes to zero. The tissue components that have absorbed the light will thermally expand to create a pressure increase, governed by equation 2.3, and subsequently contract to result in the generation of an ultrasonic wave that propagates radially through the surrounding tissue. If this signal is detected by an ultrasonic transducer (e.g. at the surface of the skin) then the recorded information can be spatially and temporally resolved to create an image of the tissue components that absorb at that specific wavelength of light [182]. If the laser wavelength is scanned through a known, specified range, then a more complex spectrally-resolved image can be reconstructed from the recorded signals based on the optical absorption spectra of the many different tissue types [185]. This technique is known as multispectral optoacoustic tomography (MSOT) (or functional photoacoustic microscopy (fPAM)) and is an imaging modality that is widely used [186, 187, 188, 189].

If the ROI within a biological environment is weakly absorbing, or too deep for sufficient light to reach it, then exogenous contrast agents can be used to enhance the optical absorption contrast between the tissue of interest and the background tissues [190]. The variety of different tissue types that the light must pass through to reach the destination site, such as skin, fat, blood, muscle, mucous tissue, dermis etc., often results in significant optical

attenuation and the generation of a weak acoustic signal [123]. The optical intensity, $I(z)$, decays exponentially with distance, z, according to,

$$I(z) = I_0 e^{-\alpha z}, \tag{2.4}$$

where I_0 is the initial light intensity and α is the optical attenuation coefficient. In tissue, α is large due to the optical scattering and absorption caused by all the distinctive tissue types, resulting in the rapid attenuation of light as it passes through. Furthermore, the large scattering contributions of the tissues cause the once omnidirectional light to quickly become diffuse and lose all directionality. The absorption and reduced scattering coefficients, μ_a (cm^{-1}) and μ_s' (cm^{-1}), have been described by Jacques et al. (2013) as a function the various absorbing chromophores (see table 2.2), and the size of the scatterers in tissue, respectively [123]. These components, which all depend on the wavelength of light, λ, can then be used to calculate μ_a and μ_s' of a tissue, given by,

$$\begin{aligned}\mu_a = {} & BS\mu_{a.\mathrm{oxy}} + B(1-S)\mu_{a.\mathrm{deoxy}} + W\mu_{a.\mathrm{water}} + Fa\mu_{a.\mathrm{fat}} + M\mu_{a.\mathrm{melanosome}} \\ & + 2.3C_{\mathrm{billi}}\epsilon_{\mathrm{billi}} + 2.3C_{\beta C}\epsilon_{\beta C},\end{aligned} \tag{2.5}$$

$$\mu_s'(\lambda) = a'\left[f_{\mathrm{Ray}}\left(\frac{\lambda}{500\,(\mathrm{nm})}\right)^{-4} + f_{\mathrm{Mie}}\left(\frac{\lambda}{500\,(\mathrm{nm})}\right)^{-b_{\mathrm{Mie}}}\right], \tag{2.6}$$

where $\mu_{a.\mathrm{oxy}}$, $\mu_{a.\mathrm{deoxy}}$, $\mu_{a.\mathrm{water}}$, $\mu_{a.\mathrm{fat}}$ and $\mu_{a.\mathrm{melanosome}}$ are the absorption coefficients of oxygenated blood, deoxygenated blood, water, fat and melanosome respectively. $\epsilon_{\mathrm{billi}}$ and $\epsilon_{\beta C}$ are the extinction coefficients of bilirubin and β-carotene respectively. $a' = \mu_s'(\lambda = 500\,\mathrm{nm})$, b_{Mie} is known as the 'scattering power', and f_{Ray} and f_{Mie} are the contributions from Rayleigh and Mie scattering, respectively. This general empirical model for evaluating tissue optical properties was based on measured characteristics, that allow the estimation of such properties and subsequent modelling of light propagation in tissue by specifying the absorption and reduced scattering coefficients in equations 2.5 and 2.6.

Exogenous contrast agents - such as AuNRs, small-molecule dyes, quantum dots, and organic or inorganic nanoparticles [191, 192] - located in a ROI are able to negate the effects of minimal optical penetration by facilitating the absorption and enhancement of the remaining light. AuNRs have shown to be effective contrast agents for PAI [174, 193, 194] by providing an enhanced optical absorption contrast against background tissue, leading to larger PA emission amplitudes being generated from highly localised and targeted areas [195]. PA images are reconstructed by acquiring 'A-lines', via the scanning of a single-element transducer or the use of a phased array beamforming technique (see chapter 5 for further discussion), and either used directly to form images - by determining time-of-flight and speed of sound measurements - or in more complex reconstruction algorithms such as back-projection [182, 196]. Multispectral optoacoustic tomography (MSOT) is another PA imaging modality that utilises the multiple spectral components of different tissues,

where image contrast is achieved by exciting the tissues according to their unique absorption spectra [197]. PA imaging is rapidly emerging as an effective alternative imaging modality for clinical use [198, 199], however further research into AuNRs is required. As discussed in section 2.2.3, AuNRs that are targeted to a specific site in the body will build up over time until there is a sufficient number to generate a detectable PA signal [200]. The amplitude of a PA signal emitted by AuNRs must be large enough to travel back through the multiple tissue types, where higher frequencies will experience a greater degree of attenuation compared with lower frequencies [201], and be detectable by a transducer probe. Generally, the probe will be located at the surface of the skin, however in some cases it may be possible to position the transducer in a closer proximity to the ROI (see section 2.5).

Another solution to increasing the PA signal amplitude generated by the absorbed laser-light is to increase the energy of the laser pulse. This increase in light intensity, incident on the surface of the skin, would subsequently result in more light reaching the target area and a larger PA emission. However, this can be problematic since high-intensity laser pulses can be damaging to tissues. A safe exposure limit for laser irradiation on skin, set out by the American National Standards Institute (ANSI) [202], provides a guide threshold for the typical laser energies and exposure durations that will cause skin or ocular damage. This is known as the Maximum Permissible Exposure (MPE), and is discussed in more detail in section 2.4.1. Nevertheless, if a therapeutic modality is developed that requires laser energies that are above this guideline exposure limit, then the MPE may be overlooked as a restrictive measure since the benefits of the therapy would negate the potential superficial damage caused by the laser. This is seen, in a more extreme case, with chemotherapy, whereby the benefits of administering the highly toxic, non-specific anticancer drugs outweighs the negative side effects.

2.4 Photothermal therapy with gold nanorods

Plasmonic photothermal therapy (PPTT) is a therapeutic modality that can utilise the unique properties of AuNRs [203]. Instead of exploiting the AuNRs ability to generate acoustic waves for non-invasive imaging, the AuNRs are used to locally destroy regions of tissue [204]. Photothermal ablation of tissue is possible without the use of AuNRs or other exogenous optical absorbers (as discussed in section 2.1), however its efficaciousness can be dramatically increased by utilising AuNRs [205]. Unlike PA imaging, where pulsed-wave (PW) lasers are essential to achieve the desired outcome, PPTT is conventionally administered with continuous wave (CW) lasers (PW and CW lasers are discussed in greater detail in section 2.4.1). While CW lasers are the most common optical source for PPTT, it has been suggested that PPTT is possible with PW lasers [206]. However, the laser pulse fluence is often high ($> 420\,\mathrm{mJ\,cm^{-2}}$) and significantly above the MPE guidelines.

Similarly to PAI, the AuNRs are used to enhance the optical absorption contrast between the target tissue and the surrounding healthy tissues [207]. A tumour containing sufficient

numbers of AuNRs is irradiated with a NIR laser that is tuned to the SPR of the AuNRs, where the incident light is absorbed and converted to heat [121]. If a CW laser is used to excite the AuNRs, then the target region will experience bulk-heating due to the long exposure times (generally on the order of minutes). Hyperthermia is achieved when the cells reach temperatures above $41 - 48\,^{\circ}\mathrm{C}$ and several processes begin to activate on the cellular level, such as protein denaturation, cell inactivation, and cell aggregation, causing irreversible damage and the eventual death of cells [208]. The pathways for cell death, via cellular apoptosis or necrosis, is largely governed by laser exposure parameters and AuNR concentration in the target tissue [209, 210]. A parameter known as the thermal isoeffective dose (TID) was developed [211] as a clinically relevant way to measure and compare 'slow' thermal treatments based on a given biological endpoint, such as cell death. It is most commonly described as the cumulative equivalent minutes held at a temperature of $43\,^{\circ}\mathrm{C}$ (CEM_{43}) and is given by,

$$\mathrm{TID} = \int_0^{\tau_{\mathrm{end}}} [R_{\mathrm{CEM}}]^{(43-T(t))} dt \tag{2.7}$$

where TID is the thermal dose in CEM_{43}, R_{CEM} is an approximated parameter equal to 0.25 for temperatures $< 43\,^{\circ}\mathrm{C}$ and 0.5 for temperatures $> 43\,^{\circ}\mathrm{C}$, $T(t)$ is the temperature at time t, and dt is the time interval. τ_{end} represents the final time point of the thermal treatment. This relationship has been found to provide a reasonable prediction of cell death *in vitro* between $40 - 47\,^{\circ}\mathrm{C}$ [208, 212].

As a stand-alone therapeutic technique, PPTT has many advantages over other conventional cancer therapies, as tissue destruction is highly localised to the areas containing AuNRs. Compared with treatments such as chemotherapy - where the relatively high doses of toxic drugs cause major damage to a wide range of healthy cells (see section 2.1) - PPTT allows for the selective destruction of cancerous tissues without causing collateral damage to the surrounding healthy tissues [213]. Additionally, PPTT is a potentially minimally invasive therapeutic approach, since surgery is not required to administer AuNRs systemically, nor to deliver light to a tumour region. However, where a tumour is located too deep for light to penetrate from the skin surface, it may be necessary to situate the laser fibre closer to the target tissue via an endoscope (see section 2.5), or in some cases, a small incision. Nevertheless, overall patient outcome is likely to be significantly better than that of many alternative medical procedures [214].

Secondary treatments can also benefit from PPTT, since the laser-induced heat can disrupt processes on the cellular level and enhance therapeutic efficacy. It has been shown that combined therapies are generally more effective than the 'sum-of-their-parts', since the heat damage can increase sensitivity to therapeutic drugs, enhance vascular and cell membrane permeability, and inhibit DNA repair mechanisms, among others [215]. Furthermore, it could be used to reduce tumour volume to improve the outcome of secondary treatments, such as surgery, or to treat tumour recurrences.

2.4.1 Lasers: continuous wave vs pulsed

There are two categories of lasers: pulsed (PW) and continuous wave (CW). CW lasers emit a continuous beam of light that generally lasts seconds or longer. The laser medium is continuously pumped by another light-source (usually another laser) resulting in the continual excitation of atoms within the lasing medium and the emission of photons [216]. CW lasers are also relatively inexpensive compared with most pulsed laser systems, while also having the advantage of compactness and portability.

High power pulsed lasers (PW), in contrast, are usually complex, bulky systems with multiple components such as gas tanks, movable crystals, and liquid cooling units, requiring longer, more sophisticated calibration and installation times. Unlike CW lasers that have a steady, constant power output, PW lasers frequently have intra-cavity delays that are built into the laser system to enable the build-up and 'storage' of energy in the lasing medium until it is released as a high-intensity burst of light [217]. Since there is a delay between exciting the lasing medium and a light pulse being emitted from the shutter, PW lasers can usually only achieve pulse repetition frequencies (PRFs) of around $10 - 20\,\text{Hz}$. The process of rapid accumulation and release of energy in very short, nano- or femto-second pulses is termed "Q-switching" and facilitates the lasers ability to generate extremely high peak powers in the order of 10^6 to 10^9 Watts. This is because the peak power, P_{peak}, is the energy transfer of a single laser pulse, given by,

$$P_{\text{peak}}(W) = \frac{E_{\text{pulse}}}{\tau_p} \tag{2.8}$$

where E_{pulse} is the energy of a single pulse, and τ_p is the duration of the pulse. The average power, P_{ave}, of a pulsed laser takes into account the time between each pulse by the following equation,

$$P_{\text{ave}}(W) = \frac{E_{\text{pulse}}}{\tau_T} = E_{\text{pulse}} \times \text{PRF(Hz)} \tag{2.9}$$

where $\tau_T = 1/\text{PRF}$ is the time-period of the pulses. This means for a single, 7 ns pulse with an energy of 1 J and PRF = 10 Hz, the peak power is 143×10^6 W and the average power is only 10 W.

The fundamental differences between CW and PW lasers lead to significant differences in the way they interact with materials. When a laser interacts with a material, and is absorbed, the energy first excites the conduction electrons and sets them oscillating [218]. This energy is then transferred to the surrounding electrons via femtosecond electron-electron relaxations, before being further transferred to the lattice, via electron-phonon collisions on a picosecond time-scale. When a material absorbs light from a CW laser, the heat is spread out over a much larger volume since the continuous nature of the incoming light allows for the heat to diffuse radially [219]. If the absorbing material is a solution of AuNRs, then this effect will be significantly enhanced as the AuNRs efficiently convert the laser energy into heat (see figure 2.4) [220]. Conversely, under pulsed laser illumination, the short ($< 10\,\text{ns}$)

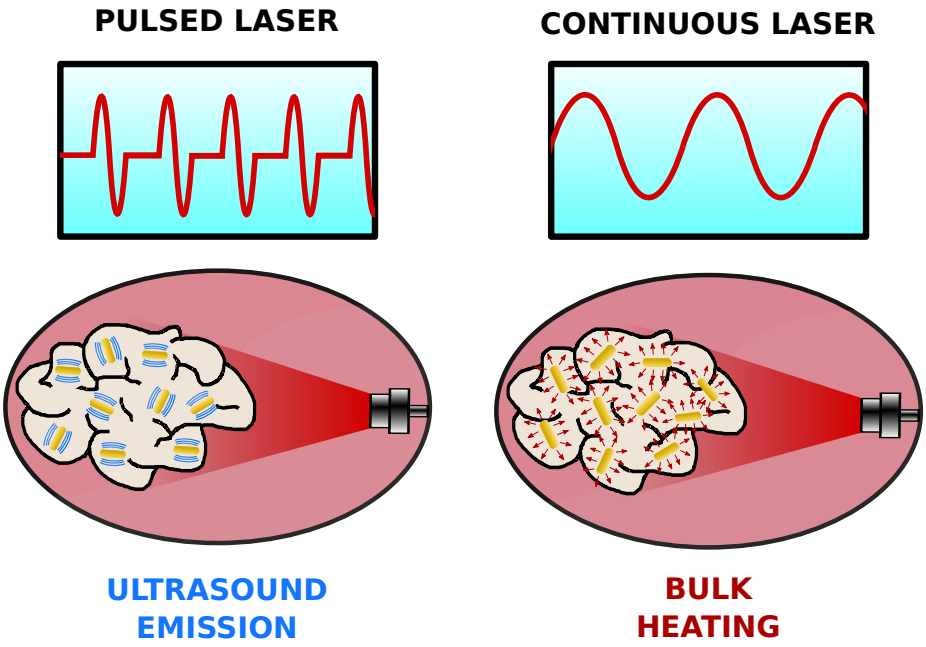

Figure 2.4: Under pulsed laser illumination, the AuNRs located in a tumour will experience a rapid increase in temperature that likely causes an expansion of both the AuNR and the localised surroundings, resulting in the emission of an ultrasonic wave. Conversely, under continuous wave laser illumination, the same AuNRs will continuously radiate heat to the surroundings, causing bulk heating of the environment.

high intensity laser pulses induce a higher initial peak temperature in the absorbers, compared with that of CW lasers. However, due to the time period between laser pulses, the absorbing region has time to cool sufficiently before each consecutive pulse. If AuNRs are the absorbing medium, then they will experience extremely high peak temperatures (and the emission of PA signals if the stress confinement condition is met), before rapidly cooling ahead of the next pulse (see figure 2.4). Thus, two distinct mechanisms exist depending on the type of laser employed: highly localised heating when PW lasers are used, and bulk, volumetric heating when CW lasers are used. There are also differences in the guidelines for the maximum exposure limit for skin (as mentioned in section 2.3). The maximum permissible exposure (MPE) is governed by the optical wavelength, λ, and duration of the laser exposure, t(s) [202]. Within the wavelength range $700\,\text{nm} \leq \lambda \leq 1400\,\text{nm}$, the MPE for skin is determined by the following,

$$\text{MPE}_{\text{skin}} = \begin{cases} 2 \times 10^{11}\, C_4\ (\text{W m}^{-2}), & \text{if } t(s) < 10^{-9} \\ 200\, C_4\ (\text{J m}^{-2}), & \text{if } 10^{-9} \leq t(s) \leq 10^{-7} \\ 1.1 \times 10^{4}\, C_4\, t(s)^{0.25}\ (\text{J m}^{-2}), & \text{if } 10^{-7} \leq t(s) \leq 10 \\ 2000\, C_4\ (\text{W m}^{-2}), & \text{if } 10 \leq t(s) \leq 30000 \end{cases} \tag{2.10}$$

where C_4 is a wavelength-dependent constant given by,

$$C_4 = \begin{cases} 10^{0.002(\lambda - 700)}, & \text{for } 700\,\text{nm} \leq \lambda \leq 1050\,\text{nm} \\ 5, & \text{for } 1050\,\text{nm} \leq \lambda \leq 1400\,\text{nm} \end{cases} \tag{2.11}$$

This relationship between laser wavelength and exposure duration gives rise to a different MPE depending on the laser employed. As the length of laser exposure is increased from a nanosecond pulse (10^{-9}) to a duration of 10 s, the MPE for skin increases from approximately 400 to 38 000 J m^{-2} (using equations 2.10 and 2.11 with a laser wavelength = 850 nm). This suggests that short pulses of light are more damaging to skin than a prolonged energy deposition. For exposures longer than 10 s, the defining limit changes from the total energy per unit area delivered to the skin (J m^{-2}) to the total power per unit area (W m^{-2}), and becomes a function of wavelength only. As the wavelength is increased from 700 to 1400 nm, the MPE for skin increases from approximately 2010 to 10 000 W m^{-2}, for exposures lasting more than 10 s, indicating that the longer NIR optical wavelengths are less damaging to skin. Since CW lasers are predominately used on the order of minutes (for example in photothermal therapy), their MPE limits are measured in terms of the total power per unit area, with a limit of $\text{MPE}_{\text{skin}} = 4000\,\text{W m}^{-2}$ ($\lambda = 850\,\text{nm}$). However, a PW laser employed for photoacoustics will operate with a pulse length on the order of a few nanoseconds and therefore its MPE is measured in terms of the total energy per unit area. For a 7 ns pulse at 850 nm, its $\text{MPE}_{\text{skin}} = 400\,\text{J m}^{-2}$. While these guidelines provide a potential upper limit on the safe exposure for skin, they do not cover other biological tissues (other than ocular

exposure) that may be exposed during therapy, such as lung tissue, and therefore they should be taken as a reference guideline only for future therapeutic development.

PPTT is conventionally administered with CW lasers to induce hyperthermia via bulk heating of a target region. This volumetric elevation in temperature can lead to the death of cells via two basic pathways: apoptosis and necrosis. Necrosis is the death of cells related to injury, disease, or low blood supply, and typically results in the loss of membrane integrity and the uncontrolled release of intracellular material into the surroundings [221]. Apoptosis differs from necrosis in that it is a form of controlled cell death, where a series of specific cellular biochemical and morphological events occur that ultimately lead to the 'programmed' elimination of ageing, superfluous, or damaged cells [222]. This method for cell death is a natural way for the body to eliminate unwanted or unneeded cells that are no longer operating as normal. If cells experience an apoptotic death, then no immunogenic or inflammatory response will be observed [210]. Conversely, if cells are destroyed via a necrotic pathway, then the release of cellular contents will initiate an inflammatory response. The cellular mechanisms and processes that govern necrosis and apoptosis have been discussed in great detail in the literature and so will not be discussed here [223, 224].

With regards to laser-based therapies, the conditions that influence whether cells undergo either necrosis or apoptosis vary based on the laser exposure parameters and whether absorbing agents, such as AuNRs, are used. It has been shown that the threshold for apoptosis and necrosis of human prostate cancer cells is between 44 °C or 45 °C when maintained at this temperature for 120 min [225]. However, this study was not performed using a laser as the heating source and instead was conducted by placing a 96-well plate onto a pre-heated hotplate for heating. This method for applying heat may result in a different temperature profile compared with that of a laser, and so comparisons must be made with caution. Another more recent study investigated CW laser-induced cell-death of a murine melanoma cell line that was incubated with AuNRs and exposed to 15 min laser irradiation [226]. It was found that, when heated to a maximum of 43 °C after 15 min laser exposure, the majority of the cells survived. However, when temperatures between $43 - 49$ °C were reached, significant cell death was observed (approximately 80 %) and the primary mechanism was apoptosis. Above 49 °C, necrosis became the leading cause of cell death. This study was consistent with previous reports on temperature thresholds, where temperatures above 50 °C were shown to induce necrosis, and temperatures below this threshold primarily induced apoptosis [227, 228]. The strong temperature dependence on the mechanisms for cell-death give rise to the ability for CW lasers to selectively destroy tissues via either the necrotic or apoptotic pathways, by simply controlling laser exposure parameters.

Unlike CW lasers, PW lasers do not induce bulk temperature changes in an absorbing region, and therefore the mechanisms for destroying tissue are different. The absorption of high-intensity light pulses likely result in the destruction of tissue via mechanical stresses and bubble cavitation [205, 229]. As a result of this, pulsed-wave plasmonic photothermal therapy (PW-PPTT) (a.k.a. photoacoustic therapy) can only induce necrotic cell-death,

since the mechanical stresses destroy the cells likely by disrupting the cell membrane and releasing the intracellular contents into the surroundings.

Although apoptosis is generally preferred over necrosis, due to the lack of immunogenic or inflammatory response, cell-death via necrosis has its potential benefits, such as the immediacy of the killing effect, no risks associated with cancer cells developing resistance to the therapy [209], increased selectivity as a result of no heat conducting from the target site and damaging surrounding healthy tissues, potentially lower laser powers compared with CW lasers, and the ability for the generated PA signals to provide simultaneous imaging during treatment [230]. Furthermore, PW-PPTT may enable the ability to combine PAI with PPTT through the use of PW lasers, and incorporate a single laser system into already existing medical technologies (see section 2.5), ultimately improving patient outcome and treatment efficiency.

2.5 Endobronchial Ultrasound (EBUS)

As discussed in section 2.1, endobronchial ultrasound (EBUS) is an existing, routine, clinical imaging technique that enables the visualisation and staging of lung cancer via needle-biopsy [232]. A bronchoscope with a curvi-linear transducer located at one end (see figure 2.5) is passed through the trachea or oesophagus and into the lung, where conventional ultrasound imaging is performed to locate possible tumour sites and access lymph node stations [233]. The bronchoscope contains a channel that runs the entire length of the bronchoscope and enables a route for a variety of tools, such as a needle, to access the tumour tissue or lymph node [234]. A curvi-linear probe is utilised to increase the imaging field of view (FOV), and the centre frequency of the probe is between $5-12\,\mathrm{MHz}$. This range of available frequencies enables flexibility in terms of the imaging resolution and depth. High frequencies allow for high spatial resolution imaging of fine shallow structures, while lower frequencies penetrate tissue more easily at the cost of resolution [235].

EBUS lends itself to other biomedical modalities that rely on acoustic signals, such as PAI, since the existing transducer probe could be utilised to receive PA signals with minimal alterations. It is possible that a laser fibre could be incorporated into a bronchoscope to illuminate the lung tissues from within the lung. The resulting PA signals could be detected by the transducer and combined with conventional B-mode ultrasound signals to provide a contrast-enhanced image with a greater amount of information than a standard B-mode image [236]. Additionally, it would provide a possible means for treating the tumour tissue with PPTT, using the same AuNRs.

However, the bronchoscope used to house the EBUS device is small (width $< 7\,\mathrm{mm}$) and the space available to incorporate additional features into the device is limited. Generally, there is only one working channel in the device, meaning only a single tool can be used at any one time. However, in some cases it is possible to remove the tool from the working channel and replace it with another, while the bronchoscope remains *in situ* [237]. Laser

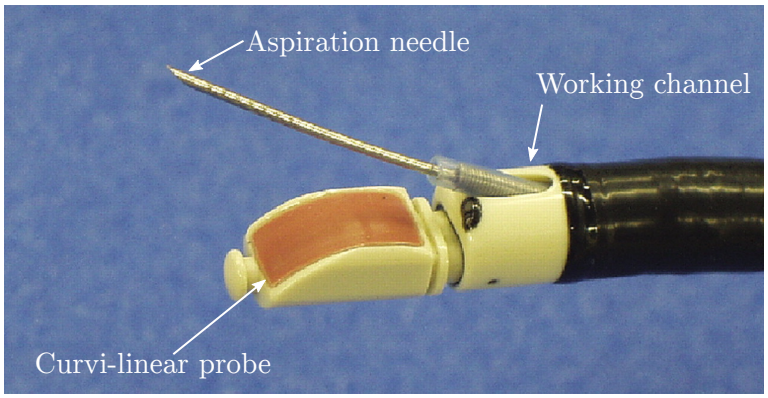

Figure 2.5: An annotated image of an endobronchial ultrasound device taken from work by Herth, et al., (2006) [231]

fibres are generally small in diameter, meaning it should be possible to develop a modified EBUS device that incorporates a laser fibre relatively easily. However, if the aim is to add both PAI and PPTT capabilities to the device then, as discussed in the previous section, it would be beneficial if the therapeutic aspect could be administered with a PW laser, as this would negate the need for potentially two laser fibres since both PAI and PW-PPTT could be achieve with the same bronchoscope-laser system.

This potential new multi-modal theranostic approach could enable the locating, staging, imaging, and treating of patients with lung cancer. However, its success would rely on the development of the multiple factors it relies on, such as the efficacy of PW-PPTT, feasibility of PAI with a typical EBUS probe, and availability of AuNRs that exhibit a high reshaping threshold (ie. photostability). The photostability of AuNRs is a particularly important aspect for theranostic applications since an AuNR that melts during the first stages of procedure (ie. imaging/staging) would no longer be effective for the therapeutic aspect, since the photothermal conversion efficacy would be significantly diminished or non-existent [238, 239]. Therefore, it is important that these issues are addressed to ensure the success of this potentially revolutionary approach to lung cancer treatment.

2.6 Gold nanorods for theranostics

As discussed in the previous sections, AuNRs have shown to be promising agents for application in optical absorption-based biomedical modalities to develop and enhance, new and existing clinical procedures. However, before AuNRs can be safely and effectively used clinically, there still remains extensive research into developing the AuNRs themselves and understanding their behaviour. This thesis aims to investigate some of the important areas surrounding the use of AuNRs for diagnostic, therapeutic, and theranostic applications.

One such area of AuNR development, that requires further investigation and optim-

isation, is their size. There have been many published reports that consider AuNRs for photoacoustic and photothermal applications, in addition to cellular interactions and toxicity, however there is very little consistency between the reports in terms of experimental setup, nanoparticle structure and modifications, nanoparticle concentration, and reported details, with often no consideration for their size on the observed outcomes. For example, Adnan et. al. (2016) synthesised gold nanoparticles of various shapes (spheres, rods, and stars) and investigated their abilities for photothermal therapy and drug delivery, however the AuNR dimensions were not reported, limiting its scope [69]. Other reports provide more detail with regards to the AuNR sizes, such as Cavigli et. al. (2014), who also synthesised their own AuNRs (CTAB-capped) with different sizes, and measured their melting thresholds as a function of size and PW laser fluence [240]. They determined a negative relationship between the melting threshold and size of the CTAB-capped AuNRs in terms of their 'effective radii' ($5 - 22\,\text{nm}$), however no 'real' dimensions were reported. Chithrani et. al. (2006) explored the intracellular uptake of two different sized AuNRs (modified by chemically replacing the CTAB capping with citric acid) by humancervical carcinoma (HeLa) cells [241]. The AuNRs of interest were equivalent in width (14 nm) but different in length (40 and 74 nm), and therefore their aspect ratio (2.86 and 5.29) and SPR peak (not reported) were different. It was found that the AuNRs with a smaller aspect ratio were more preferentially taken up by HeLa cells. A well-designed study by Gratton et. al. (2008) also examined the cellular internalisation of AuNRs (among other shapes) by HeLa cells, and found that high levels of uptake was observed for all AuNR sizes and aspect ratios, with larger sized AuNRs (diameter = 150 nm) being taken up to a greater extent than smaller volume AuNRs (diameter = 100 nm), with equivalent aspect ratios (≈ 3) [242]. The AuNRs used in this study were comparatively large in size (diameters ranging from $100 - 500\,\text{nm}$, aspect ratios from $1 - 3$) with the largest AuNR possessing a length of 1 µm. Large nanoparticles such as these are unlikely to be useful for optical absorption-based therapies since cells will not be able to internalise the AuNRs.

The vast number of available reports, such as those described previously, contain large variations in nanomaterials and experiment designs (e.g. capping agents, cell lines, surface chemistry, reported dimensions and characteristics) which makes drawing general conclusions and direct comparisons difficult. Moreover, many of the reported studies synthesised a small batch of AuNRs with specific characteristics that are relevant to that investigation, and there is no accounting for the large-scale reproducibility required for successful clinical translation. Therefore, further controlled studies into the size-dependent effects of AuNRs for optical-based biomedical modalities, that can be synthesised on a large scale with reproducible characteristics, are required to enable accurate conclusions based on AuNR size to be drawn, and the optimisation of AuNR design for eventual clinical use.

Another area in need of further investigation, is in light-based therapeutic applications of AuNRs, such as AuNR-assisted photothermal therapy. Continuous-wave (CW) lasers have generally been the research focus in the literature due to CW lasers generating bulk

heating in a target region and destroying tissue through heat damage (as discussed in section 2.4.1) [243]. There have been reports that utilise pulsed-wave (PW) lasers as the optical source for laser ablation of biological tissue, however these are few and far between, and often the experimental parameters are impractical for clinical translation. Furthermore, there is very little consideration for gold-based nanoparticles as the absorbing agent for PW-PPTT in the literature (perhaps due to the risk of AuNRs reshaping under pulsed laser illumination). The majority of nanoparticles studied for PW-PPTT are single-walled carbon nanotubes [244, 245, 246], or indocyanine green-containing nanoparticles [247, 248], among others [249, 250, 251, 252]. However, AuNRs can produce significantly stronger shock waves under pulsed laser illumination, compared with many of the other nanoparticles currently considered in the literature, and therefore can potentially be more efficient at destroying cells, while also making possible the ability to perform image-guided therapy via the monitoring of photoacoustic emissions [230].

One study that considered gold nanoparticles for PW-PPTT was conducted by Huang et. al. (2010), who compared the photothermal efficacy of CW and PW lasers for nucleus- or cytoplasm-targeted gold nanospheres (AuNS) to a human oral squamous cell carcinoma (HSC-3) cell line [206]. In this study, they found that the CW lasers were more effective at destroying cells when the AuNSs were targeted to the cytoplasm, while those targeted to the nucleus were more effective under PW laser irradiation. However, this study was limited by the optical absorbance of the nanospheres being in the visible spectrum (SPR = 526 nm) and the laser energies were exceedingly high (PW laser fluence = 101 $\mathrm{mJ\,cm^{-2}}$, CW laser power= 25 $\mathrm{W\,cm^{-2}}$, spot size = 1 mm).

A more recent study that considered rod-shaped gold nanoparticles was by Patino et. al. (2015) [253]. They investigated the use of ultra-short (100 fs) pulsed lasers to destroy pancreatic cancer cells that had been incubated with peptide-functionalised AuNRs, and found that cell-death could be achieved with a relatively low laser fluence (11.3 $\mathrm{mJ\,cm^{-2}}$). Although the fluence was low, the short femtosecond laser pulses resulted in peak powers in excess of 28 MW, and caused cell destruction via cavitation and local vapour/plasma expansion around the AuNRs (that were situated within the cells).

While the two studies mentioned previously have shown the potential for using PW lasers for the treatment of cancer cells, the experimental parameters (laser energies, nanoparticles, treatment times, etc.) need further refinement towards the eventual clinical use. Furthermore, the use of AuNRs in PW-PPTT has likely considerable benefits in the development of the technique, both in terms of treatment efficacy and additional possible modalities, such as image-guidance. Therefore, continued research into these areas is clearly needed, especially with consideration for lower laser energies/powers that are closer to the safe exposure limit laid out by the American National Standards Institute [202].

The final aspect to be investigated in this thesis, is the development and improvement of an existing biomedical approach, endobronchial ultrasound (EBUS), by utilising AuNRs. As discussed in section 2.5, there is the possibility for using AuNRs to improve upon EBUS

- an effective lung cancer diagnostic tool - by enhancing the ultrasound images with photoacoustic signals, and to help locate cancerous regions and lymph nodes in the lung, with further improvements made by enabling AuNR-assisted photothermal therapy. The existing literature in this particular area of research is limited, with very few articles considering this combination of EBUS and photoacoustics. Other techniques, such as optical coherence tomography (OCT) [254], have been discussed with regards to improving EBUS, however it appears that nothing has been implemented so far. Nevertheless, the potential for combined photoacoustic and conventional ultrasound imaging for other biomedical applications has been demonstrated [255, 256, 257], and this existing research will translate to improving EBUS. While this multimodal approach will likely require minimal adaptation to the existing technologies behind EBUS systems, further development is required before it can be realised as a clinical approach.

Chapter 3

Influence of Gold Nanorod Size in Photoacoustics

As discussed in section 2.2.2, gold nanorods (AuNRs) absorb light based primarily on their aspect ratio. Due to this fact, they can be synthesised to have many different sizes, but similar aspect ratios and therefore similar absorption peaks. It is possible that AuNR size can affect many different aspects relating to a particular biomedical modality, and in the case of photoacoustic imaging (PAI), aspects such as, photoacoustic conversion efficacy, melting thresholds, and cytotoxicity, are important to the success of the technique. There may exist an optimal sized AuNR that achieves the best outcome across these various important aspects, and currently, this optimal size is not known. Further research into the size-dependent effects of AuNRs is required before this conclusion can be drawn. In this chapter, AuNRs with four different size distributions (widths of 10, 25, 40 and 50 nm) and SPRs of 815 ± 26 nm are investigated with regards to their potential as photoacoustic contrast agents. Their size-dependent effects on photoacoustic response and photostability are observed, in addition to their toxicity and cellular uptake of a non-small cell lung cancer (NSCLC) cell line.

3.1 Introduction

Gold nanorods (AuNRs) possess characteristics such as tuneable surface plasmon resonances (SPRs) [258, 259], relative biocompatibility [70, 71], high colloidal stability [260, 261, 262], comparatively easy synthesis [113, 263, 264], and functionalisation [75, 265], that make them desirable for use in biomedical disciplines including diagnostics, therapeutics, or theranostics (as discussed in chapter 2) [266, 267, 268, 269]. Furthermore, their potential utilisation in nanomedicine as drug carriers, nano-probes, cellular labels, and biosensors is evident [116, 270, 271]. However, they are still some way off from being utilised in the clinic, as there are a number of key areas that must be addressed to ensure safety and efficacy.

In AuNR-assisted photoacoustic imaging (PAI), the amplitude of the generated photoacoustic (PA) signals is an important aspect that must be considered for two main reasons: Firstly, on the optical side, a heightened PA amplitude, as a result of employing AuNRs, facilitates the use of significantly lower laser fluences to generate an equivalent PA response. In other words, lower-powered lasers could be used to achieve the same PA response while reducing the damaging effects that high energy laser exposures can cause. A safe exposure limit, known as the maximum permissible exposure (MPE) for skin [202], provides a potential upper-limit on the laser fluences that can be employed for diagnostic applications. Furthermore, it is difficult for light to penetrate deep into biological tissues, since significant optical attenuation is observed [122, 123, 272, 273]. Secondly, on the acoustic side, PA waves are generally weak in amplitude ($\leq 10\,\mathrm{kPa}$) compared with other modalities that utilise ultrasound. For example, the typical focal peak pressures generated by clinical ultrasound scanners are in excess of 1 MPa. These low amplitude PA signals will consequently be reduced further (related to the acoustic amplitude attenuation coefficient α_a) as they travel through the various different tissues, caused by a combination of acoustic scattering, absorption, and mode conversions of the waves. This ultimately results in the rapid reduction in signal amplitude ($\alpha_a = 0.3 - 0.5\,\mathrm{dB\,cm^{-1}\,MHz^{-1}}$ for an approximate soft tissue [274]), and the already weak PA signals may become undetectable. Thus, there is a distinct problem with both generating and detecting PA signals in biological tissue, especially with several centimetres of tissue between the light source and region of interest, and the optimisation of AuNR PA emissions could help to mitigate these issues.

Plasmonic nanoparticles absorb light differently based on their size and shape [275, 276, 277], and the peak absorption wavelength of AuNRs is linearly proportional to their aspect ratio (see section 2.2) when the relative permittivity of the surrounding medium is constant [121, 278, 279]. Consequently, if the shape is fixed (i.e. rod-shaped for AuNRs) and the aspect ratio is restricted to a small range of values to enable maximum absorption in the near-infrared [280], then there may be an optimal sized AuNR at an equivalent concentration ($\mathrm{NP\,mL^{-1}}$) that maximises the PA emission amplitude. Currently this optimal size is not known, and further research into how the size of AuNRs can enhance a PA signal is required. It is also important to consider the concentration of the AuNR solutions in terms of the relative total mass ($\mathrm{\mu g\,mL^{-1}}$) since a population of smaller AuNRs will have a smaller total mass at an equivalent concentration to that of larger AuNRs. Confusion must not be made between the effects observed as a result of the change in volume over a change in concentration.

The size (or volume) of AuNRs may also have an effect on a large range of other aspects related to PAI, such as photothermal conversion efficiency [178, 281], cellular interactions and uptake [282], cytotoxicity [283], and the thermal stability of AuNRs [240, 284, 285]. These are all crucial areas in need of further investigation if AuNRs are to be used successfully as PA absorbers in a clinical environment. For example, if AuNRs, that are situated inside a tumour, begin to melt under laser irradiation then their ability to absorb the incident laser-

light will significantly diminish as the peak SPR band begins to blue-shift. This is especially problematic for 'theranostic' applications that rely on their ability to absorb light, since a reduction in optical absorption will result in reduced clinical efficacy. There have been many reports on the reshaping, melting and fragmentation of AuNRs [285, 286], but the quoted fluence reshaping threshold is often very different between sources and the size of the AuNRs is often not considered. Likewise, the cellular uptake and toxicity of AuNRs has also been investigated in the literature, however the multitude of different possible AuNR surface chemistries, and the inconsistencies between the nanoparticle shapes, sizes, incubation times, and laser parameters in these reports makes forming direct size-based conclusions difficult. Therefore, further controlled research that considers the size-dependent effects of AuNRs for PAI is warranted.

In this chapter, we investigated four different sized AuNRs that have similar aspect ratios but different sizes, in an effort to inform on their future use as contrast agents for PA imaging, or optical-based theranostics. PA emissions were recorded for each AuNR size at equivalent concentrations to determine their size-dependent effects on PA emission amplitudes, in addition to the fluence thresholds for melting, and inherent cytotoxicity to a lung cancer cell line.

3.2 Materials and methods

3.2.1 Transducer selection for detecting photoacoustic signals

Selecting the correct transducer for the detection of photoacoustic signals is important. A photoacoustic signal generated from a material will contain a wide range of frequency components, ranging from approximately $1 - 50$ MHz. However, this broadband signal is only produced when the size distribution of the optical-absorbing particles in the absorbing region is large and varied [287]. If there is a uniform size distribution of absorbing particles then the frequency spectrum emitted will be much narrower.

A spherical, focussed, broadband (10 kHz - 15 MHz) hydrophone was first used to detect the photoacoustic signals from the different sized AuNRs. This particular transducer was chosen due the potentially broadband photoacoustic signals and to maximise the detection of all the generated frequencies. However, a PA signal was not detected above the background noise. This was attributed to the fact that hydrophones sacrifice sensitivity for a wide frequency detection bandwidth, and it has been suggested that a transducer with a large bandwidth is more sensitive to the background thermal noise [288]. As a result, a 7.5 MHz, single-element, focussed transducer was chosen to replace the hydrophone. This probe was successful in detecting a photoacoustic signal from the AuNRs and the shape of the recorded signals were approximately as expected (N-shaped) - although there appeared to be other contributing factors that affected the shape of the signal (figure 3.1a). To check the frequency components of the signals, a Fast Fourier Transform (FFT) was applied. The results from this (figure 3.1b) showed a strong frequency component at 1.3 MHz and a reduction in signal

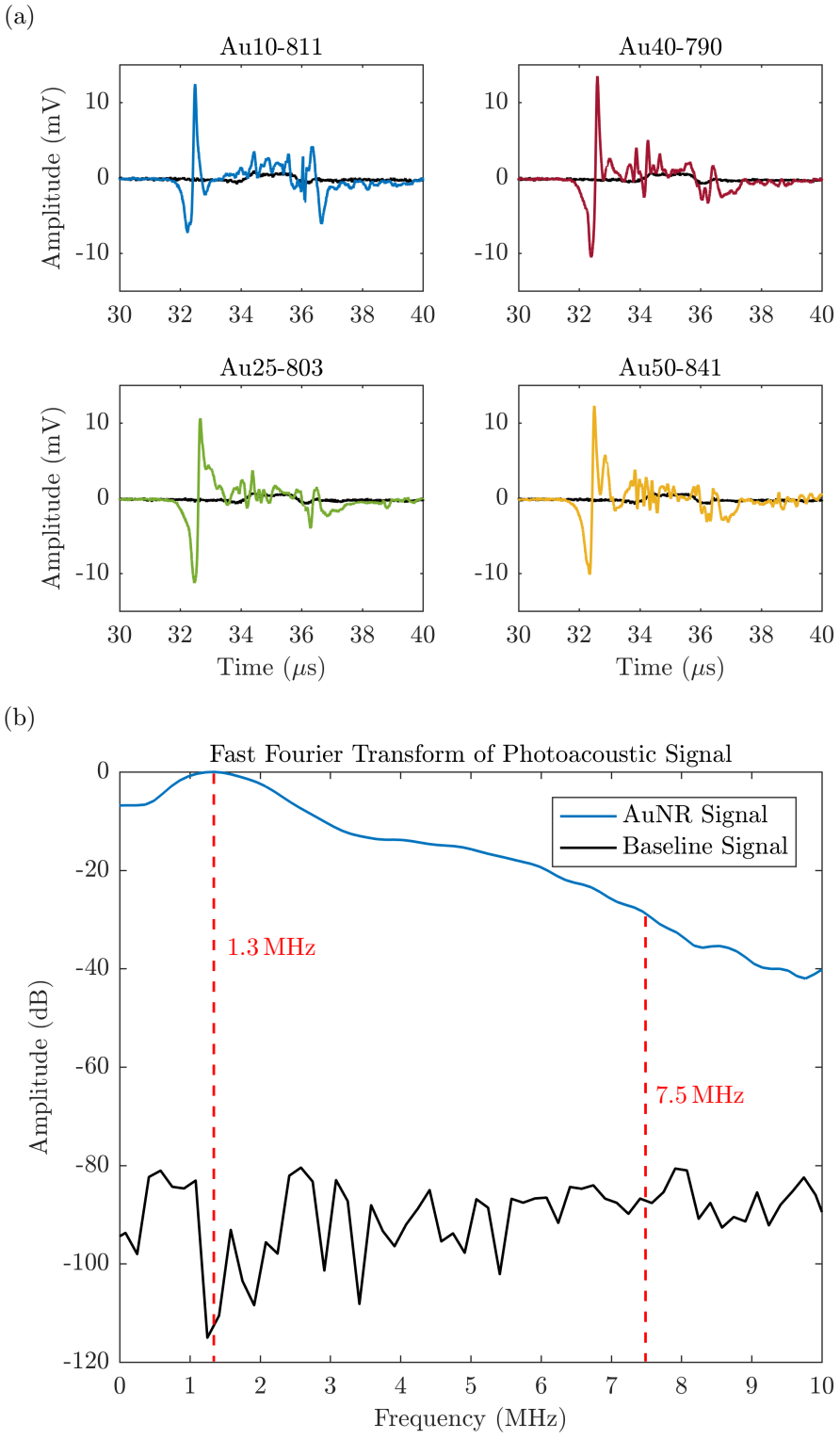

Figure 3.1: (a) Examples of the photoacoustic signals generated by four different sized AuNRs, recorded with a 7.5 MHz, single-element, focussed transducer. Coloured line represents signal from each AuNR and black line is the baseline (water), and (b) an example of an FFT applied to the photoacoustic signal generated by the Au10-811s compared with the baseline.

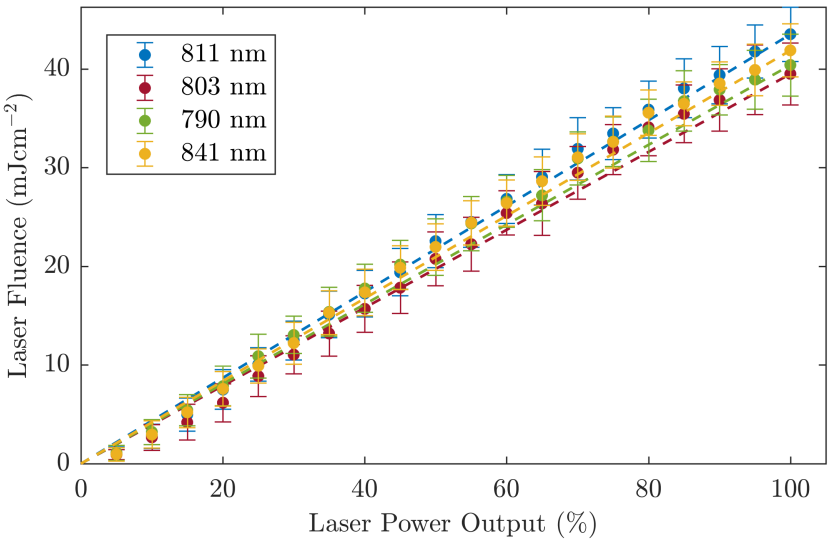

Figure 3.2: The laser energy output was calibrated for each desired wavelength as a function of the maximum output energy by altering the timing between the flash lamp and q-switch.

amplitude of approximately −28 dB at 7.5 MHz. This lead to the decision to use a focussed 1 MHz probe for the following experimental work.

3.2.2 Controlling laser energy

To facilitate the experimental work in this study, it was necessary to measure and control the energy output of the laser accurately. The laser energy was controlled via adjusting the timing between the laser flash lamp firing and the q-switch opening. The starting q-switch timing was set to 180 µs (the shortest timing permitted by the laser system and therefore the highest energy output possible). This was calibrated so that the user could specify the laser energy output as a percentage of the maximum energy achievable (figure 3.2) which provided a linear relationship. To ensure that equivalent laser fluences were used to generate a PA response from each AuNR size, the output energy of the laser was measured across 100 pulses and calibrated for each wavelength used in the study (the exact SPR of each AuNR size).

3.2.3 Characterisation of gold nanorods

Commercially bought, citrate capped AuNRs (A12, Nanopartz, USA) with certified latitudinal widths of 10 nm, 25 nm, 40 nm and 50 nm were chosen (see inset of figure 3.4) as the source of the generated PA signals so that a relationship could be made between the PA response of AuNRs with different sizes, but similar aspect ratios. AuNRs with a citrate capping were selected due to the increased biocompatibility, compared with other capping

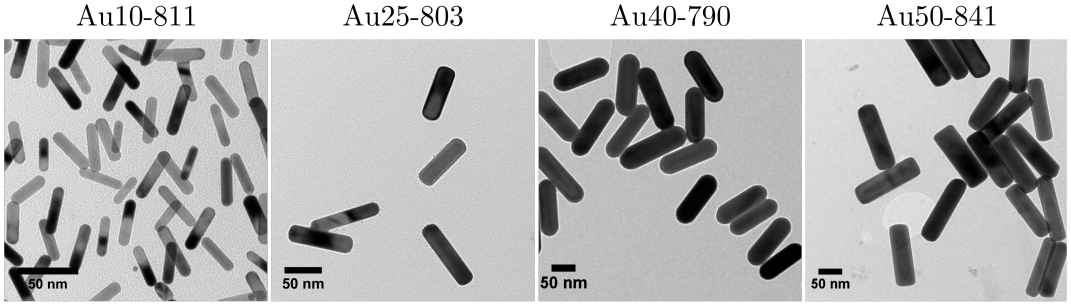

Figure 3.3: Transmission electron microscope images of the four different sized AuNRs used in this study.

Table 3.1: Dimensions and SPRs of the AuNRs used in the study, determined by TEM analysis ($n = 546$) and absorbance measurements respectively. The uncertainty of measurement is the standard deviation of the sample.

Name	Width	Length	Aspect Ratio	Peak SPR
Au10-811	9.9 ± 1.1 nm	39.7 ± 5.4 nm	3.98 ± 0.51	811 ± 2 nm
Au25-803	23.2 ± 2.6 nm	85.6 ± 9.8 nm	3.73 ± 0.63	803 ± 2 nm
Au40-790	39.8 ± 4.1 nm	122.5 ± 13.8 nm	3.10 ± 0.35	790 ± 2 nm
Au50-841	42.2 ± 4.6 nm	142.0 ± 17.0 nm	3.38 ± 0.41	841 ± 2 nm

agents, and the enhanced colloidal stability in cell media. Absorbance spectra of the AuNRs were measured and normalised to the peak absorbance (figure 3.4) to determine the longitudinal SPR of each different sized AuNR. This enabled the laser wavelength to be tuned to the maximum SPR of each AuNR to ensure maximum optical absorption. A transmission electron microscope (Tecnai™ TF20, FEI, USA) was used (figure 3.5) to take images of the purchased AuNRs (figure 3.3) with an accelerating voltage of 200 kV and varying magnification. These images were subsequently analysed to confirm the size distributions and aspect ratios of the different AuNRs. The manufacturer of the AuNRs characterise them before shipping, and have stated that a minimum of 93 % of the population of AuNRs across the four different sizes were rod shaped.

The TEM determined size distributions (table 3.1 and figure 3.6) for the Au10-811s, Au25-803s, and Au40-790s were in agreement with their corresponding peak SPRs [121], however there was a discrepancy with the Au50-841s. The Au50-841s were not measured to be 50 nm in width, as the certification suggested, and were instead found to be 42.2 ± 4.6 nm. While the Au50-841s were of a similar width to the Au40-790s, they were still larger in length and aspect ratio on average and so were still considered relevant for this study. Confirming and ensuring AuNRs are consistent between each batch is an important aspect for clinical translation, since there are minimum regulatory criteria, known as good manufacturing practice (GMP) [96], that any new medical drugs must meet to ensure consistency and quality.

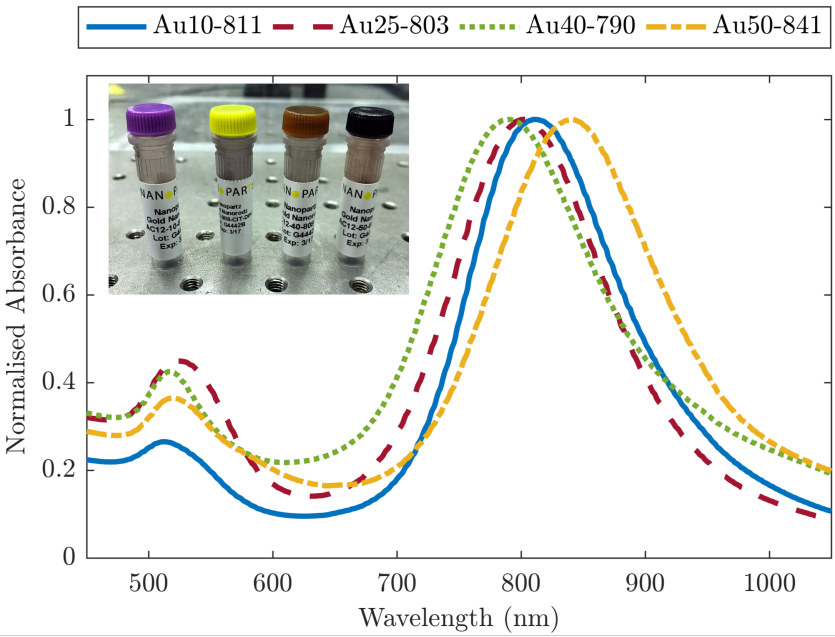

Figure 3.4: Normalised measured absorbance spectra displaying SPR peaks at 811, 803, 790, and 841 ± 2 nm, respectively. The SPR of the Au50-841s showed a 50 nm shift compared with that of the Au40-790s, which can be ascribed to a combined effect of the AuNR width and aspect ratio on the SPR position of AuNRs. Inset shows a photo of the four AuNRs.

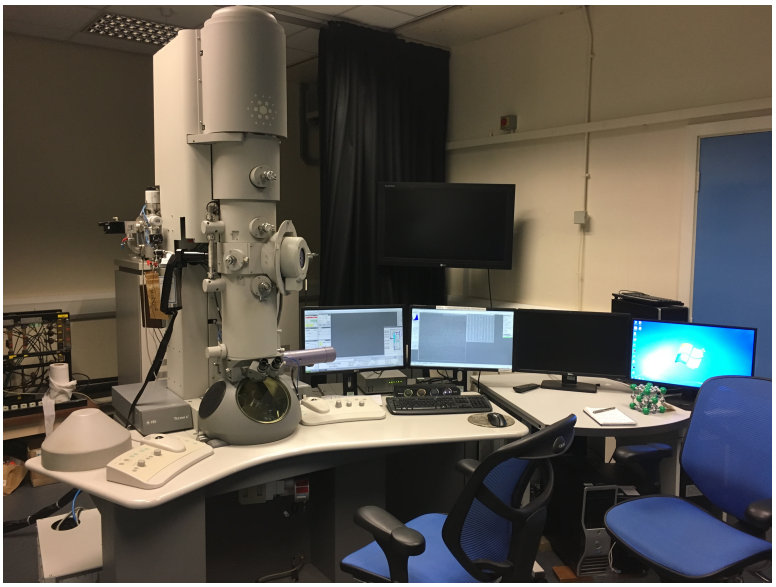

Figure 3.5: A photograph showing the transmission electron microscope used in this study, situated in the Leeds Electron Microscopy and Spectroscopy Centre (LEMAS).

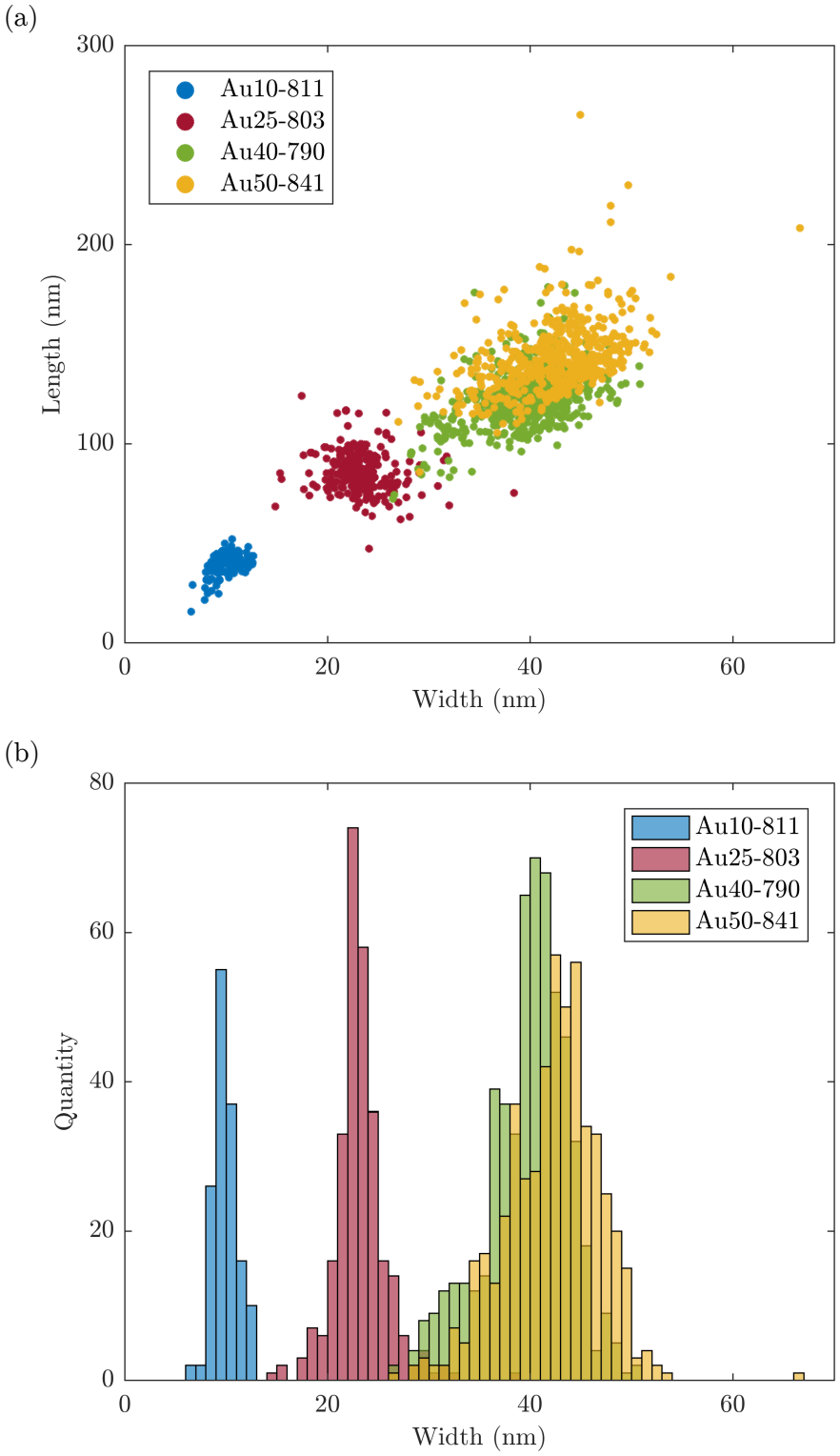

Figure 3.6: TEM measured size distributions of the four different sized AuNRs used in this chapter ($n = 546$).

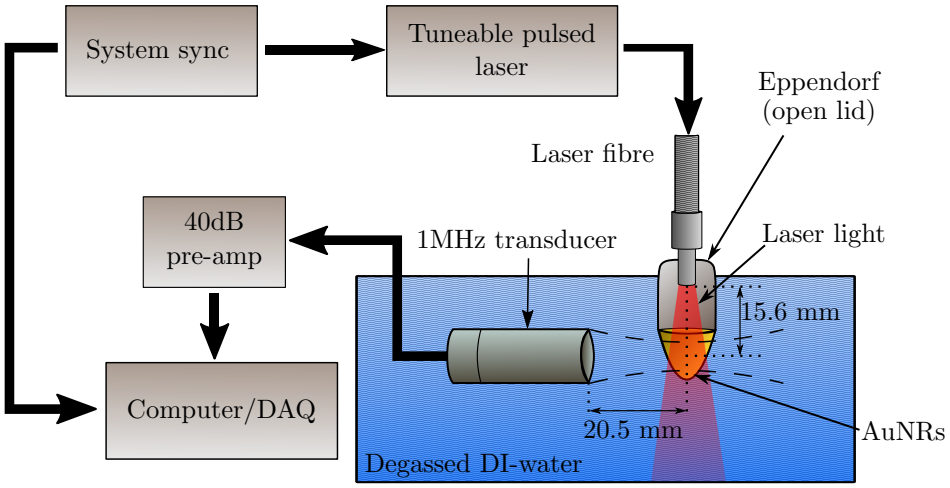

Figure 3.7: A schematic of the experimental setup used to detect the photoacoustic signals generated from Au10-811s, Au25-803s, Au40-790s, and Au50-841s.

3.2.4 Measuring the photoacoustic signal amplitude

As a result of the preliminary testing (section 3.2.1), an experimental setup was designed to accurately detect the photoacoustic response of a solution of different sized AuNRs (experimental schematic shown in figure 3.7). A pulsed tuneable laser system (Surelite™ OPO Plus, Continuum®, USA) operating at a pulse repetition frequency of 10 Hz with a pulse duration of 7 ns and spot size of 5 mm (at the focus of the transducer, 15.6 mm from tip of the fibre) was used to induce a PA response from a region of AuNRs. These parameters were chosen to ensure the stress-confinement conditions for generating a photoacoustic response were met, and a large volume of AuNRs were illuminated. The distance between the tip of the fibre and the absorbing region of AuNRs is governed by the specifications of the laser fibre (i.e. numerical aperture and core diameter) for a given spot size and should therefore be calculated for the specific fibre being used. A single-element focussed transducer (V303, Olympus, UK) with a centre frequency of 1MHz and certified −6 dB bandwidth of 76 % was mounted on a micrometre translation stage and aligned so that the transducer focus (focal length = 20.5 mm) was in the centre of the AuNR solution and at the point where the laser beam spot size was 5 mm. This transducer was chosen and based on the preliminary testing (section 3.2.1) and accurately aligned with the absorbing region to ensure that the majority of generated photoacoustic signals were recorded. Similarly to the laser fibre, the distance from the transducer element to the focus is defined by the specifications of the transducer. The laser wavelength was tuned to the exact SPR of the AuNRs being illuminated to maximise optical absorption, and the detected photoacoustic signals were subsequently passed through a 40 dB pre-amplifier (SPA.1411, Spectrum, Germany) and recorded with a data acquisition (DAQ) card (M4i.4420x8, Spectrum, Germany).

Experimental parameters and data acquisition

A solution of each AuNR size was made to the desired concentration (discussed below) by calculating the volume of DI-water required to dilute the stock solution of AuNRs (with a certified stock concentration). To measure the size-dependence of the AuNRs on calculated PA amplitude, the AuNRs were made to a concentration of $1 \times 10^{11}\,\mathrm{NP\,mL^{-1}}$ to ensure a detectable photoacoustic signal across all AuNR sizes. The incident laser fluence was then increased sequentially across a wide fluence range (approximately $1 - 40\,\mathrm{mJ\,cm^{-2}}$) in steps equal to 4 % of the highest laser output energy considered. This fluence range was chosen to enable a relationship between fluence and PA amplitude to be determined, in addition to melting thresholds. The AuNRs received 20 laser pulses per fluence step (the data was averaged to obtain a single photoacoustic amplitude), and this process was repeated 3 times on fresh samples of AuNRs. The data was averaged to account for small fluctuations in the laser output energy and to increase the signal-to-noise ratio of the waveforms. A larger number of laser pulses (and therefore averages) was tested, however it only provided a minimal increase in signal-to-noise ratio of the signal and therefore the number of repeats was kept at 20 to reduce the total laser energy incident on the AuNRs. Before laser exposure, the AuNRs were agitated in an ultrasound bath for 15 min to ensure a uniform colloidal suspension, prior to being placed inside an Eppendorf for PA emission measurements, with the laser fibre situated inside the Eppendorf (i.e. with the lid open) to reduce optical attenuation and maximise the delivered light.

To determine the concentration dependence on PA amplitude, the laser fluence was fixed at $7 \pm 1.9\,\mathrm{mJ\,cm^{-2}}$, to minimise the chance of AuNR reshaping, and fresh samples of AuNRs with concentrations ranging from $1 \times 10^{9} - 1 \times 10^{11}\,\mathrm{NP\,mL^{-1}}$ were illuminated. The experimental setup was identical otherwise.

Data processing

To calculate the PA signal amplitude, a technique similar to that used in PA image reconstruction was used [289, 290, 291]. Firstly, each averaged waveform was windowed to a 7 µs region of interest (ROI) that relates to the width of the absorbing volume (i.e. the spot size of the laser). A Hilbert transform was applied to obtain the envelope of each signal and the amplitude was calculated by integrating across the ROI. Photoacoustic signals were also obtained from the Eppendorf container filled with water, and were recorded and processed under the exact same conditions as the AuNR target. This data was subtracted from the AuNR PA amplitude to remove the effects from the container. The subsequent calculated PA amplitudes (across the entire laser fluence range) was determined from the three separate samples of AuNRs, and the average was plotted along with the standard error of the mean. Finally, to provide a baseline measurement, a noise signal was resolved by recording under the exact same conditions as discussed previously, however the shutter on the laser was closed while the laser continued to fire (i.e. no light was incident on the target). To

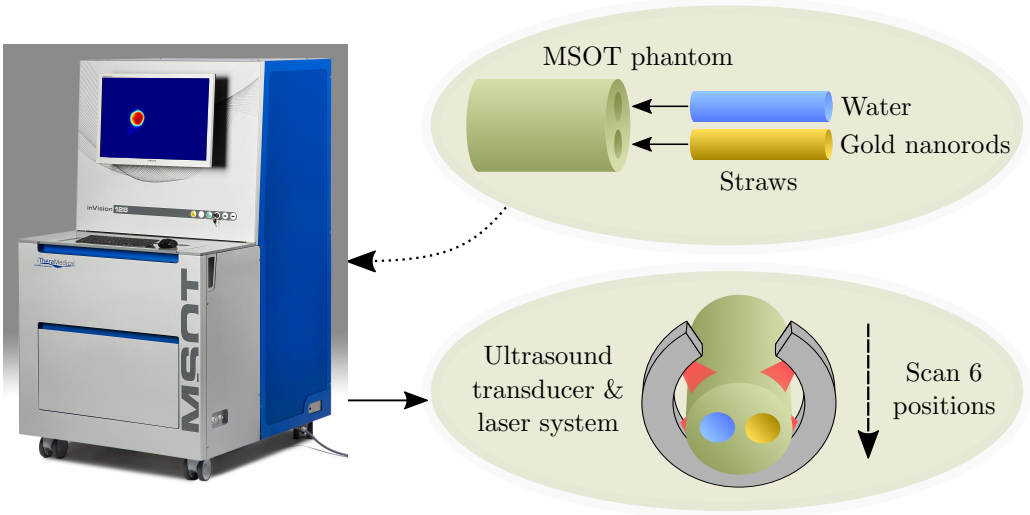

Figure 3.8: Experimental schematic showing a straw containing 1×10^{11} NP mL^{-1} of AuNRs, and a second straw containing a water baseline, being placed into a typical turbid, agar phantom before a multispectral scan is performed at 6 positions using the pre-clinical MSOT system.

determine statistical significance between the calculated PA amplitude of the AuNR and the baseline signal amplitude, a two-way analysis of variance (ANOVA) technique was used to calculate a p-value at each laser fluence studied.

3.2.5 Validation of measurements with a pre-clinical system

To compare the lab results with a commercial PAI system, PA signals were measured at the SPR of the four AuNRs using a multispectral optoacoustic tomographic (MSOT) system (MSOT inVision 128, iThera Medical, Germany). Four small thin plastic tubes containing equivalent concentrations of AuNRs (1×10^{11} NP mL^{-1}) and another four with equivalent mass concentrations (100 µg mL^{-1}) were made and inserted into a typical MSOT phantom (turbid agar phantom), along with a straw containing the supernatant of the AuNRs to act as a background signal (see figure 3.8). The phantom containing the straws was placed inside the MSOT system and a multispectral scan (680 nm to 980 nm in steps of 5 nm) was performed at 6 unique points along the straws. The maximum PA amplitude at the peak SPR of the AuNRs was recorded and averaged across the 6 data points to give a final amplitude. Images were processed using open-source software package imageJ [292].

3.2.6 An indication of gold nanorod toxicity

A cytotoxicity study was devised to provide an indication of the relationship between gold nanorod size and cellular toxicity. To establish the cytotoxicity of the four different AuNR sizes over the potential length of time AuNRs may reside inside the body, a 72 h MTT

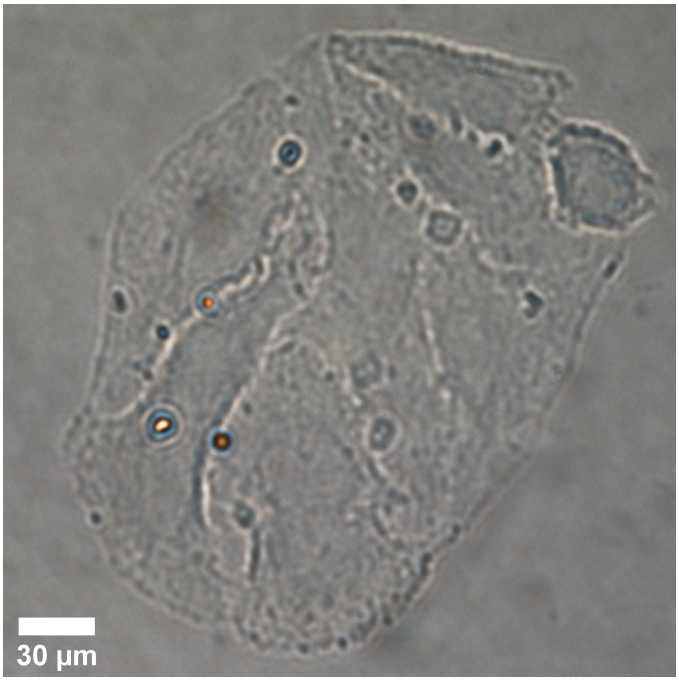

Figure 3.9: A bright-field microscope image of the human non-small cell lung epithelial carcinoma (NSCLC) cell line (A549) used in the study.

(3-[4,5-dimethylthiazol-2-yl]-2,5 diphenyl tetrazolium bromide) colorimetric assay protocol was followed [293]. This metabolic assay is a reliable and widely used method for evaluating cell viability, and it provides a quantitative indication of cell viability by measuring the enzymatic activity of cellular mitochondria [76]. There are suggestions that newer tetrazolium analogues, that are stabilised by intermediate electron acceptors, are a better option for toxicity evaluation, however these assays exhibit a net negative charge which could inhibit intracellular uptake and affect observed toxicity [294]. Conversely, MTT has an overall positive charge that facilitates easy uptake and mitochondrial reduction. Moreover, nanoparticles that interact with cellular membranes may further affect toxicity results from the newer generation of tetrazolium assays by interfering with the uptake and extracellular reduction of the tetrazolium dye [295]. Therefore, an MTT assay was considered to be the best approach for this particular study.

A human non-small cell lung epithelial carcinoma (NSCLC) cell line (A549, ATCC, UK) was selected for toxicity evaluation because NSCLCs account for the majority of lung cancer cases in the UK (approximately 80%) [296], they can be easily used in xenograft lung cancer models [297], and they have been shown to express EGFR (for future targeting studies) [298]. Furthermore, A549 cells have been considered widely in the literature in terms of cancer therapies and nanoparticle interactions [299, 300, 301], making comparisons straightforward. The intention of this study was to provide insights into the potential AuNR size-dependence on cell viability, and not to be a comprehensive investigation into

the cytotoxicity of lung cancer, and so a single cell line was deemed sufficient to demonstrate this.

A549 cells were cultured in DMEM (Dulbecco's Modified Eagle Medium) media supplemented with 10 % FBS (Fetal Bovine Serum). A bright-field image of the cell line is shown in figure 3.9. When the cells reached 80 % confluency, a 96-well plate was seeded with 1×10^3 cells per well and incubated for 24 h. The four different sized AuNRs were introduced to the cells mixed with culture medium at a concentration ranging between $1.5 \times 10^6\,\mathrm{NP\,mL^{-1}}$ to $3 \times 10^{10}\,\mathrm{NP\,mL^{-1}}$ in a 1:3 series dilution. One of the columns was reserved for a control group containing the supernatant of the AuNRs (DPBS) to ensure this was not the cause of toxicity. After 72 h incubation the AuNRs mixed with media was removed from each well and replaced with media containing MTT at a concentration of $500\,\mu\mathrm{g\,mL^{-1}}$. After a further 3 h incubation the media containing MTT was removed from each well and the 96-well plate was wrapped in foil and stored at approximately 4 °C, ready for absorbance measurements.

Before the plates were measured with a plate reader (Mithras LB 940, Berthold Technologies, Germany), 100 µL of dimethyl sulfoxide (DMSO) was added to the wells. The absorbance was measured at a reference wavelength of 630 nm to minimise the absorbance contribution from the AuNRs. The data from each column was averaged to obtain a single absorbance value for each AuNR concentration, and the background absorbance level was then subtracted from each of the other values. The cell viability was finally calculated by the ratio of mean absorbance of the sample with respect to mean absorbance of the control group (DPBS). This methodology was repeated three times on fresh samples to obtain a mean cell viability.

3.2.7 Visualisation of cellular uptake

To visualise the potential cellular uptake of different sized AuNRs, a dark-field study was conducted. A549 cells were plated onto 22×22 mm glass cover-slips in a 6-well plate at a density of $1 \times 10^5\,\mathrm{well^{-1}}$ and allowed to grow for two days. The DMEM medium was then replaced with 2 mL of the same medium containing each AuNR type at a concentration of $1 \times 10^{11}\,\mathrm{NP\,mL^{-1}}$. After 4 h incubation, the AuNR-media was removed and the cell monolayer on the cover-slip was twice-rinsed with DPBS (14190-094, Life Technologies, UK), fixed in 4 % paraformaldehyde/DPBS for 10 min at room temperature and rinsed with DPBS twice. The fixed coverslips were mounted and sealed onto glass slides. Bright and dark-field microscopy imaging was performed with an inverted microscope (Nikon Eclipse Ti-E, Nikon UK Ltd, UK) and an oil coupled 100x objective (CFI Plan Fluor, Nikon UK Ltd, UK). Images were recorded with a 5 Megapixel colour camera (DS-Fi1, Nikon UK Ltd, UK) and saved using the NIS-Elements D software (Nikon UK Ltd, UK). ImageJ was used to crop and enhance the contrast of saved images.

3.3 Results and discussion

3.3.1 Photoacoustic response of gold nanorods

Examples of the averaged recorded pre-processed photoacoustic signals are shown in figure 3.10a. The shape of the recorded photoacoustic signals can be explained by the density of absorbers in the target region [302]. The ROI was assumed to be cylindrical, with a radius of 1.3 mm (−6 dB radius of the transducer's focus) and height equal to 5 mm (spot size of the laser). The total ROI volume was approximately 26.5 µL, yielding an order of 1×10^{10} AuNRs converting the absorbed light into ultrasound. The large number of AuNRs collectively producing a photoacoustic response resulted in a pressure rise only at the outer edges of the absorbing region since the acoustic waves emitted from the centre interfered destructively [302]. This is responsible for the signal peaks at 14 µs and 18 µs.

Figure 3.10b shows the PA amplitude of each AuNR type as a function of the incident laser fluence. The PA signals from all four AuNRs were detectable above the noise at the concentration studied, however the Au10-811s produced a very weak signal in comparison. Statistical significance was established for the majority of fluence levels ($p < 0.05$), however there were a few instances where this was not the case. Firstly, at the lowest laser fluence studied, $1 \pm 0.7\,\mathrm{mJ\,cm^{-2}}$, the amplitude of emissions from all AuNR sizes were not significantly greater ($p > 0.05$) than the baseline measurements. This can be attributed to the laser fluence being too low to generate a sufficient PA signal from the AuNRs. For the Au25-803s measurements (figure 3.10b), when the fluence reached and exceeded $29 \pm 3.2\,\mathrm{mJ\,cm^{-2}}$, the detected emissions were not significantly above the baseline. Similarly, for the Au10-811s, this occurred at a laser fluence of $33 \pm 3.3\,\mathrm{mJ\,cm^{-2}}$. The reduction in the significance of the data can be ascribed to the reduction in PA amplitude due to potential melting or reshaping of the AuNRs (investigated in section 3.3.2).

All AuNR types displayed a linear relationship between incident laser fluence and PA amplitude at low fluences ($< 12\,\mathrm{mJ\,cm^{-2}}$ for the Au10-811s, Au40-790s, and Au50-841s, and $< 8\,\mathrm{mJ\,cm^{-2}}$ for the Au25s). The Au25s were the first to show a decline in signal amplitude, occurring when the fluence rose above $7 \pm 1.9\,\mathrm{mJ\,cm^{-2}}$. The PA amplitude of the Au10-811s, Au40-790s, and Au50-841s continued to increase past $7\,\mathrm{mJ\,cm^{-2}}$ and lose linearity at approximately equivalent fluences ($12\text{-}16 \pm 2\,\mathrm{mJ\,cm^{-2}}$). The thermal stability of AuNRs is governed by a balance between the rate of heat dissipation to the surroundings and the atomic surface diffusion of AuNRs. It has been suggested that thermal stability significantly decreases with increasing aspect ratio [286], and this agrees with the observed results, where the Au25-803s (aspect ratio $= 3.73 \pm 0.63$) displayed a lower thermal stability to the Au40-790s (aspect ratio $= 3.10 \pm 0.35$). The Au10-811s may show an enhanced thermal stability despite having a larger aspect ratio (3.98 ± 0.51) as they are much smaller than the other AuNRs and are able to dissipate the generated heat more rapidly to the surrounding environment [240]. Furthermore, it has been suggested that small AuNRs (8 ± 2 nm by 49 ± 8 nm) reach lower peak temperatures under pulsed illumination compared with larger

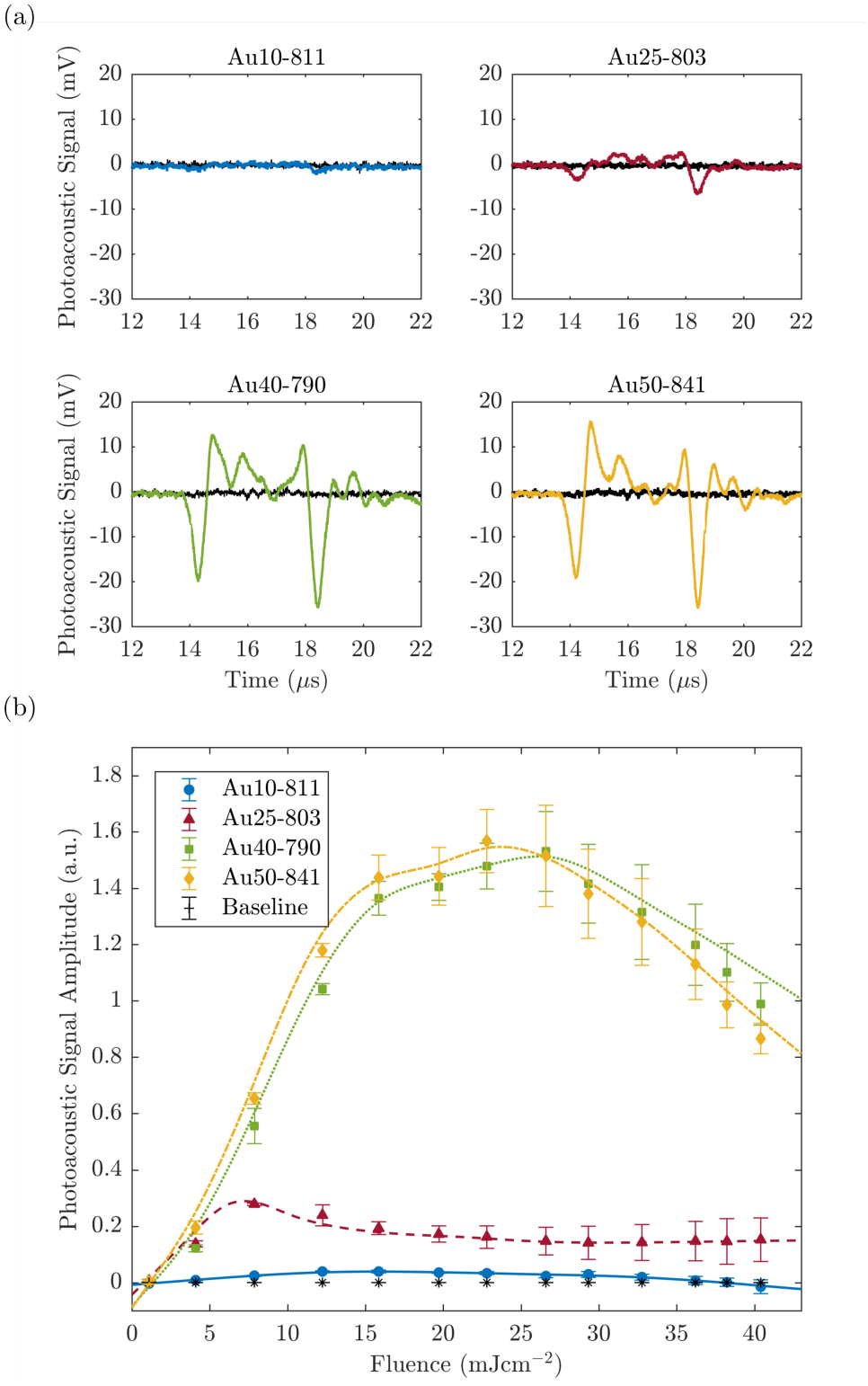

Figure 3.10: (a) Typical examples of averaged photoacoustic signals (laser fluence = 8 mJ cm^{-2}) generated by four AuNR sizes, and (b) the photoacoustic signal amplitude generated from the same four AuNRs (concentration = 1×10^{11} NP mL^{-1}), detected with a 1 MHz focussed transducer. Au10-811s (blue), Au25-803s (red), Au40-790s (green) and Au50-841s (yellow). The black line represents the water baseline signal.

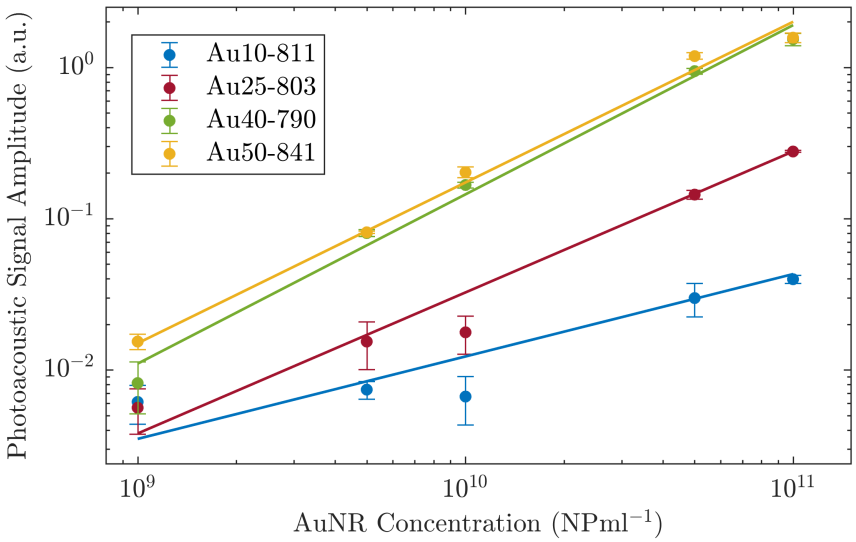

Figure 3.11: The photoacoustic amplitude of four different sized AuNRs as a function of concentration ranging from 1×10^9 to 1×10^{11} NP mL^{-1}.

AuNRs, and therefore may not reach a high enough temperature to exhibit melting [303]. It is worth noting that the quoted fluence levels here are all below 31 mJ cm^{-2} - the approximate maximum permissible exposure of skin for a single pulse (wavelength between 700-1400 nm) [202].

The two larger AuNRs (Au40-790s and Au50-841s) both displayed a similar PA relationship with increasing laser fluence, but it was the Au50-841s that ultimately produced the largest peak signal. The similarity between the two larger AuNRs is most likely due to the similarities in AuNR size distributions as confirmed by TEM analysis (see table 3.1). Furthermore, these AuNRs continued to produce an increasing PA amplitude past the point where linearity is lost (12-16 $\pm$ 2.2 mJ cm^{-2}) and began to decline in amplitude at approximately 25 $\pm$ 2.7 mJ cm^{-2}. This was due to the significant number of large AuNRs that had not fully reshaped and still able to absorb light.

The PA response of the four different sized AuNRs was measured across a range of AuNR concentrations from 1×10^9 to 1×10^{11} NP mL^{-1} and the maximum amplitude calculated (figure 3.11). A logarithmic relationship between AuNR concentration and PA amplitude was observed, indicating the importance of maximising the number of AuNRs delivered to a region *in vivo*, which could be facilitated by the functionalisation and molecular targeting of AuNRs [230]. At equivalent concentrations (NP mL^{-1}), the PA signal amplitude scales with AuNRs size, where the larger AuNRs produced the strongest PA signal. Across the entire concentration range, the Au40-790s and Au50-841s exhibited similar PA amplitudes. This was due to the Au50-841s being only slightly larger than the Au40-790s (see table 3.1) and therefore exhibiting a similar total mass (0.3 mg mL^{-1} for the Au40-790s, compared with

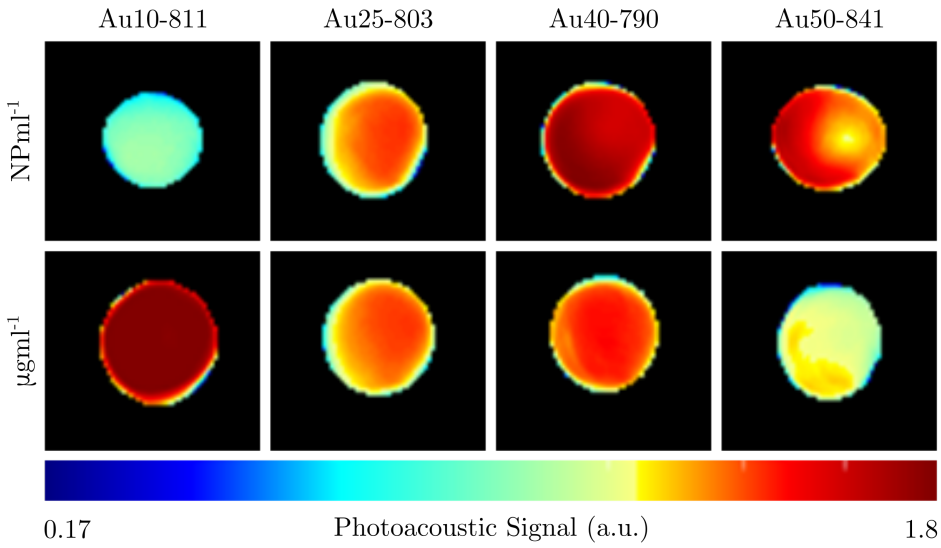

Figure 3.12: The photoacoustic response of the Au10-811s, Au25-803s, Au40-790s, and Au50-841s were measured with a multispectral optoacoustic tomographic (MSOT) system at equivalent mass ($100\,\mu g\,mL^{-1}$) and number of particles ($1 \times 10^{11}\,NP\,mL^{-1}$). The figure shows an example of MSOT images of the four AuNRs, reconstructed from the raw signal data captured with the MSOT system with a logarithmic colorbar.

$0.5\,mg\,mL^{-1}$ for the Au50-841s).

The maximum PA amplitude of the same four AuNRs was also measured using a MSOT system [197] at a fixed number of particles ($1 \times 10^{11}\,NP\,mL^{-1}$) and fixed total mass ($100\,\mu g\,mL^{-1}$). The reconstructed PA images (linear regression) are shown in figure 3.12 and the PA amplitude data is shown in figure 3.13. At equivalent particle numbers, the data is in agreement with the results in figure 3.10b, where an increase in AuNR size produced an increase in PA emission amplitude, and the Au40-790s and Au50-841s showed similar PA amplitudes. However, when the total mass was fixed between samples, the Au10-811s produced a significantly larger PA signal when compared with the other three. The smallest of the AuNRs exhibited an amplitude more than 2.5 times that of the Au40-790s, the next largest amplitude. The Au50-841s and Au25-803s produced a similar PA response, but the Au25-803s displayed the lowest photoacoustic conversion overall. A recent study by Chen et al. (2019) showed that small AuNRs ($8 \times 49\,nm$) produced an enhanced photoacoustic signal compared to larger AuNRs due to the increased heat transfer exhibited by the AuNR, facilitated by an increased surface-to-volume ratio. This may explain the large PA signal generated by the Au10-811s.

At an equivalent total mass of $100\,\mu g\,mL^{-1}$ the number of particles within each sample varied significantly. The Au10-811s contained more than an order of magnitude more particles ($1.57 \times 10^{12}\,NP\,mL^{-1}$), the Au25-803s were approximately the same concentration ($1.46 \times 10^{11}\,NP\,mL^{-1}$), and the Au40-790s and Au50-841s contained 3 and 5 times fewer

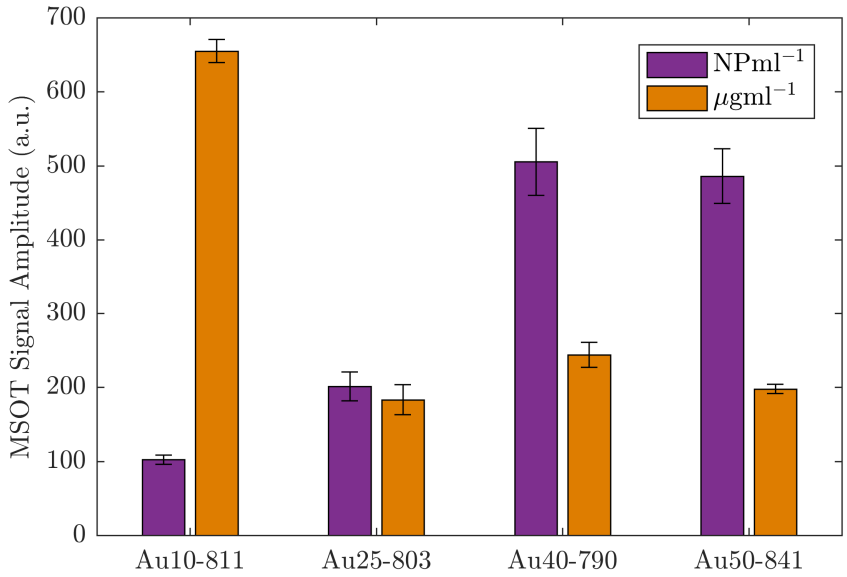

Figure 3.13: The maximum photoacoustic amplitude of the four different sized AuNRs at equivalent concentrations (purple = $1 \times 10^{11}\,\mathrm{NP\,mL^{-1}}$, orange = $100\,\mu\mathrm{g\,mL^{-1}}$) averaged across 6 repeats. Errorbars represent the standard deviation.

particles ($3.31 \times 10^{10}\,\mathrm{NP\,mL^{-1}}$ and $1.82 \times 10^{10}\,\mathrm{NP\,mL^{-1}}$), respectively. These difference in AuNR concentration agree with the observed differences in MSOT signal.

The results indicate the importance of AuNR size for PA emissions, and how the concentration of AuNRs is defined. There is a clear distinction between the effects generated by a total number of particles and total mass of gold, and this must be taken into consideration for tumour targeting, accumulation, and uptake of the AuNRs in a clinical setting [130]. For instance, if the accumulation of AuNRs *in situ* is restricted by the total number of AuNRs, regardless of size, then the data would suggest that the larger AuNRs would be more effective at achieving the desired effects since they produce the strongest PA signal per particle (see 3.13) [304]. Conversely, if the total mass is the driving factor behind tumour uptake, then clearly the smallest AuNRs ($< 25\,\mathrm{nm}$) would be most suited [141]. The Au25-803s should be avoided in either situation, however, since they produced a weak PA signal in both cases. Further studies into the size- or mass-dependent uptake for different sized AuNRs in an in vivo model are needed to address these concerns.

3.3.2 Photostability of gold nanorods

To confirm if the reduction in amplitude with increasing fluence (and subsequent increase in calculated error) was a result of the AuNRs beginning to melt and reshape, thus causing a reduction in optical absorption (at the wavelength used) and photoacoustic emission; TEM

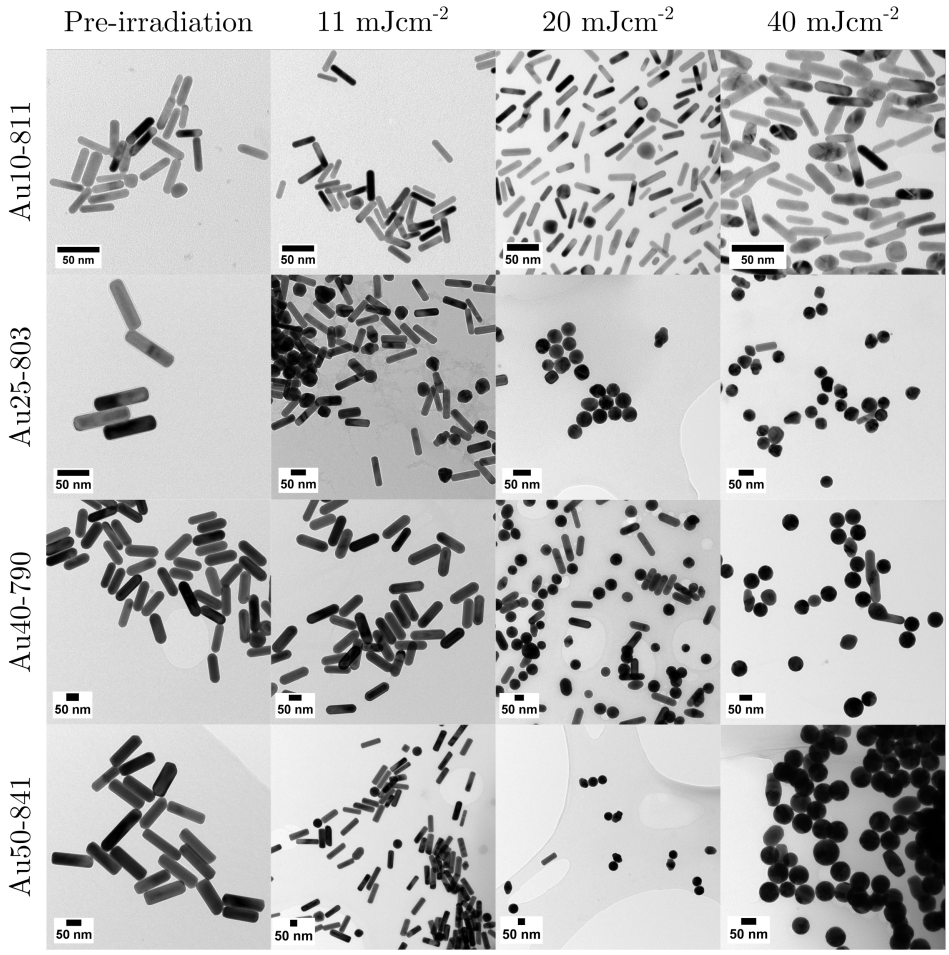

Figure 3.14: TEM images taken for each sized AuNR at specific points in the study: before laser irradiation, and after 20 pulses at $11\,\mathrm{mJ\,cm^{-2}}$, $20\,\mathrm{mJ\,cm^{-2}}$, and $40\,\mathrm{mJ\,cm^{-2}}$. Scale bars = 50 nm

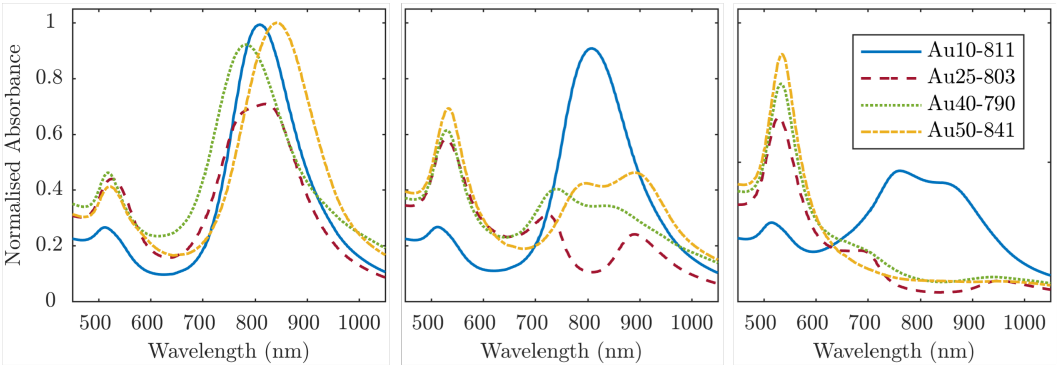

Figure 3.15: Absorbance measurements normalised to the maximum of the absorbance spectra taken before laser irradiation (figure 3.4) for each AuNR size at a concentration of 1×10^{11} NP mL^{-1} after exposure to 20 laser pulses at a fluence of 11 ± 1.7 mJ cm^{-2} (left), 20 ± 2.2 mJ cm^{-2} (middle), and 40 ± 2.6 mJ cm^{-2} (right).

images (figure 3.14) and absorbance measurements (figure 3.15) were taken after the AuNRs were exposed to specific laser fluences at key points (11 ± 1.7 mJ cm^{-2}, 20 ± 2.2 mJ cm^{-2}, and 40 ± 2.6 mJ cm^{-2}) across the range studied. Fresh samples of AuNRs were separately exposed to 20 laser pulses - the same number of pulses used in the PA study - to ensure the observed effects were not due to cumulative absorption. The absorbance spectra were normalised to the original spectra to highlight the change in SPR due to melting.

At 11 ± 1.7 mJ cm^{-2}, the Au25-803s showed partial melting and reshaping while the other three showed no reduction or flattening of the peak absorbance (the minimal reduction of the Au40-790s is within error). After 20 pulses at 20 ± 2.2 mJ cm^{-2}, there was a significant 'hole' in the peak SPR of the Au25-803s, and the TEM images confirmed that the majority of the AuNRs had melted and reshaped into spheres. Both the Au40-790s and Au50-841s also displayed a flattening and minor dip in the peak absorbance at this laser fluence, whereas the Au10-811s maintained photostability, with only a minimal reduction in peak absorbance. Finally, at a fluence of 40 ± 2.6 mJ cm^{-2}, the Au25-803s, Au40-790s and Au50-841s all demonstrated melting and reshaping of almost the entire population of AuNRs. The Au10-811s exhibited a significant reduction in peak absorbance at this laser fluence, however a considerable number of Au10-811s appeared to have remained stable, indicated by a reduction of half the peak absorbance. This would suggest that smaller AuNRs (widths < 25 nm) are more resistant to reshaping under laser illumination than larger AuNRs, and would further support the idea that small AuNRs do not reach high enough peak temperatures to exhibit melting, and are able to dissipate heat to the surroundings at a faster rate, compared with larger AuNRs [305].

The photostability of AuNRs can be affected by a number of factors, including photothermal conversion efficacy, thermal conductivity, surface diffusion, AuNR defects, thermodynamic stability, and the coating surrounding the AuNRs [306, 307]. Furthermore, the

optical absorption of the particles can have a significant effect on the reshaping of AuNRs. As the AuNR size decreases, the optical absorption of the particle will also decrease. This could suggest why the smaller AuNRs in this study were resistant to higher laser fluences. However, equivalent particle numbers of the different sized AuNRs results in the total mass of gold within the absorbing region being different. Thus, a decrease in AuNR size will result in a decrease in total mass, which could result in a maximum (or minimum) of the mass-normalised optical absorption for different sized AuNRs, and suggest why the Au25-803s appear to be significantly less photostable than any of the other AuNRs studied [276]. The melting-point depression phenomenon may also contribute to the reshaping thresholds of small AuNRs, nevertheless the overall thermal stability is mostly governed by a balance between the total absorbed light and the thermodynamic stability of the AuNRs [308, 309].

In addition to the large reduction in absorbance at the longitudinal SPR of the AuNRs, a noticeable increase in the absorbance at the latitudinal SPR is observed (see figure 3.15). This can be explained by an ever-increasing number of AuNRs reshaping into spheres (see figure 3.14), as confirmed by TEM. The Au10-811s were the only exception, where the absorbance around 532 nm does not increase despite the reduction in the 811 nm peak. TEM analysis confirmed that the majority of Au10-811s had not fully reshaped into spheres but had instead become ϕ-shaped or imperfect spheres. Figure 3.15c supports this idea as the spectra around the peak SPR broadens, indicating a distribution of particle shapes between a rod and sphere. This may be due to small AuNRs exhibiting a higher thermal coupling to the surrounding environment and therefore enabling a rapid dissipation of heat to the surrounding area, solidifying before becoming completely spherical.

Knowledge of the way in which AuNRs melt and reshape under laser illumination is crucial to the development of the modalities that rely on them. Slight changes in their size and shape can have a substantial effect on the optical interactions exhibited by the AuNRs. If melting occurred during PA tomography, or any other optical-based diagnostic or therapeutic modailty that relies on AuNRs, the quality and efficacy would diminish as a consequence. The effect that AuNR size has on optically-induced degradation is an important aspect to consider in the AuNR selection process.

3.3.3 Gold nanorod toxicity and uptake to lung cancer cells

Further to understanding how the size of AuNRs affects the induced PA response, it is also important to determine the impact that size has on cellular toxicity. Figure 3.16 shows the percentage viability of a NSCLC cell line (A549) after 72 h exposure to all four AuNRs across a range of concentrations from 1.5×10^6 NP mL^{-1} to 3×10^{10} NP mL^{-1}. Figure 3.17 shows an example bright-field image of A549 cells having metabolised MTT, turning it blue. As expected, the data suggested that an increase in concentration of AuNRs also resulted in an increase in cytotoxicity. The concentration at which cell viability drops to 50 %, known as the IC_{50}, could not be deduced for the Au10-811s or Au25-803s since the concentration used in this study did not reach a high enough level to cause major detriment to the cells.

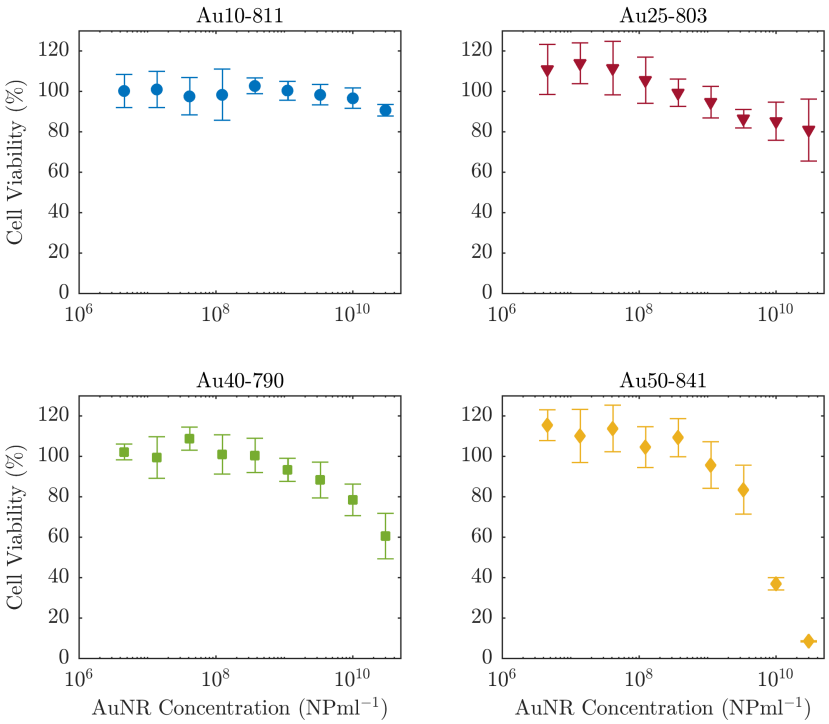

Figure 3.16: Percentage viability of an A549 lung cancer cell line after 72 h incubation with Au10-811s (blue, top-left), Au25-803s (red, top-right), Au40-790s (green, bottom-left) and Au50-841s (yellow, bottom-right) at a maximum concentration of 3×10^{10} NP mL^{-1}.

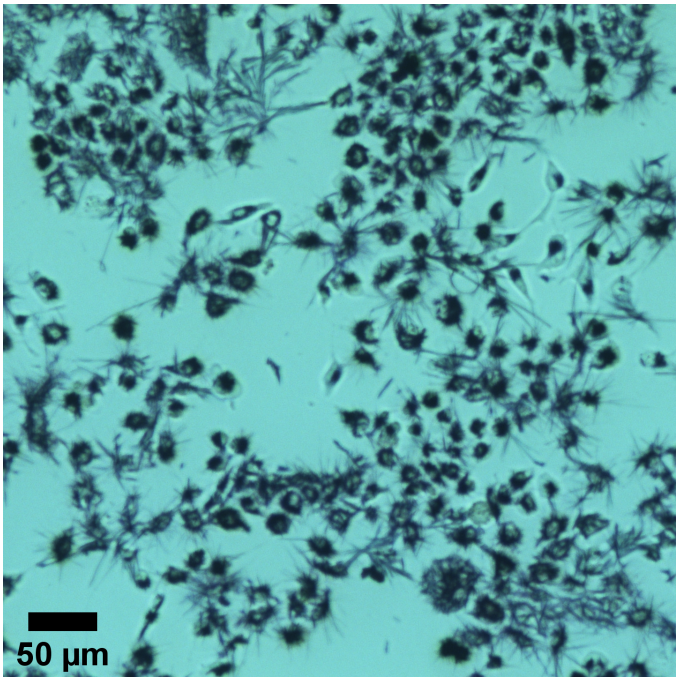

Figure 3.17: A bright-field image showing A549 cells after metabolising the added MTT and turning it blue, indicating cell viability.

A four parameter logistic regression curve was fitted to the Au40-790 and Au50-841 data to enable the IC_{50} to be determined [310]. The Au40-790s displayed noticeable toxicity to the A549 cells, however an IC_{50} value ($IC_{50} = 6.6 \times 10^{10}\,NP\,mL^{-1}$) higher than the maximum concentration studied, was extrapolated from the regression curve. The Au50-841s demonstrated the highest toxicity of the four AuNR size, where a concentration of $3 \times 10^{10}\,NP\,mL^{-1}$ resulted in necrosis or apoptosis of almost the entire cell population. An IC_{50} of $7.3 \times 10^{9}\,NP\,mL^{-1}$ was easily deduced for this AuNR size. While conclusive results cannot be drawn on the size-dependent toxicity of AuNRs to general cell populations, the data suggests that larger AuNRs exhibited a higher toxicity at equivalent concentrations compared with that of smaller AuNRs. It is important to note that at equivalent concentrations, a solution of large AuNRs contains more mass than a solution of small AuNRs.

To further understand the interactions between cells and the different sized AuNRs, bright-field and dark-field microscopy images were taken (figure 3.18) of A549 cells after incubation for 4 h in media containing each-sized AuNR. The bright-field microscopy images suggested that the cells incubated with AuNRs maintained their attachment to the glass slides and their normal morphology. It can be seen from the dark field microscopy images that the cells appear to have taken up AuNRs of each size, as observed by the scattered light. Careful examination of the dark-field microscopy images showed that the AuNRs enriched the cytoplasm of the cells instead of being evenly or randomly distributed, as would be the case for non-specific adhesion [115]. While the uptake of the AuNRs by the lung cancer cell

line cannot be determined quantitatively by dark-field microscopy, the results suggest that the larger AuNRs may have been taken up more readily than the smaller AuNRs, and have demonstrated the potential of AuNRs with varied size for cell-related applications such as photoacoustic imaging and photothermal therapy.

As this study was limited to *in vitro* testing, it was not possible to consider some of the other important aspects that could affect the choice of AuNR for biomedical use, such as the ability for AuNRs to reach a tumour site, immune response, and blood circulation time [311]. Nevertheless, future studies will benefit from the presented work by guiding the selection process of AuNRs with respect to PA response, cellular toxicity, and photostability.

3.4 Conclusions

AuNRs display highly desirable characteristics for use as molecular-targeted contrast agents in photoacoustic imaging and other optical-based diagnostics and therapeutics. It is suggested that there may be an optimal size and concentration that achieves maximum PA emission amplitudes while resisting melting and reshaping, and exhibiting minimal cytotoxicity. It was demonstrated in this chapter, that it is important to consider the size of the AuNRs when making a selection for biomedical applications, while also taking into account the concentration of AuNRs at a desired location. At equivalent $\mathrm{NP\,mL^{-1}}$, the smaller AuNRs were shown to exhibit the lowest cytotoxicity to the lung cancer cell line while also displaying the lowest PA emission amplitude, and the larger AuNRs produced the highest PA emission but were the most toxic. Conversely, if the total mass of AuNRs was fixed, then it was the smallest AuNRs that were the most effective PA converters, while the other three sizes produced similar responses. This highlights the need for further in vivo work surrounding the cellular uptake and deliverability of AuNRs to a desired location to determine the best metric for defining AuNR concentration ($\mathrm{\mu g\,mL^{-1}}$ or $\mathrm{NP\,mL^{-1}}$). Size-dependent AuNR influences on the melting and reshaping thresholds were also demonstrated, indicating that careful consideration must be made with regards to the laser fluence. The smallest AuNRs (Au10-811s) displayed the most resistance to melting over the fluence range studied, suggesting the increased photostability of small AuNRs (10 nm width). Dark-field microscopy demonstrated the potential of different sized AuNRs for cell-related applications such as photoacoustic imaging and photothermal therapy since cellular uptake was observed for all AuNR sizes. The presented study has shown that the size of AuNRs is an important aspect to consider when choosing AuNRs for biomedical uses, since it has a strong effect on many characteristics, such as PA emission amplitude, photostability, cellular uptake, and cell toxicity.

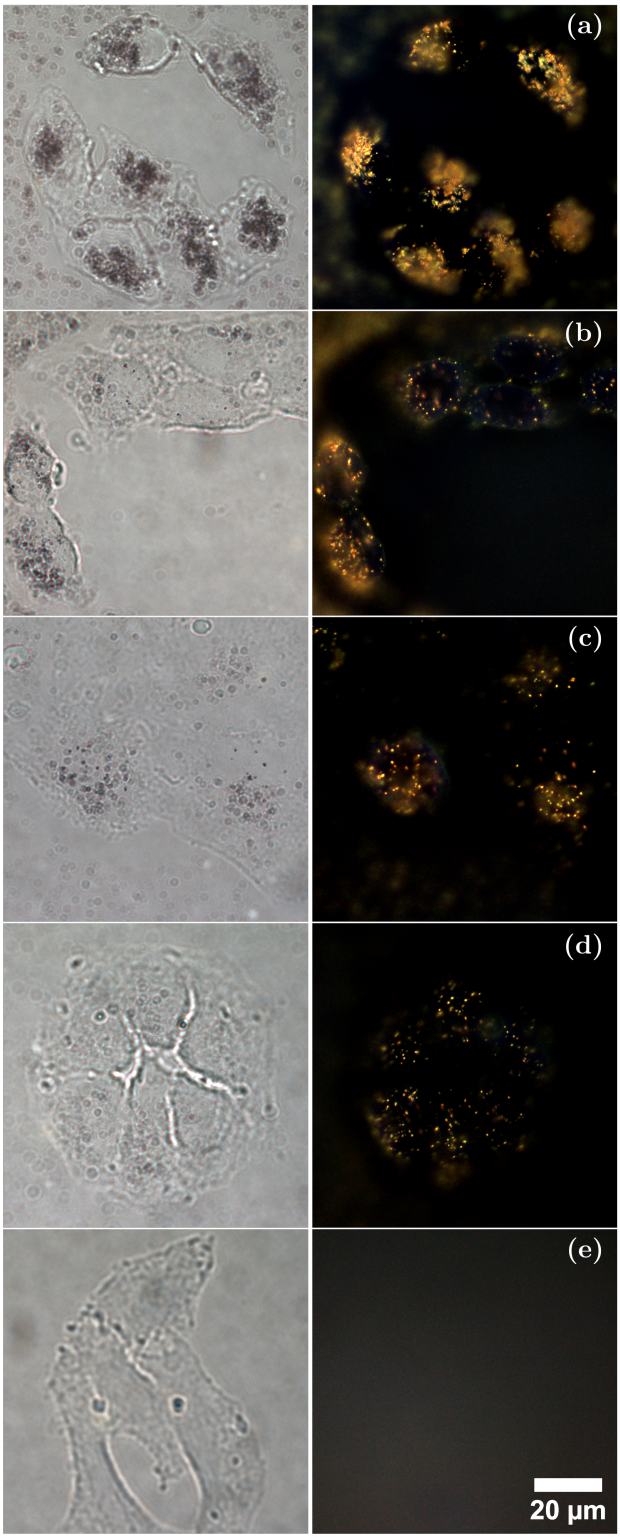

Figure 3.18: Bright-field (left) and dark-field (right) microscopy images of an A549 cell line after 4 h incubation in media containing (a) Au50-841s, (b) Au40-790s, (c) Au25-803s, (d) Au10-811s, and (e) control. AuNR images at a concentration of 1×10^{11} NP mL^{-1} for each AuNR type. All dark-field microscopy images are presented using the same brightness and contrast conditions. Scale bar = 20 µm.

Chapter 4

Plasmonic photothermal therapy with gold nanorods

Cancer is a leading cause of death worldwide with approximately 70% of deaths occurring in low- and middle-income countries [21]. Lung cancer, in particular, is the most prevalent and deadly form of cancer since there exists very few options for diagnosis or treatment. Endobronchial ultrasound (EBUS) is a routinely used diagnostic tool for staging lung cancer via needle-biopsy, and it is generally used when signs of lung cancer have been observed via X-ray or CT scan. EBUS lends itself to the possibility for combining with photoacoustic imaging (PAI), and as an extension of this, plasmonic photothermal therapy (PPTT), since the device houses an ultrasonic probe. As discussed in section 2.4, PPTT is a therapeutic modality that, when combined with AuNRs, can provide a highly selective, minimally invasive treatment option for cancer. It would be beneficial if PPTT could be administered with a pulsed-wave (PW) laser since it would reduce the potential damage to surrounding tissues by eliminating the bulk heating effect caused by continuous wave (CW) lasers. In this chapter, the use of PW lasers for PPTT is explored using multiple different sizes of AuNRs as the photoabsorbers, in addition to the impact of targeting AuNRs to lung cancer cells, and comparisons are made between the photothermal efficacy of PW lasers and continuous wave (CW) lasers.

4.1 Introduction

The photothermal effect relies heavily on a light source that can deliver a large amount of energy to a localised region, and thus a laser is often used [312]. Laser ablation (LA), a common clinical therapeutic technique that relies on lasers, is predominantly used to compliment additional therapies by reducing tumour volume [313]. It is mostly used for treating superficial and lung cancers where laser access and light delivery is feasible [314]. Continuous wave (CW) lasers with high powers (around 5 W) are employed to induce bulk heating

and irreversible thermal damage in the target tissue, however pulsed wave (PW) lasers have also shown potential for photothermal applications [315]. Depending on the type of laser system employed - either PW or CW - there will be significant differences in the observed outcomes. CW lasers are capable of inducing either apoptosis or necrosis, depending on laser intensity and AuNR distribution, whereas PW lasers can only induce necrosis [152]. These two pathways for cell death have their own advantages and disadvantages. For example, an apoptotic pathway can lead to cells developing drug and thermal resistance but does not cause immunogenic or inflammatory responses, while the opposite is true for a necrotic pathway [210]. PW lasers create a highly-localised rapid temperature increase in the target AuNRs [316], and this almost-instantaneous and high temperature increase causes large mechanical stresses (peak pressures $10 - 100\,\mathrm{MPa}$ [247]) that can induce necrotic cell death depending on particle location and laser energy. As discussed in section 2.6, there are very few reports on pulsed wave plasmonic photothermal therapy (PW-PPTT) (also known as photoacoustic plasmonic photothermal therapy (PA-PPTT)), and the majority predominately use either high energy laser pulses, ultra-short laser pulses (femtosecond), or alternative photoabsorbers, with little in the way of low-energy, nanosecond pulses that utilise AuNRs as the absorbing agent. Moreover, there are few reports addressing how the size of the AuNRs may affect the treatment efficacy of both PW-PPTT and conventional PPTT at equivalent concentrations. The optimisation of both the optical absorbers and laser parameters is crucial to the success of this technique. If PW lasers can be used to successfully and efficiently destroy target regions of tissue, with similar or superior outcomes to that of CW lasers, then new and combined diagnostic and therapeutic techniques may be possible.

The aim of this chapter is to provide an understanding of how CW and PW lasers can be used for AuNR-assisted PPTT. Firstly, the laser-induced heating of different sized AuNRs in two different media (water and cell media) across a range of concentrations will be explored, using both CW and PW lasers, to gain insight into how the AuNR size can affect observed outcomes. The same AuNRs will then be used to treat a common lung cancer cell line (A549) via both conventional PPTT and PW-PPTT to determine the treatment efficacy of PW lasers. Finally, the effects that AuNR targeting to lung cancer cells has on both CW and PW laser treatment will be investigated.

4.2 Photothermal heating of colloidal AuNR dispersions

A CW laser is capable of inducing a bulk temperature change in a target material due to the continuous deposition of energy over time. If the target is a colloidal suspension of AuNRs in a medium, and the laser wavelength is tuned to the exact longitudinal SPR of the AuNRs, then an enhanced heating effect may be observed. However, this is only true when the concentration of AuNRs is high enough to cause a measurable influence. It was therefore important to understand how the concentration of AuNRs influenced the overall

Table 4.1: Certified dimensions and SPRs of all AuNRs used in section 4.2.

Name	Width (nm)	Length (nm)	Aspect Ratio	SPR (nm)
Au10-840	10	44	4.4	840
Au40-850	40	148	3.7	845

heating effect before the study could progress any further.

4.2.1 Water

The photothermal heating of Au10-840s suspended in water was measured at increasing AuNR concentrations from 1×10^9 to 1×10^{12} NP mL^{-1} in addition to water without added AuNRs. The AuNRs were 10 nm in width with a SPR of 840 nm (see table 4.1). The AuNR solutions were placed in separate wells of a 96-well plate and irradiated from beneath the plate with a 1.5 W CW diode laser for 5 min. An infrared (IR) sensor was used to measure the temperature change of the well under laser irradiation in 1 s intervals across the duration of the laser exposure, with a 10 s 'pre-exposure' and a 20 s 'cooling off' period, making a total recorded time of 5 min 30 s. This process was repeated 6 times per data point to obtain a mean temperature change, and the results are displayed in figure 4.1.

It is worth noting that there are limitations with using an IR sensor to measure temperature as it can only determine the temperature of a surface (discussed further in section 4.2.3). This means that all measurements recording during these studies are of the bottom of plate (i.e. the plastic), and therefore the actual temperature inside the well may be slightly higher. However, this difference will likely be small due to the thickness of the plastic (1.4 mm).

The experiment was conducted at room temperature, with the variation in starting temperatures arising from a varying room temperature, and slight variations in the temperature of the water. As expected, an increase in AuNR concentration resulted in an increased laser-induced temperature compared with a target of water only (ie. without the addition of AuNRs). At low concentrations ($\leq 1 \times 10^{10}$ NP mL^{-1}) the difference in temperature is minimal (maximum 2 °C), however at AuNR concentrations beyond this, the difference is more prominent with a maximum achieved temperature of 73.7 ± 1.3 °C after 5 min.

4.2.2 Cell media

Small AuNRs (Au10-840s)

A more accurate representation of the final experimental study is a suspension of AuNRs in cell media since the cells will need to be surrounded by cell media to survive. Thus, the previous study was repeated with the Au10-840s suspended in cell media (DMEM). A few additional AuNR concentrations (5.5×10^{10} NP mL^{-1}, 4×10^{11} NP mL^{-1} and 7×10^{11} NP mL^{-1}) were also recorded to provide greater detail of the temperature curves at high AuNR concen-

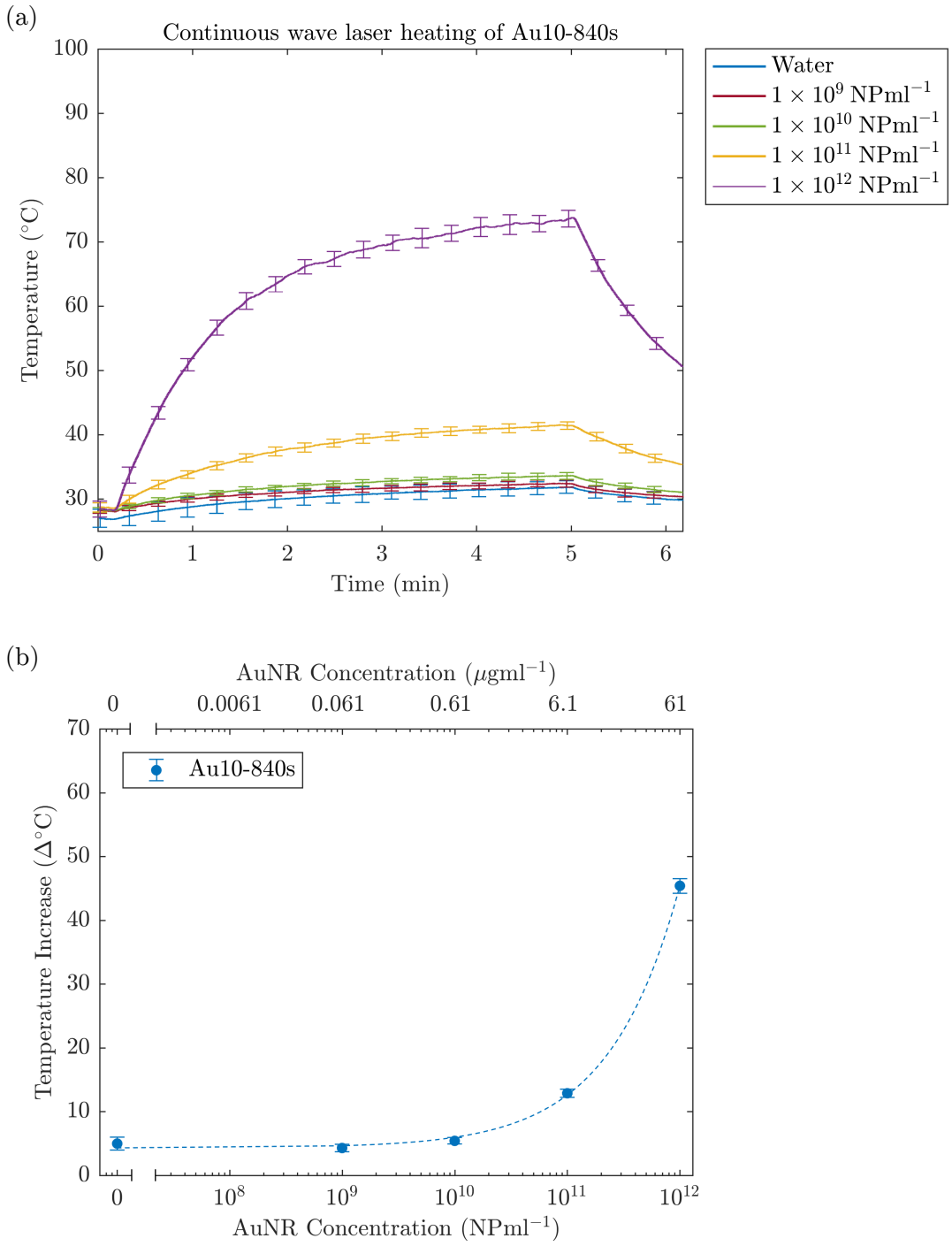

Figure 4.1: (a) Temperature profile monitored with an infrared sensor during continuous-wave (CW) laser-heating of water containing increasing concentrations of Au10-840s, and (b) the peak temperature increase achieved for each concentration. The laser was turned on after 10 s and turned off after a 5 min exposure, with a cooling off period of 20 s. Errorbars represent the standard deviation across 6 averages.

trations. For the purposes of this chapter, AuNRs with a width $\leq 25\,\text{nm}$ will be considered 'small' and those larger than this will be termed 'large'.

A similar trend was observed with the AuNRs in cell media (figure 4.2) compared with the AuNR-water suspensions (figure 4.1), where an increase in AuNR concentration saw an increase in temperature rise across the duration of the laser exposure, however the average temperature was generally higher ($+4\,^{\circ}\text{C}$ at $1 \times 10^{11}\,\text{NP}\,\text{mL}^{-1}$ and $+8.5\,^{\circ}\text{C}$ at $1 \times 10^{12}\,\text{NP}\,\text{mL}^{-1}$). This could be attributed to the fact that the cell media has a higher absorbance in the near-infrared, compared with water, and the laser wavelength was tuned to 840 nm to match the peak absorbance of the AuNRs. To assess this, the absorbance spectrum of DMEM cell media was measured with a spectrophotometer and referenced to that of water. As can be seen in figure 4.3, the absorbance around 840 nm is higher than that of water (approximately 3 %), and as a result the media itself was absorbing some of the incident laser energy and generating heat.

After the CW laser was turned on, the solution of AuNRs experienced a rapid change in temperature and slowly began to plateau as the exposure time approached 5 min. The majority of the heating (93 %) occurred in the first 3 min of laser exposure before the rate of thermal transfer from the AuNR solution to the surroundings approached the rate at which the AuNRs could convert the absorbed light into heat. As the concentration of AuNRs was increased, the larger number of absorbing AuNRs provided a higher photothermal conversion efficiency, as a larger proportion of light was absorbed and converted to heat. This allowed the liquid to reach a higher temperature before the rate of heat flow achieved equilibrium.

Figure 4.4 shows the peak temperature change achieved after the full 5 min laser exposure, compared with the starting temperature. The top axis shows the AuNR concentration represented in terms of mass ($\mu\text{g}\,\text{mL}^{-1}$) and the bottom axis in terms of number of AuNRs ($\text{NP}\,\text{mL}^{-1}$). Again, at concentrations below $1 \times 10^{10}\,\text{NP}\,\text{mL}^{-1}$, the change in temperature was minimal, and there was no difference between AuNRs suspended in water and AuNRs suspended in cell media. However, at a AuNR concentration of $1 \times 10^{11}\,\text{NP}\,\text{mL}^{-1}$, a maximum temperature increase of $17.5 \pm 1.5\,^{\circ}\text{C}$ was achieved for the AuNRs in cell media, and at $1 \times 10^{12}\,\text{NP}\,\text{mL}^{-1}$, the maximum change in temperature was $53.5 \pm 2.2\,^{\circ}\text{C}$. A more clinically useful parameter, that can be determined from these temperature curves, is the thermal isoeffective dose (TID). It provides a way to compare different thermal treatments by a measure of the number of equivalent minutes the tissue is maintained at $43\,^{\circ}\text{C}$ (CEM_{43}), and can be calculated using equation 2.7, discussed in chapter 2. Accordingly, the TID for AuNRs in cell media with a concentration of 5.5×10^{10} and $1 \times 10^{11}\,\text{NP}\,\text{mL}^{-1}$ was 0.2 and 10 CEM_{43}, respectively. At the higher concentrations of 4×10^{11}, 7×10^{11}, and $1 \times 10^{12}\,\text{NP}\,\text{mL}^{-1}$, the TID was 8.3×10^{5}, 3.5×10^{9}, and 4.9×10^{12} CEM_{43}, respectively. These thermal doses are significantly higher than the majority of relevant threshold values for determining the destruction of biological tissue, and would likely result in the total destruction of cells if conducted in biological tissue. However, this preliminary study was performed with high concentration, colloidal dispersions of AuNRs that are situated in cellular media and under

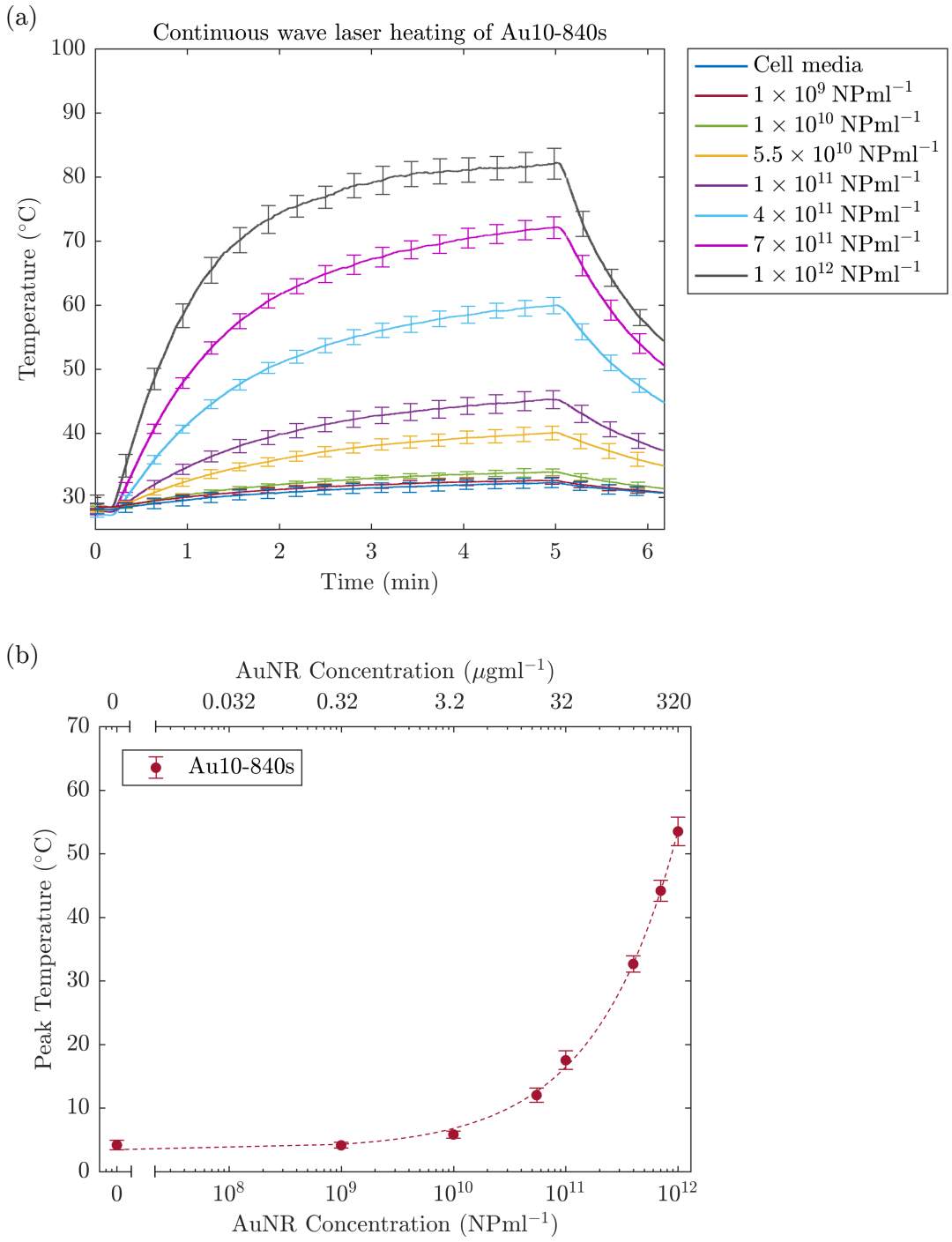

Figure 4.2: (a) Temperature profile monitored with an infrared sensor during continuous-wave (CW) laser-heating of cell media containing increasing concentrations of Au10-840s,and (b) the peak temperature change after 5 min laser exposure. The laser was turned on after 10 s with a cooling off period of 20 s. Errorbars represent the standard deviation across 6 averages.

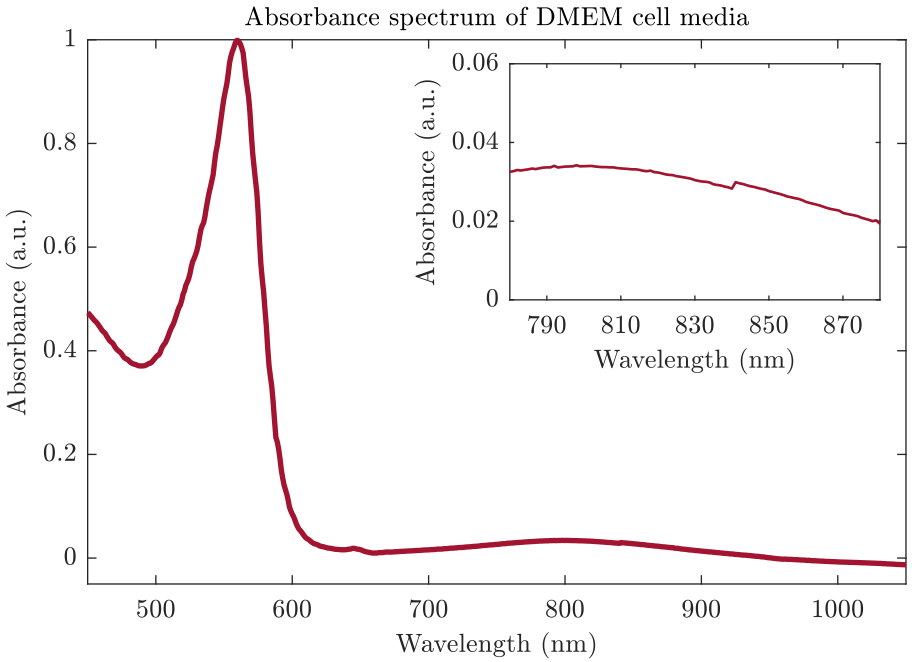

Figure 4.3: Measured absorbance spectrum of DMEM (Dulbecco's Modified Eagle Medium) cell media. Inset shows a close-up of the data in the near infrared.

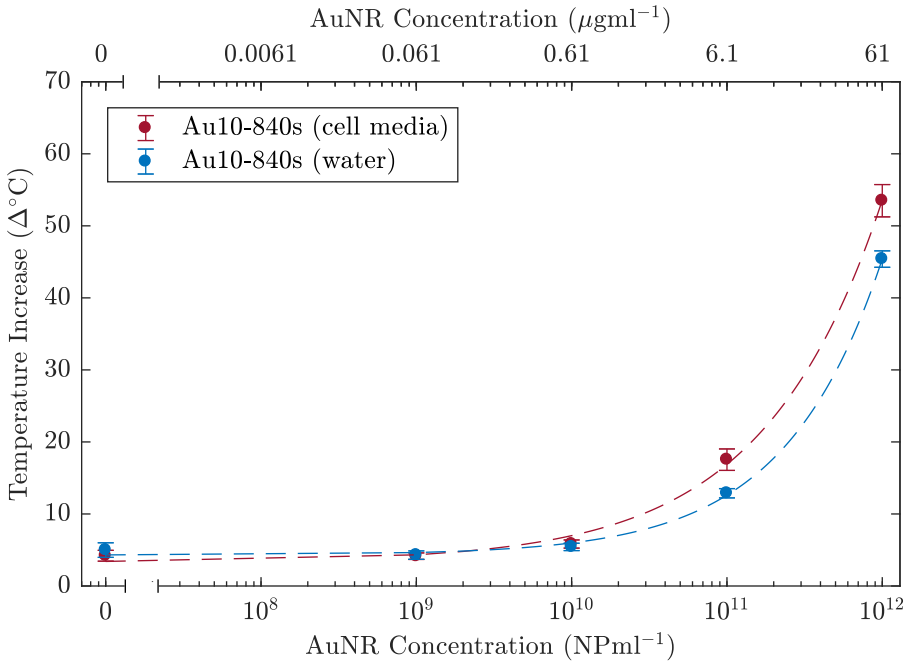

Figure 4.4: Peak temperature change after 5 min continuous-wave (CW) laser exposure for Au10-840s at increasing concentrations in water (blue) and cell culture media (red).

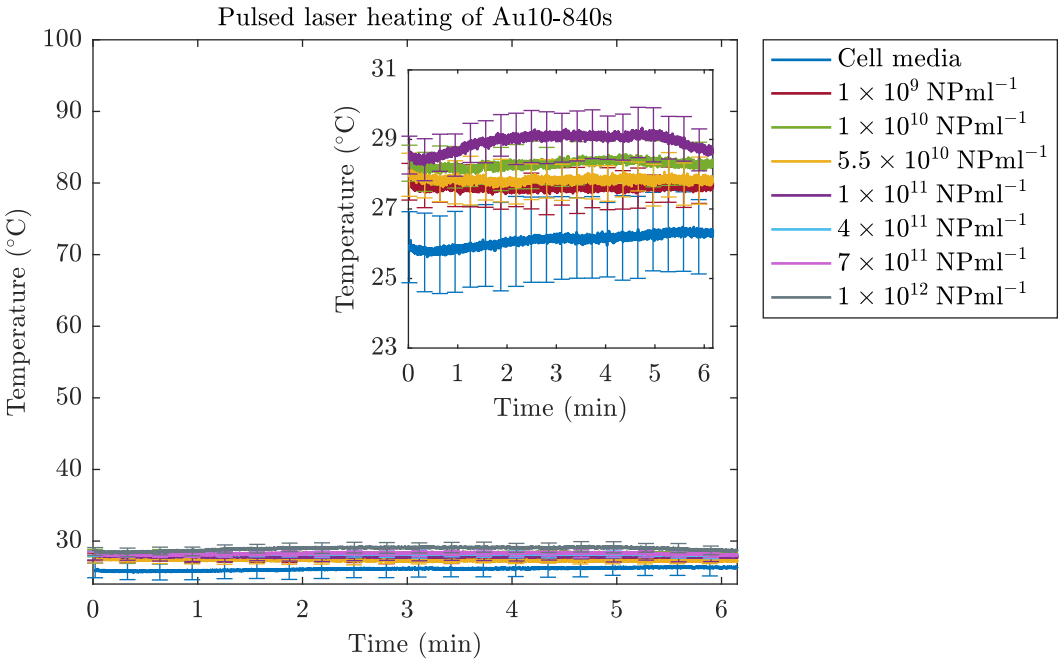

Figure 4.5: Temperature profile monitored with an infrared sensor during pulsed-wave (PW) laser-heating of cell media containing increasing concentrations of Au10-840s. The laser was turned on after 10 s and turned off after a 5 min exposure with a cooling off period of 20 s. Errorbars represent the standard deviation across 6 averages. The inset shows the same data with an expanded temperature scale for clarity.

almost direct exposure to laser irradiation. This scenario is very different compared with what may be seen *in vivo*, where inhomogeneous dispersions of AuNRs may receive laser light that has been attenuated by several millimetres of tissue. Nevertheless, it is important to understand how the temperature curves and AuNR concentrations affect the calculated thermal dose in this *in vitro* scheme, so that comparisons can be made with the future PPTT studies of lung cancer cells.

In the current literature, there is a large range of TID(CEM_{43}) values that have been determined to induce cell death. For example, it has been shown that a TID of 240 CEM_{43} *in vivo* results in the coagulative necrosis of prostate tissue using high intensity focused ultrasound (HIFU) [317]. Other reports have shown that 9.9 CEM_{43} caused thermal tissue damage in dog liver [318], and $288 - 1.5 \times 10^4$ CEM_{43} resulted in complete necrosis of human skin [319]. The reported values appear to fluctuate depending on tissue type, exposure times, and method of heat delivery. Aspects such as the rate of heating have also been suggested to affect overall tissue damage and alter the calculated TID(CEM_{43}) threshold [320].

The previous study was repeated with the CW laser swapped out for a PW laser to enable a comparison to be made between the two laser types. The PW laser was the same laser system described in chapter 3 with the wavelength tuned to 854 nm (to match that of the CW

laser) and a fluence = 35 mJ cm^{-2} (energy per pulse = 22.3 mJ, spot size = 9 mm). These laser parameters were chosen due to being within the maximum permissible exposure (MPE) limitations for skin. As can be seen in figure 4.5, the temperature remained unchanged across the entire exposure time regardless of AuNR concentration. The temperature variation between the highest and lowest curves is approximately 6 °C, and this was attributed to the variation in initial water and room temperature. The fluctuation for each individual curve is within 2 °C across all repeats.

The AuNRs used for the CW and PW laser studies were equivalent in all attributes (width = 10 nm, SPR = 840 nm), yet the observed thermal outcomes using each laser was different. With a CW laser, the temperature of the AuNR suspension reached in excess of 80 °C, while there was no measured change in temperature with the PW laser, even with the highest concentration of AuNRs (1×10^{12} NP mL^{-1}). This confirms the unique differences between CW and PW lasers, where CW lasers induce bulk heating and PW lasers do not. Furthermore, for therapeutic purposes, the method for monitoring the efficacy of treatment using a PW laser will likely need to be different to that of a CW laser, since there will be no temperature change to monitor to provide an indication of cell-death. Additionally, the concentration of AuNRs governed the initial rate of temperature rise and the maximum temperature achievable under CW laser irradiation, suggesting that careful consideration must be made regarding the concentration of AuNRs for therapy.

Large AuNRs (Au40-850s)

Currently, there does not exist a universally recognised AuNR size for therapeutic purposes and so it is crucial that the effects of different sized AuNRs are considered. The previous study was based around small AuNRs (Au10-840s), thus it was repeated with AuNRs that have a similar aspect ratio (and therefore SPR) to the Au10-840s but with a larger width (40 nm) and therefore size (see table 4.1). Again, cell media was used as the suspension fluid.

Figure 4.6a shows the photothermal heating of Au40-850s under CW laser irradiation (power = 1.5 W) at increasing concentrations from $2 \times 10^7 - 2 \times 10^{10}$ NP mL^{-1} and the maximum temperature achieved after 5 min exposure is shown as a function of AuNR concentration in figure 4.6b. As expected, an increase in concentration corresponded to an increase in the rate at which the solution heated, as well as an increase in the maximum temperature reached after 5 min exposure. At the highest concentration (2×10^{10} NP mL^{-1} or 64 µg mL^{-1}), the maximum temperature reached was approximately 83 ± 5 °C, and at an equivalent mass, the Au10-840s achieved a similar peak temperature of 85 ± 5 °C (figure 4.7), while at equivalent number of particles, the smaller AuNRs produced only a 38 ± 4 °C temperature rise. This highlights the importance of how the AuNR concentration is defined between AuNR sizes, since to achieve an equivalent temperature rise between AuNR sizes, there must be an equivalent total mass in the absorbing region. The delivery of AuNRs to a tumour site is a complex process, and it may not be possible to deliver an equivalent total

mass of AuNRs to a tumour for different AuNR sizes. There are many studies that report on the deliverability of nanoparticles to tumours [130, 321, 322, 323], however none appear to address the important issue of whether an equivalent dose of small or large nanoparticles, in total number of particles or total mass, will achieve optimal delivery efficiencies.

For completeness, the photothermal heating of Au40-850s was also measured under PW laser irradiation with equivalent parameters (fluence = $35\,\mathrm{mJ\,cm^{-2}}$, energy per pulse = 22.3 mJ, spot size = 9 mm, and wavelength = 854 nm). As was expected, no temperature rise was observed across the entire laser exposure for any AuNR concentration.

The results presented in this section are important in the context of treating a tumour with PPTT. If the concentration of AuNRs is high, and a CW laser is used, then the tumour region may reach exceedingly high temperatures and cause damage to surrounding healthy tissues as a result of heat conducting to the surroundings. Conversely, if the concentration is too low then a sufficient temperature rise may never be reached. This signifies the importance for developing a method for monitoring temperature during therapy to provide an indication of when therapy should cease. Conversely, if a PW laser is used for treatment, then thermal monitoring will not provide an indication of treatment efficacy since no temperature rise will be observed, suggesting that a different indicator will be needed to determine therapeutic efficacy.

4.2.3 Validation of infrared camera temperature monitoring

The temperature monitoring during PPTT of a cell population presents a challenge. To ensure the toxicity results are accurate and reliable, it is essential that no contaminants (such as bacteria) make their way into the vessels containing the cells, as any form of contamination can affect the overall toxicity. This limitation requires that the cells are not openly exposed to the air at any point within the experimental procedure, unless the air is sterile (such as the inside of a bio-cabinet). Thus, it is impracticable to have foreign object, such as a thermocouple, situated inside the well of a 96-well plate in addition to the cell population, since the thermocouple would have to be completely sterile and the lid would have to be removed or partially open to allow access for the thermocouple. For this reason, it was decided that a thermal imaging camera would be the best approach for monitoring the temperature changes during therapy. While the thermal camera can only measure the temperature of a surface (such as the plastic bottom of the 96-well plate - see figure 4.10), it would enable the experiment to be conducted without the risk of contamination.

The difference between the two temperature monitoring methods were compared under similar conditions to the experimental procedure, however without the inclusion of cells. Colloidal AuNRs were added to wells of a 96-well plate and a CW laser operating at 1.5 W was used to induce heating. The laser was switched on after 10 s and remained on for 5 min (300 s) before a 20 s 'cooling off' period. A K-type thermocouple was placed inside the well containing colloidal AuNRs to measure the temperature of the liquid directly, while an infrared thermal camera was used to monitor the temperature from beneath the plate (i.e.

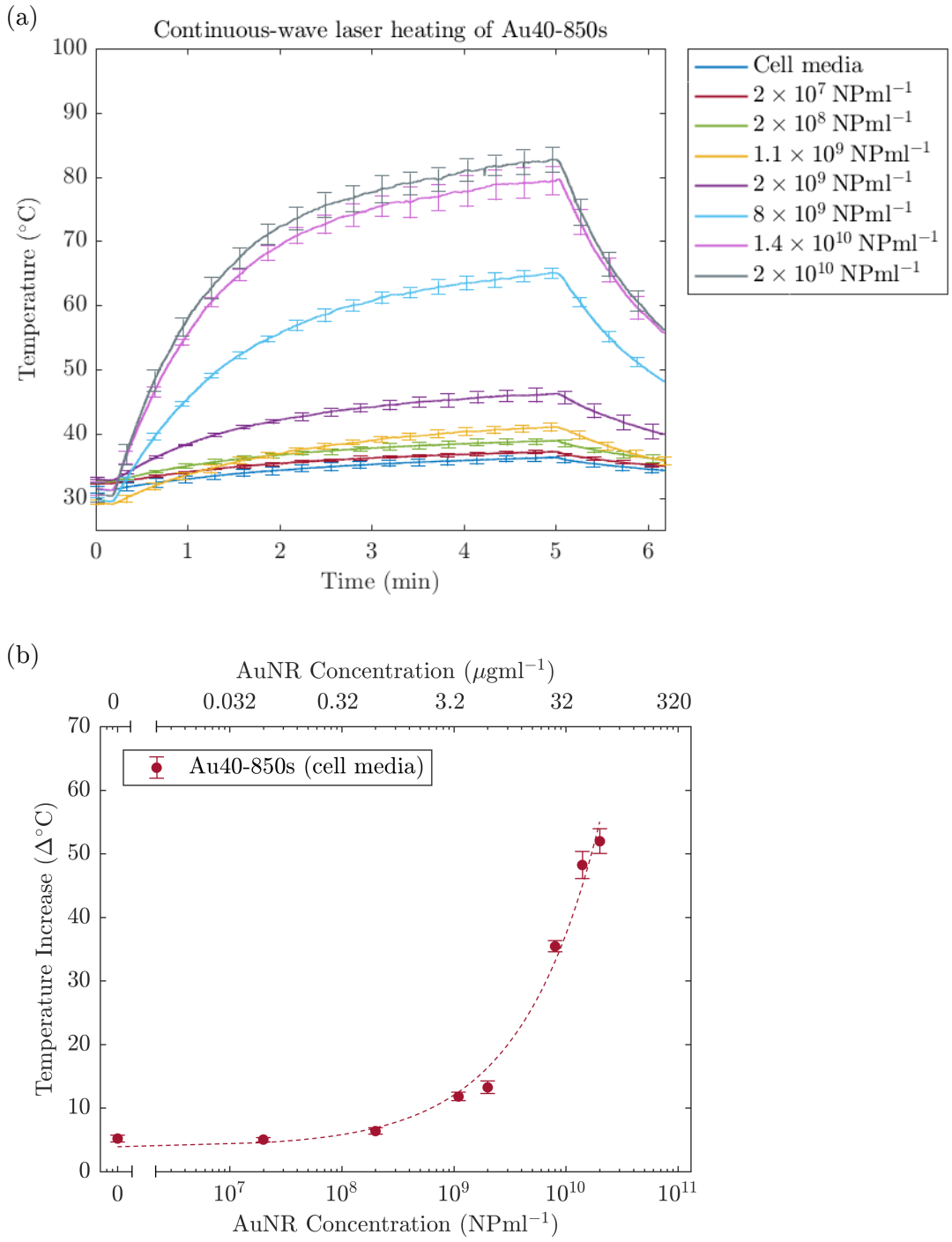

Figure 4.6: (a) Temperature profile monitored with an infrared sensor during continuous-wave (CW) laser-heating of cell media containing increasing concentrations of Au40-850s, and (b) the peak temperature change after 5 min continuous-wave (CW) laser exposure. The laser was turned on after 10 s, with a cooling off period of 20 s. Errorbars represent the standard deviation across 6 averages.

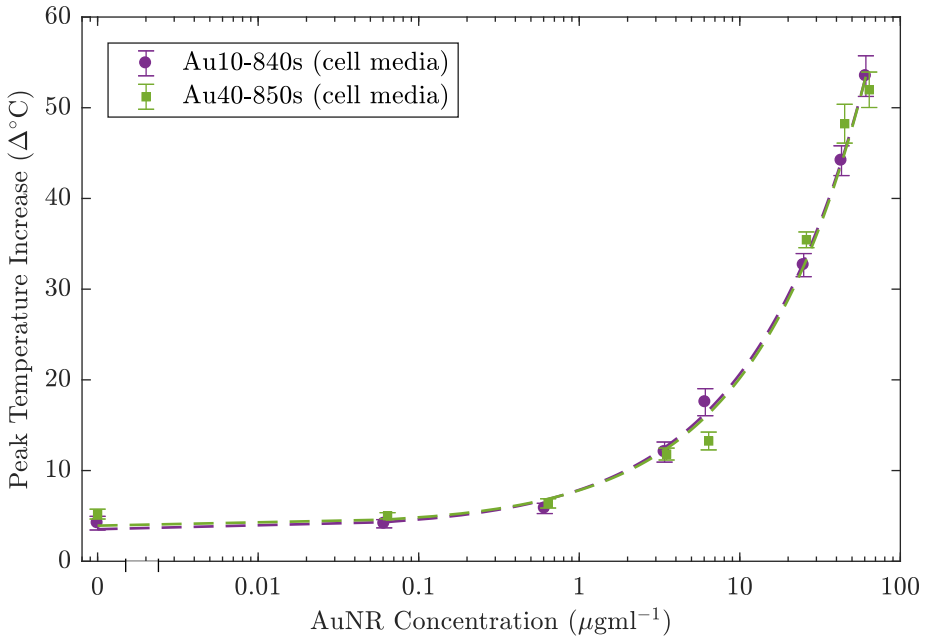

Figure 4.7: Peak temperature change after 5 min continuous-wave (CW) laser exposure for Au10-840s (purple) and Au40-850s (green) at increasing concentrations in cell culture media.

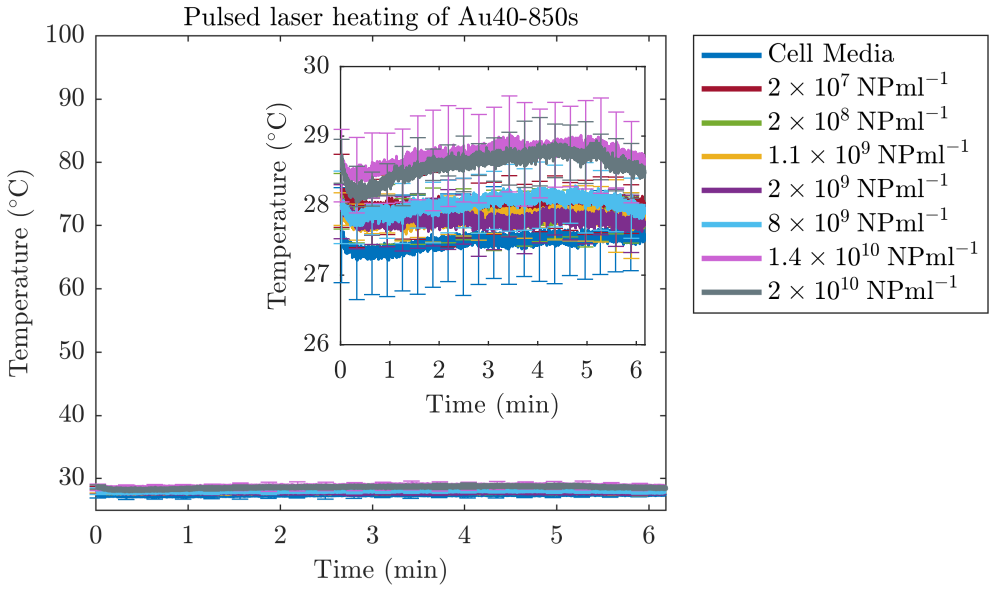

Figure 4.8: Temperature profile monitored with an infrared sensor during pulsed-wave (PW) laser-heating of cell media containing increasing concentrations of Au40-850s. The laser was turned on after 10 s and turned off after a 5 min exposure with a cooling off period of 20 s. Errorbars represent the standard deviation across 6 averages. The inset shows the same data with an expanded temperature scale.

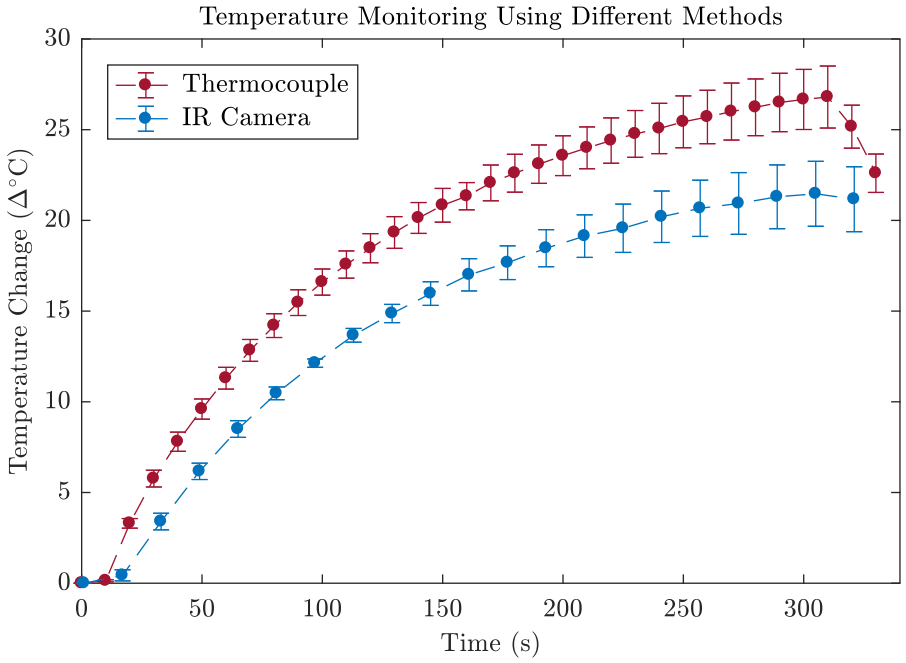

Figure 4.9: A comparison between monitoring the temperature change of laser-induced heating of colloidal gold with a K-type thermocouple (red) and infrared thermal camera (blue).

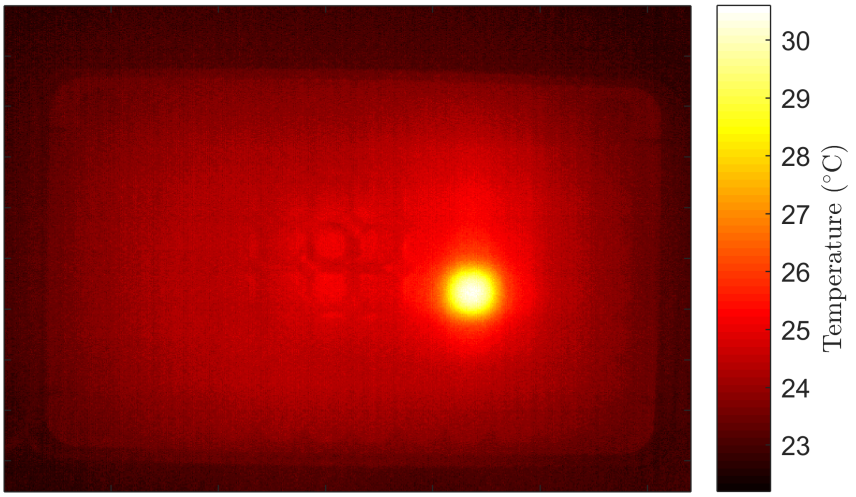

Figure 4.10: An image recorded with the thermal imaging camera employed in this chapter. Bright region shows the elevated temperature of the area under CW laser illumination.

the bottom of the 96-well plate). Figure 4.9 shows the change in temperature measured with both the thermocouple and infrared camera. As expected, there is a difference between the two temperature monitoring methods. The thermocouple recorded a maximum temperature increase of $26.8 \pm 1.7\,°C$, compared with $21.5 \pm 1.8\,°C$ for the thermal camera - a maximum difference of $5.3\,°C$.

It is safe to assume that the thermal camera will underestimate the temperature of the liquid since the heat generated in the AuNRs must propagate through the plastic to be detected by the IR camera. Conversely, it is likely that the thermocouple will overestimate the temperature as the AuNRs may adhere to the tip of the thermocouple and directly heat the thermocouple itself. Therefore, the actual temperature experienced by the cells will lie somewhere in between these values and be no more than $5.3\,°C$ higher than the thermal camera measurement, which is within the error range for this study. It is important to note that using a thermal camera is the standard method for monitoring temperature changes during photothermal therapy in the literature.

4.3 Photothermal therapy of lung cancer cells

The AuNRs used in this study were the same as the AuNRs used in the PA study in chapter 3, however table 4.2 has been provided for convenience. The main focus of the presented research was to determine the capability of a single PW laser system, combined with AuNRs of varying sizes but similar SPRs, for the treatment of lung cancer.

A human non-small cell lung epithelial carcinoma cell line (A549, ATCC, UK) was cultured in DMEM (Dulbecco's Modified Eagle Medium) media supplemented with 10 % FBS (Fetal Bovine Serum). When the cells reached 80 % confluency, a 96-well plate was seeded with 1×10^3 cells per well and incubated for 24 h. The plate was split into five sections (see figure 4.11b): a reference section containing nothing but cell media, a control section containing cells with media only, and three sections containing cells incubated with AuNRs. Two of the sections containing AuNRs were reserved for laser irradiation by two different lasers (details below), and the final section served as an AuNR toxicity reference. The AuNRs used in the study were purchased (A12, Nanopartz, USA) and the dimensions and SPRs confirmed via TEM analysis and spectrophotometry (see table 4.2). A solution of

Table 4.2: Dimensions and SPRs of the AuNRs used in the study, determined by TEM analysis and absorbance measurements respectively. The uncertainty of measurement is the standard deviation of the sample.

Name	Width	Length	Aspect Ratio	Peak SPR
Au10-811	9.9 ± 1.1 nm	39.7 ± 5.4 nm	3.98 ± 0.51	811 ± 2 nm
Au25-803	23.2 ± 2.6 nm	85.6 ± 9.8 nm	3.73 ± 0.63	803 ± 2 nm
Au40-790	39.8 ± 4.1 nm	122.5 ± 13.8 nm	3.10 ± 0.35	790 ± 2 nm
Au50-841	42.2 ± 4.6 nm	142.0 ± 17.0 nm	3.38 ± 0.41	841 ± 2 nm

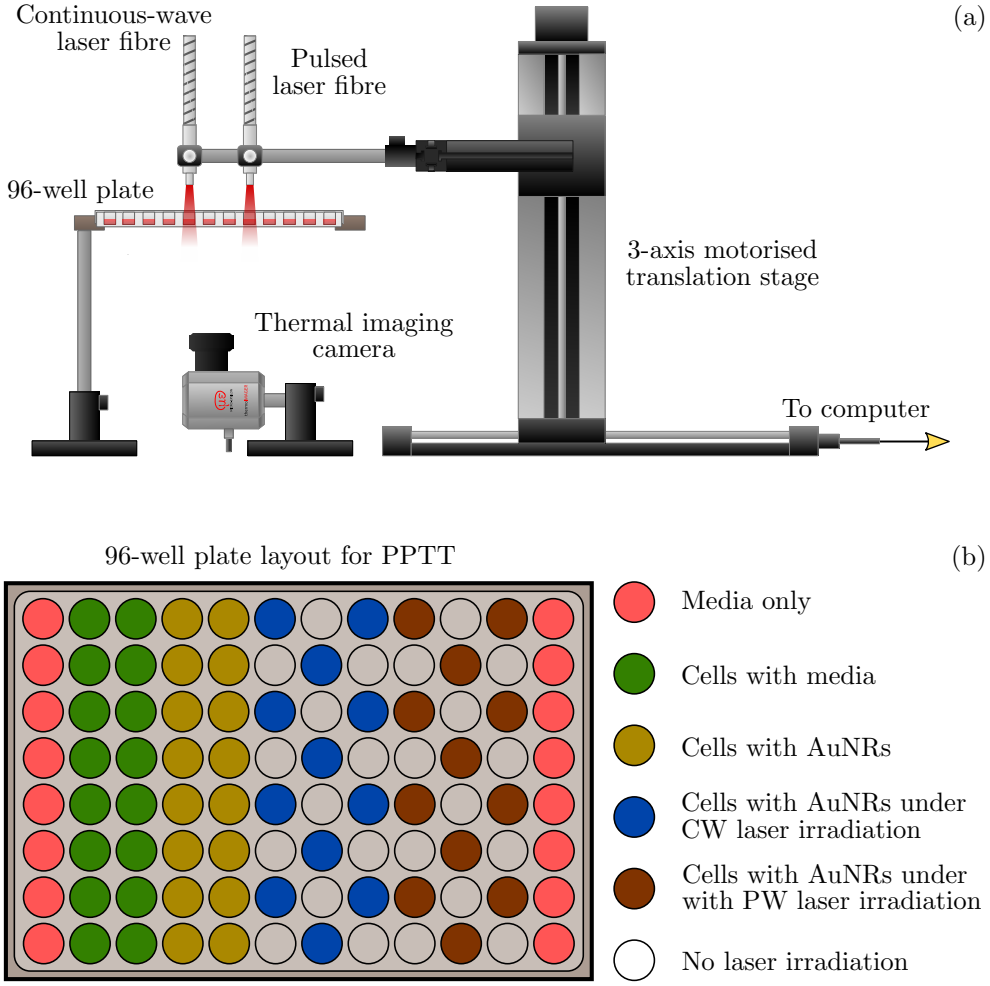

Figure 4.11: (a) A motorised stage enables the two laser fibres to be scanned across the 96-well plate, while a thermal imaging camera records the temperature of the bottom of the plate. (b) A schematic depicting how the 96-well plate is split for the experimental procedure. The wells under laser irradiation (CW = blue, PW = brown) were alternated to reduce the effects from laser treatment of neighbouring wells.

AuNRs in media was added to the relevant sections of the 96-well plate at a concentration of 20 µg mL^{-1} and were left to incubate for 24 h before being either: 1) treated with a laser with the AuNRs still remaining (i.e. with free-floating AuNRs), or 2) treated with a laser after replacing the media-AuNR solution with fresh media (to remove free-floating AuNRs). These two strategies were considered to discern the differences between the photothermal effects from a large number of absorbing AuNRs (that were both surrounding and taken up by the cells), compared with only AuNRs that have been taken up by cells and were located in close proximity. This enabled a more detailed evaluation of how the cellular uptake of AuNRs, in addition to the total number of AuNRs in the absorbing region, affects laser-induced toxicity.

Two lasers were used to induce cell death at different locations: A pulsed tuneable laser system (Surelite™ OPO Plus, Continuum®, USA) operating at a pulse repetition frequency of 10 Hz with a pulse duration of 7 ns, spot size of 9 mm (at the bottom of the 96-well plate) and fluence of 25 mJ cm^{-2}; and a continuous wave diode laser (B4-852-1500-15C, Sheaumann Laser, USA) operating at 1.5 W across a spot size of 9 mm with a fixed wavelength at 854 nm. The pulsed laser system was tuned to the same wavelength as the CW laser (854 nm) to ensure an accurate comparison could be made between the two laser types, by facilitating an equivalent optical absorption by the AuNRs. The wells that were targeted with the lasers were alternated (see figure 4.11b) to reduce any effects from the laser heating of neighbouring wells, and each well was exposed for a total of 5 min. Laser fibres were mounted onto a 3-axis motorised translation stage (see figure 4.11a) to enable the scanning of the fibre tips across the 96-well plate. The cells were irradiated for 5 min from above the plate, while an infrared thermal imaging camera (thermoIMAGER TIM 640, Micro-epsilon-Messtechnik GmbH & Co KG, Ortenburg, Germany) recorded the temperature change of the wells from below, by taking a frame every second for the duration of the exposure. The thermal camera was synchronised with the laser system through the use of an SDK provided by the manufacturer, and this also enabled the direct acquisition of thermal image data into MATLAB for further analysis.

4.3.1 Quantification of cell viability

After treatment, a standard MTT (3-[4,5-dimethylthiazol-2-yl]-2,5 diphenyl tetrazolium bromide) colorimetric assay protocol was followed [293] to establish the level of cell death between the two laser types. This metabolic assay provides an indication of cell viability by measuring the enzymatic activity of cellular mitochondria [76].

After laser irradiation, the media from each well of the 96-well plate was replaced with fresh media and the plate was placed in the incubator. 24 h later, the media was removed from each well and a solution of media containing MTT (500 µg mL^{-1}) was added. After a further 3.5 h incubation the media containing MTT was removed from each well and the 96-well plate was wrapped in foil and stored at approximately 4 °C ready for absorbance measurements.

Before measuring the plates with a plate reader (Mithras LB 940, Berthold Technologies, Germany), 100 µL DMSO was added to each well. The divided sections of the plate were averaged to obtain a single absorbance value for each AuNR concentration, and the background absorbance level was subtracted from each of the other values. The cell viability was finally calculated by the ratio of mean absorbance of the sample with respect to mean absorbance of the control group (cells with media and no laser or AuNR exposure).

4.3.2 Continuous wave vs pulsed laser treatment of lung cancer cells

Figure 4.12a shows the results of the PPTT treatment of lung cancer cells under CW laser. The cells exposed to CW laser irradiation without the inclusion of AuNRs showed no change in cell viability compared with the control group, suggesting that a 1.5 W CW laser system is not capable of therapy on its own. The AuNRs themselves (without laser treatment) showed a minimal level of toxicity, with a cell viability of approximately 80 %, due to the relatively high concentration ($20\,\mu g\,mL^{-1}$) of AuNRs incubated with the cells. When the cells were treated with both AuNRs and CW laser irradiation, significant cell death ($> 50\,\%$) was observed for all AuNR sizes. The lowest cell viability was exhibited by the CW laser combined with Au10-811 and the highest cell viability was from the Au25-803s, suggesting that the smaller AuNRs were either more efficient at inducing cellular necrosis or apoptosis through thermal damage, or the AuNRs were located in a position relative to the cells that lead to more proficient damage.

Figure 4.12b shows the temperature of the target regions that correspond to the data in figure 4.12a, as monitored with the thermal camera. The peak temperature after 5 min CW laser irradiation lies within the range $48.1 \pm 0.9\,°C - 51.1 \pm 1.0\,°C$ for all the data points, suggesting that bulk heating was the cause of cell-death for all experimental parameters, since an increase in peak temperature showed a reduction in cell viability. To induce hyperthermia in cells it has been reported that the temperature must reach between $42 - 47\,°C$, and according to the IR-camera measurements (figure 4.12b), all of the targets reached, and in some cases exceeded, this temperature range. In terms of the TID delivered to the cells, an increase in the calculated CEM_{43} values appeared to correspond to an reduction in cell viability. For the target regions containing free-floating AuNRs, TID values were calculated to be 290, 80, 170, and 150 CEM_{43} for the Au10-811s, Au25-803s, Au40-790s and Au50-841s, respectively. Likewise, a TID of 120, 40, 60, and 50 CEM_{43} was calculated for the Au10-811s, Au25-803s, Au40-790s, and Au50-849s, respectively, when the free-floating AuNRs were removed. As discussed previously, the reported threshold CEM_{43} values for tissue destruction and cell death vary significantly depending on tissue type, method of heat delivery, and the rate of temperature increase, making direct comparison difficult. Furthermore, the original TID was designed to operate in the $40 - 47\,°C$ range and so deviations in the behaviour of the formula outside of this range can be expected. However, the presented results show a positive correlation between thermal dose and cell death, and therefore the

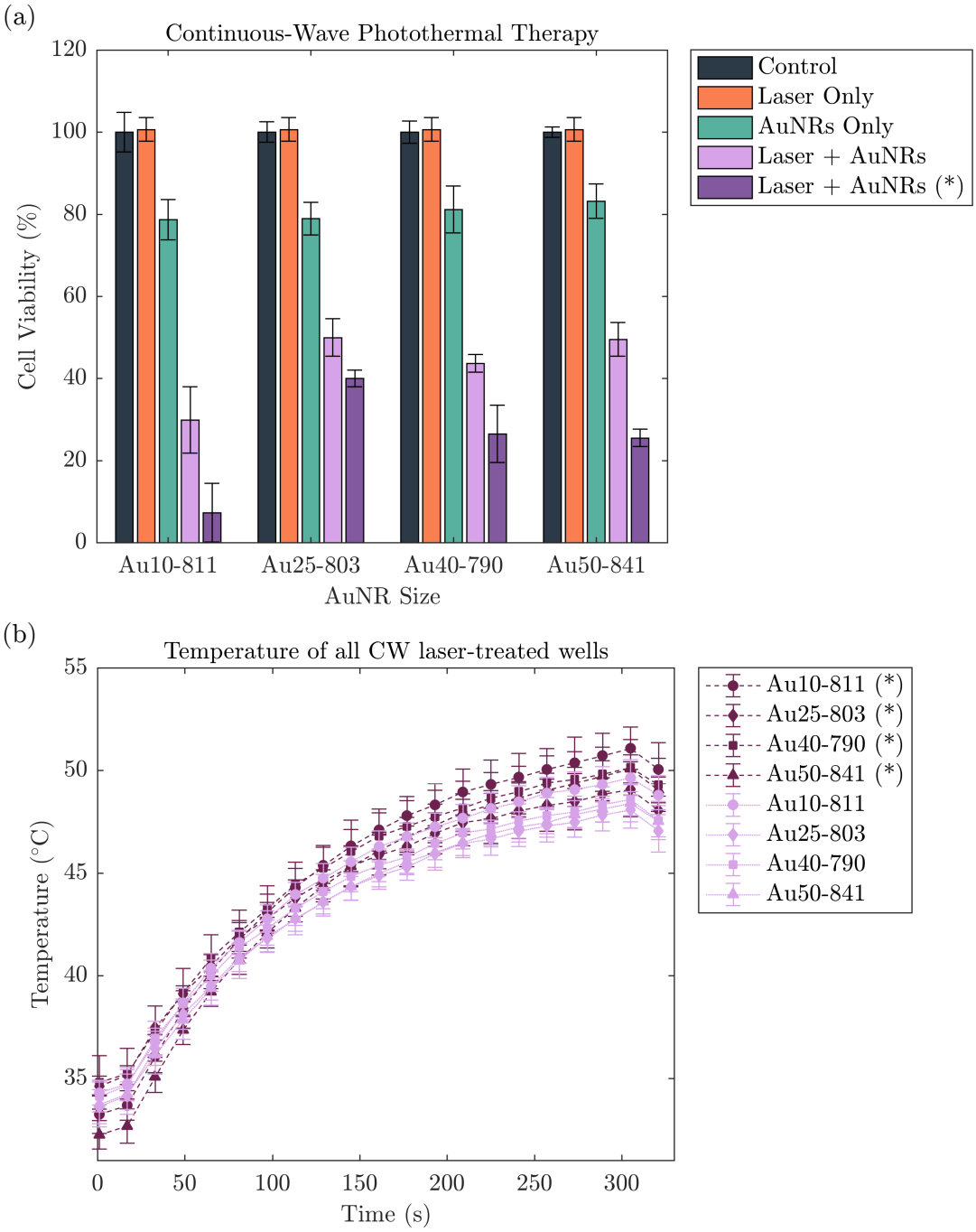

Figure 4.12: (a) Cell viability of a lung cancer cell line (A549) under different experimental parameters: a control group representing no incubation with AuNRs or laser exposure (grey), after exposure to CW laser irradiation without AuNRs (orange), after incubation with different sized AuNRs without laser irradiation (green), after incubation with different sized AuNRs followed by CW laser exposure after removing free-floating AuNRs (light purple), after incubation with different sized AuNRs followed by a CW laser exposure without removing free-floating AuNRs (dark purple (*)). (b) Monitored temperature of the wells under CW laser irradiation. The total laser exposure time was 5 min. Errorbars represent the standard deviation.

TID parameter could potentially be used to determine therapeutic efficacy with CW lasers and AuNRs.

A PW laser was also used to treat cells under the same conditions. This was done to enable a comparison to be made between the PPTT efficacy of the different laser types. A fluence of $25\,\mathrm{mJ\,cm^{-2}}$ was used to irradiate the cells and keep within the MPE guidelines for skin - a potentially important limiting factor. Figure 4.13a shows the cell viability of the PW laser-treated cells, and figure 4.13b shows the monitored temperature distribution of the wells. The PW laser treatment did not cause any damage to the lung cancer cells on its own (i.e. without AuNRs), however, under equivalent conditions as the CW laser exposure, the PW laser induced significant cell-death when AuNRs were introduced. The laser was not sufficient to cause damage to cells without the introduction of photoabsorbers such as AuNRs. There was minimal difference between the viability of the cells that had free-floating AuNRs remaining in the wells and those that had the AuNRs removed, suggesting that the AuNRs that had been taken up by the cells were the main contributors to cell-damage, and the remaining AuNRs, that were situated on top or around the cells, had little to no effect. This is due to the PW laser generating an intense and rapid temperature increase in the AuNRs that is distributed in extreme proximity to the AuNRs (approximately 70 nm from the AuNR during an 8 ns pulse [324]), meaning that the AuNR must be positioned such that the heat can cause damage to the cells or disrupt cellular membranes and cause irreparable damage to cells by the large mechanical stresses induced from the AuNRs absorbing the high-intensity laser pulses [230]. Nevertheless, it is clear that bulk heating was not a contributing factor since figure 4.13b showed no measurable increase in temperature throughout the duration of the experimental procedure. Consequently, it was not possible to determine a TID for this treatment.

The smallest AuNRs studied (Au10-811s) were the most effective therapeutic agents, destroying almost 80 % of the lung cancer cells, whereas the least effective were the Au25-803s, killing approximately half of the cell population. The two larger AuNRs (Au40-790s and Au50-841s) were only marginally more effective at inducing cell-death than the Au25-803s. The differences between the total cellular uptake of the different sized AuNRs will have a significant effect on overall cellular toxicity under laser illumination. A well-cited study by Chithrani et al. (2007) suggested that AuNRs display a negative relationship between AuNR aspect ratio and cellular uptake [141], however the AuNRs used in that study were different in size and either transferrin-coated (to help uptake via endocytosis), CTAB-coated, or not coated at all. The many differences between those used in the study by Chithrani et al. and those considered in this study make a direct comparison difficult. Other more recent research has shown that there are a large number of factors that govern the uptake of AuNRs by cells, such as AuNR coating, colloidal stability, volume, and surface functionalisation, among others [325, 326]. Some studies have suggested that large aspect ratio AuNRs can increase cellular uptake due to being in contact with the cell membrane for longer, facilitating the clustering of AuNRs and increasing cell membrane bending energies

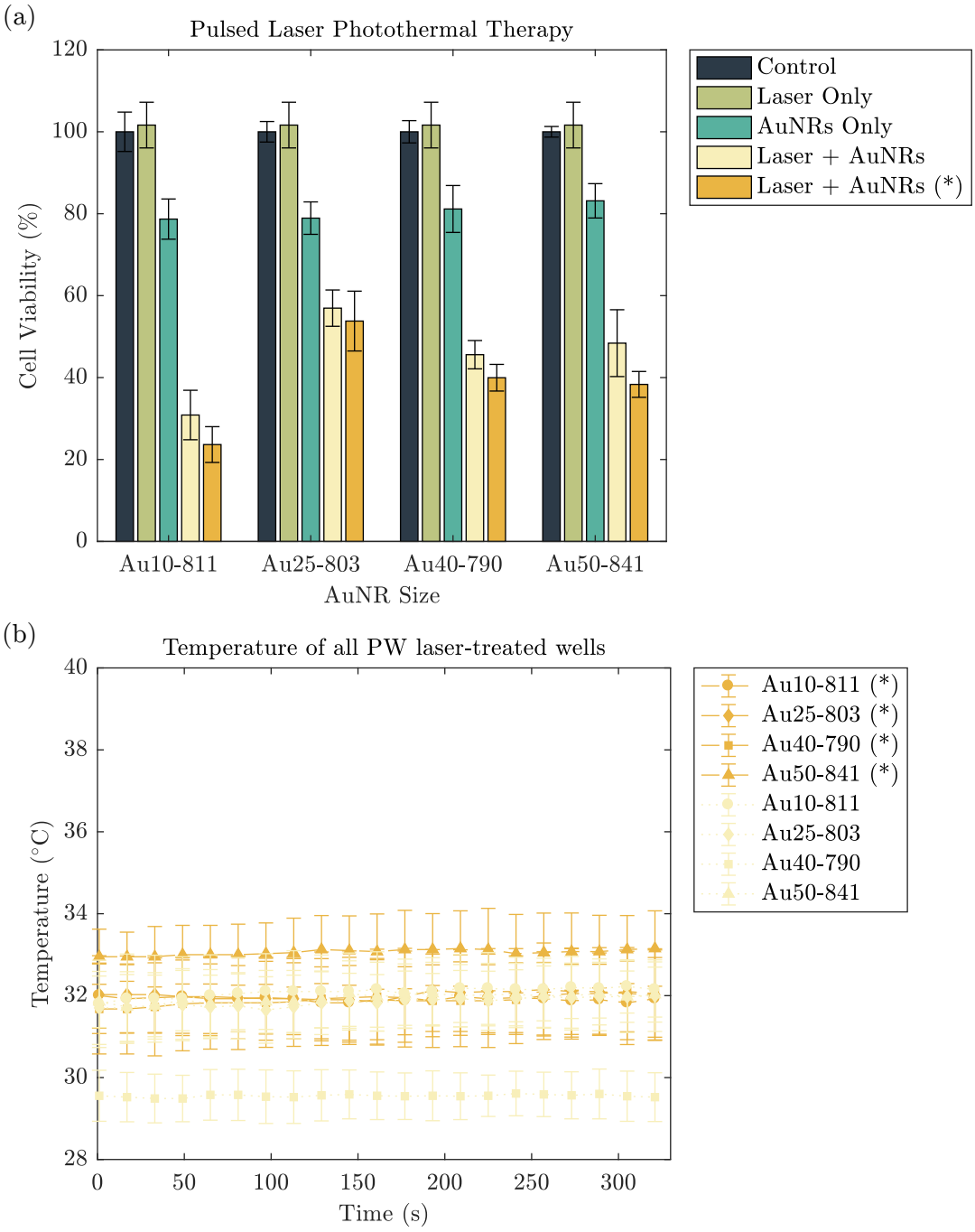

Figure 4.13: (a) Cell viability of a lung cancer cell line (A549) under different experimental parameters: a control group representing no incubation with AuNRs or laser exposure (grey), after exposure to PW laser irradiation without AuNRs (light green), after incubation with different sized AuNRs without laser irradiation (dark green), after incubation with different sized AuNRs followed by PW laser exposure after removing free-floating AuNRs (light yellow), after incubation with different sized AuNRs followed by a PW laser exposure without removing free-floating AuNRs (dark yellow (*)). (b) Monitored temperature of the wells under PW laser irradiation. The total laser exposure time was 5 min. Errorbars represent the standard deviation.

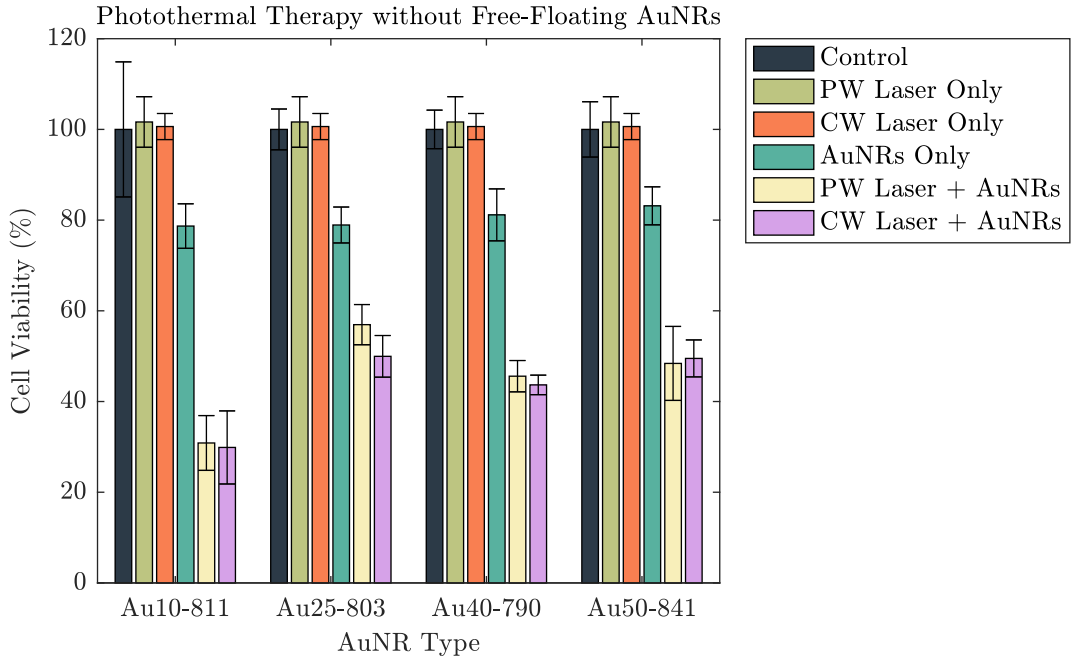

Figure 4.14: Cell viability of a lung cancer cell line (A549) under different experimental parameters: a control group representing no incubation with AuNRs or laser exposure (grey), after exposure to PW laser irradiation without AuNRs (light green), after exposure to CW laser irradiation without AuNRs (orange), after incubation with different sized AuNRs without laser irradiation (dark green), after incubation with different sized AuNRs followed by PW laser exposure with free-floating AuNRs removed (yellow), after incubation with different sized AuNRs followed by a CW laser exposure with free-floating AuNRs removed (purple (*)). The total laser exposure time was 5 min. Errorbars represent the standard deviation.

[327]. However, this is not consistent across all studies. For example, Qiu et al. (2010) reported that smaller aspect ratio AuNRs (< 4) showed higher uptake levels compared with longer ones and concluded that AuNR size has a significant effect on cellular uptake in combination with aspect ratio. The current research seems to suggest that there may be an AuNR with optimal size and aspect ratio that facilitates high uptake levels (and therefore PPTT efficacy) and may explain the differences in PPTT-induced toxicity for the four AuNRs in this study.

As discussed, the location of the AuNRs in relation to the different parts of the cell (i.e. cytoplasm, nucleus etc.) is an important factor governing the efficacy of PPTT and it has been suggested that a particular laser type (either CW or PW) is more effective at inducing cell death depending on this location [206]. According to Huang et al. (2010), a CW laser is more effective (i.e. requires lower laser energies) when the AuNRs are situated in the cytoplasm, whereas a PW is more effective for nucleus-targeted AuNRs. Figures 4.14 and 4.15 show the PPTT toxicity data from figures 4.12 and 4.13 to enable easy comparison

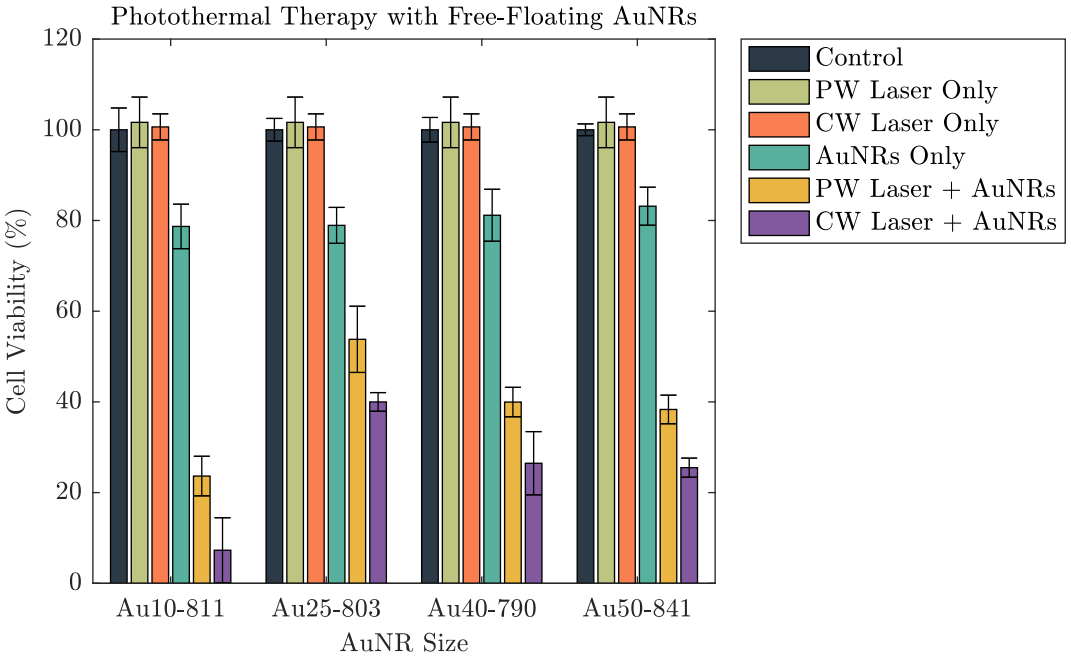

Figure 4.15: Cell viability of a lung cancer cell line (A549) under different experimental parameters: a control group representing no incubation with AuNRs or laser exposure (grey), after exposure to PW laser irradiation without AuNRs (light green), after exposure to CW laser irradiation without AuNRs (orange), after incubation with different sized AuNRs without laser irradiation (dark green), after incubation with different sized AuNRs followed by PW laser exposure with free-floating AuNRs (yellow), after incubation with different sized AuNRs followed by a CW laser exposure with free-floating AuNRs (purple (*)). The total laser exposure time was 5 min. Errorbars represent the standard deviation.

between the PPTT efficacy of CW and PW lasers. When the free-floating AuNRs were removed and only AuNRs that had been taken up by the cells remained (figure 4.14), the difference in cell viability between the CW and PW lasers was minimal for all AuNR sizes considered. However, in the case where the free-floating AuNRs were left in the media, the CW laser produced a measurable increase in cell toxicity. As discussed previously, the extra AuNRs in the solution enabled the CW laser to produce significantly more heat than when they were removed, and the increased heat resulted in larger, more wide-spread damage to the cells. As for the PW laser irradiation, the extra free-floating AuNRs did not facilitate an increase in cell damage since heating was not the primary therapeutic pathway and the location of the AuNRs was the most important aspect. This data suggests that PW lasers are capable of destroying lung cancer cells with an almost equivalent efficiency as a CW laser, however the location of the AuNRs is the most important factor governing the efficacy of cell death.

4.4 Targeting AuNRs to lung cancer cells

The functionalisation of AuNRs to molecularly target specific binding sites, such as epidermal growth factor receptors (EGFR), is increasingly seen as an essential aspect of using AuNRs for biomedical purposes. This is largely due to the need for high numbers of AuNRs to be localised in a tumour region for a sufficient PA or PPTT effect to be observed. Furthermore, relying solely on the EPR effect to accumulate AuNRs in target tissue may not be sufficient [328]. If the particular target ligand is known, then the AuNRs can be functionalised with monoclonal antibodies (for example anti-EGFR) that will enable monovalent affinity. This is a highly desirable characteristic that can result in a much larger accumulation of AuNRs at a particular site. It is known that many forms of cancer express EGFR-positive ligands and it has therefore become a common method for molecular targeting. To determine the EGFR expression of A549 cancer cells, an immunofluorescence (IF) staining was performed using a standard IF protocol. Briefly, the A549 cells were grown in a 6-well plate on microscope coverslips. Once 70 % confluence was reached, the media was removed and the cell monolayer was washed with Dulbecco's Phosphate-Buffered Saline (DPBS). 4 % PFA (Paraformaldehyde) was added and left for 15 minute at room temperature to fix the cells to the coverslips. The coverslips were then washed twice with DPBS before being permeabilised with a solution of DPBS and 0.3 % Triton X-100. The coverslips were then washed twice in DPBS, followed by sample blocking in 10 % FBS (fetal bovine serum) for 1 h. The blocking buffer was removed and Alexa Flour 488-conjugated anti-EGFR antibodies, diluted in 5 % FBS, was added to the coverslips and incubated for 2 h at room temperature. Finally, the coverslips were washed 3 times in DPBS and mounted on microscope slides using DAPI (4,6-diamidino-2-phenylindole) reagent (ProLong Gold Antifade Mountant). The same protocol was repeated to form a control group without adding the conjugated antibodies. The level of EGFR expression (as determined from the IF images

Table 4.3: Certified dimensions and SPRs of all AuNRs used in section 4.4.

AuNR Name	Width (nm)	Length (nm)	Aspect Ratio	SPR (nm)
S-Au40-849	40	148	3.7	849

in figure 4.16) in A549 cells was not as high as expected. Nevertheless, EGFR expression was observed during the IF staining and therefore it was decided that the effect of targeting AuNRs to the EGFR receptors would be investigated.

To begin with, AuNR-targeting was considered using dark-field microscopy. As discussed previously (section 2.2.1), if AuNRs are to be used clinically then it is crucial that large-scale synthesis with consistent properties and uniform distributions is possible. Hence, highly concentrated Streptavidin-conjugated AuNRs were purchased (see table 4.3) from Nanopartz - a company that are able to synthesis AuNRs on a large scale with repeatable characteristics - to enable them to be easily functionalised with an anti-EGFR targeting ligand (figure 4.17). A protocol was designed to enable the comparison of cellular uptake for targeted versus untargeted S-Au40-849s at three different time-points: 4 h, 8 h, and 24 h. These were chosen to provide an indication of the time-scales required for wide-spread affinity of the targeted AuNRs to the lung cancer cells. Furthermore, in chapter 3, high levels of uptake were seen after 4 h incubation. The biotinylated antibody used in this study was a mouse monoclonal antibody (ab24293, abcam) and the amount required to facilitate the conjugation with the AuNRs was explored along-side the targeting efficiency. A series of 21 microscope coverslips were soaked in ethanol overnight before being allowed to dry completely, and were then placed inside a separate well of six 6-well plates. For each time-point there was enough cover-slips to allow for: one blank (3), two untargeted (6), two targeted with 10 µL biotinylated antibody (6), and two targeted with 20 µL biotinylated antibody (6). A human non-small cell lung epithelial carcinoma cell line (A549, ATCC, UK) was cultured in DMEM (Dulbecco's Modified Eagle Medium) media supplemented with 10 % FBS (Fetal Bovine Serum). When the cells reached 80 % confluency, the 6-well plates were seeded with 4×10^3 cells per well and incubated for 48 h. Before the AuNRs were added to the wells, a functionalising protocol was followed (see figure 4.18). The stock S-Au40-849s (concentration = 4×10^{12} NP mL^{-1} = 13.2 mg mL^{-1}) were first sonicated for 15 min to minimise aggregation and then 45 µL of the stock S-Au40-849s was split between three sterile Eppendorfs (i.e. 15 µL per Eppendorf). The first Eppendorf (named 'UT') was reserved for untargeted AuNRs, 10 µL of the biotinylated antibody was added to the second Eppendorf (named 'T10'), and 20 µL of the biotinylated antibody was added to the final Eppendorf (named 'T20'). All of the Eppendorfs were then topped up with Dulbecco's phosphate-buffered saline (DPBS, 14190-094, Life Technologies, UK) to a total volume of 40 µL (i.e. 25 µL DPBS in Eppendorf UT, 15 µL DPBS in Eppendorf T10, and 5 µL DPBS in Eppendorf T20). All three Eppendorfs were then sonicated for 10 min before being placed on a vortex for 30 min to facilitate the conjugation of the AuNRs and antibodies. The AuNRs

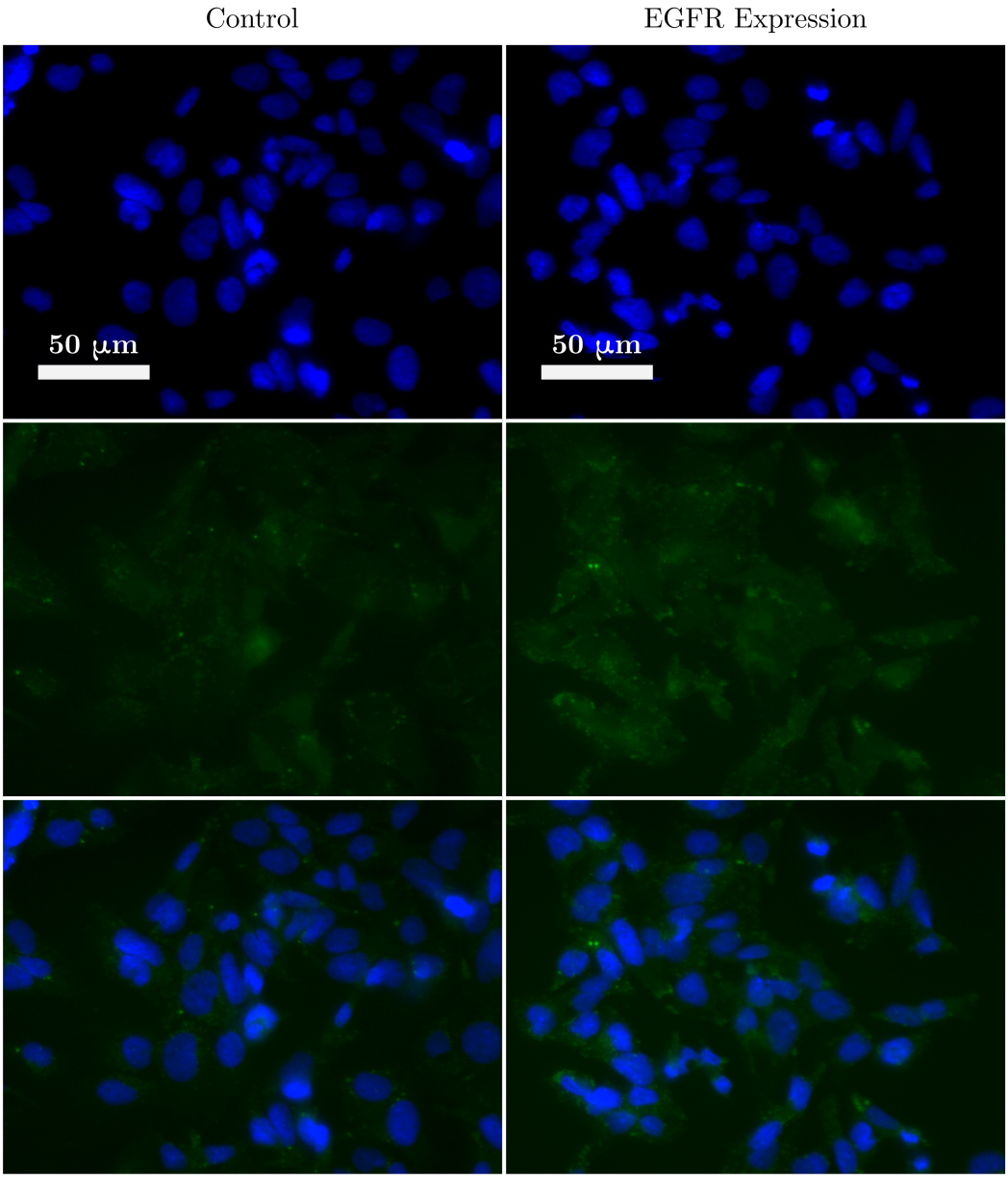

Figure 4.16: A fluorescence image of lung cancer cells (A549) showing the expression of anti-EGFR receptors. Blue represents the staining of the cell nucleus and green shows the expression of EGFR.

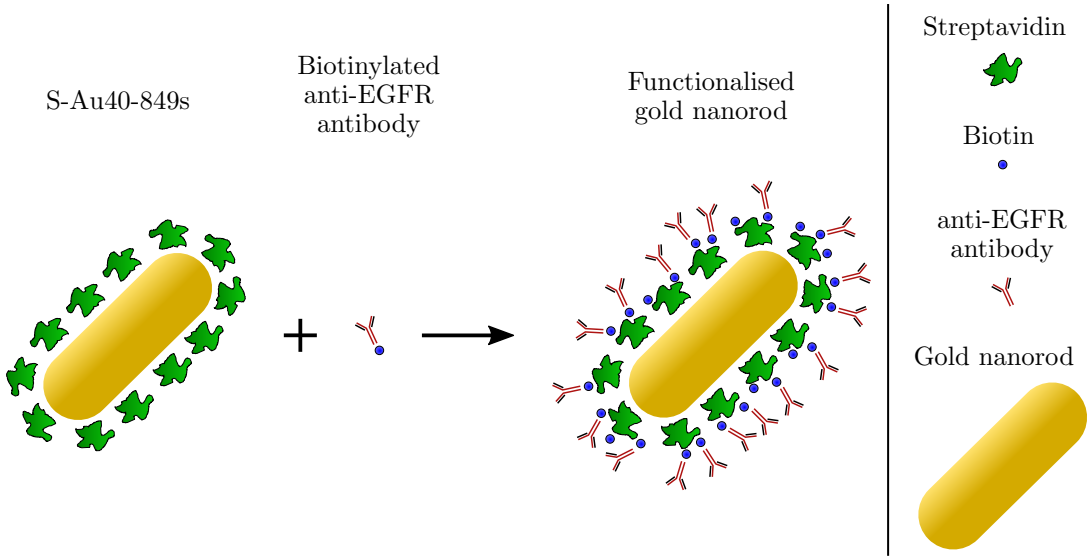

Figure 4.17: The biotinylated anti-EGFR antibodies exhibit high affinity to the Streptavidin proteins that are already conjugated to the AuNR.

were then purified by centrifuging for 10 min at a relative centrifugal force (r.c.f.) of 5.9, followed by the removal of the supernatant and addition of 40 µL DPBS, and then further mixing was performed with the vortex for 2 min followed by sonication for 10 min. After repeating the purification process twice, the supernatant was replaced with 100 µL DMEM media before being added to separate 15 mL falcon tubes filled with DMEM media to a total volume of 6 mL. Finally, each falcon tube was vortexed for 2 min and sonicated for 10 min before the media-AuNR solutions were added to the 6-well plates at a total volume of 2 mL per well, giving a final AuNR concentration of 30 µg mL^{-1}. The plates were then incubated for different lengths of time (4 h, 8 h, and 24 h) before a standard protocol for preparing microscope slides for dark-field imaging was followed. A549 cells were plated onto 22×22 mm glass cover-slips in a 6-well plate at a density of 1×10^5 $well^{-1}$ and allowed to grow for two days. The AuNR-media was removed from each well and the cell monolayer on the cover-slip was twice-rinsed with DPBS, fixed in 4 % paraformaldehyde/DPBS for 10 min at room temperature and rinsed with DPBS five times. The fixed coverslips were then mounted and sealed onto glass slides. Bright and dark-field microscopy imaging was performed with an inverted microscope (Nikon Eclipse Ti-E, Nikon UK Ltd, UK) using an oil coupled 100x objective (CFI Plan Fluor, Nikon UK Ltd, UK). Images were recorded with a 5 Megapixel colour camera (DS-Fi1, Nikon UK Ltd, UK) and saved using the NIS-Elements D software (Nikon UK Ltd, UK). Open-source software package ImageJ [292] was used to crop and enhance the contrast of saved images. To ensure valid comparisons could be made, all of the images were enhanced in the same way.

A large number of images (N = 248) were acquired by scanning pseudorandomly across

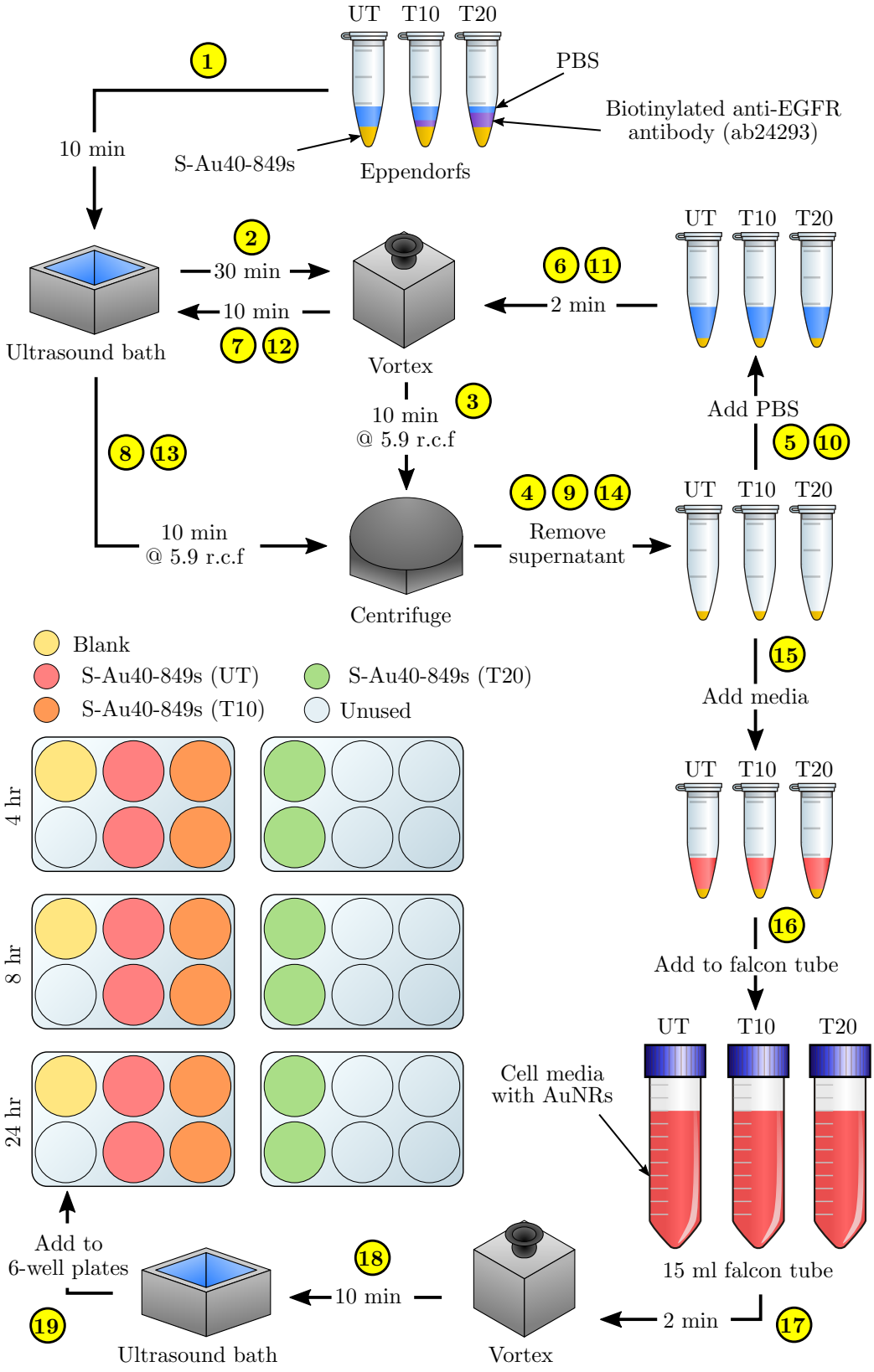

Figure 4.18: A schematic depicting the functionalisation process for the S-Au40-849s. UT = untargeted AuNRs, T10 = targeted AuNRs (10 µL antibody), T20 = targeted AuNRs (20 µL antibody).

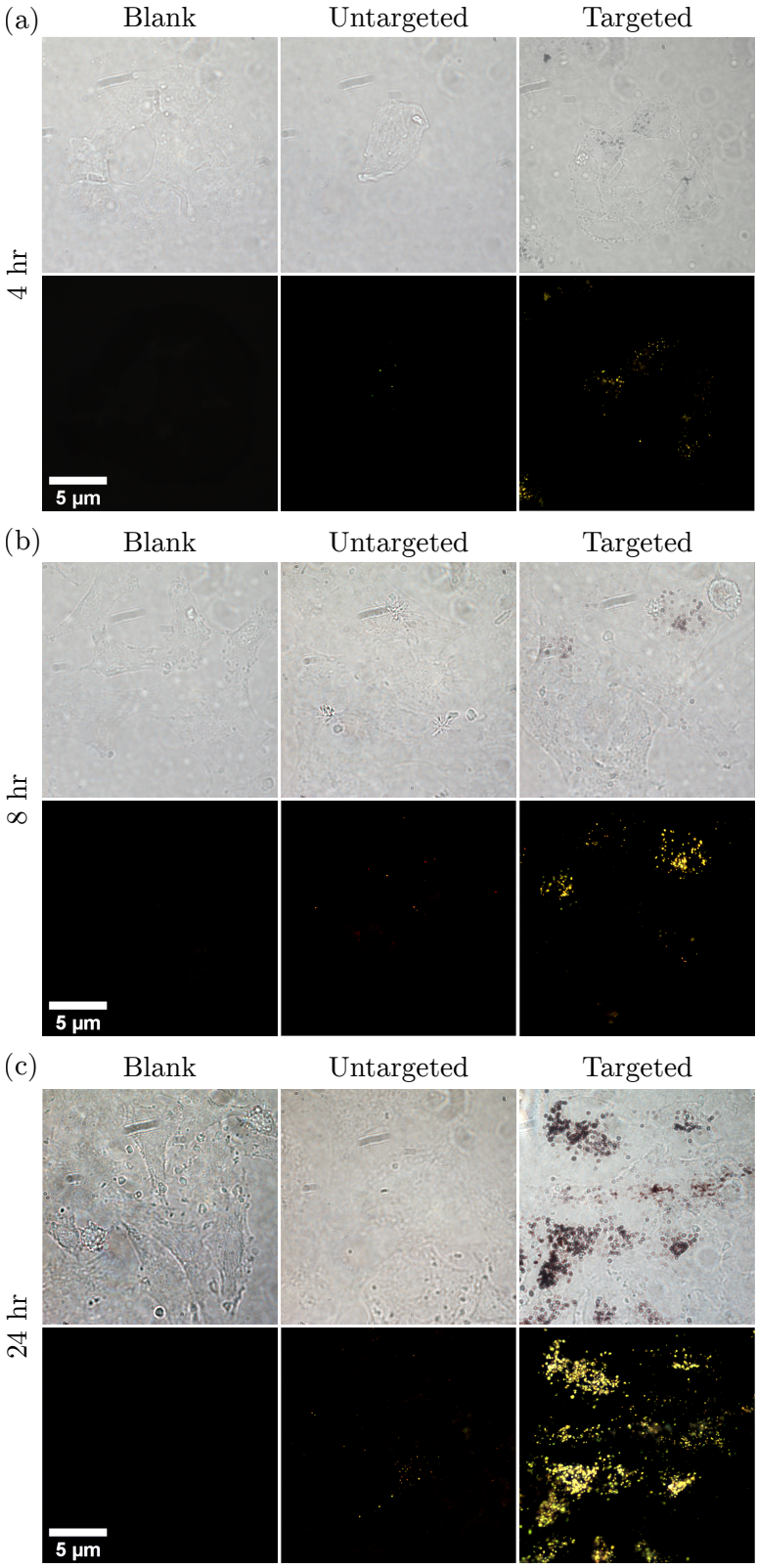

Figure 4.19: Bright- and dark-field images of lung cancer cells (A549) incubated with untargeted versus targeted S-Au40-849s for (a) 4 h, (b) 8 h, and (c) 24 h. The S-Au40-849s have different surface properties to those in the previous studies.

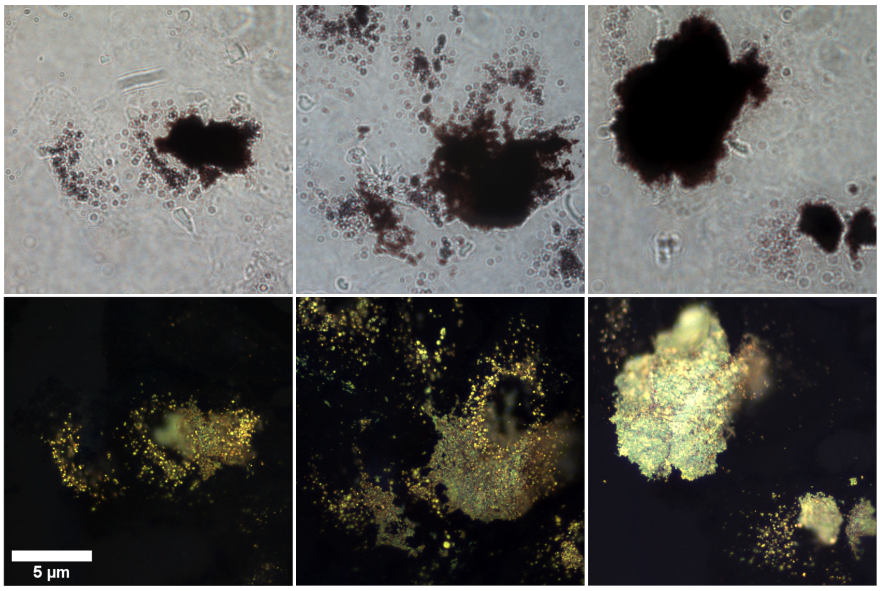

Figure 4.20: Large AuNR aggregates were apparent when a high volume (20 µL) of biotinylated anti-EGFR antibodies were used in the conjugation process of the S-Au40-849s.

the entire microscope slide to cover the majority of the sample and ensure an accurate representation of the cellular uptake across the entire slide was observed. Figure 4.19 shows a selection of those images to illustrate the typical distribution observed after analysing all obtained images. The untargeted S-Au40-849s displayed little-to-no cellular uptake across all of the time points considered in this study, which was surprising since it might be expected that after 24 h incubation, much higher levels of uptake would be seen compared to that which was observed here. In comparison with the dark-field images taken of the citrate-capped AuNRs in section 3.3, there was considerably less cellular uptake of the untargeted S-Au40-849s. This was likely due to the streptavidin ligands that were already conjugated to the surface of the AuNRs, limiting the penetration of the S-Au40-849s into the lung cancer cells, since streptavidin has a relatively large molecular weight (approximately 60 000 Da) and has been shown to restrict cellular uptake [329]. Furthermore, the potentially reduced biocompatibility of untargeted S-Au40-849s may negatively affect cellular uptake. Conversely, the targeted S-Au40-849s significantly enhanced AuNR uptake by the lung cancer cells after 8 h and 24 h (potentially via affinity to EGFR receptors) and while minimal uptake was observed after 4 h incubation with the A549 cells, there was an increase in overall uptake compared with their untargeted counterparts. The conjugation of the S-Au40-849 AuNRs with the anti-EGFR monoclonal antibodies had a considerable effect on the overall uptake when incubated with the lung cancer cells for longer than 4 h and the results provide a compelling argument to use molecularly targeted AuNRs for the selective delivery of high concentrations of AuNRs to malignant tissues.

The volume of biotinylated antibodies (10 µL or 20 µL) that was used in the conjugation process appeared to affect the aggregation of AuNRs. As can be seen from figure 4.20, large aggregates formed when 20 µL biotinylated antibodies was used in the conjugation process. The AuNR aggregates did appear to be bound to the surface of the A549 cells, however the large number of AuNRs making up the aggregates lead to a decrease in the distribution of AuNRs across the cell sample. When 10 µL was used, a reduction in AuNR aggregates was seen and the overall distribution of AuNRs throughout the cell population was more uniform.

4.4.1 Photothermal therapy with targeted AuNRs

The functionalisation and subsequent cellular uptake of the S-Au40-849s in the previous section showed positive results and therefore justified investigating how the targeting of the AuNRs to lung cancer cells may affect the toxicity under both CW and PW laser irradiation. A protocol akin to the previous section (figure 4.18, section 4.4) for conjugating the S-Au40-849s to anti-EGFR monoclonal antibodies was followed, however the 6-well plates were replaced with two 96-well plates and were seeded with A549 cells at a concentration of 1×10^5 cells per well. The experimental setup was the same as figure 4.11 (section 4.3), however untargeted (UT) AuNRs were added to one plate and targeted (T10) AuNRs were added to the other - both at a concentration of 30 µg mL^{-1} - and left to incubate for either 4 h or 24 h. Immediately prior to laser exposure, the media in the wells of the 96-well plate was removed, the cell monolayer washed once with DPBS, and then 100 µL of fresh media was added. This washing step was performed to minimise the number of AuNRs remaining in the wells that were not bound to the cell surface receptors or taken up by the cells. Both of the laser systems were operating under the same parameters as in the previous section to enable a fair comparison to be made (5 min exposure duration, PW fluence = 25 mJ cm^{-2}, CW power = 1.5 W).

Figure 4.21 and 4.22 show the cell viability evaluation results of the A549 cells after incubation with both untargeted and targeted S-Au40-849s for 4 h and 24 h, respectively. After a 4 h incubation period, there was no discernable reduction in cell viability induced from the AuNRs, either on their own or following laser irradiation. The lack of photothermal ablation can be attributed to an insufficient number of AuNRs remaining in the absorbing region after washing. This is in agreement with the cellular uptake study (figure 4.19) where a 4 h incubation period resulted in minimal uptake of both untargeted and targeted S-Au40-849s. Conversely, after 24 h incubation with S-Au40-849s (figure 4.22), reduced cell viability was observed in some cases. The AuNRs that received no laser exposure did not reduce the viability of the lung cancer cells, independent of whether they had been functionalised with the anti-EGFR ligands. This was in contrast to the study in the previous section where a small but notable reduction in cell viability (approximately 20 %) was observed. The difference between these data sets can be attributed to the differences in the surface chemistry of the AuNRs used here, compared with the ones in the previous study. In this

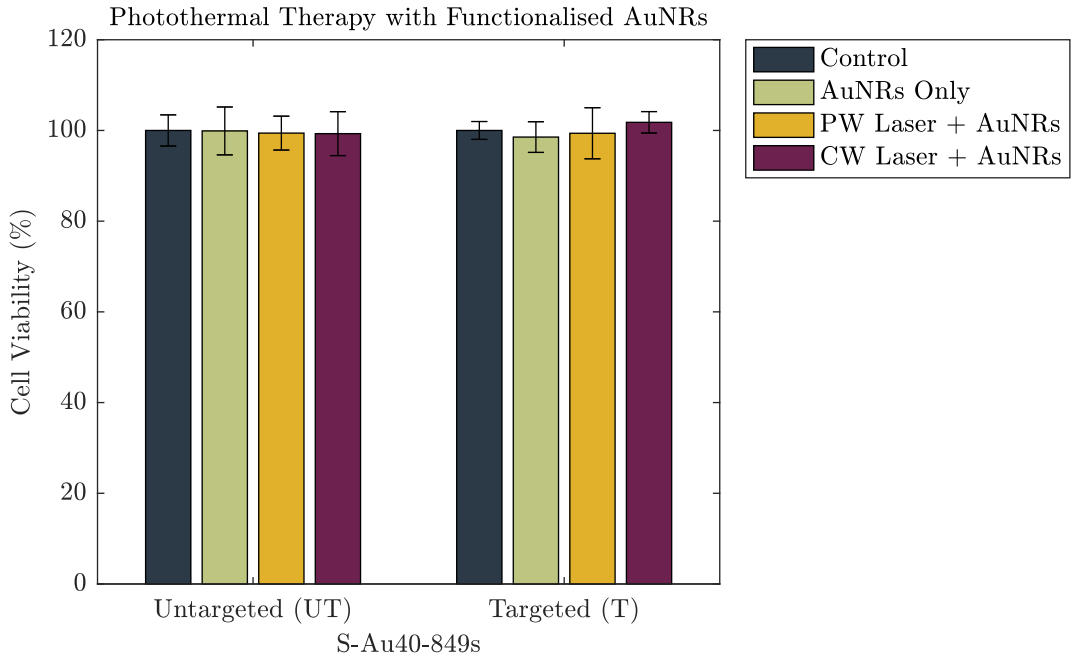

Figure 4.21: The cell viability of a lung cancer cell line after 4 h incubation with either untargeted S-Au40-849s or targeted S-Au40-849s.

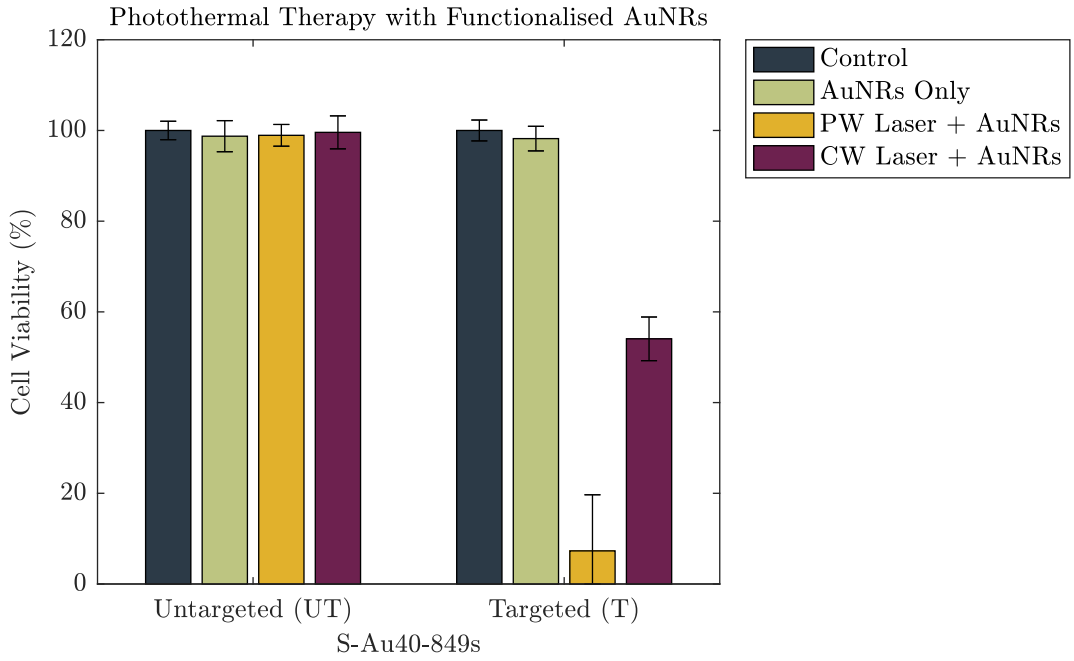

Figure 4.22: The cell viability of a lung cancer cell line after 24 h incubation with either untargeted S-Au40-849s or targeted S-Au40-849s.

case, the AuNRs were either surrounded by streptavidin proteins - which reduce cellular uptake (as seen in section 4.19) and therefore reduce toxic effects - or were conjugated with anti-EGFR ligands and were bound to the surface receptors on the cell membrane, limiting penetration into the cells. The cells that experienced a combination of untargeted S-Au40-849s and either CW or PW laser irradiation, also did not display a reduction in cell viability after the 5 min laser exposure. As discussed previously, the untargeted AuNRs had limited penetration into the cell membranes due to the large streptavidin molecules bound to the surface of the AuNRs and so were likely almost entirely removed during the washing stage.

Perhaps the most significant result was that the PW laser reduced the viability of 93 ± 12 % of the population of lung cancer cells when combined with anti-EGFR targeting S-Au40-849s (after 24 h incubation), in comparison to the CW which destroyed almost half (46 %) of the cells. There are likely multiple contributing factors to the enhanced PPTT efficacy of the PW laser. The first reason may be that the efficacy of the CW laser for inducing cell-death is at its highest when there are a large number of AuNRs in the absorbing region and the light can be efficiently converted into wide-spread, bulk heating. The washing of the cell monolayer removed any AuNRs that weren't bound to the cell surface and the number remaining in the path of the laser will not have been high enough to induce hyperthermia. The AuNRs that did persist would still have absorbed the incoming laser-light and converted it into heat, causing damage to the cells, however the overall heat generated from the exposure was not enough to provide a broad destruction of cells. The second reason may be due to an enhanced optical absorption and bubble-formation around the AuNRs under PW exposure due to AuNR clustering. It has been shown that the accumulation of antibody-conjugated AuNRs on the surface of a cell membrane can further facilitate the self-assembly of the AuNRs into nanoclusters [324]. This in turn leads to an enhancement of the bubble formation around the AuNRs under high intensity laser pulses and subsequently an increase in damage to the cellular membrane. Zharox et al. (2005) concluded that pulsed lasers were more effective at inducing cell death when AuNRs formed nanoclusters on the cell membrane, and this is in agreement with our findings.

4.5 Conclusions

Cancer of the lung is a particularly difficult form of cancer to treat due largely to the inability to access the tumour site. Gold nanorod assisted photothermal therapy has the potential to treat lung cancer by targeting AuNRs to the tumour tissue and irradiating the tumour from a close proximity by inserting a laser fibre through the mouth and into the lung. The conventional approach to PPTT is to use CW lasers as the light source to induce bulk heating in a target region and subsequently induce hyperthermia, however this has its drawbacks such as the potential for damage to healthy tissue due to heat 'leaking' into the surrounding tissue and the need for high concentrations of AuNRs to produce sufficient heating. PW lasers have been explored as potential alternatives for destroying malignant tissues since there are

possible advantages over CW lasers, such as a 'mechanical' method for cell damage that does not increase resistance to drugs or heat, a highly localised destruction of cell tissue without the chance of damage to healthy tissue, and the potential for simultaneous imaging during therapy by monitoring the photoacoustic signals. Irrespective of the laser system used, the need for exogenous photo-absorbing agents such as AuNRs is critical to the enhancement and versatility of these light-based therapies.

The effect of AuNR size (or volume) on the photothermal efficacy was explored using two laser systems - continuous wave and pulsed wave - operating below the maximum permissible exposure guidelines. CW lasers induce bulk temperature changes in an absorbing medium whereas localised heating occurs when PW lasers are used. This suggests that PW lasers are only able to destroy cancer cells via a necrotic pathway, which reduces the risk of the cells developing drug or heat resistance but can cause immunogenic or inflammatory responses due to the immediate expulsion of the cells internals. Conversely, depending on the laser exposure parameters, CW lasers have been shown in the literature to induce cell death via either apoptosis or necrosis (although this particular aspect was not addressed in this study). Understanding these important distinctions between the two laser types is imperative for guiding therapy design. The relevant temperatures required to initiate the destruction of cells and the inducement of hyperthermia is in excess of 42 °C, which is only approximately 5 °C above internal body temperature. The length of time the cells remain at elevated temperatures has an effect on the therapeutic efficiency and a clinically relevant parameter known as the thermal issoeffective dose (TID) is often used to compare thermal treatments. There is a large range of TID threshold values in the literature for determining when complete destruction of tissue is achieved and this is due to the differences between the cellular compositions of different tissues. If TID values are to be used as a clinical measure of therapy, it is necessary to determine a TID threshold for the specific tissue that is being treated, otherwise it may be difficult to ensure maximum therapeutic effect.

Following on from the initial findings, a more detailed and relevant study was conducted to determine the toxicity of 4 different sized AuNRs with similar aspect ratios on a lung cancer cell line under a range of experimental parameters. It was shown that the AuNR size is a governing factoring in overall photothermal efficacy at equivalent AuNR particle concentrations and laser exposure parameters. The smallest AuNRs used in the study (Au10-811s) were the most effective at inducing cell death in all cases, killing almost the entire population of cells when combined with a CW laser and free-floating AuNRs. The least effective overall were the Au25-803s, and this may be due to a number of reasons such as limited uptake, and reduced photothermal conversion efficacy. The PW laser, while not as effective at damaging the lung cancer cells as the CW laser, still displayed significant toxicity when combined with AuNRs. There was also minimal difference between the toxicity of the PW laser when combined with either an excess of AuNRs surrounding the cells or when the excess AuNRs were removed, suggesting that the location of the AuNRs was an important part governing toxicity. The AuNRs that had been taken up by the cells and situated in the

cytoplasm were causing the majority of the damage, due to the mechanical stresses induced by the high-intensity laser pulses, whereas with the CW laser, the availability of the excess AuNRs to generate heat resulted in a significant difference in overall toxicity. These results are important for clinical application because they suggest that the location of AuNRs in relation to the cells is important for the efficiency of plasmonic photothermal therapy.

Further to the consideration of AuNR size on photothermal efficacy, the effect of targeting AuNRs to the lung cancer cells was explored. AuNRs with a similar size and aspect ratio to those used previously were purchased with streptavidin proteins conjugated to the surface, enabling the AuNRs to be easily functionalised with anti-EGFR targeting ligands. Lung cancer cells (along with many other malignant tissues) have been shown to overexpress anti-EGFR receptors and provide a potential method for increasing AuNR delivery efficiency to the cells - a critical aspect to the success of this therapy. The cellular uptake of untargeted S-Au40-849s was compared with that of targeted ones, and the results demonstrated the importance of molecularly targeting AuNRs for increased uptake. The untargeted AuNRs showed minimal uptake across the cell samples after the longest incubation time studied (24 h), however the accumulation and uptake of targeted AuNRs was evident. Under laser irradiation, targeting also provided a significant advantage over untargeted AuNRs, when the incubation time was long enough (24 h). After 4 h there was no observed reduction in cell viability for any of the parameters studied, which agreed with the uptake study. However, a 24 h incubation resulted in an observable reduction in cell viability in some cases. The untargeted AuNRs were not able to reduce cell viability under any laser exposure parameters. In the case for targeted AuNRs, the PW laser was the most efficient laser system, destroying almost 93 % of the total population of lung cancer cells, compared with almost half for the CW laser. This reversal in photothermal efficacy between the laser types may be due to the AuNRs forming nanoclusters, facilitated by the anti-EGFR targeting ligands, and increasing the mechanical stresses induced by the PW laser.

The results presented in this chapter highlight the subtleties in how the design of AuNRs and choice of laser system can influence the outcomes for photothermal therapy. In terms of the therapeutic efficacy of different sized un-targeted AuNRs, it appears that smaller AuNRs (width = 10 nm) are most suited as photoabsorbers under both CW and PW laser illumination, whereas AuNRs with a width of 25 nm were the least suited. The location of AuNRs was a critical aspect for therapeutic efficacy, and targeting them to bind specifically to cell-receptors, such as EGFR, can improve cellular uptake and overall therapeutic outcome. Furthermore, if the eventual goal is to use AuNRs as clinical therapeutic agents then it is crucial that the production of AuNRs with consistent and uniform dimensions, properties and coatings, can be scaled-up to a level that ensures the practicality and safety of wide-spread clinical use.

Chapter 5

Contrast-enhanced photoacoustic imaging with gold nanorods

Photoacoustic imaging (PAI) is capable of providing functional anatomical and molecular information through the use of endogenous and exogenous contrast agents. It combines the high spectral selectivity of optical-based approaches with the high resolution of ultrasound imaging. The inherent nature of PAI lends itself to be combined with conventional ultrasound B-mode imaging due to similarities in the signal detection and image processing. Ultrasound imaging is used to clinically evaluate and stage non-small cell lung cancer (NSCLC) via a technique known as endobronchial ultrasound-guided transbronchial needle aspiration. There is the potential to increase the usefulness of this modality by combining it with other techniques such as PAI with gold nanorods. The aim of this chapter is to demonstrate the potential for incorporating PAI into an endobronchial ultrasound device for the enhancement of this routine diagnostic technique, and provide the groundwork for progression in this area.

5.1 Introduction

As a stand-alone modality, PAI shows greater tissue specificity and differentiation than conventional ultrasound imaging as the technique is 'absorption-based' and distinct biological regions (such as oxygenated and deoxygenated blood, fat, melanin, etc.) absorb different wavelengths of light. This facilitates the ability to scan through various known wavelengths of light, record the corresponding photoacoustic (PA) signals generated, and then build up a composite image of the various tissue-types [182]. The specificity of the technique can be further enhanced through the use of exogenous contrast agents. Plasmonic nanoparticles, such

as gold nanorods (AuNRs), can provide an additional optical absorption contrast against the background tissues. If, for example, the AuNRs have accumulated in tumour tissue (which may be difficult to see with other imaging modalities) by exploiting the enhanced permeability and retention (EPR) effect, and the peak absorption wavelength (or surface plasmon resonance (SPR)) of the AuNRs is known, then the tissue can be easily identified against the background tissue. This is especially true if the AuNRs have been molecularly targeted to specifically target the tumour tissue of interest.

One of the most difficult forms of cancer to diagnose and treat is lung cancer and as a result it is one of the most common causes of cancer-related deaths worldwide [330]. The prognosis and course of treatment is guided by the important process of clinically staging the cancer. Currently this can be a lengthy process involving multiple invasive and non-invasive procedures, such as CT scans, bronchoscopy, radiology-guided biopsy sampling, and mediastinoscopy [237]. The diagnosis and prognosis from these complex and expensive procedures can take a long time to complete (often several weeks) and can allow the disease to continue to develop into a less treatable, more complex disease with the final treatment decision being invalid by the time it has been made. A technique known as endobronchial ultrasound (EBUS) can facilitate the mediastinal staging of lung cancer via needle biopsy [331]. Known as EBUS-guided transbronchial needle aspiration (EBUS-TBNA), it is often only used after a CT-scan or other aforementioned examination when there are already signs of a tumour. However, it has the potential to be used as a primary investigation tool to diagnose and stage patients with suspected lung cancer since it shows a high sensitivity (90 %) for the detection of mediastinal nodal metastases - higher than other currently used investigatory procedures [237] - and the technology could be combined with AuNR-assisted imaging and therapeutic techniques, such as PAI and plasmonic photothermal therapy (PPTT). AuNRs targeted to the tumour site could be illuminated with a laser incorporated into the EBUS device and provide another level of contrast to the ultrasound images through PAI. Furthermore, there is a potential treatment avenue via plasmonic photothermal therapy using the same AuNRs and laser system. The underlying technology required to combine these modalities together already exists, and doing-so could enable the ability to locate, diagnose, stage, and treat a lung tumour within a single modality, all while reducing the time and costs commonly required.

There is very little literature that considers this new approach to EBUS and the following chapter aims to provide the groundwork for future research into this important area. To begin with, the methods for generating and receiving ultrasonic waves using transducer arrays were discussed in context of relevant beamforming techniques. This was to provide an introduction into how ultrasound signals can be transmitted and received, and insight into the reasons for using steered focussed beams for mimicking EBUS later in the chapter, since any beamformer can be applied to almost any type of transducer. This was followed by an investigation and discussion into the suitability of three different transducer arrays for imitating EBUS, using one of the previously discussed beamformers, and its potential for en-

hancement with photoacoustics. Finally, the concept of combining conventional ultrasound imaging with PAI, in the context of future integration with EBUS, was considered.

5.2 Beamforming

Beamforming is a signal processing technique that is used in a broad range of applications and relies on the propagation of waves [332]. It is used to provide spatial and directional selectivity of signals that have been sent and/or received by an array of sensors, and results in the enhancement of signals that might otherwise be lost [333]. Beamforming is an essential aspect of medical ultrasound and there are a considerable number of beamforming techniques employed depending on the desired application and outcomes [334]. Beamforming is used in both the transmission and receiving of ultrasound signals. In transmission, it can be used to electronically steer a beam without changing the physical angle of an array by applying delays to each element in the array. In receive, it is used to determine where the signals originated from by calculating the time-of-flight of received signals from a specific point in space. Furthermore, some beamforming techniques allow for dynamically focusing the received beams by applying delays to each element to compensate for the propagation delay differences between the point of interest and the array of receiving elements. This generally works better for signals in the near-field because the (assumed) spherical wavefronts emitted or reflected from a specific point in the near-field will be more curved than those at greater distances and the time-delays will therefore be larger.

In medical ultrasound, the majority of beamforming techniques are based on the standard delay-and-sum (DAS) method [335]. In DAS, each point of the beamformed image is created by applying a delay to the radio-frequency (RF) data received on each element of the array - based on the time required for the signal to travel from the transmitter to the field point and then return to the receiving element - before being summed together. This technique is the foundation for a large number of variations, such as delay multiply and sum (DMAS) and filter delay multiply and sum (FDMAS), however the ultimate aim of improving the image quality is the same. All of the work in this chapter is based on the DAS beamformer.

5.2.1 Transmission beamforming

There a multiple ways to electronically influence a transmitted wavefront, generated by an ultrasound array, without physically moving the transducer. A few of these techniques are discussed in this section.

Plane wave

Plane wave imaging (PWI) is the simplest method described in this chapter for generating an ultrasound wave - other than using a single element transducer - and is achieved by exciting all of the elements in a transducer array at the same time, producing a flat wavefront that

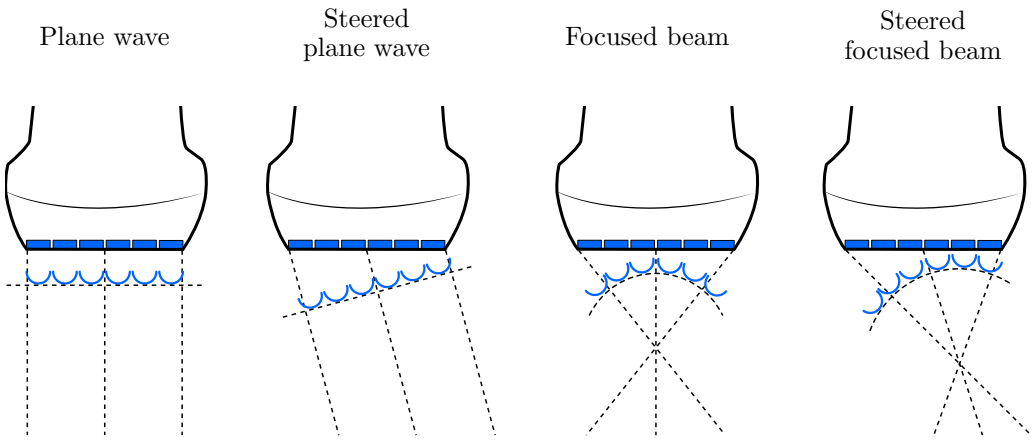

Figure 5.1: A simple diagram showing how the wavefront of a transmitted beam can be altered by applying different delays to each channel in the array.

propagates perpendicular to the surface of the transducer (see figure 5.1). This method of beamforming is the fastest transmission scheme available and can achieve very high frame rates, on the order of 10 kHz [336]. This is because the frame rate is limited by the time it takes to record one image, t_{image}, which is given by,

$$t_{\text{image}} = \frac{N_{\text{lines}} \times 2 \times z}{\gamma} \tag{5.1}$$

where N_{lines} is the number of lines required to create the image, z is the image depth, and γ is the speed of sound in the medium. In the case of PWI, the number of lines is equal to 1 since only a single transmission is used to create the image, meaning the frame rate is only limited by the time it takes for the ultrasound wave to propagate from the transducer surface to the deepest desired location and return. While this technique allows for ultrafast imaging, it does so at the expense of image contrast and resolution.

Steered plane wave

Transmitting steered plane waves is a slight alteration to the basic PWI format. A delay is applied to each successive element in the array by a linearly increasing amount, resulting in a wavefront that is angled (see figure 5.1). The pulse repetition frequency (PRF) using this method is lower than standard PWI due to the added delay between the first and last element for each transmitted wavefront. However, this technique for wave generation can improve image resolution and contrast, compared with standard PWI, if multiple transmissions at different angles are used (see section 5.2.2 below). This technique was developed to improve upon the image quality of PWI while still maintaining very high frame rates (> 1 kHz [337]), and depending on the desired outcomes, the image quality can be increased or decreased at

the expense of frame rate.

Focused beam

Focused beams are generated by increasing the delays from the outer to inner elements of the array (mirrored along the central axis), leading to a spherical wavefront that converges to a point at the centre of that concentric ring (see figure 5.1). This beamforming method enhances the pressure and signal amplitude at the focal region and can help to improve image contrast. The array is usually split into a subgroup (or sub-aperture) of elements, for example 32 elements in a 128-element array, and the sub-aperture is used to transmit and record a focused beam along the central axis. The sub-aperture is translated along the transducer surface by adding one element to one side of the group and removing one element from the other. In this way, a series of focused beams centralised along the longitudinal axis of each sub-aperture is generated and an image can be formed line-by-line with a focal region perpendicular to the imaging plane. This technique is generally used with linear and curvi-linear arrays to enhance lateral resolution and is the most common method for clinical ultrasound imaging.

Steered focused beam

Generating a steered beam that focuses to a specific point (or region) is the most complex transmission beamforming technique described in this section, and is essentially a combination of the steered plane wave and focused beam methods above. Delays are applied to the elements asymmetrically about the central axis of the transducer so that the generated beam has a spherical wavefront that converges to a focal point situated off the central axis (see figure 5.1). This scheme enables an image to be formed with a greater contrast ratio and resolution along the focal region and can provide an increased field of view (FOV) as the beam is swept in an arc. Generally this technique is reserved for phased array transducers as they are able to steer the beam with large angles without deteriorating image quality by introducing side lobes, while possessing a small footprint that is useful for imaging between the ribs in applications such as echocardiography.

5.2.2 Receive beamforming

Applying delays to beamform the acoustic signal during transmission is one method for altering and enhancing the received signals, however it is also possible (and often more beneficial) to beamform the received signals with post-processing. If the reflected signals are recorded on the entire array of elements then receive beamforming can enhance the resolution, contrast, and dynamic range of the resultant image [338]. With receive beamforming it is possible to create the final image on a pixel-by-pixel basis using a technique called 'dynamic' or 'adaptive' beamforming. This works in much the same way as transmission focusing since the behaviour of acoustic waves is reciprocated in both directions. The 'focus'

is dynamically altered based on the time-of-flight to that specific point in space, and the received signals on the entire array are delayed and summed based on this calculation. If we consider a point in space (x_f, z_f), the complete time-of-flight of an ultrasound wave, $t_i(x_f, z_f)$, is a sum of the time it takes for a transmitted ultrasound wave to propagate to that point, $t_{\mathrm{TX}}(x_f, z_f)$, and the time it takes to return to the transducer array, $t_{\mathrm{RX}}(x_f, z_f)$, given by,

$$t_i(x_f, z_f) = t_{\mathrm{TX}}(x_f, z_f) + t_{\mathrm{RX}}(x_f, z_f) \tag{5.2}$$

$$= \frac{z_f}{\gamma} + \frac{\sqrt{z_f^2 + (x_i, x_f)^2}}{\gamma} \tag{5.3}$$

where x_i is lateral position of element i, x_f is the lateral position of the point, z_f is the depth of the point, and γ is the speed of sound in the medium. Using this equation, the total time-of-flight to a specific point in space can be calculated for each element, t_i, in the array, and the original radio frequency (RF) data can then be delayed and summed to form a single B-mode imaging point. This process is repeated for every point (or pixel) in the imaging space until the full B-mode image is formed.

Compound plane wave imaging

In PWI, the full array of elements of a linear transducer is used to insonify the imaging region with a single, parallel plane wave (see section 5.2.1) and the entire array is subsequently used to record the backscattered echoes [339]. Compound plane wave imaging (CPWI) introduces the emission of a series of plane waves that are steered at different angles, θ_n (where n is the number of angles). Each transmission is recorded on the full array and, similarly to equation 5.2, the necessary delays are applied to each element according to the transmit and receive time delays, given by,

$$t_i(x_f, z_f) = t_{\mathrm{TX}}(x_f, z_f) + t_{\mathrm{RX}}(x_f, z_f) \tag{5.4}$$

$$= \frac{z_f \cos\theta_n + x_f \sin\theta_n + \frac{L}{2}\sin\theta_n}{\gamma} + \frac{\sqrt{z_f^2 + (x_i, x_f)^2}}{\gamma} \tag{5.5}$$

where L is the length of the aperture. Using these delays, an image is formed for each transmitted/received signal and the multiple coherently aligned images are finally summed together to produce a single rectangular image with increased contrast and resolution compared with single transmissions, due to the suppression of speckle. The more angles (and therefore transmissions) that are used to generate the final image, the more information that is gathered for a specific point in space and the more accurately the time delays can be calculated, however this is at detriment to overall frame rate. Generally this technique is used when ultrafast frame rates are required, such as when attempting to monitor moving objects like tissue motion, blood motion and the movement of contrast agents through the

vascular system [340], as it can typically achieve frame rates that are 100-fold compared to 'line-by-line' imaging [341].

Phased B-mode imaging

Phased B-mode imaging is a technique that produces a series of 'A-lines' that originate from the centre of the array. Steered focused beams (discussed in the previous section 5.2.1) are generated using all the elements of the array, with each line focused to a specified depth and steered through a series of angles calculated depending on the required FOV. The entire array is again used to record the scattered signals for post-processing where delays are applied (calculated by the time-of-flight to the intended focal point) and summed together. The resultant image is a circular sector with a large FOV that can span as much as 90°. A phased array is the most appropriate transducer for this type of application because they are designed with small pitch sizes (the distance between each element on the array), and often lower centre frequencies, that enable the beams to be steered at large angles without introducing side-lobes.

Photoacoustic imaging

Unlike the two imaging modes discussed previously, capturing PA data does not require the transmission of an ultrasound pulse. Instead, the transducer is solely used to record the signals generated from a laser pulse interacting with a material or a contrast agent. In this case, the entire array of elements is used to record the PA signals and the image is reconstructed based only on the receive time delays, $t_{\mathrm{RX}}(x_f, z_f)$, since the signal originates from the imaging space and propagates back towards the transducer. To ensure the signals are accurately located within the imaging space, the imaging system must be synced with the laser system that is generating the photoacoustic signal. The travel time for a pulse of light is considered to be instantaneous and the photoacoustic waves emitted by the absorbers in the imaging space are assumed to be generated at the exact moment the laser fires. Therefore, recording begins when the laser pulse is emitted and the location of the photoacoustic signals are accurately positioned relative to a B-mode image by doubling the time-of-flight of the received signals to account for the halved propagation time compared with a transmitted ultrasound wave.

5.3 Transducers for EBUS mimicking

Due to the prohibitive cost of purchasing an EBUS system (upwards of £60k) the work presented in this chapter was not performed using an EBUS probe. Instead, the following work was implemented with a custom-built ultrasound array research platform (UARP) (see figure 5.2), which allowed for a greater flexibility with regards to the imaging parameters and excitation schemes, in addition to the ability to easily integrate it with a laser system.

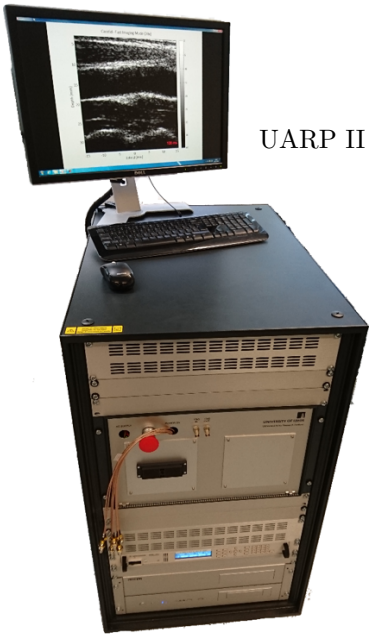

UARP II

CIRS phantom

Linear (L11-4) Phased (P4-2) Phased (P9-1)

Figure 5.2: Images of the UARP II system, CIRS tissue-mimicking test phantom, and the three transducer probes used in this study: linear (L11-4), phased (P4-2), and waterproof-phased (P9-1).

Table 5.1: Specifications of the three transducers available for imitating an EBUS system.

Transducer	Centre frequency	−6 dB Bandwidth	Elements	Pitch
Linear L11-4	7.55 MHz	4 − 11 MHz	128	0.3 mm
Phased L4-2	2.78 MHz	2 − 4 MHz	64	0.3 mm
Phased L9-1	5 MHz	1 − 9 MHz	64	0.15 mm

Ultimately this provided a platform to imitate the EBUS technique and the combination with PAI.

Three different transducers (see table 5.1 for specifications and figure 5.2 for images) were available as imaging probes for the study and all three were investigated for suitability as EBUS-mimicking devices. Due to the commercial nature of currently-available EBUS systems, many of the specific details of the system are not publicly available, making it difficult to imitate the technique exactly. However, reasonable assumptions were made with regards to these unknown aspects. The transducer employed in a commercial EBUS system is a curvi-linear array and the probe is likely to be made up of 64 elements. Thus, the number of elements was fixed to 64 when transmitting and recording signals from each of the different transducers. Furthermore, the typical centre frequencies of EBUS probes are 5, 7.5, 10, and 12 MHz, with 7.5 MHz being the most common, and so this was also closely replicated. This range of possible frequencies enables the clinician to select a probe based on the desired imaging parameters. Due to the centre frequency remaining fixed for each specific transducer, the resolution also remains fixed. For example, a lower frequency probe (5 MHz) facilitates the imaging of deeper locations within the lung, at the cost of image resolution. Conversely, a higher frequency probe (12 MHz) provides high resolution images of shallow regions. The range of available EBUS probes enables the detection and imaging of a large number of lymph nodes within the lung, since both shallow and deep lymph nodes can be resolved depending on the probe chosen. Another important parameter is the signal-to-noise ratio (SNR) of an ultrasound image. However, unlike resolution (which is usually a fixed parameter due to the excitation frequency), the SNR is governed by factors that can change on a case-by-case basis, such as transmit energy and the strength of acoustic reflections in tissue. Generally, the parameters chosen for optimal imaging in EBUS will be a balance between sufficient image resolution needed to accurately determine and locate lymph nodes, and the SNR.

A CIRS test phantom was used as a basis for testing the transducers and a series of images were recorded with various excitation parameters (outlined below). The CIRS phantom is a multi-purpose ultrasound phantom that is the standard for quality assurance and performance testing in ultrasound. In all cases, focussed beams were transmitted to a specific depth to enhance the signal in that region and the beams were steered and beamformed to varying degrees to mimic the typical images received using a clinical EBUS system. The raw data was captured from the transducer probe to enable a higher level of flexibility when post-processing at a later date. The raw data was frequency filtered between varying band-

widths depending on the specifics of the study, such as the type of transducer used, imaging depth, and excitation frequency. This was followed by line-by-line beamforming in polar coordinates using a delay-and-sum (DAS) beamformer. Figure 5.3a shows an example of a single line of raw data (recorded with the centre channel) and figure 5.3b shows a 3D mesh of a beamformed image in decibels (dB), referenced to the maximum signal intensity of the image.

5.3.1 Linear (L11-4)

The linear array transducer has a total of 128-elements and a high centre frequency (7.55 MHz) that is designed for high resolution imaging of shallow tissue regions such as peripheral vasculature. The pitch size of 0.3 mm and high centre frequency imply that it is not suitable for generating ultrasound waves with large beam steering angles due to the introduction of side-lobes. Generally, a maximum steering angle of 5° is used for CPWI. However, aim was to mimic the typical images and large FOVs obtained with EBUS systems, and so the transducer was tested on a CIRS tissue-mimicking phantom with a 60° FOV using steered focused beams (figure 5.4). The lateral resolution and signal-to-noise ratio (SNR) of the central wire at the focal depth of 10, 20, 30, and 50 mm is given in table 5.2. The real diameter of the wire is 0.1 mm. The high centre frequency facilitates the high resolution of the images, despite only using the centre 64 elements of the array. At deep locations (> 50 mm), the image became noisy, and the wires were harder to resolve. This is true even when the focal depth was increased beyond 50 mm, since the natural elevation focus (or intrinsic focus) of this transducer is 18 mm, and increasing the electronic focus significantly beyond this natural limit will begin to have diminishing effects. Despite the large steering angles (maximum 30°), the appearance of grating lobes in the beamformed images was not obvious. This was likely due to the homogenous nature of the test phantom used for imaging. The signal from the scatters was large enough to mask the grating lobes.

5.3.2 Phased (P4-2)

The P4-2 phased array was approximately 3 cm wide (half the size of the linear array) and contained only 64 elements. This is because they are generally used for imaging in small spaces where a large array would not be effective, such as between the ribs in the chest area. The pitch size is equivalent to the linear array (L11-4), but the low centre frequency (2.78 MHz) enables this probe to easily steer transmitted beams with large steering angles. The low centre frequency and narrow bandwidth also enable the transducer to easily image deep locations within the body (elevation focus $= 50 - 70$ mm), making it perfect for cardiac imaging, however image resolution is reduced as a result. Figure 5.5 shows the beamformed images of the same CIRS test phantom used for the linear probe, and in approximately the same location, but with the P4-2 array. The transducer was excited with a 4 MHz sine wave and the images were filtered between $2 - 5$ MHz. The resolution and SNR values are

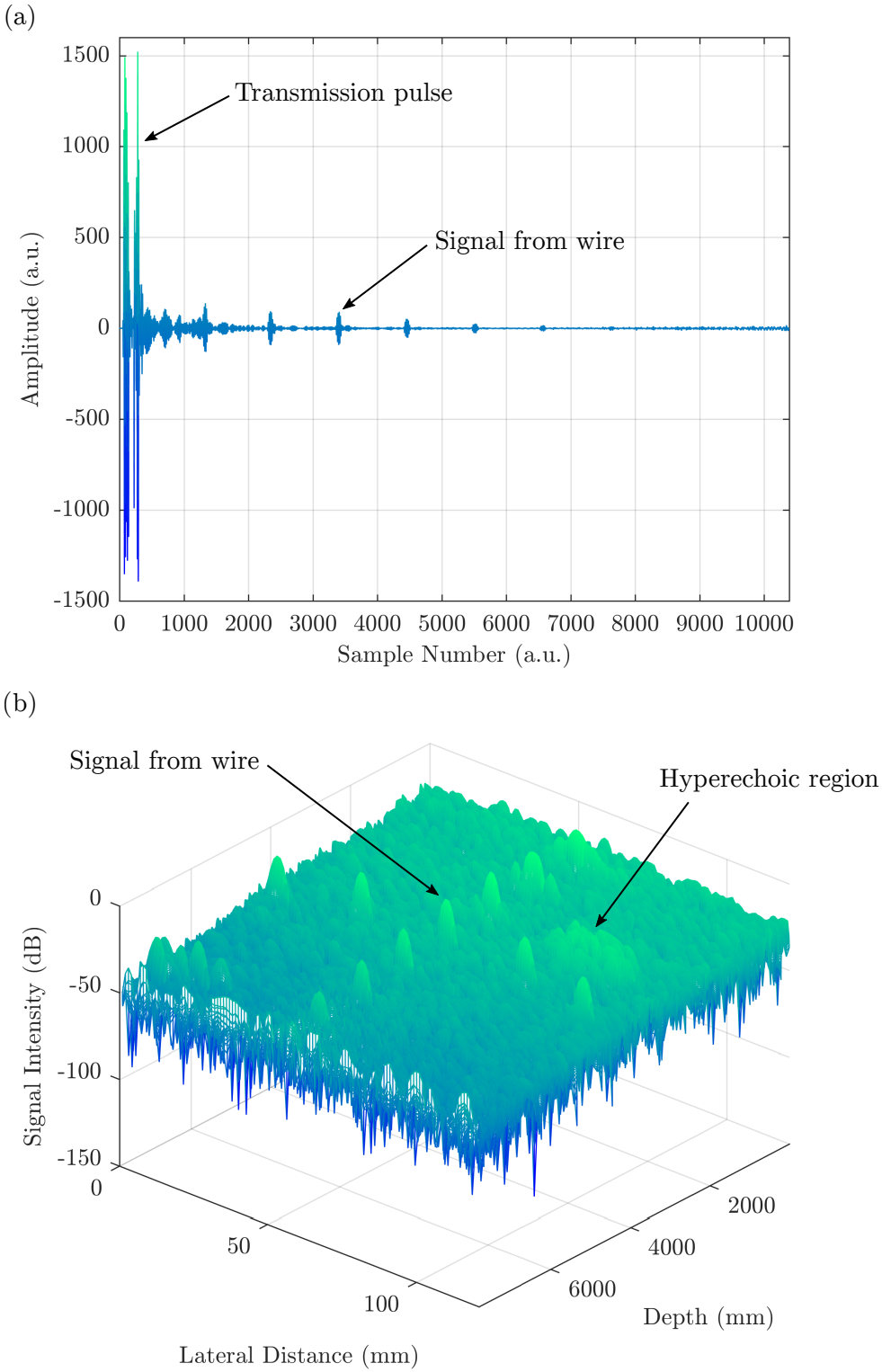

Figure 5.3: An example of (a) a single recorded line of raw data from the centre channel of a phased array (P9-1), and (b) a 3D mesh of the beamformed image in decibels.

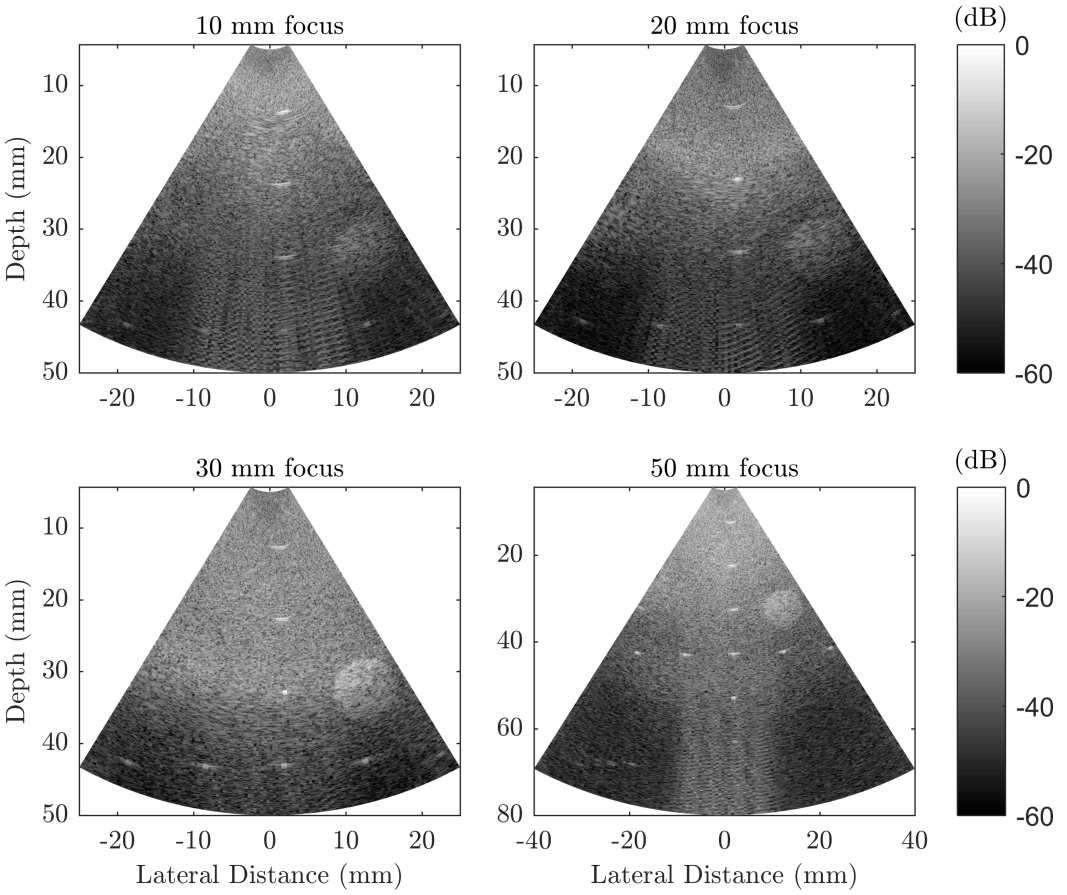

Figure 5.4: Ultrasound B-mode images of a CIRS test phantom using the linear array transducer (L11-4) with an excitation frequency of 7.55 MHz, 60° FOV, and focal depth of 10 mm (top-left), 20 mm (top-right), 30 mm (bottom-left), and 50 mm (bottom-right).

Table 5.2: Calculated parameters for the linear array (L11-4) at different focal depths, corresponding to figure 5.4.

Focus	Lateral Resolution	Signal-to-Noise (dB)
10 mm	0.97 ± 1 mm	9.3
20 mm	0.60 ± 1 mm	9.6
30 mm	0.58 ± 1 mm	10.9
50 mm	0.92 ± 1 mm	17.8

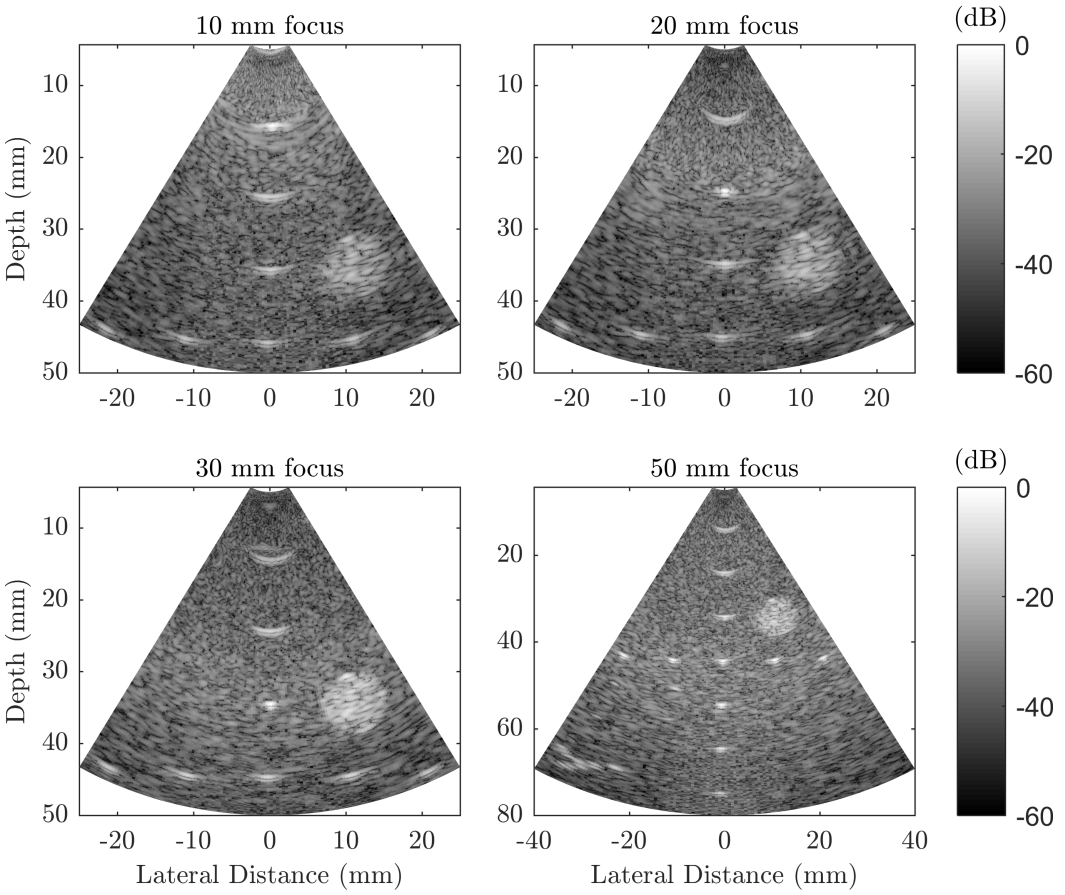

Figure 5.5: Ultrasound B-mode images of a CIRS test phantom using the phased array transducer (P4-2) with an excitation frequency of 4 MHz, 60° FOV, and focal depth of 10 mm (top-left), 20 mm (top-right), 30 mm (bottom-left), and 50 mm (bottom-right).

Table 5.3: Calculated parameters for the phased array (P4-2) at different focal depths, corresponding to figure 5.5.

Focus	Lateral Resolution	Signal-to-Noise (dB)
10 mm	3.13 ± 1 mm	18.4
20 mm	1.50 ± 1 mm	16.1
30 mm	1.50 ± 1 mm	18.4
50 mm	2.31 ± 1 mm	19.3

given in table 5.3, and the wire in the shallow focal region (10 mm) of the phantom was poorly resolved (3.13 ± 0.1 mm) compared to those at 20 and 30 mm (resolution = 1.5 and 1.5 ± 0.1 mm, respectively). The resolution and speckle pattern was overall poorer than that of the linear array and, as mentioned previously, was due to the low centre frequency and narrow bandwidth of the probe. In general, this probe is not suited for mimicking EBUS systems as the centre frequency is below that of clinical systems (minimum 5 MHz) and the narrow bandwidth will limit its ability to detect any photoacoustic signals when attempting to combine it with PAI.

5.3.3 Phased (P9-1)

The P9-1 phased array has the widest bandwidth (90 % −6 dB) of any of the transducers used in this study, and the slightly higher centre frequency of 5 MHz facilitates its ability to create higher resolution images compared to the P4-2. To compensate for the higher centre frequency and to enable large transmission steering angles, the distance between the elements is smaller (pitch size = 0.15 mm) than the other two probes. The transducer was excited at its centre frequency with a 60° FOV, and the recorded signals were filtered across the −6 dB bandwidth of the transducer (figure 5.6). This probe was easily able to resolve both the shallow and deeper located wires in the CIRS phantom and the resolution at the focal depths of 10, 20, 30, and 50 mm was 1.03, 1.19, 1.43, and 2.31 ± 0.1 mm (table 5.4) - overall higher than that of the P4-2 due to the higher transmission frequency and wide bandwidth. As a probe for combined B-mode EBUS imaging and PAI, this transducer is a suitable choice since it is able to detect frequencies as low as 1 MHz through to 9 MHz - lending itself to identifying photoacoustic signals - and can be excited at higher frequencies that match those of typical EBUS systems. As discussed in section 2.3, photoacoustic signals are potentially broadband (depending largely on the size of the absorbers) and so a transducer that is sensitive across a broad frequency range will capture a greater proportion of the signal.

5.3.4 Wider FOVs

Clinical EBUS systems have a minimum FOV of 60°, however some can achieve up to 80° [342]. This is accomplished with a curvi-linear, convex probe that additionally facilitates the high-frequency range ($5 - 12$ MHz). Therefore, the three transducers were used to image the CIRS phantom with a half steering angle of 40° (i.e 80° FOV) and the focus was kept consistent at a depth of 30 mm below the phantom surface. The beamformed images for all three probes are shown in figure 5.7. The wire nearest to the focal region in all three images was easily resolved, with a resolution of 0.85, 1.43, and 1.5 ± 0.1 mm for the L11-4, P9-1, and P4-2, respectively. Comparing the three images, it appeared that the P9-1 provided the best image quality for all of the features. For example, the P4-2 had difficulty with resolving the shallower wires when the focal depth was fixed to 30 mm, where the resolution of the

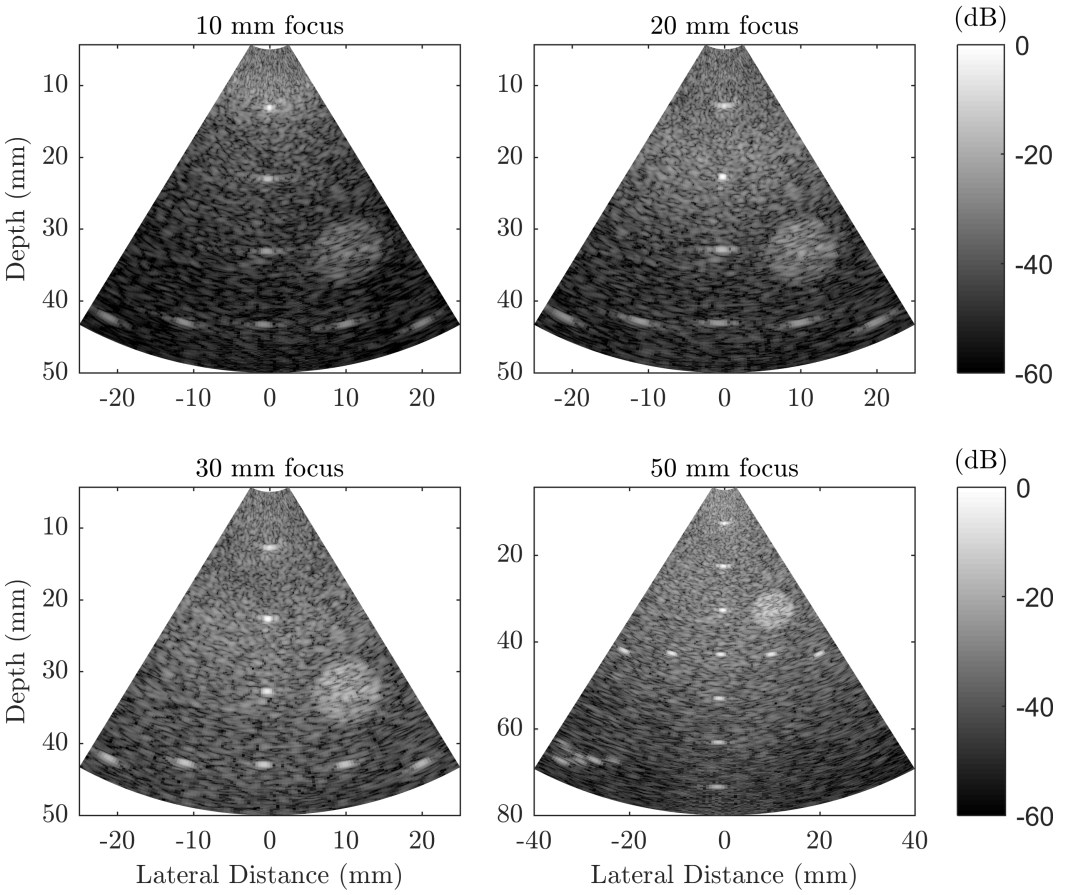

Figure 5.6: Ultrasound B-mode images of a CIRS test phantom using the phased array transducer (P9-1) with an excitation frequency of 5 MHz, 60° FOV, and focal depth of 10 mm (top-left), 20 mm (top-right), 30 mm (bottom-left), and 50 mm (bottom-right).

Table 5.4: Calculated parameters for the phased array (P9-1) at different focal depths, corresponding to figure 5.6.

Focus	Lateral Resolution	Signal-to-Noise (dB)
10 mm	1.03 ± 1 mm	16.1
20 mm	1.19 ± 1 mm	19.3
30 mm	1.43 ± 1 mm	20.6
50 mm	2.31 ± 1 mm	21.5

wires at 10 and 20 mm was 5.47 and 4.63 ± 0.1 mm. Furthermore, the full set of 5 horizontal wires located at approximately 42 mm can be seen in the P9-1 image, while the right-most wire is not visible for the L11-4 and the 2 outer wires in the P4-2 image are beginning to be lost to the background speckle.

The benefit of the wide FOV in EBUS is the ability to 'see' an increased area of tissue and to enable the clinician to easily locate the lymph nodes for biopsy. With both of the phased arrays, the features nearer the edges of the image (the circular hyperechoic region on the right-hand side, and the first two wires 30 mm deep) are more prominent than with the linear. Furthermore, it is possible to determine the next hyperechoic region (see figure 5.2 for the CIRS phantom layout) with the phased arrays. The ability for the phased probes to steer the ultrasound beams without degrading image quality is evident with these images, and the P9-1 is able to produce the clearest and most well-defined images compared with the other two, owed largely to its wide bandwidth. Overall, these results suggest that the P9-1 array is most suited for application in EBUS-mimicking, with the L11-4 also performing adequately. The P4-2 was deemed unsuitable for further use due to its poor general image quality across the parameters studied.

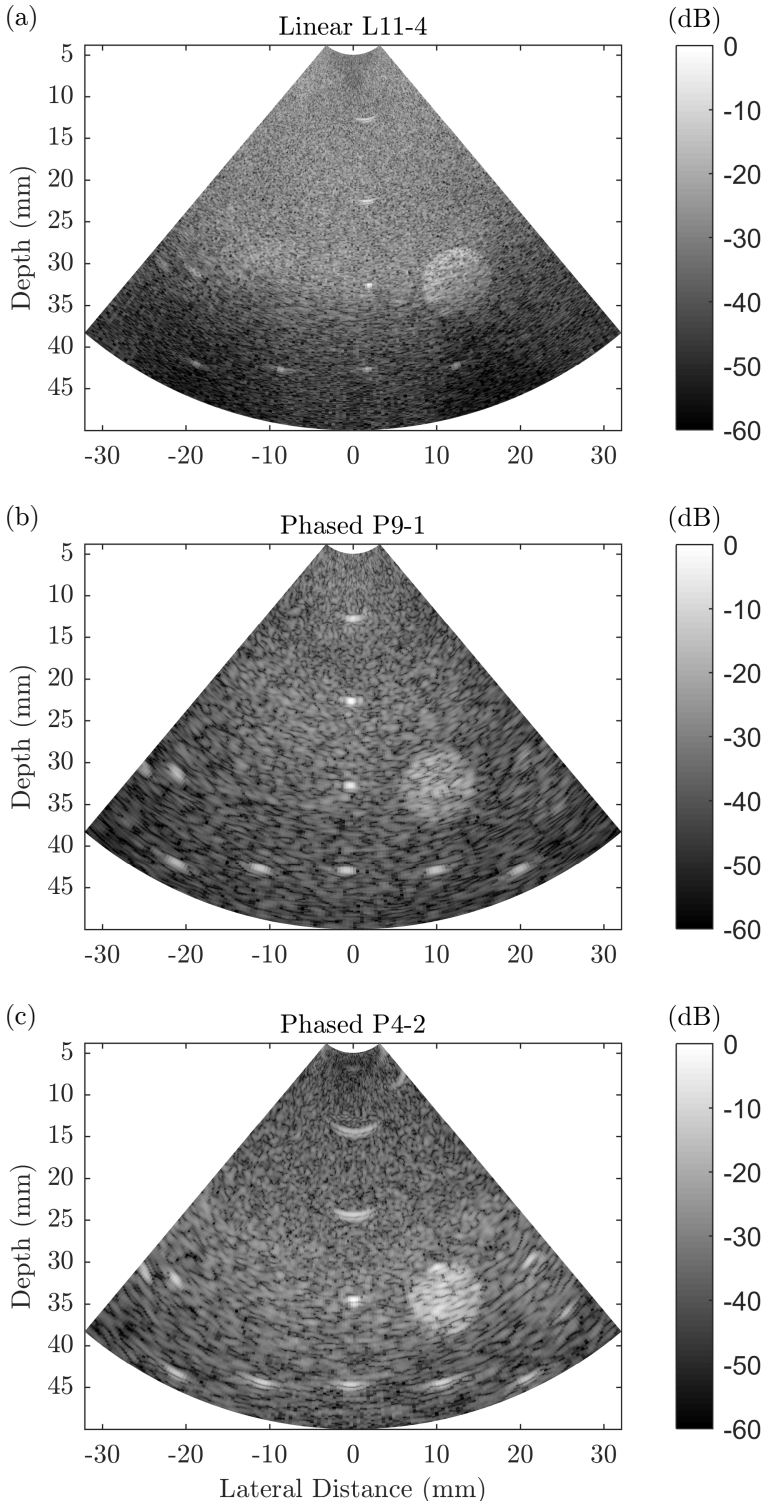

Figure 5.7: Ultrasound B-mode images of a CIRS test phantom using three different probes: (a) Linear L11-4 (7.55 MHz centre frequency), (b) Phased L1-9 (7 MHz centre frequency), (c) Phased L2-4 (4 MHz centre frequency), all with a 30 mm focus and 80° FOV.

5.4 Imaging tissue-mimicking phantoms with gold nanorod inclusions

To investigate combining conventional B-mode ultrasound with AuNR-mediated photoacoustic imaging, a tissue model was required. A section of ex vivo tissue could be used for this part of the study, however it was important that the region of tissue that contained AuNRs was a known and defined volume to enable the accuracy of photoacoustic imaging to be determined. Therefore, it was necessary to conceive a replacement tissue model that reasonably approximated real tissue and its scattering/absorption properties. Thus, a tissue-mimicking phantom based on agar and gelatin was created as a suitable replacement.

5.4.1 Fabricating an agar tissue-mimicking phantom

The recipe was devised and adapted from original work by Ricky et al. (1995) [343] and Madsen et al. (2005) [344] (table 5.5). 5.76 g (3.6% by mass) of agar powder (Acros Organics, Geel, Belgium) was mixed with 132.64 mL filtered, degassed water (82.9% by volume) and 0.8 g of gelatine powder (0.5% by mass). The mixture was heated to 96 °C and maintained at this temperature for approximately 30 min while being continuously degassed. The mixture was left to cool to approximately 70 °C before 1.6 g (1% by mass) of Germall plus (Gracefruit, Stirlingshire, U.K.) and 16 g Glycerin (10% by mass) was added and mixed. A small amount of the mixture was poured into a separate container where Au50-849s were added to a final concentration of 20 µg mL^{-1} and mixed together. This AuNR-agar mixture was poured into three wells of a 96-well plate and left to set into a cylindrical shape. Once set, the three AuNR-agar cylinders were removed and placed into a larger rectangular plastic container at increasing distances of 3 mm, 10 mm, and 20 mm away from the edge of the container. The rest of the mixture was then carefully poured around the inclusions and left to set.

5.4.2 Plane wave imaging with a linear array

To validate the combined ultrasound and PAI technique, the phantom was imaged using the CPWI beamforming method with the 128-element linear array transducer (L11-4, Verasonics Inc., WA, USA) with a central frequency $f_c = 7.55$ MHz and a certified -6 dB bandwidth of 91 %, together with the Ultrasound Array Research Platform (UARP) II, to image the

Table 5.5: Recipe components for fabricating an agar tissue-mimicking phantom.

Component	Quantity	Proportion
Agar powder	5.76 g	3.6 % (w/v)
Filtered, degassed water	132.64 mL	82.9 % (v/v)
Gelatine powder	0.8 g	0.5 % (w/v)
Germall plus	1.6 g	1 % (w/v)
Glycerin	16 g	10 % (w/v)

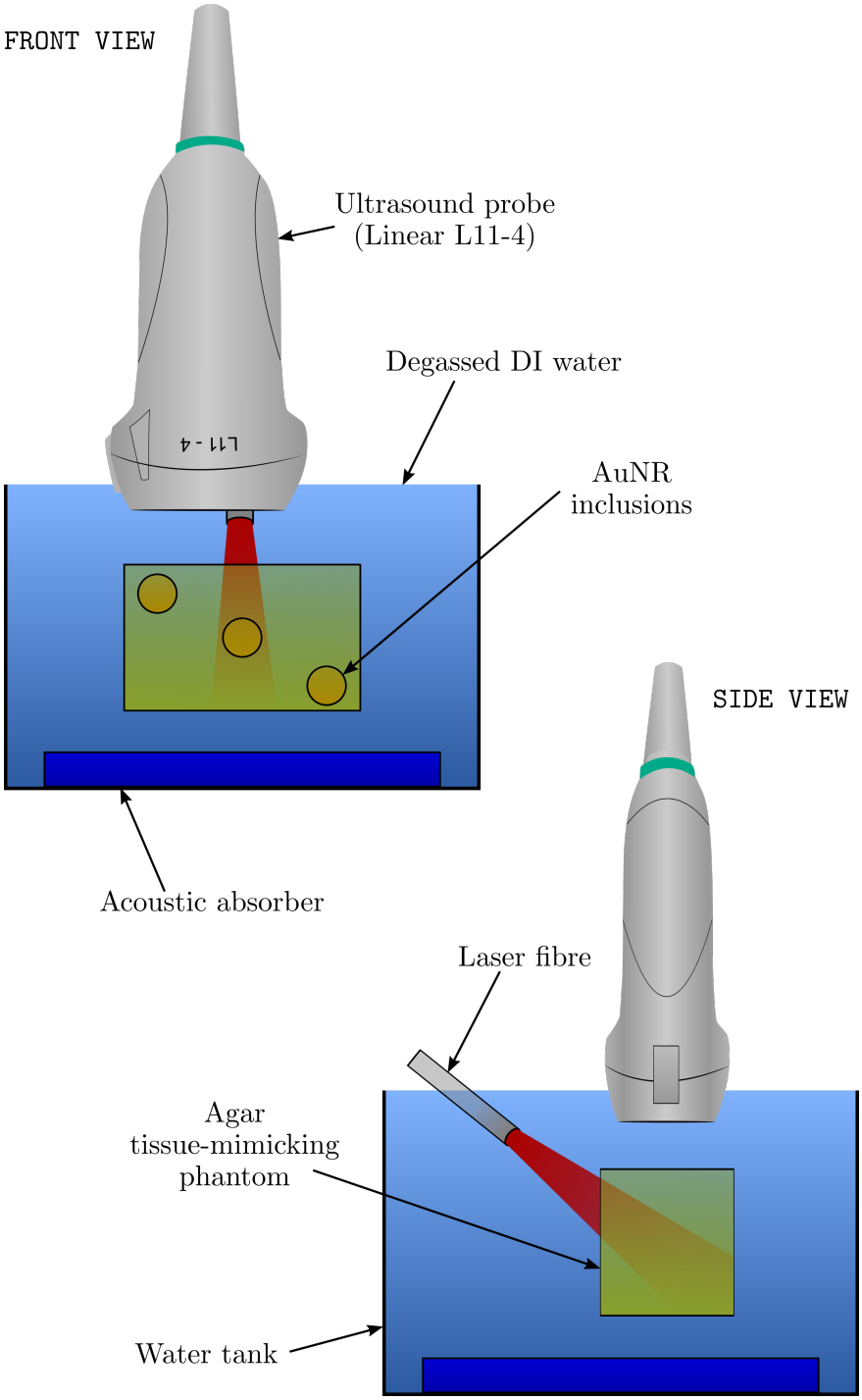

Figure 5.8: An agar tissue-mimicking phantom was created with 3 inclusions of AuNRs at increasing depths (5 mm, 10 mm, and 20 mm). An ultrasound probe (Linear L11-4) was used to insonify the phantom using plane waves and capture the reflected sound waves, in addition to capturing the photoacoustic signals generated by the AuNR inclusions under pulsed laser irradiation. Schematic shows both the front- and side-view of the experimental setup.

phantom both actively (plane wave, 9 compounding angles) and passively (photoacoustic signal, 100 averages). The phantom containing the AuNR inclusions was placed inside a tank of degassed, filtered, and de-ionised water (see figure 5.8)

The same PW laser system used in all the previous studies was used to generate PA signals from the AuNR inclusions with a laser fluence = $19 \pm 2\,\mathrm{mJ\,cm^{-2}}$ at the surface of the phantom. The laser Q-switch was synced with the trigger of the UARP II to enable the passive recording of PA signals generated by the laser. A background signal was also recorded under the same conditions as the photoacoustic signals but with the laser shutter closed. This enabled the background noise to be removed from the raw averaged PA data before the images were reconstructed using a delay-and-sum (DAS) beamformer [196]. Finally, the reconstructed PA image was overlaid onto the plane wave B-mode image.

Figure 5.9 shows the beamformed images at the various stages of the post-processing. The 9 compounding angles produced an image of the agar phantom with a well defined surface. Axial filtering in the frequency domain between the $-6\,\mathrm{dB}$ bandwidth of the transducer, and lateral filtering of $\gamma/2f_c$ was applied to enhance the contrast and resolution of the image. There was no clear evidence of the AuNR inclusion in the B-mode image, suggesting that the phantom was well-made with perfectly matched boundaries between the inclusion and the rest of the phantom, and no trapped pockets of air. The photoacoustic signal that was averaged across 100 laser pulses resulted in the removal of almost all the background noise, and the inclusion can be clearly seen. However, the image was not completely void of noise (as can been seen by the horizontal signal located at a depth of approximately 24 mm in figure 5.9d). Thus, a background signal was recorded (figure 5.9d) and subtracted from the averaged PA image. The horizontal 'strip' of noise can be clearly seen in the background signal and was caused by inherent noise from the electronics of the imaging system itself. Once subtracted from the averaged PA image, the noise was successfully removed. Similarly to the B-mode image, the PA signals were axially and laterally filtered to help improve the image quality. The clearest PA images were recreated by axially filtering between $2-6\,\mathrm{MHz}$ (figure 5.9), suggesting that the PA signals emitted by the AuNRs were predominately within this frequency range. Subsequently, the separate B-mode image and processed PA image were overlaid to create the final combined image (figure 5.10). In the final overlaid image, the PA signal intensity was referenced to the peak signal in the B-mode image.

The inclusion of AuNRs was clearly visible above the background ultrasound image, and was only discernable under pulsed laser illumination. The circular cross-sectional shape was well defined except at the lower left side of the inclusion. This is a result of a combination between the angle of incidence of the laser pulse, high concentration (and therefore high optical absorption) of the inclusion, and the inhomogeneity of the distribution of AuNRs. The laser light was incident from the rear of the phantom and just below the surface, and the signal generated by the pulse hitting the back of the phantom can been seen in the photoacoustic overlay (a small, bright signal originating from a location just above the AuNR inclusion and approximately 1 mm below the surface). This meant the laser pulse

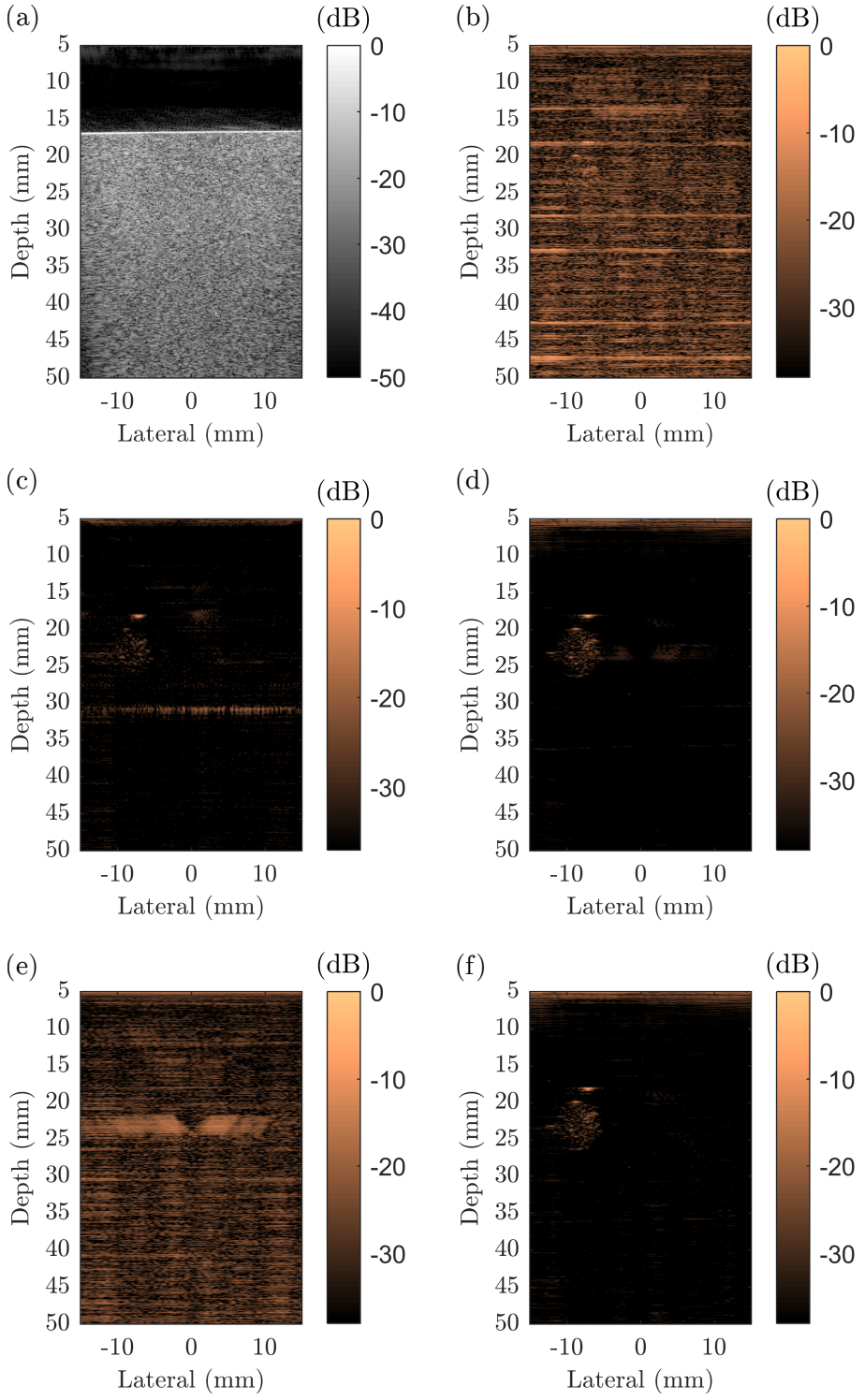

Figure 5.9: (a) Plane-wave B-mode image of an agar phantom containing an inclusion of Au50-841s with 9 compounding angles, a photoacoustic image with (b) a single laser pulse and (c) 100 laser pulses (bandwidth filtered), (d) 100 laser pulses (filtered $2-6\,\mathrm{MHz}$), (e) a background signal recorded during laser firing but shutter closed (i.e. no laser light emitted), and (f) the final 128 frame photoacoustic image with the background signal removed.

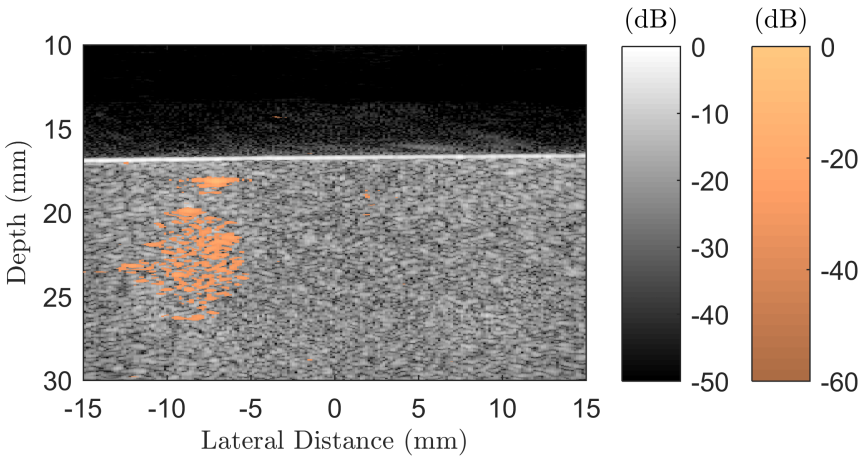

Figure 5.10: A combined photoacoustic image of an agar tissue-mimicking phantom with an inclusion of AuNRs 3 mm below the surface. Both decibel scales are referenced to the peak signal.

was passing through the phantom directed from right to left, and as the light was absorbed by the AuNRs, the amount of light available to be absorbed by the AuNRs in the lower left of the inclusion was reduced, leading to a reduction in PA signal intensity.

After confirming that the PA signals could indeed be detected from the shallow regions, the ability for PAI of deeper locations was tested. A AuNR inclusion at approximately 10 mm and 20 mm was illuminated with an equivalent laser energy and number of pulses as used previously, and the same technique (described in figure 5.9) was used to generate the combined images. The PA signal intensity originating from 10 mm below the surface is high (figure 5.11a) and comparable to the shallow region imaged previously, despite the reduced optical intensity due to attenuation caused by the increased penetration depth and turbid phantom. The circular cross section of the inclusion is discernable, however akin to the shallow inclusion, the signal in the upper-left is stronger than the lower-right due to the angle of the laser pulse. Increasing the depth further to 20 mm (figure 5.11b) results in a significantly reduced PA signal intensity. Only the upper portion of the inclusion is visible under laser irradiation with little-to-no signal originating from the lower half. In real biological tissues, laser light incident on the skin surface begins to lose directionality after several millimetres [273] due to the large number of optical scatters and strong scattering coefficients of skin and epidermis ($> 60\,\mathrm{cm}^{-1}$ at 500 nm [123]). In an agar phantom, the size of the scatterers ($< 1\,\mu\mathrm{m}$) are not as large as those in tissue ($10 - 100\,\mu\mathrm{m}$) and therefore the scattering events are not as strong. However, as the light penetrates deeper into the phantom, scattering (and absorption) events do take place and the light begins to diffuse.

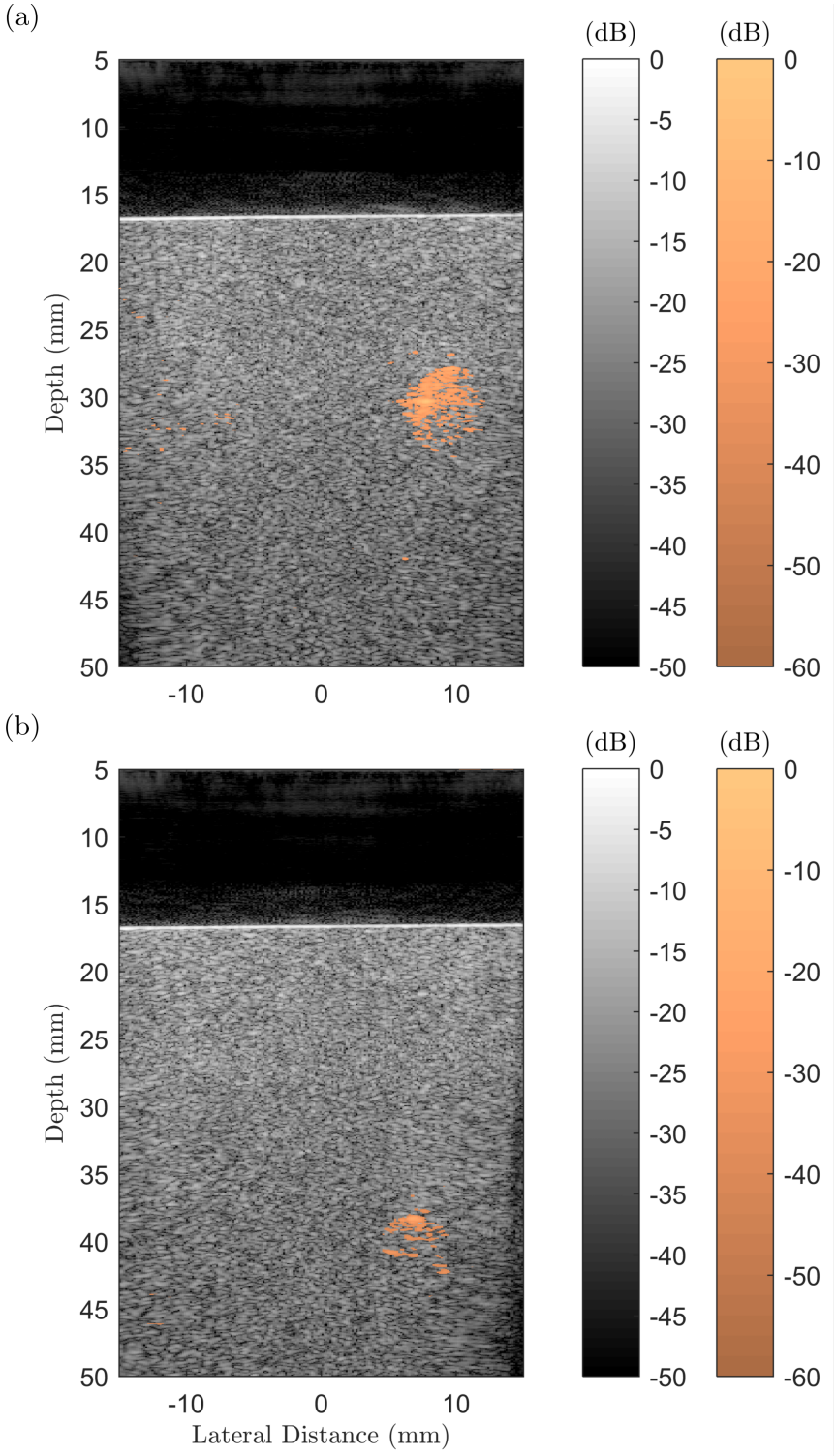

Figure 5.11: Combined photoacoustic images of an agar tissue-mimicking phantom with an inclusion of AuNRs (a) 10 mm and (b) 20 mm below the surface. Both decibel scales are referenced to the peak signal.

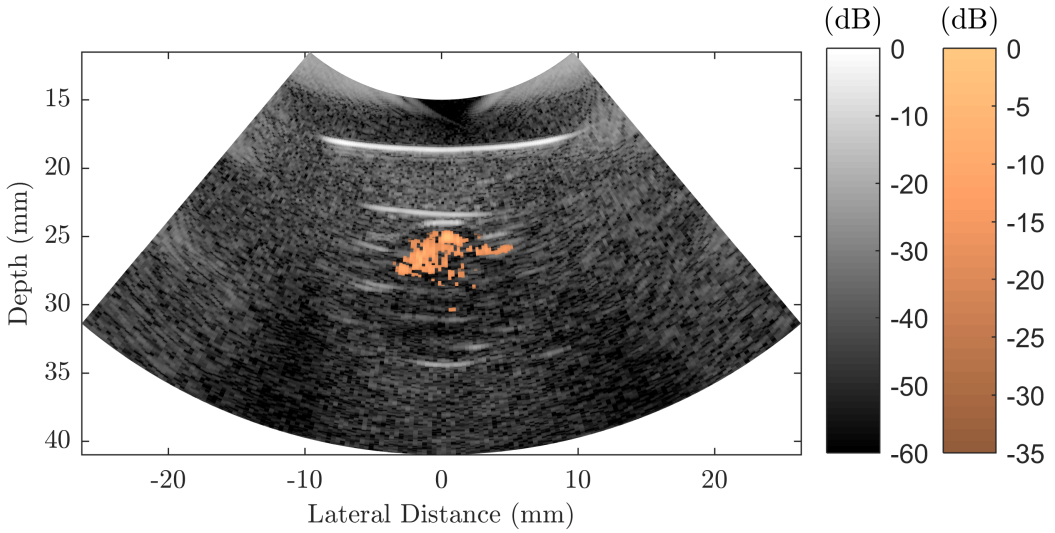

Figure 5.12: A combined ultrasound B-mode and photoacoustic image of an agar phantom with an inclusion of AuNRs approximately 5 mm below the surface using a linear array (L11-4) in the style of EBUS (i.e. 80° FOV). Strong reflections are visible from both the ultrasound pulses and photoacoustic signals due to large trapped bubbles.

After 20 mm, the light has lost a significant amount of its energy at the surface and this is shown by the reduced PA signal from the deep inclusion.

5.4.3 Steered focused beam imaging

To mimic EBUS, a series of B-mode and PA images were recorded and beamformed with a wide FOV. A new phantom was created following a similar recipe and procedure to the previous one (section 5.4.1), with the exception of slightly larger inclusions (approximately 11 mm) to imitate a larger tumour volume. Steered focussed beams were used to obtain an 80° FOV and the focal region was fixed at 30 mm. Figure 5.12 shows the combined image recorded using the linear array (L11-4). Unfortunately, the fabrication of the phantom was not homogeneous and large bubbles had formed inside the phantom during the mixing process, leading to strong reflections from both the transmitted ultrasound pulses and the PA signals. These are visible by the high intensity white horizontal lines in the B-mode image (except for the uppermost line at approximately 17 mm which represents the top surface of the phantom). As a result of this, the inclusion was clearly distinguishable from the background speckle pattern in the B-mode image. The reduced and incomplete PA signal was also affected by the large bubbles surrounding the inclusion and led to the signal only originating from the upper portion of the inclusion where the laser intensity was highest.

Consequently, a new phantom was created in an attempt to reduce the trapped bubbles and create a more homogenous phantom. Figure 5.13a shows the combined beamformed B-mode and PA image of the new phantom, recorded using the linear array (L11-4). While

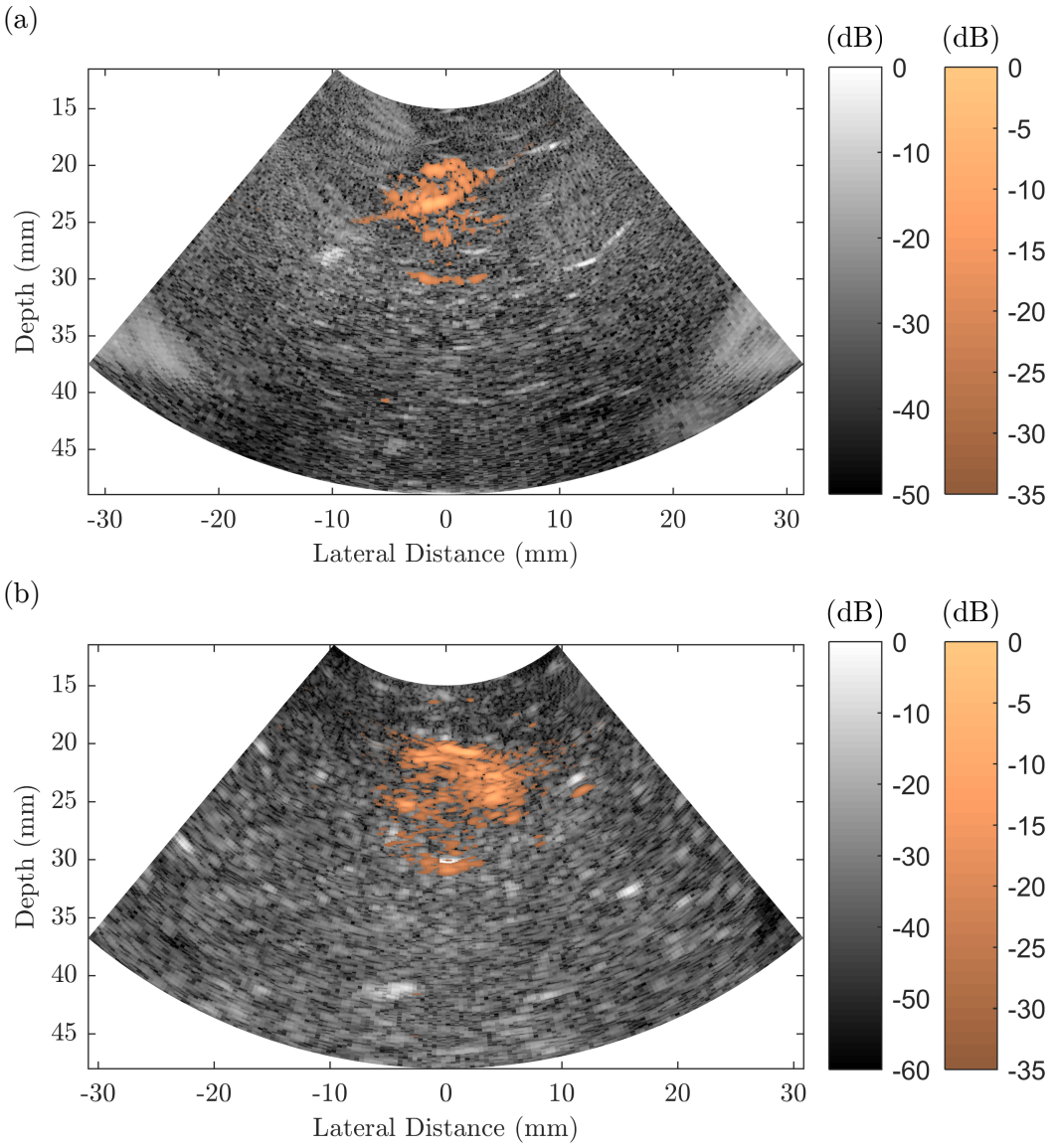

Figure 5.13: A combined ultrasound B-mode and photoacoustic image of a new agar phantom with an inclusion of AuNRs approximately 5 mm below the surface using (a) a linear array (L11-4) and (b) a phased array (P9-1), in the style of EBUS (i.e. 80° FOV).

there were still bubbles present in this phantom the diameters were significantly smaller and were not obtrusive to the desired aim. The B-mode signals were axially filtered between $4 - 11\,\text{MHz}$ ($-6\,\text{dB}$ bandwidth of the probe) and the PA signals were filtered between $4 - 8\,\text{MHz}$. The AuNR inclusion is mostly visible with the exception of a portion of the lower region. The bottom edge of the inclusion is visible, suggesting that the distribution of AuNRs within the inclusion was not uniform. This is possible since the small amount of agar mixture used to create the inclusion cools and sets rapidly making it difficult to achieve a homogenous distribution of AuNRs while mixing the two together.

The same phantom and inclusion was further imaged with the phased array probe (P9-1) to determine if the previously discussed (section 5.3.3) potential benefits of the P9-1 array leads to a more complete photoacoustic image. The B-mode image and PA image was axially filtered between $4 - 9\,\text{MHz}$ and $3 - 8\,\text{MHz}$, respectively, to improve the image quality, and figure 5.13b shows the resultant combined B-mode and PA image. The background B-mode speckle is largely uniform and free of noise and clutter. The recorded PA signal generated by the inclusion of AuNRs is distributed across the entire volume of the inclusion. This is in comparison to the image recorded with the L11-4 where large portions were missing. The enhanced uniformity of the PA signal throughout the inclusion volume can be partly attributed to the wide bandwidth of the phased P9-1 array. The frequency spectrum of the PA signal predominately lay within $2 - 8\,\text{MHz}$ (see figures 5.14 and 5.15) and a significant proportion came from the lower frequencies ($< 5\,\text{MHz}$). The P9-1 is more sensitive at these lower frequencies compared with the L11-4 and consequently was able to capture the full range of the signals frequency spectrum while minimising noise. In addition, the contribution to the PA signal from the upper end of the frequency spectrum was less than that of the lower frequencies, and both the linear and phased arrays picked up significant noise at this range. Furthermore, the overall sensitivity of the P9-1 probe is higher than that of the L11-4. PA signals are weak in amplitude compared with reflected ultrasound pulses generated by a transducer, and the P9-1 was able to detect these weaker PA signals more easily than the linear. A combination of these factors led to an overall clearer and more well-defined image.

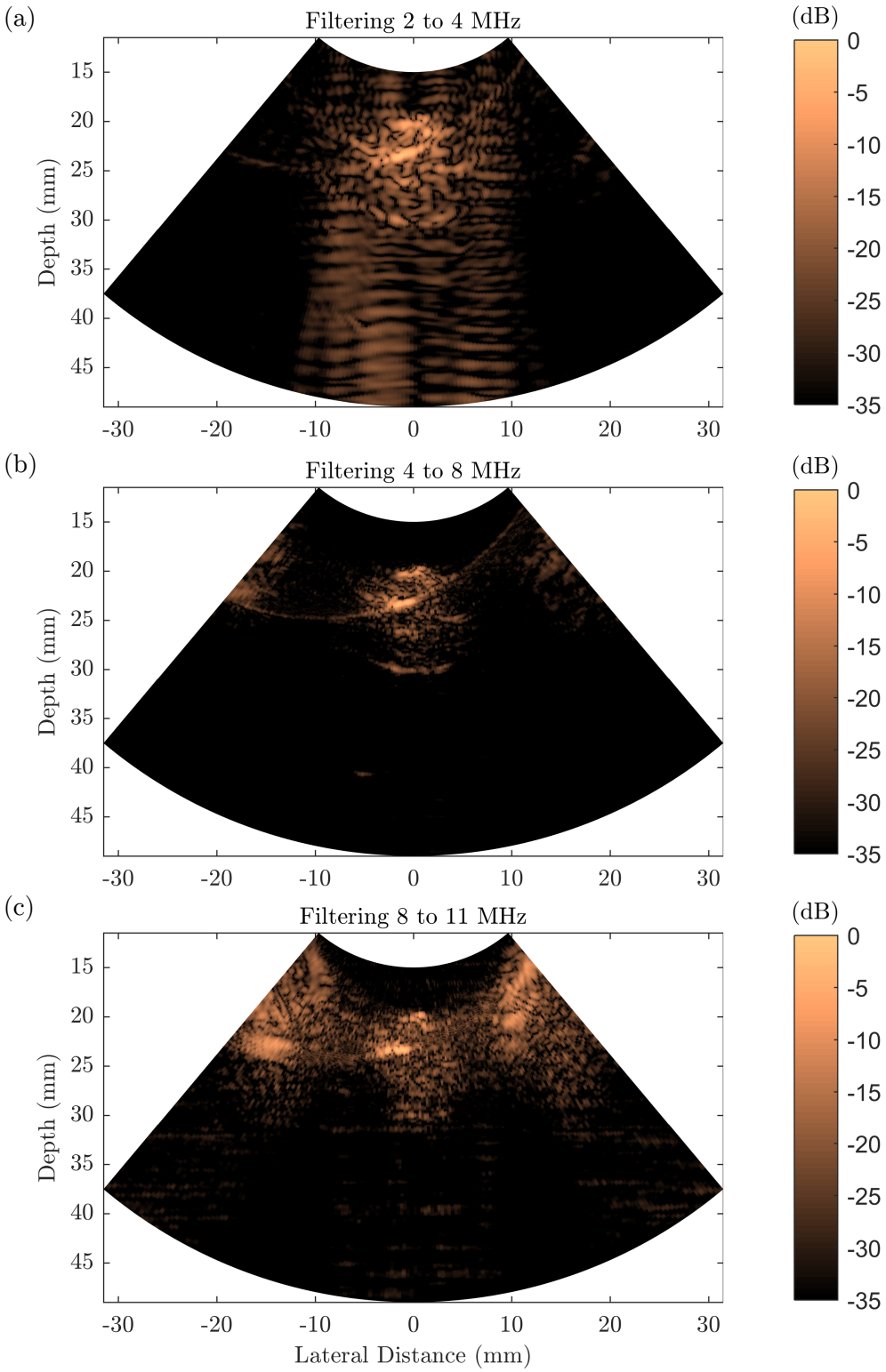

Figure 5.14: The recorded photoacoustic signal is spread across a range of frequencies and the transducer bandwidth affects signal detection. The photoacoustic signal recorded with the linear array (L11-4) is filtered between (a) $2-4\,\mathrm{MHz}$, (b) $4-8\,\mathrm{MHz}$, and (c) $8-11\,\mathrm{MHz}$.

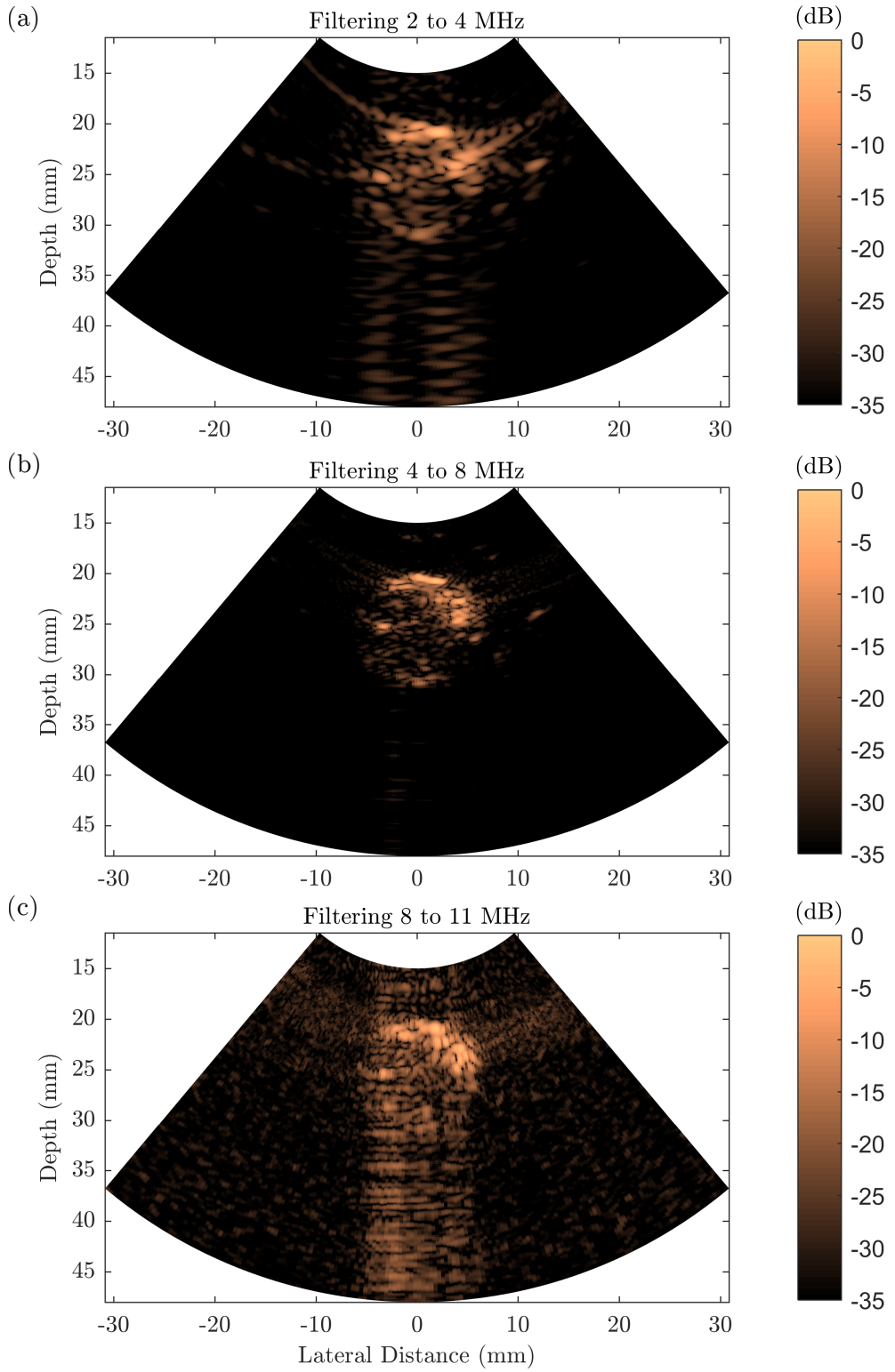

Figure 5.15: The recorded photoacoustic signal is spread across a range of frequencies and the transducer bandwidth affects signal detection. The photoacoustic signal recorded with the phased array (L9-1) is filtered between (a) $2-4$ MHz, (b) $4-8$ MHz, and (c) $8-11$ MHz.

5.5 Conclusions

The possibility of incorporating PA imaging into an EBUS system was explored using the ultrasound array research platform (UARP) and tissue-mimicking phantoms. The unavailability of an EBUS system meant it was necessary to imitate the technique as closely as possible with the UARP and the transducers available. Nevertheless, the UARP enabled a greater degree of flexibility with regards to incorporating and syncing a laser with the system, in addition to image processing and beamforming. A linear array and two phased arrays were explored as possible options for this combined modality and a CIRS tissue-mimicking test phantom provided an accurate and consistent method for investigating the transducers. The wide field of view (FOV) of EBUS transducers meant that steered focused beams were the best beamforming method for replicating typical EBUS images. It was found that the low frequency phased array (P4-2) was not suited for this approach as the narrow bandwidth meant detection of PA signals would be poor and the B-mode image quality was sub-optimal. Therefore, the P4-2 probe was discarded. The linear array, while providing higher resolution image, was poor at deep locations and unable to accurately produce images with a wide FOV. The wide-band phased array (P9-1) generated accurate B-mode images and possessed the bandwidth to enhance PA signal detection. Therefore, in the absence of an EBUS probe, it is suggested that a P9-1 array should be used to closely imitate EBUS.

When recording photoacoustic signals, there are a few important considerations that must be made. Firstly, the employment of a wide bandwidth transducer is recommended to ensure that a large proportion of the frequency content of the photoacoustic signals is detected, and for detecting photoacoustic signals from AuNRs, a transducer that is sensitive at the lower frequencies ($2 - 4\,\text{MHz}$) may be required. Secondly, the post-processing and receive beamforming of the recorded PA signals was important for producing a clear final image. Photoacoustic signals are generally weak in amplitude and require multiple averages to filter out background noise and reveal the 'true' photoacoustic signal. Furthermore, accurate frequency filtering of the photoacoustic signals improved image quality and noise suppression. Finally, it was shown that AuNR-mediated photoacoustic imaging is possible at clinically relevant depths for EBUS, since the AuNR inclusions were observable at all the depths investigated (3 mm, 10 mm, 20 mm), although only the upper portion of the inclusions was visible for the deepest location. The scattering and loss of directionality of the laser pulse as the beam propagated through the phantom meant laser intensity diminished with increasing depths, showing the potential depth limitations of PAI.

Combined ultrasound and PAI of larger AuNR inclusions, with a diameter of approximately 11 mm to replicate a larger tumour volume, were recorded using both the L11-4 and P9-1 in the style of EBUS images with a large FOV (80°). Both probes were able to discern almost the entire 'tumour' region, however the phased array produced the highest quality image, largely due to its ability to detect low frequency signals with minimal noise. These results confirmed that a wide-bandwidth transducer is more effective for recording photoacoustic signals generated by AuNRs since a larger proportion of the emitted signals

can be recorded and less information is lost. These results highlight the necessary requirements for a multimodal transducer for combined ultrasound and PAI in an EBUS device. EBUS is an already effective biomedical technique that has been shown to be enhanced further with minimal adaptation. The work presented in this chapter provides the necessary groundwork for progressing this technique.

Chapter 6

Conclusions

The continued development and advancement of plasmonic nanoparticles is enabling the creation and sustained improvement of new biomedical modalities that can potentially revolutionise modern medicine. The work presented in this thesis aimed to explore and progress the use of plasmonic gold nanorods for combined theranostic applications, framed in the context of translating gold nanorods from a core understanding of their dynamics through to clinical application, and in particular their use in lung cancer. A summary of the presented work is provided with some overarching conclusions, followed by a discussion regarding future work and finally some closing remarks.

6.1 Summary and conclusions

Gold nanorods have the potential to create new combined light-based theranostic modalities that can improve patient outcome by reducing negative side-effects and increasing diagnostic and treatment times, in addition to further improving upon already existing clinical routines.

Chapter 2 presented the necessary knowledge to understand the rest of the work in this thesis. Cancer is a leading cause of death worldwide, and the complex nature of the disease combined with the large variations between cases make it difficult to diagnose and treat. One of the biggest issues with current cancer treatments are that they are invasive and can cause serious side effects for the patient. There is a strong need for new, minimally invasive procedures that selectively destroy cancerous tissues while leaving healthy tissues unharmed. Gold nanoparticles have a large set of desirable characteristics that make them excellent mediators of new and existing biomedicines, and have shown promise for use in minimally-invasive cancer care. If the final aim is to use gold nanoparticles in routine medical procedures across the world, then large-scale synthesis is a considerable challenge that must be addressed. All of the properties of gold nanoparticles - size, shape, SPRs, surface coating, functionalisation, etc - must be highly controllable *en masse* to meet the rigorous criteria required for wide-spread clinical use. Furthermore, the 'small' nature of

nanoparticles, combined with their potentially complex compositions, makes studying their biological interactions *in vivo* difficult, and even more-so when translating them for human use. However, extensive studies that cover all aspects of introducing gold nanoparticles into the body, such as aggregation, protein adsorption, cellular interactions, biodistribution, renal clearance, etc, are required to ensure the safety and efficacy of the treatments.

The photoacoustic effect is a powerful phenomenon that enables non-invasive, non-ionising imaging modalities that combine the high contrast and spectral specificity of optical-based approaches with the high spatial resolution of ultrasound. Gold nanoparticles can be used to enhance the photoacoustic effect and provide important additional information that further extends the potential applications. Functionalised AuNRs targeted to a specific location in the body, such as a tumour site, can provide an optical absorption contrast between the background and malignant tissues, that can be exploited through the use of pulsed laser irradiation. Furthermore, the exact same AuNRs situated in the tumour volume can additionally act as photoabsorbers for plasmonic photothermal therapy. This therapeutic technique - usually conducted with continuous wave lasers - is able to destroy diseased tissues by inducing a bulk temperature increase in target region while minimising damage to surrounding healthy tissues. It is potentially possible to enhance this therapy further by substituting continuous wave lasers for pulsed lasers. This seemingly small but crucial change could open up additional benefits such as the further reduction of damage to healthy tissues, simultaneous imaging and therapy, and reduced cell toxicity and drug resistance due to mechanical damage. Gold nanoparticles, and the light-based modalities that rely on them, have the capacity to provide a combined theranostic approach for the diagnosis and treatment of lung cancer. For example, endobronchial ultrasound is a routine clinical procedure that already possesses the underlying technology to be easily combined with such nanoparticle-mediated techniques, and could provide a way to locate, diagnose, stage and treat a lung tumour with a single modality.

6.1.1 Chapter 3

The main focus of chapter 3 was to explore the effect of gold nanorod size on a variety of factors, such as photoacoustic response, photostability, cellular toxicity and uptake. Since gold nanoparticles can be synthesised into almost any shape and size it is important to understand what effect this might have on the wide range of aspects related to biomedical applications. Gold nanorods absorb light based predominately on their aspect ratio, and since it is desirable for them to absorb light in the near-infrared (due to increased optical penetration depths) and can be almost any size, there are a large number of AuNR sizes that are potential candidates as contrast agents. Therefore, four different sized AuNRs with similar aspect ratios, and consequently similar surface plasmon resonances, were investigated. Aside from their comparable dimensions, these AuNRs were chosen due to their commercial access and 'off-the-shelf' accessibility. As discussed previously, if AuNRs are to be used clinically then it is essential that they can be reproduced in large quantities with

highly controllable properties, and the AuNRs used in this study satisfied these conditions. Under pulsed laser illumination it was possible to generate a photoacoustic signal from all of the AuNRs studied (section 3.3). The concentration of AuNRs played a significant part in determining their photoacoustic response, and more importantly, the way in which the concentrations were defined was significant. This poses crucial questions as to the governing factors that control the uptake of AuNRs. For example, if the deliverability of AuNRs to a tumour is controlled predominately by the number of AuNRs then the best results would likely be seen with larger AuNRs. If instead it is governed by total mass, then the smallest AuNRs used in the study were the most effective photoacoustic signal generators. In either case, it is evident that reasonably large numbers of AuNRs are required (upwards of $1 \times 10^9\,\mathrm{NP\,mL^{-1}}$) to generate a sufficient photoacoustic signal, and improving on the deliverability of AuNRs to a desired region is a particularly important area that must be optimised. To address this concern, controlled in vivo studies are required that specifically consider the dependence of mass or nanoparticle number on the uptake of target tissue.

AuNRs are susceptible to thermal reshaping under pulsed laser illumination and since their surface plasmon resonances are governed by their specific rod-shape and aspect ratio, photothermal degradation is a pivotal risk for the efficacy of biomedical modalities that rely on their ability to absorb light. If they are to be used in a combined theranostic approach, then it is critical that they are able to withstand the conditions necessary to complete each of the individual techniques in order for them to maintain their beneficial properties through to the final treatment. It was found that large AuNRs were less photothermally stable than their smaller counterparts (section 3.3), and was attributed to a higher peak temperature under nanosecond pulsed irradiation. The large AuNRs (widths of 40 and 50 nm) saw melting and reshaping at relatively low fluences ($20\,\mathrm{mJ\,cm^{-2}}$), however the least stable were the 25 nm wide AuNRs. For theranostic modalities that require AuNRs to maintain their strong optical absorption, the results suggest that small AuNRs (width ≤ 10 nm) are able to withstand extended periods of laser illumination and would be more suitable for this application. There is a large amount of literature surrounding the photostability of nanoparticles, however the vast range of nanoparticles and laser parameters used in those studies make it difficult to draw decisive conclusions. For example, gold nanoparticles of different shapes and sizes can have a variety of coatings and can be further complicated by the addition of functionalising ligands. One or a combination of these factors can have a considerable effect on photothermal degradation (as well as many of the other investigated factors) and so it is important to understand how simple nanoparticles behave before exploring more complex arrangements. For example, gold nanorods with a reduced graphene oxide coating have shown enhanced photothermal conversion efficiencies compared with non-coated ones [345], while silica-coated AuNRs show improved photostability but generated a reduced photothermal effect [346].

Biocompatibility and toxicity is also critical to the progression and development of AuNRs for biomedical use. There are a range of factors that can affect the toxicity of

AuNRs to cells, including surface coating, surface charge, and colloidal stability. In chapter 3, it was found that their size also governed their toxicity to lung cancer cells, with larger AuNRs exhibiting increased toxicity compared with smaller ones at equivalent concentrations ($NP\,mL^{-1}$). It is important to understand that an equivalent number of particles that have a different amount of mass per particle results in an overall difference in total mass. Thus, larger AuNRs will have an increased total mass compared with smaller ones, which may have an affect on overall toxicity to cells. There is a lack of consensus in the literature surrounding the size-dependent toxicity of AuNRs due to the vast range of variables (coating, functionalities, experimental methods, cell lines, etc) across each study, however the presented findings are in agreement with studies on the toxicity of spherical gold nanoparticles [347, 348], where generally an increase in size lead to an increase in toxicity.

A limitation of the work in chapter 3 is that only four different sized AuNRs were explored. This was largely due to the availability of different sized AuNRs that absorbed light at a similar wavelength. Therefore, it would be beneficial to explore an even greater range of AuNR sizes (that absorb in the near infrared) with respect to the parameters investigated in chapter 3. Since smaller AuNRs have shown to be the most promising candidates, it would follow to study a range of even smaller AuNRs for their potential use in photoacoustic imaging. Nevertheless, clear size-dependent relationships were observed in the presented work and solid conclusions were able to be drawn.

6.1.2 Chapter 4

The main aims of chapter 4 were to investigate AuNRs with similar dimensions and properties as in chapter 3 but for use as photoabsorbers for photothermal applications, and to explore the use of pulsed lasers for therapeutic application. Continuous wave lasers are often used for plasmonic photothermal therapy as they deliver a steady stream of optical energy that photothermal absorbers can use to damage tissues by generating heat. It is an effective way of destroying tissue as it only requires a reasonably small temperature increase in the target region to begin to cause irreversible damage. However, there are potential problems with this approach, such as damage to healthy tissues through heat conducting into the surroundings and cells developing a resistance to heat or drugs due to thermal damage. Pulsed lasers, on the other hand, require photoabsorbers to damage tissues, and result in a rapid and intense temperature rise in extreme proximity to the absorbers, with no bulk heating. Using pulsed lasers for therapy would negate the negative effects of continuous wave lasers while also providing additional benefits, such as simultaneous imaging during therapy via the photoacoustic effect.

The concentration of absorbers, or in this case gold nanorods, is essential to treatment success since too few will produce an insufficient temperature rise for thermal damage. In chapter 4, two different sized AuNRs with SPRs around 850 nm were investigated, and were chosen due to the 854 nm fixed wavelength of the continuous wave laser. Furthermore, the AuNRs were from a large-scale synthesis process with repeatable characteristics and

properties, similarly to the study in chapter 3. It was found that the AuNR size did not affect the overall peak temperature increase at equivalent concentrations ($\mu g\,mL^{-1}$) achieved under continuous laser irradiation, while no change in temperature was observed when a pulsed laser was used. This suggests that, for therapeutic applications, it likely does not matter what sized AuNR is used to achieve a desired temperature under CW laser irradiation, and more focus can be placed on the other factors that AuNR size may affect, such as the aspects discussed in the chapter 3 (deliverability, toxicity, etc.).

The effect that AuNR size has on the toxicity to lung cancer cells under laser irradiation was explored. Lung cancer was chosen as the treatment target to further the idea that the techniques discussed in this thesis could be applied for thernostic applications in lung cancer. Both continuous wave and pulsed lasers were used as optical sources, and the differences in the number of AuNRs in the path of the laser beam was explored. For continuous wave lasers, an increase in cell toxicity was observed when AuNRs that had not been taken up by the cells were still situated around the cells. While, with a pulsed laser, it was only the AuNRs that had been taken up by the lung cancer cells that were the leading cause of death. This was attributed to the fact that a larger number of AuNRs absorbing continuous laser light produced a higher temperature increase in the cell media, and therefore thermal damage was higher, while the location of the AuNRs was much more significant in determining cell death for a pulsed laser due to the mechanical stresses induced by the laser pulses and the extreme heat only occurring within close proximity to the AuNRs. This has important implications for clinical translation, since if pulsed lasers are to be employed for therapeutic purposes then the location of the AuNRs in relation to the target cells is important for successful treatment. Conversely, with continuous wave lasers, the AuNR location may not be as important as long as there is a sufficient distribution of AuNRs within the target area. The size of the AuNRs generally did not have a substantial effect on the laser-induced toxicity, except for the smallest AuNRs considered in the study (width $< 10\,nm$) which produced the highest photothermal efficacy. In all cases, these small AuNRs were the most effective agents for cell destruction, regardless of the experimental parameters, and the enhanced therapeutic effect was attributed to both their ability to be taken up by the cells more proficiently, and their increased surface-to-volume ratio.

Functionalising and targeting AuNRs to diseased tissue is potentially a highly effective method for not only ensuring that the AuNRs are delivered to a desired location in the body, but also to increase the total number that specifically accumulate in that region and consequently improve diagnostic/therapeutic efficacy. Furthermore, targeting has the capacity to reduce the dose that is administered to a patient and still achieve sufficient uptake at the target location. This can reduce the negative side-effects caused by large doses, lessening the need for prohibitively large-scale production, and lowering treatment costs. There is, however, a debate as to how effective targeting is in a 'real-world' scenario where in vivo results have shown only slight improvements to delivering efficiency. Nevertheless, the body of work and concepts underpinning targeting - the dynamics of cell growth, proliferation,

and cellular composition on a molecular level - is solid, and presently appears to be the only substantial mechanism for improving therapeutic efficacy. The targeting efficiency and subsequent effect on laser-induced therapy of EGFR-targeting AuNRs was investigated in chapter 4, and was found to have a positive effect on both cellular uptake and destruction of lung cancer cells under both continuous and pulsed laser irradiation. Perhaps the most surprising result was that targeted gold nanorods facilitated an enhanced therapeutic effect under pulsed laser illumination compared with continuous wave. This significant decrease in cell viability was further attributed to the location of the AuNRs with respect to the cells, and the number of AuNRs contributing to cell destruction, facilitated by the enhanced affinity of the AuNRs to the lung cancer cells. The anti-EGFR-conjugated AuNRs were situated in close proximity to the membrane of the cells, and were potentially arranged in clusters, that enabled the mechanical stresses and bubble formations around the AuNRs to disrupt and damage the cell walls.

Overall, it seems that pulsed lasers can indeed be used for therapeutic (as well as diagnostic and imaging) purposes, and chapter 4 provided a solid understanding of how the size, location, and targeting of AuNRs can drastically affect the observed outcomes under pulsed and continuous wave laser generation.

6.1.3 Chapter 5

In the final chapter, the focus was shifted from understanding the principles and effects that gold nanorods can have on diagnostics, imaging and therapy, to demonstrating the possibility for improving a clinical diagnostic tool: endobronchial ultrasound. This important technique is routinely used to guide a needle biopsy for the diagnosing and staging lung cancer, and does so with exceptional sensitivity. It is currently used as a secondary method for determining the progress of a lung tumour, however it has the potential to be a primary investigatory procedure, and one that could facilitate the locating, diagnosing, staging, and treating of a tumour with a single modality. This theranostic tool could be achieved by incorporating a laser fibre into an endobronchial device that would allow the addition of a photoacoustic component to the already existing ultrasound capabilities, and potentially further enhance the usefulness of the probe by enabling a treatment avenue via photothermal therapy, all mediated with the aid of AuNRs targeted to the diseased lung tissue. The technology to accomplish this combined multimodality already exists - except for the continued development and refinement of AuNRs - and with minimal adaptation could become a reality.

The unavailability of an endobronchial ultrasound system meant that the technique needed to be mimicked with a custom, in-house built ultrasound research platform that enabled a high level of flexibility for combining conventional ultrasound with photoacoustic imaging. Three transducers were explored for suitability with imitating the typical parameters associated with endobronchial ultrasound probes, such as frequency, number of elements, and field of view. It was determined that the wideband phased array was most suited for

this application due to its ability to be excited at frequencies ($5 - 9\,\text{MHz}$) comparable to EBUS ($5 - 12\,\text{MHz}$), capacity to record the low amplitude and potentially broad spectrum of photoacoustic signals, and generate images with a wide field of view (80°). These specific requirements apply for any future probe that may be implemented into a combined endobronchial ultrasound and photoacoustic imaging system, since a high frequency enables high resolution imaging of shallow regions that enable the locating of lymph nodes, and the wide bandwidth allows the detection of the potentially broad photoacoustic frequency spectrum to form an image of the entire region emitting the photoacoustic signals.

Plane-wave B-mode images were recorded using a linear array transducer along with photoacoustic signals generated by small inclusions of gold nanorods at increasing depths in a tissue-mimicking agar phantom. The ultrasound images of the phantom were formed without the visibility of the inclusion - as may be the case with a tumour *in vivo* - and the inclusion only appeared under pulse laser illumination. Moreover, the inclusion at the deepest location was able to be resolved, although not entirely, due to the reduction in laser intensity and loss of directionality as the light penetrated deeper into the phantom. This is an important aspect to consider in a clinical scenario as tumours that are situated deep inside tissue will be harder to resolve with photoacoustic imaging since laser penetration will be reduced. This is the limiting factor with optical-based biomedical approaches and is the reason that near-infrared light is preferred due to increased penetration in tissues. Accurate and meaningful filtering of the photoacoustic signals was a crucial aspect to resolving a clear image. A significant proportion of the photoacoustic signals were located at the lower end of the frequency spectrum ($< 4\,\text{MHz}$) and the wide-band phased array had the bandwidth to detect these weak, low frequency signals without picking up high levels of noise. Post-processing and accurate filtering enabled almost the entire volume of the large inclusion to be resolved.

Chapter 5 demonstrated the ability for successful combination of endobronchial ultrasound with photoacoustic imaging, and the potential advantages of doing so. Taking this body of work forward, the natural next step would to be to acquire an endobronchial ultrasound system and look into incorporating a laser fibre into the endoscope to demonstrate cellular PPTT.

6.2 Future work

There are many routes for investigation that follow-on from the work presented in this thesis, and some of the more interesting ones will be discussed here.

Firstly, one of the biggest issues to arise from this work, was the lack of knowledge surrounding the *in vivo* cellular uptake of gold nanorods dependent on equivalent total mass or number of nanoparticles. The literature quote nanoparticle concentrations in terms of equivalent mass ($\mu\text{g}\,\text{mL}^{-1}$), number of particles ($\text{NP}\,\text{mL}^{-1}$), or number of moles (nmol), across the vast range of nanoparticle compositions, shapes, sizes, and coatings, and little is

known regarding whether it is possible to deliver an equivalent concentration of nanoparticles to a target region across different sizes. Therefore, a size-dependent study for cellular uptake *in vivo* is currently in progress across a range of gold nanorod sizes similar to the ones in the presented work (widths of 10, 25, 40, and 50 nm) to determine whether injections of equivalent concentrations (mass and number of nanoparticles) affects the total cellular uptake exhibited by tumour tissues and other vital organs. Furthermore, it would be valuable to obtain gold nanorods with a range of widths between $5 - 25$ nm, to determine the effects of small gold nanorods on the parameters studied in this thesis.

Secondly, due to the promising results observed using a pulsed laser to induce cell death with EGFR-targeted AuNRs, it would be beneficial to study more closely the route cause of cell-death, and more specifically, conduct acoustic-monitoring of the potential bubble formation and collapse caused by the pulsed laser-heating of aggregated AuNRs, mediated by the anti-EGFR targeting ligands. This would provide further understanding of the mechanisms through which pulsed lasers can induce cell death, and may lead to improved theranostic modalities.

Finally, to continue the work in chapter 5, it would be useful to acquire a commercial, clinical endobronchial ultrasound probe to evaluate and develop the integration of a laser fibre into the existing diagnostic system. This could then be tested in more sophisticated tissue-mimicking phantoms, with a long-term aim of investigating the newly developed combined endobronchial ultrasound and photoacoustic imaging *in vivo*, with optimised targeted gold nanorods.

6.3 Final Remarks

The use of nanotechnology in biomedicine is an exciting area of research with a huge potential to revolutionise the medical world, however continued research and development into the many complex aspects of nanoparticles is critical to its success. The work in this thesis has demonstrated the ability for gold nanorods to be used in combined theranostic applications and has positive implications for future work. Precision treatments, that are tailored to the specifics of individual patients and consider the subtle differences between each and every case, are the future of medicine, and it is only a matter of time before we master the ability to exploit these differences and ultimately conquer one of the biggest challenges humanity has ever faced, cancer.

References

[1] O. B. Knights, S. Ye, N. Ingram, D. M. J. Cowell, A. F. Markham, S. Freear, and J. R. McLaughlan, "Optimising gold nanorod size for maximum photoacoustic response while minimising cell toxicity," *Proc. Mtgs. Acoust.*, vol. 30, no. 1, pp. 020 001–, Jun. 2017.

[2] O. Knights and J. McLaughlan, "Gold nanorods for light-based lung cancer theranostics," *International journal of molecular sciences*, vol. 19, no. 11, p. 3318, 2018.

[3] O. B. Knights, D. M. Cowell, T. M. Carpenter, S. Freear, and J. R. McLaughlan, "Plasmonic gold nanoparticles for combined photoacoustic imaging and plasmonic photothermal therapy using a pulsed laser," in *2018 IEEE International Ultrasonics Symposium (IUS)*. IEEE, 2018, pp. 1–4.

[4] O. B. Knights, S. Ye, N. Ingram, S. Freear, and J. R. McLaughlan, "Optimising gold nanorods for photoacoustic imaging in vitro," *Nanoscale Advances*, 2019.

[5] M. Faraday, "The Bakerian Lecture: Experimental Relations of Gold (and Other Metals) to Light," *Philosophical Transactions of the Royal Society of London Series I*, vol. 147, pp. 145–181, 1857.

[6] J. Tyndall, "On the blue colour of the sky, the polarization of skylight, and on the polarization of light by cloudy matter generally," *Proceedings of the Royal Society of London*, vol. 17, pp. 223–233, 1869.

[7] J. Strutt, "Lviii. on the scattering of light by small particles," *Philosophical Magazine*, vol. 41, no. 275, pp. 447–454, Jun. 1871.

[8] L. Rayleigh, "On the diffraction of light by spheres of small relative index," *Proceedings of the Royal Society of London A: Mathematical, Physical and Engineering Sciences*, vol. 90, no. 617, pp. 219–225, 1914.

[9] C. V. Raman and B. Ray, "On the transmission colours of sulphur suspensions," *Proceedings of the Royal Society of London A: Mathematical, Physical and Engineering Sciences*, vol. 100, no. 702, pp. 102–109, 1921.

[10] G. Mie, "Beitrge zur optik trber medien, speziell kolloidaler metallsungen," *Annalen der Physik*, vol. 330, no. 3, pp. 377–445, 1908.

[11] D. J. de Aberasturi, A. B. Serrano-Montes, and L. M. Liz-Marzán, "Modern applications of plasmonic nanoparticles: from energy to health," *Advanced Optical Materials*, vol. 3, no. 5, pp. 602–617, 2015.

[12] I. I. Slowing, J. L. Vivero-Escoto, C.-W. Wu, and V. S.-Y. Lin, "Mesoporous silica nanoparticles as controlled release drug delivery and gene transfection carriers," *Advanced drug delivery reviews*, vol. 60, no. 11, pp. 1278–1288, 2008.

[13] T. Sun, Y. S. Zhang, B. Pang, D. C. Hyun, M. Yang, and Y. Xia, "Engineered nanoparticles for drug delivery in cancer therapy," *Angewandte Chemie International Edition*, vol. 53, no. 46, pp. 12 320–12 364, 2014.

[14] Y. Li, Y. Huang, Z. Wang, F. Carniato, Y. Xie, J. P. Patterson, M. P. Thompson, C. M. Andolina, T. B. Ditri, J. E. Millstone *et al.*, "Polycatechol nanoparticle mri contrast agents," *Small*, vol. 12, no. 5, pp. 668–677, 2016.

[15] A. J. Haes and R. P. Van Duyne, "A nanoscale optical biosensor:â€‰ sensitivity and selectivity of an approach based on the localized surface plasmon resonance spectroscopy of triangular silver nanoparticles," *Journal of the American Chemical Society*, vol. 124, no. 35, pp. 10 596–10 604, 2002.

[16] A. B. Chinen, C. M. Guan, J. R. Ferrer, S. N. Barnaby, T. J. Merkel, and C. A. Mirkin, "Nanoparticle probes for the detection of cancer biomarkers, cells, and tissues by fluorescence," *Chemical reviews*, vol. 115, no. 19, pp. 10 530–10 574, 2015.

[17] N. S. Abadeer and C. J. Murphy, "Recent progress in cancer thermal therapy using gold nanoparticles," *The Journal of Physical Chemistry C*, vol. 120, no. 9, pp. 4691–4716, 2016.

[18] G. A. Sotiriou, "Biomedical applications of multifunctional plasmonic nanoparticles," *Wiley Interdisciplinary Reviews: Nanomedicine and Nanobiotechnology*, vol. 5, no. 1, pp. 19–30, 2013.

[19] A. C. Anselmo and S. Mitragotri, "Nanoparticles in the clinic," *Bioengineering & translational medicine*, vol. 1, no. 1, pp. 10–29, Jun. 2016.

[20] B. W. Stewart and C. P. Wild, Eds., *World Cancer Report 2014*. International Agency for Research on Cancer, 2014.

[21] World Health Organisation (WHO). (2018, September) Cancer fact sheet no.297. World Health Organisation.

[22] P. Nowell, "The clonal evolution of tumor cell populations," *Science*, vol. 194, no. 4260, pp. 23–28, 1976.

[23] I. Dagogo-Jack and A. T. Shaw, "Tumour heterogeneity and resistance to cancer therapies," *Nature Reviews Clinical Oncology*, vol. 15, pp. 81–, Nov. 2017.

[24] P. G. Corrie, "Cytotoxic chemotherapy: clinical aspects," *Medicine*, vol. 36, no. 1, pp. 24 – 28, 2008.

[25] L. Rasmussen and A. Arvin, "Chemotherapy-induced immunosuppression." *Environmental Health Perspectives*, vol. 43, pp. 21–25, Feb. 1982.

[26] R. J. Gibson and D. M. K. Keefe, "Cancer chemotherapy-induced diarrhoea and constipation: mechanisms of damage and prevention strategies," *Supportive Care in Cancer*, vol. 14, no. 9, pp. 890–900, 2006.

[27] J. E. Groopman and L. M. Itri, "Chemotherapy-induced anemia in adults: Incidence and treatment," *Journal of the National Cancer Institute*, vol. 91, no. 19, pp. 1616–1634, 1999.

[28] V. Chadha and S. Shenoi, "Hair loss in cancer chemotherapeutic patients," *Indian J Dermatol Venereol Leprol*, vol. 69, no. 2, pp. 131–132, Mar. 2003.

[29] D. Castellano, R. Hitt, H. Corts-Funes, A. Romero, and J. L. Rodriguez-Peralto, "Side effects of chemotherapy," *Journal of Clinical Oncology*, vol. 18, no. 3, p. 695, 2000.

[30] T. Iwamoto, "Clinical application of drug delivery systems in cancer chemotherapy: review of the efficacy and side effects of approved drugs," *Biological and Pharmaceutical Bulletin*, vol. 36, no. 5, pp. 715–718, 2013.

[31] E. B. C. T. C. Group *et al.*, "Effects of chemotherapy and hormonal therapy for early breast cancer on recurrence and 15-year survival: an overview of the randomised trials," *The Lancet*, vol. 365, no. 9472, pp. 1687 – 1717, 2005.

[32] J.-J. Monsuez, J.-C. Charniot, N. Vignat, and J.-Y. Artigou, "Cardiac side-effects of cancer chemotherapy," *International journal of cardiology*, vol. 144, no. 1, pp. 3–15, 2010.

[33] K. Lotfi-Jam, M. Carey, M. Jefford, P. Schofield, C. Charleson, and S. Aranda, "Nonpharmacologic strategies for managing common chemotherapy adverse effects: a systematic review," *Journal of Clinical Oncology*, vol. 26, no. 34, pp. 5618–5629, 2008.

[34] Cancer Research UK. (2019) What is radiotherapy? [Online]. Available: https://www.cancerresearchuk.org/about-cancer/cancer-in-general/treatment/radiotherapy/about.

[35] Cancer Research UK. (2019) Surgery. [Online]. Available: https://www.cancerresearchuk.org/about-cancer/cancer-in-general/treatment/surgery.

[36] F. A. Scappaticci, L. Fehrenbacher, T. Cartwright, J. D. Hainsworth, W. Heim, J. Berlin, F. Kabbinavar, W. Novotny, S. Sarkar, and H. Hurwitz, "Surgical wound healing complications in metastatic colorectal cancer patients treated with bevacizumab," *Journal of surgical oncology*, vol. 91, no. 3, pp. 173–180, 2005.

[37] Cancer Research UK. (2019) Laser therapy. [Online]. Available: https://www.cancerresearchuk.org/about-cancer/lung-cancer/advanced/treatment/help-you-breathe/laser-therapy.

[38] C. J. Diederich, "Thermal ablation and high-temperature thermal therapy: overview of technology and clinical implementation," *International journal of hyperthermia*, vol. 21, no. 8, pp. 745–753, 2005.

[39] P. Lee, E. Kupeli, and A. C. Mehta, "Therapeutic bronchoscopy in lung cancer: laser therapy, electrocautery, brachytherapy, stents, and photodynamic therapy," *Clinics in chest medicine*, vol. 23, no. 1, pp. 241–256, 2002.

[40] P. Wust, B. Hildebrandt, G. Sreenivasa, B. Rau, J. Gellermann, H. Riess, R. Felix, and P. Schlag, "Hyperthermia in combined treatment of cancer," *The lancet oncology*, vol. 3, no. 8, pp. 487–497, 2002.

[41] I. Takahashi, Y. Emi, S. Hasuda, Y. Kakeji, Y. Maehara, and K. Sugimachi, "Clinical application of hyperthermia combined with anticancer drugs for the treatment of solid tumors," *Surgery*, vol. 131, no. 1, pp. S78–S84, 2002.

[42] R. A. Smith, A. C. von Eschenbach, R. Wender, B. Levin, T. Byers, D. Rothenberger, D. Brooks, W. Creasman, C. Cohen, C. Runowicz *et al.*, "American cancer society guidelines for the early detection of cancer: update of early detection guidelines for prostate, colorectal, and endometrial cancers: Also: update 2001testing for early lung cancer detection," *CA: a cancer journal for clinicians*, vol. 51, no. 1, pp. 38–75, 2001.

[43] S. D. Murgu, "Diagnosing and staging lung cancer involving the mediastinum," *Chest*, vol. 147, no. 5, pp. 1401–1412, 2015.

[44] K. Yasufuku, A. Pierre, G. Darling, M. de Perrot, T. Waddell, M. Johnston, G. da Cunha Santos, W. Geddie, S. Boerner, L. W. Le *et al.*, "A prospective controlled trial of endobronchial ultrasound-guided transbronchial needle aspiration compared with mediastinoscopy for mediastinal lymph node staging of lung cancer," *The Journal of thoracic and cardiovascular surgery*, vol. 142, no. 6, pp. 1393–1400, 2011.

[45] C. Gridelli, A. Rossi, D. P. Carbone, J. Guarize, N. Karachaliou, T. Mok, F. Petrella, L. Spaggiari, and R. Rosell, "Non-small-cell lung cancer," *Nature Reviews Disease Primers*, vol. 1, p. 15009, 2015.

[46] O. V. Salata, "Applications of nanoparticles in biology and medicine," *Journal of nanobiotechnology*, vol. 2, no. 1, p. 3, 2004.

[47] M. De, P. S. Ghosh, and V. M. Rotello, "Applications of nanoparticles in biology," *Advanced Materials*, vol. 20, no. 22, pp. 4225–4241, 2008.

[48] Y. Diebold and M. Calonge, "Applications of nanoparticles in ophthalmology," *Progress in retinal and eye research*, vol. 29, no. 6, pp. 596–609, 2010.

[49] S. Venkataraman, J. L. Hedrick, Z. Y. Ong, C. Yang, P. L. R. Ee, P. T. Hammond, and Y. Y. Yang, "The effects of polymeric nanostructure shape on drug delivery," *Advanced drug delivery reviews*, vol. 63, no. 14-15, pp. 1228–1246, 2011.

[50] W. J. Stark, P. R. Stoessel, W. Wohlleben, and A. Hafner, "Industrial applications of nanoparticles," *Chemical Society Reviews*, vol. 44, no. 16, pp. 5793–5805, 2015.

[51] J. Wang and J. Qiu, "A review of organic nanomaterials in photothermal cancer therapy," *Cancer Research Frontiers*, vol. 2, no. 1, pp. 67–84, 2016.

[52] M. Jesus and V. Grazu, *Nanobiotechnology: inorganic nanoparticles vs organic nanoparticles*. Elsevier, 2012, vol. 4.

[53] R. Kumar and S. Lal, "Synthesis of organic nanoparticles and their applications in drug delivery and food nanotechnology: A review," *Journal of Nanomaterials & Molecular Nanotechnology*, vol. 3, 2014.

[54] J. F. Lovell, C. S. Jin, E. Huynh, H. Jin, C. Kim, J. L. Rubinstein, W. C. Chan, W. Cao, L. V. Wang, and G. Zheng, "Porphysome nanovesicles generated by porphyrin bilayers for use as multimodal biophotonic contrast agents," *Nature materials*, vol. 10, no. 4, p. 324, 2011.

[55] J. Yao and L. V. Wang, "Photoacoustic tomography: fundamentals, advances and prospects," *Contrast media & molecular imaging*, vol. 6, no. 5, pp. 332–345, 2011.

[56] K. Yang, H. Xu, L. Cheng, C. Sun, J. Wang, and Z. Liu, "In vitro and in vivo near-infrared photothermal therapy of cancer using polypyrrole organic nanoparticles," *Advanced materials*, vol. 24, no. 41, pp. 5586–5592, 2012.

[57] Y. Yang, J. Liu, C. Liang, L. Feng, T. Fu, Z. Dong, Y. Chao, Y. Li, G. Lu, M. Chen *et al.*, "Nanoscale metal–organic particles with rapid clearance for magnetic resonance imaging-guided photothermal therapy," *ACS nano*, vol. 10, no. 2, pp. 2774–2781, 2016.

[58] Y. Jiang and K. Pu, "Advanced photoacoustic imaging applications of near-infrared absorbing organic nanoparticles," *Small*, vol. 13, no. 30, p. 1700710, 2017.

[59] Y. Lyu and K. Pu, "Recent advances of activatable molecular probes based on semiconducting polymer nanoparticles in sensing and imaging," *Advanced Science*, vol. 4, no. 6, p. 1600481, 2017.

[60] C. Xie, P. K. Upputuri, X. Zhen, M. Pramanik, and K. Pu, "Self-quenched semiconducting polymer nanoparticles for amplified in vivo photoacoustic imaging," *Biomaterials*, vol. 119, pp. 1–8, 2017.

[61] D. Jaque, C. Richard, B. Viana, K. Soga, X. Liu, and J. G. Solé, "Inorganic nanoparticles for optical bioimaging," *Advances in Optics and Photonics*, vol. 8, no. 1, pp. 1–103, 2016.

[62] S. M. Ng, M. Koneswaran, and R. Narayanaswamy, "A review on fluorescent inorganic nanoparticles for optical sensing applications," *Rsc Advances*, vol. 6, no. 26, pp. 21 624–21 661, 2016.

[63] K. Cherukula, K. Manickavasagam Lekshmi, S. Uthaman, K. Cho, C.-S. Cho, and I.-K. Park, "Multifunctional inorganic nanoparticles: Recent progress in thermal therapy and imaging," *Nanomaterials*, vol. 6, no. 4, p. 76, 2016.

[64] B. Hammer, J. Norskov *et al.*, "Why gold is the noblest of all the metals," *Nature*, vol. 376, no. 6537, pp. 238–240, 1995.

[65] P. Bernstein, *The Power of Gold: The History of an Obsession.* Wiley, 2000.

[66] J. Aaseth, M. Haugen, and Ø. Førre, "Rheumatoid arthritis and metal compounds-perspectives on the role of oxygen radical detoxification," *Analyst*, vol. 123, no. 1, pp. 3–6, 1998.

[67] W. F. Kean and I. R. L. Kean, "Clinical pharmacology of gold," *Inflammopharmacology*, vol. 16, no. 3, pp. 112–125, 2008.

[68] M. B. Cortie, "The weird world of nanoscale gold," *Gold Bulletin*, vol. 37, no. 1-2, pp. 12–19, 2004.

[69] N. N. Adnan, Y. Cheng, N. M. Ong, T. T. Kamaruddin, E. Rozlan, T. W. Schmidt, H. T. Duong, and C. Boyer, "Effect of gold nanoparticle shapes for phototherapy and drug delivery," *Polymer Chemistry*, vol. 7, no. 16, pp. 2888–2903, 2016.

[70] E. Connor, J. Mwamuka, A. Gole, C. Murphy, and M. Wyatt, "Gold nanoparticles are taken up by human cells but do not cause acute cytotoxicity," *Small*, vol. 1, no. 3, pp. 325–327, 2005.

[71] J. Khan, B. Pillai, T. Das, Y. Singh, and S. Maiti, "Molecular effects of uptake of gold nanoparticles in hela cells," *ChemBioChem*, vol. 8, no. 11, pp. 1237–1240, 2007.

[72] C. J. M. Nikhil R. Jana, Latha Gearheart, "Wet chemical synthesis of high aspect ratio cylindrical gold nanorods," *The Journal of Physical Chemistry B*, vol. 105, no. 19, pp. 4065–4067, 2001.

[73] Y. Zheng, X. Zhong, Z. Li, and Y. Xia, "Successive, seed-mediated growth for the synthesis of single-crystal gold nanospheres with uniform diameters controlled in the range of 5–150 nm," *Particle & Particle Systems Characterization*, vol. 31, no. 2, pp. 266–273, 2014.

[74] B. Nikoobakht, , and M. A. El-Sayed, "Preparation and growth mechanism of gold nanorods (nrs) using seed-mediated growth method," *Chemistry of Materials*, vol. 15, no. 10, pp. 1957–1962, 2003.

[75] T. S. Hauck, A. A. Ghazani, and W. C. Chan, "Assessing the effect of surface chemistry on gold nanorod uptake, toxicity, and gene expression in mammalian cells," *Small*, vol. 4, no. 1, pp. 153–159, 2008.

[76] A. M. Alkilany and C. J. Murphy, "Toxicity and cellular uptake of gold nanoparticles: what we have learned so far?" *Journal of Nanoparticle Research*, vol. 12, no. 7, pp. 2313–2333, 2010.

[77] A. P. Leonov, J. Zheng, J. D. Clogston, S. T. Stern, A. K. Patri, and A. Wei, "Detoxification of gold nanorods by treatment with polystyrenesulfonate," *ACS Nano*, vol. 2, no. 12, pp. 2481–2488, 2008.

[78] H. Takahashi, Y. Niidome, T. Niidome, K. Kaneko, H. Kawasaki, and S. Yamada, "Modification of gold nanorods using phosphatidylcholine to reduce cytotoxicity," *Langmuir*, vol. 22, no. 1, pp. 2–5, 2006.

[79] J. Kimling, M. Maier, B. Okenve, V. Kotaidis, H. Ballot, and A. Plech, "Turkevich method for gold nanoparticle synthesis revisited," *The Journal of Physical Chemistry B*, vol. 110, no. 32, pp. 15 700–15 707, 2006.

[80] J. Turkevich, P. C. Stevenson, and J. Hillier, "A study of the nucleation and growth processes in the synthesis of colloidal gold," *Discussions of the Faraday Society*, vol. 11, pp. 55–75, 1951.

[81] G. Frens, "Controlled nucleation for the regulation of the particle size in monodisperse gold suspensions," *Nature physical science*, vol. 241, no. 105, p. 20, 1973.

[82] J. G. Mehtala, D. Y. Zemlyanov, J. P. Max, N. Kadasala, S. Zhao, and A. Wei, "Citrate-stabilized gold nanorods," *Langmuir*, vol. 30, no. 46, pp. 13 727–13 730, 2014.

[83] C. J. Murphy, A. M. Gole, J. W. Stone, P. N. Sisco, A. M. Alkilany, E. C. Goldsmith, and S. C. Baxter, "Gold nanoparticles in biology: beyond toxicity to cellular imaging," *Accounts of chemical research*, vol. 41, no. 12, pp. 1721–1730, 2008.

[84] N. G. Basts, J. Comenge, and V. Puntes, "Kinetically controlled seeded growth synthesis of citrate-stabilized gold nanoparticles of up to 200 nm: Size focusing versus ostwald ripening," *Langmuir*, vol. 27, no. 17, pp. 11 098–11 105, 2011.

[85] V. Iswarya, J. Manivannan, A. De, S. Paul, R. Roy, J. Johnson, R. Kundu, N. Chandrasekaran, A. Mukherjee, and A. Mukherjee, "Surface capping and size-dependent toxicity of gold nanoparticles on different trophic levels," *Environmental Science and Pollution Research*, vol. 23, no. 5, pp. 4844–4858, 2016.

[86] J. Piella, N. G. Bastús, and V. Puntes, "Size-controlled synthesis of sub-10-nanometer citrate-stabilized gold nanoparticles and related optical properties." *Chemistry of Materials*, vol. 28, no. 4, pp. 1066–1075, 2016.

[87] M. A. Dobrovolskaia, A. K. Patri, J. Zheng, J. D. Clogston, N. Ayub, P. Aggarwal, B. W. Neun, J. B. Hall, and S. E. McNeil, "Interaction of colloidal gold nanoparticles with human blood: effects on particle size and analysis of plasma protein binding profiles," *Nanomedicine: Nanotechnology, Biology and Medicine*, vol. 5, no. 2, pp. 106–117, 2009.

[88] T. S. Hauck, A. A. Ghazani, and W. C. Chan, "Assessing the effect of surface chemistry on gold nanorod uptake, toxicity, and gene expression in mammalian cells," *Small*, vol. 4, no. 1, pp. 153–159, 2008.

[89] Y.-P. Jia, B.-Y. Ma, X.-W. Wei, and Z.-Y. Qian, "The in vitro and in vivo toxicity of gold nanoparticles," *Chinese Chemical Letters*, vol. 28, no. 4, pp. 691–702, 2017.

[90] C. Grabinski, N. Schaeublin, A. Wijaya, H. DCouto, S. H. Baxamusa, K. Hamad-Schifferli, and S. M. Hussain, "Effect of gold nanorod surface chemistry on cellular response," *ACS nano*, vol. 5, no. 4, pp. 2870–2879, 2011.

[91] K. Unfried, C. Albrecht, L.-O. Klotz, A. Von Mikecz, S. Grether-Beck, and R. P. Schins, "Cellular responses to nanoparticles: target structures and mechanisms," *Nanotoxicology*, vol. 1, no. 1, pp. 52–71, 2007.

[92] K. L. Aillon, Y. Xie, N. El-Gendy, C. J. Berkland, and M. L. Forrest, "Effects of nanomaterial physicochemical properties on in vivo toxicity," *Advanced drug delivery reviews*, vol. 61, no. 6, pp. 457–466, 2009.

[93] Y. Pan, A. Leifert, D. Ruau, S. Neuss, J. Bornemann, G. Schmid, W. Brandau, U. Simon, and W. Jahnen-Dechent, "Gold nanoparticles of diameter 1.4 nm trigger necrosis by oxidative stress and mitochondrial damage," *Small*, vol. 5, no. 18, pp. 2067–2076, 2009.

[94] S. K. Balasubramanian, J. Jittiwat, J. Manikandan, C.-N. Ong, E. Y. Liya, and W.-Y. Ong, "Biodistribution of gold nanoparticles and gene expression changes in the liver and spleen after intravenous administration in rats," *Biomaterials*, vol. 31, no. 8, pp. 2034–2042, 2010.

[95] Y.-C. Yeh, B. Creran, and V. M. Rotello, "Gold nanoparticles: preparation, properties, and applications in bionanotechnology," *Nanoscale*, vol. 4, no. 6, pp. 1871–1880, 2012.

[96] I. Peñuelas and P. H. Elsinga, "The clinical translation process in europe," in *Radiopharmaceutical Chemistry*. Springer, 2019, pp. 607–618.

[97] C. Li, D. Li, G. Wan, J. Xu, and W. Hou, "Facile synthesis of concentrated gold nanoparticles with low size-distribution in water: temperature and ph controls," *Nanoscale research letters*, vol. 6, no. 1, p. 440, 2011.

[98] Y. Sun and Y. Xia, "Shape-controlled synthesis of gold and silver nanoparticles," *Science*, vol. 298, no. 5601, pp. 2176–2179, 2002.

[99] J. Y. Song, H.-K. Jang, and B. S. Kim, "Biological synthesis of gold nanoparticles using magnolia kobus and diopyros kaki leaf extracts," *Process Biochemistry*, vol. 44, no. 10, pp. 1133–1138, 2009.

[100] R. Herizchi, E. Abbasi, M. Milani, and A. Akbarzadeh, "Current methods for synthesis of gold nanoparticles," *Artificial cells, nanomedicine, and biotechnology*, vol. 44, no. 2, pp. 596–602, 2016.

[101] C. Zou, B. Yang, D. Bin, J. Wang, S. Li, P. Yang, C. Wang, Y. Shiraishi, and Y. Du, "Electrochemical synthesis of gold nanoparticles decorated flower-like graphene for high sensitivity detection of nitrite," *Journal of colloid and interface science*, vol. 488, pp. 135–141, 2017.

[102] M. Sengani, A. M. Grumezescu, and V. D. Rajeswari, "Recent trends and methodologies in gold nanoparticle synthesis–a prospective review on drug delivery aspect," *OpenNano*, vol. 2, pp. 37–46, 2017.

[103] A. K. Salem, P. C. Searson, and K. W. Leong, "Multifunctional nanorods for gene delivery," *Nature materials*, vol. 2, no. 10, p. 668, 2003.

[104] T. Niidome, M. Yamagata, Y. Okamoto, Y. Akiyama, H. Takahashi, T. Kawano, Y. Katayama, and Y. Niidome, "Peg-modified gold nanorods with a stealth character for in vivo applications," *Journal of Controlled Release*, vol. 114, no. 3, pp. 343 – 347, 2006.

[105] A. M. Alkilany, P. K. Nagaria, C. R. Hexel, T. J. Shaw, C. J. Murphy, and M. D. Wyatt, "Cellular uptake and cytotoxicity of gold nanorods: molecular origin of cytotoxicity and surface effects," *small*, vol. 5, no. 6, pp. 701–708, 2009.

[106] L. Vigderman, P. Manna, and E. R. Zubarev, "Quantitative replacement of cetyl trimethylammonium bromide by cationic thiol ligands on the surface of gold nanorods and their extremely large uptake by cancer cells," *Angewandte Chemie International Edition*, vol. 51, no. 3, pp. 636–641, 2012.

[107] Y. Tang, Y. Shen, L. Huang, G. Lv, C. Lei, X. Fan, F. Lin, Y. Zhang, L. Wu, and Y. Yang, "In vitro cytotoxicity of gold nanorods in a549 cells," *Environmental toxicology and pharmacology*, vol. 39, no. 2, pp. 871–878, 2015.

[108] P. M. Favi, M. M. Valencia, P. R. Elliott, A. Restrepo, M. Gao, H. Huang, J. J. Pavon, and T. J. Webster, "Shape and surface chemistry effects on the cytotoxicity and cellular uptake of metallic nanorods and nanospheres," *Journal of Biomedical Materials Research Part A*, vol. 103, no. 12, pp. 3940–3955, 2015.

[109] B. B. Karakoçak, R. Raliya, J. T. Davis, S. Chavalmane, W.-N. Wang, N. Ravi, and P. Biswas, "Biocompatibility of gold nanoparticles in retinal pigment epithelial cell line," *Toxicology in Vitro*, vol. 37, pp. 61–69, 2016.

[110] H. Jiang, D. Chen, D. Guo, N. Wang, Y. Su, X. Jin, G. Tong, and X. Zhu, "Zwitterionic gold nanorods: low toxicity and high photothermal efficacy for cancer therapy," *Biomaterials science*, vol. 5, no. 4, pp. 686–697, 2017.

[111] W. L. Barnes, A. Dereux, and T. W. Ebbesen, "Surface plasmon subwavelength optics," *Nature*, vol. 424, pp. 824–, Aug. 2003.

[112] V. Amendola, R. Pilot, M. Frasconi, O. M. Maragò, and M. A. Iatì, "Surface plasmon resonance in gold nanoparticles: a review," *Journal of Physics: Condensed Matter*, vol. 29, no. 20, p. 203002, apr 2017.

[113] J. Perez-Juste, I. Pastoriza-Santos, L. M. Liz-Marzn, and P. Mulvaney, "Gold nanorods: Synthesis, characterization and applications," *Coordination Chemistry Reviews*, vol. 249, no. 1718, pp. 1870 – 1901, 2005.

[114] P. Biagioni, J.-S. Huang, and B. Hecht, "Nanoantennas for visible and infrared radiation," *Reports on Progress in Physics*, vol. 75, no. 2, p. 024402, jan 2012.

[115] X. Huang, I. H. El-Sayed, W. Qian, and M. A. El-Sayed, "Cancer cell imaging and photothermal therapy in the near-infrared region by using gold nanorods," *Journal of the American Chemical Society*, vol. 128, no. 6, pp. 2115–2120, 2006.

[116] X. Huang, S. Neretina, and M. A. El-Sayed, "Gold nanorods: From synthesis and properties to biological and biomedical applications," *Advanced Materials*, vol. 21, no. 48, pp. 4880–4910, 2009.

[117] E. Hutter and J. Fendler, "Exploitation of localized surface plasmon resonance," *Advanced Materials*, vol. 16, no. 19, pp. 1685–1706, 10 2004.

[118] I. Freestone, N. Meeks, M. Sax, and C. Higgitt, "The lycurgus cupa roman nanotechnology," *Gold bulletin*, vol. 40, no. 4, pp. 270–277, 2007.

[119] P. K. Jain, K. S. Lee, I. H. El-Sayed, and M. A. El-Sayed, "Calculated absorption and scattering properties of gold nanoparticles of different size, shape, and composition: applications in biological imaging and biomedicine," *The journal of physical chemistry B*, vol. 110, no. 14, pp. 7238–7248, 2006.

[120] S. Link, M. B. Mohamed, and M. A. El-Sayed, "Simulation of the optical absorption spectra of gold nanorods as a function of their aspect ratio and the effect of the medium dielectric constant," *The Journal of Physical Chemistry B*, vol. 103, no. 16, pp. 3073–3077, 1999.

[121] X. Huang and M. A. El-Sayed, "Gold nanoparticles: Optical properties and implementations in cancer diagnosis and photothermal therapy," *Journal of Advanced Research*, vol. 1, no. 1, pp. 13 – 28, 2010.

[122] A. N. Bashkatov, E. A. Genina, V. I. Kochubey, and V. V. Tuchin, "Optical properties of human skin, subcutaneous and mucous tissues in the wavelength range from 400 to 2000 nm," *Journal of Physics D: Applied Physics*, vol. 38, no. 15, p. 2543, 2005.

[123] S. L. Jacques, "Optical properties of biological tissues: a review," *Physics in Medicine and Biology*, vol. 58, no. 11, p. R37, 2013.

[124] R. Weissleder, "A clearer vision for in vivo imaging," *Nature biotechnology*, vol. 19, no. 4, pp. 316–316, 2001.

[125] A. M. Smith, M. C. Mancini, and S. Nie, "Second window for in vivo imaging," *Nature nanotechnology*, vol. 4, no. 11, pp. 710–711, Nov. 2009.

[126] V. Ntziachristos, A. Yodh, M. Schnall, and B. Chance, "Concurrent mri and diffuse optical tomography of breast after indocyanine green enhancement," *Proceedings of the National Academy of Sciences*, vol. 97, no. 6, pp. 2767–2772, 2000.

[127] M.-F. Tsai, S.-H. G. Chang, F.-Y. Cheng, V. Shanmugam, Y.-S. Cheng, C.-H. Su, and C.-S. Yeh, "Au nanorod design as light-absorber in the first and second biological near-infrared windows for in vivo photothermal therapy," *ACS nano*, vol. 7, no. 6, pp. 5330–5342, 2013.

[128] L. Vigderman, B. P. Khanal, and E. R. Zubarev, "Functional gold nanorods: Synthesis, self-assembly, and sensing applications," *Advanced Materials*, vol. 24, no. 36, pp. 4811–4841, 2012.

[129] H. Häkkinen, "The gold–sulfur interface at the nanoscale," *Nature chemistry*, vol. 4, no. 6, p. 443, 2012.

[130] S. Wilhelm, A. J. Tavares, Q. Dai, S. Ohta, J. Audet, H. F. Dvorak, and W. C. Chan, "Analysis of nanoparticle delivery to tumours," *Nature reviews materials*, vol. 1, no. 5, p. 16014, 2016.

[131] E. Blanco, H. Shen, and M. Ferrari, "Principles of nanoparticle design for overcoming biological barriers to drug delivery," *Nature biotechnology*, vol. 33, no. 9, p. 941, 2015.

[132] M. Ferrari, "Frontiers in cancer nanomedicine: directing mass transport through biological barriers," *Trends in biotechnology*, vol. 28, no. 4, pp. 181–188, 2010.

[133] A. M. Alkilany, L. B. Thompson, S. P. Boulos, P. N. Sisco, and C. J. Murphy, "Gold nanorods: their potential for photothermal therapeutics and drug delivery, tempered by the complexity of their biological interactions," *Advanced drug delivery reviews*, vol. 64, no. 2, pp. 190–199, 2012.

[134] D. Docter, D. Westmeier, M. Markiewicz, S. Stolte, S. Knauer, and R. Stauber, "The nanoparticle biomolecule corona: lessons learned–challenge accepted?" *Chemical Society Reviews*, vol. 44, no. 17, pp. 6094–6121, 2015.

[135] I. Lynch, T. Cedervall, M. Lundqvist, C. Cabaleiro-Lago, S. Linse, and K. A. Dawson, "The nanoparticle–protein complex as a biological entity; a complex fluids and surface science challenge for the 21st century," *Advances in colloid and interface science*, vol. 134, pp. 167–174, 2007.

[136] J. Liu and Q. Peng, "Protein-gold nanoparticle interactions and their possible impact on biomedical applications," *Acta biomaterialia*, vol. 55, pp. 13–27, 2017.

[137] Y. Akiyama, T. Mori, Y. Katayama, and T. Niidome, "The effects of peg grafting level and injection dose on gold nanorod biodistribution in the tumor-bearing mice," *Journal of Controlled Release*, vol. 139, no. 1, pp. 81–84, 2009.

[138] M. Lundqvist, J. Stigler, G. Elia, I. Lynch, T. Cedervall, and K. A. Dawson, "Nanoparticle size and surface properties determine the protein corona with possible implications for biological impacts," *Proceedings of the National Academy of Sciences*, vol. 105, no. 38, pp. 14 265–14 270, 2008.

[139] I. Lynch and K. A. Dawson, "Protein-nanoparticle interactions," *Nano today*, vol. 3, no. 1-2, pp. 40–47, 2008.

[140] I. Lynch, A. Salvati, and K. A. Dawson, "Protein-nanoparticle interactions: what does the cell see?" *Nature nanotechnology*, vol. 4, no. 9, p. 546, 2009.

[141] B. D. Chithrani and W. C. Chan, "Elucidating the mechanism of cellular uptake and removal of protein-coated gold nanoparticles of different sizes and shapes," *Nano letters*, vol. 7, no. 6, pp. 1542–1550, 2007.

[142] S. Vesaratchanon, A. Nikolov, and D. T. Wasan, "Sedimentation in nano-colloidal dispersions: effects of collective interactions and particle charge," *Advances in colloid and interface science*, vol. 134, pp. 268–278, 2007.

[143] A. S. Abdoon, E. A. Al-Ashkar, O. M. Kandil, A. M. Shaban, H. M. Khaled, M. A. El Sayed, M. M. El Shaer, A. H. Shaalan, W. H. Eisa, A. A. G. Eldin *et al.*, "Efficacy and toxicity of plasmonic photothermal therapy (pptt) using gold nanorods (gnrs) against mammary tumors in dogs and cats," *Nanomedicine: Nanotechnology, Biology and Medicine*, vol. 12, no. 8, pp. 2291–2297, 2016.

[144] J. D. Byrne, T. Betancourt, and L. Brannon-Peppas, "Active targeting schemes for nanoparticle systems in cancer therapeutics," *Advanced Drug Delivery Reviews*, vol. 60, no. 15, pp. 1615 – 1626, 2008.

[145] J. C. Forster, W. M. Harriss-Phillips, M. J. Douglass, and E. Bezak, "A review of the development of tumor vasculature and its effects on the tumor microenvironment," *Hypoxia (Auckland, N.Z.)*, vol. 5, pp. 21–32, Apr. 2017.

[146] Y. Matsumura and H. Maeda, "A new concept for macromolecular therapeutics in cancer chemotherapy: mechanism of tumoritropic accumulation of proteins and the antitumor agent smancs," *Cancer research*, vol. 46, no. 12 Part 1, pp. 6387–6392, 1986.

[147] A. K. Iyer, G. Khaled, J. Fang, and H. Maeda, "Exploiting the enhanced permeability and retention effect for tumor targeting," *Drug Discovery Today*, vol. 11, no. 1718, pp. 812 – 818, 2006.

[148] H. Maeda, "The enhanced permeability and retention (epr) effect in tumor vasculature: the key role of tumor-selective macromolecular drug targeting," *Advances in Enzyme Regulation*, vol. 41, no. 1, pp. 189 – 207, 2001.

[149] M. A. Phillips, M. L. Gran, and N. A. Peppas, "Targeted nanodelivery of drugs and diagnostics," *Nano today*, vol. 5, no. 2, pp. 143–159, Apr. 2010.

[150] A. J. Clark, D. T. Wiley, J. E. Zuckerman, P. Webster, J. Chao, J. Lin, Y. Yen, and M. E. Davis, "Crlx101 nanoparticles localize in human tumors and not in adjacent, nonneoplastic tissue after intravenous dosing," *Proceedings of the National Academy of Sciences*, vol. 113, no. 14, pp. 3850–3854, 2016.

[151] U. Prabhakar, H. Maeda, R. K. Jain, E. M. Sevick-Muraca, W. Zamboni, O. C. Farokhzad, S. T. Barry, A. Gabizon, P. Grodzinski, and D. C. Blakey, "Challenges and key considerations of the enhanced permeability and retention effect for nanomedicine drug delivery in oncology," 2013.

[152] W. Yang, H. Liang, S. Ma, D. Wang, and J. Huang, "Gold nanoparticle based photothermal therapy: Development and application for effective cancer treatment," *Sustainable Materials and Technologies*, 2019.

[153] S. Nie, "Understanding and overcoming major barriers in cancer nanomedicine," *Nanomedicine (London, England)*, vol. 5, no. 4, pp. 523–528, Jun. 2010.

[154] X. Qian, X.-H. Peng, D. O. Ansari, Q. Yin-Goen, G. Z. Chen, D. M. Shin, L. Yang, A. N. Young, M. D. Wang, and S. Nie, "In vivo tumor targeting and spectroscopic detection with surface-enhanced raman nanoparticle tags," *Nat Biotech*, vol. 26, no. 1, pp. 83–90, Jan. 2008.

[155] X. Huang, X. Peng, Y. Wang, Y. Wang, D. M. Shin, M. A. El-Sayed, and S. Nie, "A reexamination of active and passive tumor targeting by using rod-shaped gold nanocrystals and covalently conjugated peptide ligands," *ACS nano*, vol. 4, no. 10, pp. 5887–5896, 2010.

[156] L. V. Wang, "Multiscale photoacoustic microscopy and computed tomography," *Nature photonics*, vol. 3, no. 9, pp. 503–509, 2009.

[157] M. O. Oyewumi, R. A. Yokel, M. Jay, T. Coakley, and R. J. Mumper, "Comparison of cell uptake, biodistribution and tumor retention of folate-coated and peg-coated gadolinium nanoparticles in tumor-bearing mice," *Journal of Controlled Release*, vol. 95, no. 3, pp. 613 – 626, 2004.

[158] J. RK, "Transport of molecules, particles, and cells in solid tumors." *Annual Review Biomedical Engineering*, no. 1523-9829, pp. 241–63, 1999.

[159] X. Huang, I. H. El-Sayed, W. Qian, and M. A. El-Sayed, "Cancer cell imaging and photothermal therapy in the near-infrared region by using gold nanorods," *Journal of the American Chemical Society*, vol. 128, no. 6, pp. 2115–2120, 2006.

[160] R. S. Herbst and D. M. Shin, "Monoclonal antibodies to target epidermal growth factor receptor–positive tumors: a new paradigm for cancer therapy," *Cancer*, vol. 94, no. 5, pp. 1593–1611, 2002.

[161] L. Cheng, F.-Z. Huang, L.-F. Cheng, Y.-Q. Zhu, Q. Hu, L. Li, L. Wei, and D.-W. Chen, "Ge11-modified liposomes for non-small cell lung cancer targeting: preparation, ex vitro and in vivo evaluation," *International journal of nanomedicine*, vol. 9, p. 921, 2014.

[162] M. Zhang, H. S. Kim, T. Jin, and W. K. Moon, "Near-infrared photothermal therapy using egfr-targeted gold nanoparticles increases autophagic cell death in breast cancer," *Journal of Photochemistry and Photobiology B: Biology*, vol. 170, pp. 58–64, 2017.

[163] K. Liu, Y. Zheng, X. Lu, T. Thai, N. A. Lee, U. Bach, and J. J. Gooding, "Biocompatible gold nanorods: One-step surface functionalization, highly colloidal stability, and low cytotoxicity," *Langmuir*, vol. 31, no. 17, pp. 4973–4980, 2015.

[164] H. Moon, D. Kumar, H. Kim, C. Sim, J.-H. Chang, J.-M. Kim, H. Kim, and D.-K. Lim, "Amplified photoacoustic performance and enhanced photothermal stability of reduced graphene oxide coated gold nanorods for sensitive photoacoustic imaging," *ACS nano*, vol. 9, no. 3, pp. 2711–2719, 2015.

[165] C. Leng, X. Zhang, F. Xu, Y. Yuan, H. Pei, Z. Sun, L. Li, and Z. Bao, "Engineering gold nanorod–copper sulfide heterostructures with enhanced photothermal conversion efficiency and photostability," *Small*, vol. 14, no. 12, p. 1703077, 2018.

[166] J. A. Yang, H. T. Phan, S. Vaidya, and C. J. Murphy, "Nanovacuums: Nanoparticle uptake and differential cellular migration on a carpet of nanoparticles," *Nano Letters*, vol. 13, no. 5, pp. 2295–2302, 2013.

[167] E. Grzincic, J. Yang, J. Drnevich, P. Falagan-Lotsch, and C. Murphy, "Global transcriptomic analysis of model human cell lines exposed to surface-modified gold nanoparticles: The effect of surface chemistry," *Nanoscale*, vol. 7, no. 4, pp. 1349–1362, 2015.

[168] X. Feng, L. Sosa-Vargas, S. Umadevi, T. Mori, Y. Shimizu, and T. Hegmann, "Discotic liquid crystal-functionalized gold nanorods: 2-and 3d self-assembly and macroscopic alignment as well as increased charge carrier mobility in hexagonal columnar liquid crystal hosts affected by molecular packing and π–π interactions," *Advanced Functional Materials*, vol. 25, no. 8, pp. 1180–1192, 2015.

[169] N. D. Burrows, W. Lin, J. G. Hinman, J. M. Dennison, A. M. Vartanian, N. S. Abadeer, E. M. Grzincic, L. M. Jacob, J. Li, and C. J. Murphy, "Surface chemistry of gold nanorods," *Langmuir*, vol. 32, no. 39, pp. 9905–9921, 2016.

[170] A. Albanese, P. S. Tang, and W. C. Chan, "The effect of nanoparticle size, shape, and surface chemistry on biological systems," *Annual review of biomedical engineering*, vol. 14, pp. 1–16, 2012.

[171] L. M. Liz-Marzán, M. Giersig, and P. Mulvaney, "Synthesis of nanosized gold- silica core- shell particles," *Langmuir*, vol. 12, no. 18, pp. 4329–4335, 1996.

[172] S. Liu and M.-Y. Han, "Silica-coated metal nanoparticles," *Chemistry–An Asian Journal*, vol. 5, no. 1, pp. 36–45, 2010.

[173] S. Lal, S. E. Clare, and N. J. Halas, "Nanoshell-enabled photothermal cancer therapy: impending clinical impact," *Accounts of chemical research*, vol. 41, no. 12, pp. 1842–1851, 2008.

[174] Y.-S. Chen, W. Frey, S. Kim, P. Kruizinga, K. Homan, and S. Emelianov, "Silica-coated gold nanorods as photoacoustic signal nanoamplifiers," *Nano Letters*, vol. 11, no. 2, pp. 348–354, 2011.

[175] C. Hanske, M. N. Sanz-Ortiz, and L. M. Liz-Marzán, "Silica-coated plasmonic metal nanoparticles in action," *Advanced Materials*, vol. 30, no. 27, p. 1707003, 2018.

[176] S. Liu and M. Han, "Synthesis, functionalization, and bioconjugation of monodisperse, silica-coated gold nanoparticles: Robust bioprobes," *Advanced Functional Materials*, vol. 15, no. 6, pp. 961–967, 2005.

[177] W.-C. Wu and J. B. Tracy, "Large-scale silica overcoating of gold nanorods with tunable shell thicknesses," *Chemistry of Materials*, vol. 27, no. 8, pp. 2888–2894, 2015.

[178] G. Baffou and R. Quidant, "Thermo-plasmonics: using metallic nanostructures as nano-sources of heat," *Laser & Photonics Reviews*, vol. 7, no. 2, pp. 171–187, 2013.

[179] Y. Zhao, W. Liu, Y. Tian, Z. Yang, X. Wang, Y. Zhang, Y. Tang, S. Zhao, C. Wang, Y. Liu *et al.*, "Anti-egfr peptide-conjugated triangular gold nanoplates for computed tomography/photoacoustic imaging-guided photothermal therapy of non-small cell lung cancer," *ACS applied materials & interfaces*, vol. 10, no. 20, pp. 16 992–17 003, 2018.

[180] V. Z. V. Letokhov, *Laser Optoacoustic Spectroscopy*, 1st ed., ser. 37. Springer-Verlag Berlin Heidelberg, 1986.

[181] M. Xu and L. V. Wang, "Photoacoustic imaging in biomedicine," *Review of scientific instruments*, vol. 77, no. 4, p. 041101, 2006.

[182] P. Beard, "Biomedical photoacoustic imaging," *Interface Focus*, vol. 1, no. 4, pp. 602–631, May 2011.

[183] M. Xu and L. V. Wang, "Photoacoustic imaging in biomedicine," *Review of scientific instruments*, vol. 77, no. 4, p. 041101, 2006.

[184] L. V. Zhigilei and B. J. Garrison, "Microscopic mechanisms of laser ablation of organic solids in the thermal and stress confinement irradiation regimes," *Journal of Applied Physics*, vol. 88, no. 3, pp. 1281–1298, 2000.

[185] A. Taruttis and V. Ntziachristos, "Advances in real-time multispectral optoacoustic imaging and its applications," *Nature Photonics*, vol. 9, pp. 219–, Mar. 2015.

[186] L. R. McNally, M. Mezera, D. E. Morgan, P. J. Frederick, E. S. Yang, I.-E. Eltoum, and W. E. Grizzle, "Current and emerging clinical applications of multispectral optoacoustic tomography (msot) in oncology," *Clinical cancer research*, vol. 22, no. 14, pp. 3432–3439, 2016.

[187] G. Diot, S. Metz, A. Noske, E. Liapis, B. Schroeder, S. V. Ovsepian, R. Meier, E. Rummeny, and V. Ntziachristos, "Multispectral optoacoustic tomography (msot) of human breast cancer," *Clinical Cancer Research*, vol. 23, no. 22, pp. 6912–6922, 2017.

[188] F. Knieling, C. Neufert, A. Hartmann, J. Claussen, A. Urich, C. Egger, M. Vetter, S. Fischer, L. Pfeifer, A. Hagel *et al.*, "Multispectral optoacoustic tomography for assessment of crohns disease activity," *New England Journal of Medicine*, vol. 376, no. 13, pp. 1292–1294, 2017.

[189] Y. Wu, S. Huang, J. Wang, L. Sun, F. Zeng, and S. Wu, "Activatable probes for diagnosing and positioning liver injury and metastatic tumors by multispectral optoacoustic tomography," *Nature communications*, vol. 9, no. 1, p. 3983, 2018.

[190] G. P. Luke, D. Yeager, and S. Y. Emelianov, "Biomedical applications of photoacoustic imaging with exogenous contrast agents," *Annals of biomedical engineering*, vol. 40, no. 2, pp. 422–437, 2012.

[191] D. Wu, L. Huang, M. S. Jiang, and H. Jiang, "Contrast agents for photoacoustic and thermoacoustic imaging: A review," *International Journal of Molecular Sciences*, vol. 15, no. 12, p. 23616, 2014.

[192] J. Weber, P. C. Beard, and S. E. Bohndiek, "Contrast agents for molecular photoacoustic imaging," *Nature methods*, vol. 13, no. 8, p. 639, 2016.

[193] L. V. Wang and S. Hu, "Photoacoustic tomography: in vivo imaging from organelles to organs," *Science*, vol. 335, no. 6075, pp. 1458–1462, 2012.

[194] J. E. Lemaster and J. V. Jokerst, "What is new in nanoparticle-based photoacoustic imaging?" *WIREs Nanomed Nanobiotechnol*, vol. 9, no. 1, pp. e1404–, Apr. 2016.

[195] J. R. McLaughlan, R. A. Roy, H. Ju, and T. W. Murray, "Ultrasonic enhancement of photoacoustic emissions by nanoparticle-targeted cavitation," *Opt. Lett.*, vol. 35, no. 13, pp. 2127–2129, Jul 2010.

[196] M. Xu and L. V. Wang, "Universal back-projection algorithm for photoacoustic computed tomography," *Phys. Rev. E*, vol. 71, p. 016706, Jan 2005.

[197] V. Ntziachristos and D. Razansky, "Molecular imaging by means of multispectral optoacoustic tomography (msot)," *Chemical reviews*, vol. 110, no. 5, pp. 2783–2794, 2010.

[198] L. R. McNally, M. Mezera, D. E. Morgan, P. J. Frederick, E. S. Yang, I.-E. Eltoum, and W. E. Grizzle, "Current and emerging clinical applications of multispectral optoacoustic tomography (msot) in oncology," *Clinical Cancer Research*, vol. 22, no. 14, pp. 3432–3439, 2016.

[199] M. Schwarz, A. Buehler, J. Aguirre, and V. Ntziachristos, "Three-dimensional multispectral optoacoustic mesoscopy reveals melanin and blood oxygenation in human skin in vivo," *Journal of Biophotonics*, vol. 9, no. 1-2, pp. 55–60, 2016.

[200] A. Agarwal, S. W. Huang, M. O'Donnell, K. C. Day, M. Day, N. Kotov, and S. Ashkenazi, "Targeted gold nanorod contrast agent for prostate cancer detection by photoacoustic imaging," *Journal of Applied Physics*, vol. 102, no. 6, 2007.

[201] K. B. Bader, M. J. Crowe, J. L. Raymond, and C. K. Holland, "Effect of frequency-dependent attenuation on predicted histotripsy waveforms in tissue-mimicking phantoms," *Ultrasound in medicine & biology*, vol. 42, no. 7, pp. 1701–1705, 2016.

[202] *American National Standard for Safe Use of Lasers*, ANSI, American National Standards Institute Std., 2014.

[203] D. Jaque, L. Martinez Maestro, B. del Rosal, P. Haro-Gonzalez, A. Benayas, J. L. Plaza, E. Martin Rodriguez, and J. Garcia Sole, "Nanoparticles for photothermal therapies," *Nanoscale*, vol. 6, pp. 9494–9530, 2014.

[204] S. Jain, D. G. Hirst, and J. M. O'Sullivan, "Gold nanoparticles as novel agents for cancer therapy," *The British Journal of Radiology*, vol. 85, no. 1010, pp. 101–113, Jan. 2011.

[205] L. Tong, Y. Zhao, T. B. Huff, M. N. Hansen, A. Wei, and J.-X. Cheng, "Gold nanorods mediate tumor cell death by compromising membrane integrity," *Advanced Materials*, vol. 19, no. 20, pp. 3136–3141, 2007.

[206] X. Huang, B. Kang, W. Qian, M. A. Mackey, P. C. Chen, A. K. Oyelere, I. H. El-Sayed, and M. A. El-Sayed, "Comparative study of photothermolysis of cancer cells with nuclear-targeted or cytoplasm-targeted gold nanospheres: continuous wave or pulsed lasers," *Journal of Biomedical Optics*, vol. 15, no. 5, pp. 058 002–058 002–7, 2010.

[207] X. Huang and M. A. El-Sayed, "Plasmonic photo-thermal therapy (pptt)," *Alexandria Journal of Medicine*, vol. 47, no. 1, pp. 1–9, 2011.

[208] J. L. Roti Roti, "Cellular responses to hyperthermia (40–46 c): Cell killing and molecular events," *International Journal of hyperthermia*, vol. 24, no. 1, pp. 3–15, 2008.

[209] J. R. Melamed, R. S. Edelstein, and E. S. Day, "Elucidating the fundamental mechanisms of cell death triggered by photothermal therapy," *ACS nano*, vol. 9, no. 1, pp. 6–11, 2015.

[210] M. Pérez-Hernández, P. del Pino, S. G. Mitchell, M. Moros, G. Stepien, B. Pelaz, W. J. Parak, E. M. Gálvez, J. Pardo, and J. M. de la Fuente, "Dissecting the molecular mechanism of apoptosis during photothermal therapy using gold nanoprisms," *ACS nano*, vol. 9, no. 1, pp. 52–61, 2014.

[211] S. A. Sapareto and W. C. Dewey, "Thermal dose determination in cancer therapy," *International Journal of Radiation Oncology* Biology* Physics*, vol. 10, no. 6, pp. 787–800, 1984.

[212] P. X. Mouratidis, I. Rivens, J. Civale, R. Symonds-Tayler, and G. ter Haar, "Relationship between thermal dose and cell death for rapid ablative and slow hyperthermic heating," *International Journal of Hyperthermia*, pp. 1–15, 2019.

[213] R. S. Riley and E. S. Day, "Gold nanoparticle-mediated photothermal therapy: applications and opportunities for multimodal cancer treatment," *Wiley Interdisciplinary Reviews: Nanomedicine and Nanobiotechnology*, vol. 9, no. 4, p. e1449, 2017.

[214] L. C. Kennedy, L. R. Bickford, N. A. Lewinski, A. J. Coughlin, Y. Hu, E. S. Day, J. L. West, and R. A. Drezek, "A new era for cancer treatment: Gold-nanoparticle-mediated thermal therapies," *Small*, vol. 7, no. 2, pp. 169–183, 2011.

[215] T. S. Hauck, T. L. Jennings, T. Yatsenko, J. C. Kumaradas, and W. C. Chan, "Enhancing the toxicity of cancer chemotherapeutics with gold nanorod hyperthermia," *Advanced Materials*, vol. 20, no. 20, pp. 3832–3838, 2008.

[216] R. Paschotta, *Field Guide to Lasers*. SPIE Press Book, 2008.

[217] A. Siegman, *Lasers*. University Science Books, 1986.

[218] J. Han and Y. Li, *Lasers - Applications in Science and Industry*, K. Jakubczak, Ed. InTech, 2011.

[219] D. Harris-Birtill, M. Singh, Y. Zhou, A. Shah, P. Ruenraroengsak, M. E. Gallina, G. B. Hanna, A. E. Cass, A. E. Porter, J. Bamber *et al.*, "Gold nanorod reshaping in vitro and in vivo using a continuous wave laser," *PloS one*, vol. 12, no. 10, p. e0185990, 2017.

[220] S. Jain, D. Hirst, and J. O'sullivan, "Gold nanoparticles as novel agents for cancer therapy," *The British journal of radiology*, vol. 85, no. 1010, pp. 101–113, 2012.

[221] B. Niemann and S. Rohrbach, "Metabolically relevant cell biology–role of intracellular organelles for cardiac metabolism," in *The Scientist's Guide to Cardiac Metabolism*. Elsevier, 2016, pp. 19–38.

[222] C. P. Tanase, I. Ogrezeanu, and C. Badiu, "5 - apoptosis," in *Molecular Pathology of Pituitary Adenomas*, C. P. Tanase, I. Ogrezeanu, and C. Badiu, Eds. London: Elsevier, 2012, pp. 45 – 52.

[223] G. Kroemer, B. Dallaporta, and M. Resche-Rigon, "The mitochondrial death/life regulator in apoptosis and necrosis," *Annual review of physiology*, vol. 60, no. 1, pp. 619–642, 1998.

[224] Y. Kiraz, A. Adan, M. K. Yandim, and Y. Baran, "Major apoptotic mechanisms and genes involved in apoptosis," *Tumor Biology*, vol. 37, no. 7, pp. 8471–8486, 2016.

[225] A. S. Song, A. M. Najjar, and K. R. Diller, "Thermally induced apoptosis, necrosis, and heat shock protein expression in three-dimensional culture," *Journal of biomechanical engineering*, vol. 136, no. 7, p. 071006, 2014.

[226] Y. Zhang, X. Zhan, J. Xiong, S. Peng, W. Huang, R. Joshi, Y. Cai, Y. Liu, R. Li, K. Yuan *et al.*, "Temperature-dependent cell death patterns induced by functionalized gold nanoparticle photothermal therapy in melanoma cells," *Scientific reports*, vol. 8, no. 1, p. 8720, 2018.

[227] X. Huang, P. K. Jain, I. H. El-Sayed, and M. A. El-Sayed, "Determination of the minimum temperature required for selective photothermal destruction of cancer cells with the use of immunotargeted gold nanoparticles," *Photochemistry and photobiology*, vol. 82, no. 2, pp. 412–417, 2006.

[228] M. R. Ali, M. A. Rahman, Y. Wu, T. Han, X. Peng, M. A. Mackey, D. Wang, H. J. Shin, Z. G. Chen, H. Xiao *et al.*, "Efficacy, long-term toxicity, and mechanistic studies of gold nanorods photothermal therapy of cancer in xenograft mice," *Proceedings of the National Academy of Sciences*, vol. 114, no. 15, pp. E3110–E3118, 2017.

[229] C. M. Pitsillides, E. K. Joe, X. Wei, R. R. Anderson, and C. P. Lin, "Selective cell targeting with light-absorbing microparticles and nanoparticles," *Biophysical Journal*, vol. 84, no. 6, pp. 4023 – 4032, 2003.

[230] J. Zhong, L. Wen, S. Yang, L. Xiang, Q. Chen, and D. Xing, "Imaging-guided high-efficient photoacoustic tumor therapy with targeting gold nanorods," *Nanomedicine: Nanotechnology, Biology and Medicine*, vol. 11, no. 6, pp. 1499–1509, 2015.

[231] F. J. Herth, A. Ernst, R. Eberhardt, P. Vilmann, H. Dienemann, and M. Krasnik, "Endobronchial ultrasound-guided transbronchial needle aspiration of lymph nodes in the radiologically normal mediastinum," *European Respiratory Journal*, vol. 28, no. 5, pp. 910–914, 2006.

[232] C. Casadio, J. Guarize, S. Donghi, C. Di Tonno, C. Fumagalli, D. Vacirca, P. DellOrto, F. De Marinis, L. Spaggiari, G. Viale *et al.*, "Molecular testing for targeted therapy in advanced non–small cell lung cancer: suitability of endobronchial ultrasound transbronchial needle aspiration," *American journal of clinical pathology*, vol. 144, no. 4, pp. 629–634, 2015.

[233] M. Gomez and G. A. Silvestri, "Endobronchial ultrasound for the diagnosis and staging of lung cancer," *Proceedings of the American Thoracic Society*, vol. 6, no. 2, pp. 180–186, 2009.

[234] T. Balamugesh and F. Herth, "Endobronchial ultrasound: A new innovation in bronchoscopy," *Lung India: Official Organ of Indian Chest Society*, vol. 26, no. 1, p. 17, 2009.

[235] M. M. Vernon and M. B. Lewin, "Fetal and neonatal echocardiography," in *Avery's Diseases of the Newborn*. Elsevier, 2018, pp. 779–789.

[236] J.-M. Yang, C. Favazza, R. Chen, J. Yao, X. Cai, K. Maslov, Q. Zhou, K. K. Shung, and L. V. Wang, "Simultaneous functional photoacoustic and ultrasonic endoscopy of internal organs in vivo," *Nature Medicine*, vol. 18, pp. 1297–, Jul. 2012.

[237] N. Navani, M. Nankivell, D. R. Lawrence, S. Lock, H. Makker, D. R. Baldwin, R. J. Stephens, M. K. Parmar, S. G. Spiro, S. Morris *et al.*, "Lung cancer diagnosis and staging with endobronchial ultrasound-guided transbronchial needle aspiration compared with conventional approaches: an open-label, pragmatic, randomised controlled trial," *The Lancet Respiratory Medicine*, vol. 3, no. 4, pp. 282–289, 2015.

[238] Y.-S. Chen, W. Frey, S. Kim, K. Homan, P. Kruizinga, K. Sokolov, and S. Emelianov, "Enhanced thermal stability of silica-coated gold nanorods for photoacoustic imaging and image-guided therapy," *Opt. Express*, vol. 18, no. 9, pp. 8867–8878, 2010.

[239] W. Albrecht, T.-S. Deng, B. Goris, M. A. van Huis, S. Bals, and A. van Blaaderen, "Single particle deformation and analysis of silica-coated gold nanorods before and after femtosecond laser pulse excitation," *Nano letters*, vol. 16, no. 3, pp. 1818–1825, 2016.

[240] L. Cavigli, M. de Angelis, F. Ratto, P. Matteini, F. Rossi, S. Centi, F. Fusi, and R. Pini, "Size affects the stability of the photoacoustic conversion of gold nanorods," *The Journal of Physical Chemistry C*, vol. 118, no. 29, pp. 16 140–16 146, 2014.

[241] B. D. Chithrani, A. A. Ghazani, and W. C. Chan, "Determining the size and shape dependence of gold nanoparticle uptake into mammalian cells," *Nano letters*, vol. 6, no. 4, pp. 662–668, 2006.

[242] S. E. Gratton, P. A. Ropp, P. D. Pohlhaus, J. C. Luft, V. J. Madden, M. E. Napier, and J. M. DeSimone, "The effect of particle design on cellular internalization pathways," *Proceedings of the National Academy of Sciences*, vol. 105, no. 33, pp. 11 613–11 618, 2008.

[243] E. B. Dickerson, E. C. Dreaden, X. Huang, I. H. El-Sayed, H. Chu, S. Pushpanketh, J. F. McDonald, and M. A. El-Sayed, "Gold nanorod assisted near-infrared plasmonic photothermal therapy (pptt) of squamous cell carcinoma in mice," *Cancer letters*, vol. 269, no. 1, pp. 57–66, 2008.

[244] B. Kang, Y. Dai, S. Chang, and D. Chen, "Explosion of single-walled carbon nanotubes in suspension induced by a large photoacoustic effect," *Carbon*, vol. 6, no. 46, pp. 978–981, 2008.

[245] B. Kang, D. Yu, Y. Dai, S. Chang, D. Chen, and Y. Ding, "Cancer-cell targeting and photoacoustic therapy using carbon nanotubes as bomb agents," *Small*, vol. 5, no. 11, pp. 1292–1301, 2009.

[246] F. Zhou, S. Wu, Y. Yuan, W. R. Chen, and D. Xing, "Mitochondria-targeting photoacoustic therapy using single-walled carbon nanotubes," *Small*, vol. 8, no. 10, pp. 1543–1550, 2012.

[247] J. Zhong, S. Yang, X. Zheng, T. Zhou, and D. Xing, "In vivo photoacoustic therapy with cancer-targeted indocyanine green-containing nanoparticles," *Nanomedicine*, vol. 8, no. 6, pp. 903–919, 2013.

[248] B. Yan and H. Qin, "Indocyanine green loaded graphene oxide for high-efficient photoacoustic tumor therapy," *Journal of Innovative Optical Health Sciences*, vol. 9, no. 04, p. 1642001, 2016.

[249] J. Zhong, S. Yang, L. Wen, and D. Xing, "Imaging-guided photoacoustic drug release and synergistic chemo-photoacoustic therapy with paclitaxel-containing nanoparticles," *Journal of controlled release*, vol. 226, pp. 77–87, 2016.

[250] J. Zhong, S. Yang, and D. Xing, "Photoacoustic therapy using perfluorohexane-containing nanoparticles," in *2016 Asia Communications and Photonics Conference (ACP)*. IEEE, 2016, pp. 1–3.

[251] L. Du, H. Qin, T. Ma, T. Zhang, and D. Xing, "In vivo imaging-guided photothermal/photoacoustic synergistic therapy with bioorthogonal metabolic glycoengineering-activated tumor targeting nanoparticles," *ACS nano*, vol. 11, no. 9, pp. 8930–8943, 2017.

[252] M. Zhou, B. Singhana, Y. Liu, Q. Huang, T. Mitcham, M. J. Wallace, R. J. Stafford, R. R. Bouchard, and M. P. Melancon, "Photoacoustic-and magnetic resonance-guided photothermal therapy and tumor vasculature visualization using theranostic magnetic gold nanoshells," *Journal of biomedical nanotechnology*, vol. 11, no. 8, pp. 1442–1450, 2015.

[253] T. Patino, U. Mahajan, R. Palankar, N. Medvedev, J. Walowski, M. Münzenberg, J. Mayerle, and M. Delcea, "Multifunctional gold nanorods for selective plasmonic photothermal therapy in pancreatic cancer cells using ultra-short pulse near-infrared laser irradiation," *Nanoscale*, vol. 7, no. 12, pp. 5328–5337, 2015.

[254] R. Hou, T. Le, S. D. Murgu, Z. Chen, and M. Brenner, "Recent advances in optical coherence tomography for the diagnoses of lung disorders," *Expert review of respiratory medicine*, vol. 5, no. 5, pp. 711–724, 2011.

[255] R. G. Kolkman, P. J. Brands, W. Steenbergen, and T. G. van Leeuwen, "Real-time in vivo photoacoustic and ultrasound imaging," *Journal of biomedical optics*, vol. 13, no. 5, p. 050510, 2008.

[256] T. Harrison, J. C. Ranasinghesagara, H. Lu, K. Mathewson, A. Walsh, and R. J. Zemp, "Combined photoacoustic and ultrasound biomicroscopy," *Optics express*, vol. 17, no. 24, pp. 22 041–22 046, 2009.

[257] J. J. Niederhauser, M. Jaeger, R. Lemor, P. Weber, and M. Frenz, "Combined ultrasound and optoacoustic system for real-time high-contrast vascular imaging in vivo," *IEEE transactions on medical imaging*, vol. 24, no. 4, pp. 436–440, 2005.

[258] A. Bouhelier, R. Bachelot, G. Lerondel, S. Kostcheev, P. Royer, and G. P. Wiederrecht, "Surface plasmon characteristics of tunable photoluminescence in single gold nanorods," *Phys. Rev. Lett.*, vol. 95, p. 267405, Dec 2005.

[259] Y. Huang, K. Xia, N. He, Z. Lu, L. Zhang, Y. Deng, and L. Nie, "Size-tunable synthesis of gold nanorods using pyrogallol as a reducing agent," *Science China Chemistry*, vol. 58, no. 11, pp. 1759–1765, 2015.

[260] Y.-Y. Yu, S.-S. Chang, C.-L. Lee, and C. C. Wang, "Gold nanorods: electrochemical synthesis and optical properties," *The Journal of Physical Chemistry B*, vol. 101, no. 34, pp. 6661–6664, 1997.

[261] V. Sharma, K. Park, and M. Srinivasarao, "Colloidal dispersion of gold nanorods: Historical background, optical properties, seed-mediated synthesis, shape separation and self-assembly," *Materials Science and Engineering: R: Reports*, vol. 65, no. 1, pp. 1–38, 2009.

[262] G. Zhang, Z. Yang, W. Lu, R. Zhang, Q. Huang, M. Tian, L. Li, D. Liang, and C. Li, "Influence of anchoring ligands and particle size on the colloidal stability and in vivo biodistribution of polyethylene glycol-coated gold nanoparticles in tumor-xenografted mice," *Biomaterials*, vol. 30, no. 10, pp. 1928–1936, 2009.

[263] F. Kim, J. H. Song, and P. Yang, "Photochemical synthesis of gold nanorods," *Journal of the American Chemical Society*, vol. 124, no. 48, pp. 14 316–14 317, 2002.

[264] L. Uson, V. Sebastian, M. Arruebo, and J. Santamaria, "Continuous microfluidic synthesis and functionalization of gold nanorods," *Chemical Engineering Journal*, vol. 285, pp. 286 – 292, 2016.

[265] D. Pissuwan, S. M. Valenzuela, C. M. Miller, and M. B. Cortie, "A golden bullet? selective targeting of toxoplasma gondii tachyzoites using antibody-functionalized gold nanorods," *Nano letters*, vol. 7, no. 12, pp. 3808–3812, 2007.

[266] A. M. Alkilany, P. K. Nagaria, C. R. Hexel, T. J. Shaw, C. J. Murphy, and M. D. Wyatt, "Cellular uptake and cytotoxicity of gold nanorods: Molecular origin of cytotoxicity and surface effects," *Small*, vol. 5, no. 6, pp. 701–708, 2009.

[267] W. I. Choi, J.-Y. Kim, C. Kang, C. C. Byeon, Y. H. Kim, and G. Tae, "Tumor regression in vivo by photothermal therapy based on gold-nanorod-loaded, functional nanocarriers," *ACS Nano*, vol. 5, no. 3, pp. 1995–2003, 2011.

[268] W. I. Choi, A. Sahu, Y. H. Kim, and G. Tae, "Photothermal cancer therapy and imaging based on gold nanorods," *Annals of biomedical engineering*, vol. 40, no. 2, pp. 534–546, 2012.

[269] W. Cai, T. Gao, H. Hong, and J. Sun, "Applications of gold nanoparticles in cancer nanotechnology," *Nanotechnology, science and applications*, vol. 2008, no. 1, pp. 17–32, Sep. 2008.

[270] T. B. Huff, L. Tong, Y. Zhao, M. N. Hansen, J.-X. Cheng, and A. Wei, "Hyperthermic effects of gold nanorods on tumor cells," *Nanomedicine*, vol. 2, no. 1, pp. 125–132, Feb. 2007.

[271] E. Boisselier and D. Astruc, "Gold nanoparticles in nanomedicine: preparations, imaging, diagnostics, therapies and toxicity," *Chemical society reviews*, vol. 38, no. 6, pp. 1759–1782, 2009.

[272] S. L. Jacques, "Corrigendum: Optical properties of biological tissues: a review," *Physics in Medicine and Biology*, vol. 58, no. 14, p. 5007, 2013.

[273] ——, "Coupling 3d monte carlo light transport in optically heterogeneous tissues to photoacoustic signal generation," *Photoacoustics*, vol. 2, no. 4, pp. 137–142, Dec. 2014.

[274] M. L. Palmeri and K. R. Nightingale, "On the thermal effects associated with radiation force imaging of soft tissue," *IEEE Transactions on Ultrasonics, Ferroelectrics, and Frequency Control*, vol. 51, no. 5, pp. 551–565, May 2004.

[275] S. Link and M. A. El-Sayed, "Size and temperature dependence of the plasmon absorption of colloidal gold nanoparticles," *The Journal of Physical Chemistry B*, vol. 103, no. 21, pp. 4212–4217, 1999.

[276] P. K. Jain, K. S. Lee, I. H. El-Sayed, M. A. El-Sayed *et al.*, "Calculated absorption and scattering properties of gold nanoparticles of different size, shape, and composition: applications in biological imaging and biomedicine," *Journal of Physical Chemistry B*, vol. 110, no. 14, p. 7238, 2006.

[277] S. Ye, G. Marston, J. R. McLaughlan, D. O. Sigle, N. Ingram, S. Freear, J. J. Baumberg, R. J. Bushby, A. F. Markham, K. Critchley, P. L. Coletta, and S. D. Evans, "Theranostics: Engineering gold nanotubes with controlled length and near-infrared absorption for theranostic applications," *Advanced Functional Materials*, vol. 25, no. 14, pp. 2204–2204, 2015.

[278] S. Link, M. Mohamed, and M. El-Sayed, "Simulation of the optical absorption spectra of gold nanorods as a function of their aspect ratio and the effect of the medium dielectric constant," *Journal of Physical Chemistry B*, vol. 103, no. 16, pp. 3073–3077, 1999.

[279] S. Link and M. El-Sayed, "Erratum: Simulation of the optical absorption spectra of gold nanorods as a function of their aspect ratio and the effect of the medium dielectric constant," *Journal of Physical Chemistry B*, vol. 109, no. 20, pp. 10 531–10 532, 2005.

[280] G. P. Luke, D. Yeager, and S. Y. Emelianov, "Biomedical applications of photoacoustic imaging with exogenous contrast agents," *Annals of Biomedical Engineering*, vol. 40, no. 2, pp. 422–437, 2012.

[281] S. Jain, D. G. Hirst, and J. M. O'Sullivan, "Gold nanoparticles as novel agents for cancer therapy," *The British Journal of Radiology*, vol. 85, no. 1010, pp. 101–113, Feb. 2012.

[282] X. Liu, N. Huang, H. Li, Q. Jin, and J. Ji, "Surface and size effects on cell interaction of gold nanoparticles with both phagocytic and nonphagocytic cells," *Langmuir*, vol. 29, no. 29, pp. 9138–9148, Jul. 2013.

[283] N. Lewinski, V. Colvin, and R. Drezek, "Cytotoxicity of nanoparticles," *Small*, vol. 4, no. 1, pp. 26–49, 2008.

[284] R. Zou, Q. Zhang, Q. Zhao, F. Peng, H. Wang, H. Yu, and J. Yang, "Thermal stability of gold nanorods in an aqueous solution," *Colloids and Surfaces A: Physicochemical and Engineering Aspects*, vol. 372, no. 13, pp. 177 – 181, 2010.

[285] C. Ungureanu, R. Kroes, W. Petersen, T. A. M. Groothuis, F. Ungureanu, H. Janssen, F. W. B. van Leeuwen, R. P. H. Kooyman, S. Manohar, and T. G. van Leeuwen, "Light interactions with gold nanorods and cells: Implications for photothermal nanotherapeutics," *Nano Lett.*, vol. 11, no. 5, pp. 1887–1894, May 2011.

[286] A. B. Taylor, A. M. Siddiquee, and J. W. M. Chon, "Below melting point photothermal reshaping of single gold nanorods driven by surface diffusion," *ACS Nano*, vol. 8, no. 12, pp. 12 071–12 079, Dec. 2014.

[287] E. Hysi, D. Dopsa, and M. C. Kolios, "Photoacoustic radio-frequency spectroscopy (pa-rfs): A technique for monitoring absorber size and concentration," in *SPIE BiOS*. International Society for Optics and Photonics, 2013, pp. 85 813W–85 813W.

[288] V. G. Andreev, A. A. Karabutov, and A. A. Oraevsky, "Detection of ultrawide-band ultrasound pulses in optoacoustic tomography," *IEEE Transactions on Ultrasonics, Ferroelectrics, and Frequency Control*, vol. 50, no. 10, pp. 1383–1390, Oct 2003.

[289] Z. Sheng, L. Song, J. Zheng, D. Hu, M. He, M. Zheng, G. Gao, P. Gong, P. Zhang, Y. Ma, and L. Cai, "Protein-assisted fabrication of nano-reduced graphene oxide for combined invivo photoacoustic imaging and photothermal therapy," *Biomaterials*, vol. 34, no. 21, pp. 5236 – 5243, 2013.

[290] M. Eghtedari, A. Oraevsky, J. A. Copland, N. A. Kotov, A. Conjusteau, and M. Motamedi, "High sensitivity of in vivo detection of gold nanorods using a laser optoacoustic imaging system," *Nano Lett.*, vol. 7, no. 7, pp. 1914–1918, Jul. 2007.

[291] J. Wang, T. Liu, S. Jiao, R. Chen, Q. Zhou, K. K. Shung, L. V. Wang, and H. F. Zhang, "Saturation effect in functional photoacoustic imaging," *Journal of Biomedical Optics*, vol. 15, no. 2, pp. 021 317–, Dec. 2010.

[292] C. A. Schneider, W. S. Rasband, and K. W. Eliceiri, "Nih image to imagej: 25 years of image analysis," *Nature Methods*, vol. 9, pp. 671–, Jun. 2012.

[293] J. van Meerloo, G. J. L. Kaspers, and J. Cloos, *Cell Sensitivity Assays: The MTT Assay.* Totowa, NJ: Humana Press, 2011, pp. 237–245.

[294] M. V. Berridge, P. M. Herst, and A. S. Tan, "Tetrazolium dyes as tools in cell biology: new insights into their cellular reduction," *Biotechnology annual review*, vol. 11, pp. 127–152, 2005.

[295] V. Patravale, P. Dandekar, and R. Jain, "Nanotoxicology: evaluating toxicity potential of drug-nanoparticles," pp. 123–155, 2012.

[296] National Health Service (NHS). (2019, March) Lung cancer: Overview.

[297] S.-q. Feng, G.-j. Wang, J.-w. Zhang, Y. Xie, R.-b. Sun, F. Fei, J.-q. Huang, Y. Wang, J.-y. Aa, and F. Zhou, "Combined treatment with apatinib and docetaxel in a549 xenograft mice and its cellular pharmacokinetic basis," *Acta Pharmacologica Sinica*, vol. 39, no. 10, p. 1670, 2018.

[298] F. Zhang, S. Wang, L. Yin, Y. Yang, Y. Guan, W. Wang, H. Xu, and N. Tao, "Quantification of epidermal growth factor receptor expression level and binding kinetics on cell surfaces by surface plasmon resonance imaging," *Analytical chemistry*, vol. 87, no. 19, pp. 9960–9965, 2015.

[299] Y. Chang, S.-T. Yang, J.-H. Liu, E. Dong, Y. Wang, A. Cao, Y. Liu, and H. Wang, "In vitro toxicity evaluation of graphene oxide on a549 cells," *Toxicology letters*, vol. 200, no. 3, pp. 201–210, 2011.

[300] R. Foldbjerg, D. A. Dang, and H. Autrup, "Cytotoxicity and genotoxicity of silver nanoparticles in the human lung cancer cell line, a549," *Archives of toxicology*, vol. 85, no. 7, pp. 743–750, 2011.

[301] M. Sathishkumar, S. Pavagadhi, A. Mahadevan, and R. Balasubramanian, "Biosynthesis of gold nanoparticles and related cytotoxicity evaluation using a549 cells," *Ecotoxicology and environmental safety*, vol. 114, pp. 232–240, 2015.

[302] X. L. Deán-Ben and D. Razansky, "On the link between the speckle free nature of optoacoustics and visibility of structures in limited-view tomography," *Photoacoustics*, vol. 4, no. 4, pp. 133–140, 2016.

[303] Y.-S. Chen, Y. Zhao, S. J. Yoon, S. S. Gambhir, and S. Emelianov, "Miniature gold nanorods for photoacoustic molecular imaging in the second near-infrared optical window," *Nature Nanotechnology*, pp. –, 2019.

[304] A. Albanese and W. C. Chan, "Effect of gold nanoparticle aggregation on cell uptake and toxicity," *ACS nano*, vol. 5, no. 7, pp. 5478–5489, 2011.

[305] E.-S. A. Al-Sherbini, "Uv–visible light reshaping of gold nanorods," *Materials chemistry and physics*, vol. 121, no. 1-2, pp. 349–353, 2010.

[306] S. Link, Z. L. Wang, and M. A. El-Sayed, "How does a gold nanorod melt?" *J. Phys. Chem. B*, vol. 104, no. 33, pp. 7867–7870, Aug. 2000.

[307] G. Gonzlez-Rubio, A. Guerrero-Martnez, and L. M. Liz-Marzn, "Reshaping, fragmentation, and assembly of gold nanoparticles assisted by pulse lasers," *Acc. Chem. Res.*, vol. 49, no. 4, pp. 678–686, Apr. 2016.

[308] K. Koga, T. Ikeshoji, and K.-i. Sugawara, "Size-and temperature-dependent structural transitions in gold nanoparticles," *Physical review letters*, vol. 92, no. 11, p. 115507, 2004.

[309] G. Gonzlez-Rubio, P. Daz-Nez, A. Rivera, A. Prada, G. Tardajos, J. Gonzlez-Izquierdo, L. Baares, P. Llombart, L. G. Macdowell, M. Alcolea Palafox, L. M. Liz-Marzn, O. Pea-Rodrguez, and A. Guerrero-Martnez, "Femtosecond laser reshaping yields gold nanorods with ultranarrow surface plasmon resonances," *Science*, vol. 358, no. 6363, pp. 640–, Nov. 2017.

[310] G. Cardillo, "Four parameters logistic regression - there and back again," 2012.

[311] Z. Li, S. Tang, B. Wang, Y. Li, H. Huang, H. Wang, P. Li, C. Li, P. K. Chu, and X.-F. Yu, "Metabolizable small gold nanorods: Size-dependent cytotoxicity, cell uptake and in vivo biodistribution," *ACS Biomaterials Science & Engineering*, vol. 2, no. 5, pp. 789–797, May 2016.

[312] I. H. El-Sayed, X. Huang, and M. A. El-Sayed, "Selective laser photo-thermal therapy of epithelial carcinoma using anti-egfr antibody conjugated gold nanoparticles," *Cancer letters*, vol. 239, no. 1, pp. 129–135, 2006.

[313] A. Oto, I. Sethi, G. Karczmar, R. McNichols, M. K. Ivancevic, W. M. Stadler, S. Watson, and S. Eggener, "Mr imaging–guided focal laser ablation for prostate cancer: phase i trial," *Radiology*, vol. 267, no. 3, pp. 932–940, 2013.

[314] Q. Zhao, G. Tian, F. Chen, L. Zhong, and T. Jiang, "Ct-guided percutaneous laser ablation of metastatic lung cancer: three cases report and literature review," *Oncotarget*, vol. 8, no. 2, p. 2187, 2017.

[315] X. Huang, W. Qian, I. H. El-Sayed, and M. A. El-Sayed, "The potential use of the enhanced nonlinear properties of gold nanospheres in photothermal cancer therapy," *Lasers in Surgery and Medicine: The Official Journal of the American Society for Laser Medicine and Surgery*, vol. 39, no. 9, pp. 747–753, 2007.

[316] Z. Qin and J. C. Bischof, "Thermophysical and biological responses of gold nanoparticle laser heating," *Chemical Society Reviews*, vol. 41, no. 3, pp. 1191–1217, 2012.

[317] J. D. Hazle, C. J. Diederich, M. Kangasniemi, R. E. Price, L. E. Olsson, and R. J. Stafford, "Mri-guided thermal therapy of transplanted tumors in the canine prostate using a directional transurethral ultrasound applicator," *Journal of Magnetic Resonance Imaging: An Official Journal of the International Society for Magnetic Resonance in Medicine*, vol. 15, no. 4, pp. 409–417, 2002.

[318] S. D. Prionas, M. A. Taylor, L. F. Fajardo, N. I. Kelly, T. S. Nelsen, and G. M. Hahn, "Thermal sensitivity to single and double heat treatments in normal canine liver," *Cancer research*, vol. 45, no. 10, pp. 4791–4797, 1985.

[319] M. W. Dewhirst, B. Viglianti, M. Lora-Michiels, M. Hanson, and P. Hoopes, "Basic principles of thermal dosimetry and thermal thresholds for tissue damage from hyperthermia," *International journal of hyperthermia*, vol. 19, no. 3, pp. 267–294, 2003.

[320] M. Dewhirst, B. L. Viglianti, M. Lora-Michiels, P. J. Hoopes, and M. A. Hanson, "Thermal dose requirement for tissue effect: experimental and clinical findings," in *Thermal Treatment of Tissue: Energy Delivery and Assessment II*, vol. 4954. International Society for Optics and Photonics, 2003, pp. 37–58.

[321] R. K. Jain and T. Stylianopoulos, "Delivering nanomedicine to solid tumors," *Nature reviews Clinical oncology*, vol. 7, no. 11, p. 653, 2010.

[322] L. Brannon-Peppas and J. O. Blanchette, "Nanoparticle and targeted systems for cancer therapy," *Advanced drug delivery reviews*, vol. 64, pp. 206–212, 2012.

[323] V. P. Chauhan, T. Stylianopoulos, J. D. Martin, Z. Popović, O. Chen, W. S. Kamoun, M. G. Bawendi, D. Fukumura, and R. K. Jain, "Normalization of tumour blood vessels improves the delivery of nanomedicines in a size-dependent manner," *Nature nanotechnology*, vol. 7, no. 6, p. 383, 2012.

[324] V. Zharov, R. Letfullin, and E. Galitovskaya, "Microbubbles-overlapping mode for laser killing of cancer cells with absorbing nanoparticle clusters," *Journal of Physics D: Applied Physics*, vol. 38, no. 15, p. 2571, 2005.

[325] C. Kinnear, L. Rodriguez-Lorenzo, M. Clift, B. Goris, S. Bals, B. Rothen-Rutishauser, and A. Petri-Fink, "Decoupling the shape parameter to assess gold nanorod uptake by mammalian cells," *Nanoscale*, vol. 8, no. 36, pp. 16 416–16 426, 2016.

[326] S. Behzadi, V. Serpooshan, W. Tao, M. A. Hamaly, M. Y. Alkawareek, E. C. Dreaden, D. Brown, A. M. Alkilany, O. C. Farokhzad, and M. Mahmoudi, "Cellular uptake of nanoparticles: journey inside the cell," *Chemical Society Reviews*, vol. 46, no. 14, pp. 4218–4244, 2017.

[327] H. Gao, W. Shi, and L. B. Freund, "Mechanics of receptor-mediated endocytosis," *Proceedings of the National Academy of Sciences*, vol. 102, no. 27, pp. 9469–9474, 2005.

[328] F. Danhier, "To exploit the tumor microenvironment: Since the epr effect fails in the clinic, what is the future of nanomedicine?" *Journal of Controlled Release*, vol. 244, pp. 108–121, 2016.

[329] W. Ahmed, A. Elhissi, V. Dhanak, and K. Subramani, "Carbon nanotubes: Applications in cancer therapy and drug delivery research," in *Emerging Nanotechnologies in Dentistry*. Elsevier, 2018, pp. 371–389.

[330] A. Jemal, F. Bray, M. M. Center, J. Ferlay, E. Ward, and D. Forman, "Global cancer statistics," *CA: a cancer journal for clinicians*, vol. 61, no. 2, pp. 69–90, 2011.

[331] H. Sorger, E. F. Hofstad, T. Amundsen, T. Langø, and H. O. Leira, "A novel platform for electromagnetic navigated ultrasound bronchoscopy (ebus)," *International journal of computer assisted radiology and surgery*, vol. 11, no. 8, pp. 1431–1443, 2016.

[332] B. D. Van Veen and K. M. Buckley, "Beamforming: A versatile approach to spatial filtering," *IEEE assp magazine*, vol. 5, no. 2, pp. 4–24, 1988.

[333] P. Viswanath, D. N. C. Tse, and R. Laroia, "Opportunistic beamforming using dumb antennas," in *Proceedings IEEE International Symposium on Information Theory,*. IEEE, 2002, p. 449.

[334] S. H. C. Ortiz, T. Chiu, and M. D. Fox, "Ultrasound image enhancement: A review," *Biomedical Signal Processing and Control*, vol. 7, no. 5, pp. 419–428, 2012.

[335] R. Mucci, "A comparison of efficient beamforming algorithms," *IEEE Transactions on Acoustics, Speech, and Signal Processing*, vol. 32, no. 3, pp. 548–558, 1984.

[336] G. Matrone, A. S. Savoia, G. Caliano, and G. Magenes, "The delay multiply and sum beamforming algorithm in ultrasound b-mode medical imaging," *IEEE transactions on medical imaging*, vol. 34, no. 4, pp. 940–949, 2015.

[337] G. Montaldo, M. Tanter, J. Bercoff, N. Benech, and M. Fink, "Coherent plane-wave compounding for very high frame rate ultrasonography and transient elastography," *IEEE transactions on ultrasonics, ferroelectrics, and frequency control*, vol. 56, no. 3, pp. 489–506, 2009.

[338] J.-F. Synnevag, A. Austeng, and S. Holm, "Benefits of minimum-variance beamforming in medical ultrasound imaging," *IEEE transactions on ultrasonics, ferroelectrics, and frequency control*, vol. 56, no. 9, pp. 1868–1879, 2009.

[339] A. Austeng, C.-I. C. Nilsen, A. C. Jensen, S. P. Näsholm, and S. Holm, "Coherent plane-wave compounding and minimum variance beamforming," in *2011 IEEE International Ultrasonics Symposium*. IEEE, 2011, pp. 2448–2451.

[340] L. Nie, S. Harput, D. M. Cowell, and S. Freear, "Velocity estimation error reduction in stenosis areas using a correlation correction method," in *2016 IEEE International Ultrasonics Symposium (IUS)*. IEEE, 2016, pp. 1–4.

[341] M. Tanter and M. Fink, "Ultrafast imaging in biomedical ultrasound," *IEEE transactions on ultrasonics, ferroelectrics, and frequency control*, vol. 61, no. 1, pp. 102–119, 2014.

[342] P. A. VanderLaan, H. H. Wang, A. Majid, and E. Folch, "Endobronchial ultrasound-guided transbronchial needle aspiration (ebus-tbna): An overview and update for the cytopathologist," *Cancer cytopathology*, vol. 122, no. 8, pp. 561–576, 2014.

[343] D. W. Rickey, P. Picot, D. Christopher, and A. Fenster, "A wall-less vessel phantom for doppler ultrasound studies," *Ultrasound in medicine & biology*, vol. 21, no. 9, pp. 1163–1176, 1995.

[344] E. L. Madsen, M. A. Hobson, H. Shi, T. Varghese, and G. R. Frank, "Tissue-mimicking agar/gelatin materials for use in heterogeneous elastography phantoms," *Physics in Medicine & Biology*, vol. 50, no. 23, p. 5597, 2005.

[345] D.-K. Lim, A. Barhoumi, R. G. Wylie, G. Reznor, R. S. Langer, and D. S. Kohane, "Enhanced photothermal effect of plasmonic nanoparticles coated with reduced graphene oxide," *Nano letters*, vol. 13, no. 9, pp. 4075–4079, 2013.

[346] S. Hwang, J. Nam, S. Jung, J. Song, H. Doh, and S. Kim, "Gold nanoparticle-mediated photothermal therapy: current status and future perspective," *Nanomedicine*, vol. 9, no. 13, pp. 2003–2022, 2014.

[347] I. Fratoddi, I. Venditti, C. Cametti, and M. V. Russo, "How toxic are gold nanoparticles? the state-of-the-art," *Nano Research*, vol. 8, no. 6, pp. 1771–1799, 2015.

[348] C. Carnovale, G. Bryant, R. Shukla, and V. Bansal, "Size, shape and surface chemistry of nano-gold dictate its cellular interactions, uptake and toxicity," *Progress in Materials Science*, vol. 83, pp. 152–190, 2016.